FLOW SIMULATIONS OF AXISYMMETRIC PROLATE PARTICLES IN A CYLINDRICAL PORE

by

Muhammad Jasim

A Thesis Presented to the Faculty of the
American University of Sharjah
College of Engineering
in Partial Fulfillment
of the Requirements
for the Degree of

Master of Science in
Mechanical Engineering

Sharjah, United Arab Emirates

January, 2015

Approval Signatures

We, the undersigned, approve the Master's Thesis of Muhammad Jasim.

Thesis Title: Flow Simulations of Axisymmetric Prolate Particles in a Cylindrical Pore

Signature	**Date of Signature** (dd/mm/yyyy)
Dr. Essam Wahba Associate Professor, Department of Mechanical Engineering Thesis Advisor	
Dr. Saad Ahmed Associate Professor, Department of Mechanical Engineering Thesis Committee Member	
Dr. Rami Hawileh Associate Professor, Department of Civil Engineering Thesis Committee Member	
Dr. Essam Wahba Interim Head, Department of Mechanical Engineering	
Dr. Mohamed El Tarhuni Associate Dean, College of Engineering	
Dr. Leland Blank Dean, College of Engineering	
Dr. Khaled Assaleh Interim Vice Provost for Research and Graduate Studies	

Acknowledgments

I would like to express the deepest and sincerest sense of gratitude to my advisor, Dr. Essam Moustafa Wahba, who guided me throughout the various phases of this thesis. A true mentor, he remained patient through my initial learning period and my mistakes. I would also like to thank Dr. Rami Antoun Haweeleh, Dr. Saad Ahmed, and Dr. Mehmet Fatih Orhan for providing their time to review and their feedback to improve this work with their expertise and valuable perspective.

I am forever indebted to the Department of Mechanical Engineering at the American University of Sharjah for the education I received throughout my studies.

Finally, I would also like to thank my beloved family, including my parents and my siblings, for their continued support and understanding.

Abstract

The motion of small particles in a fluid is a classical fluid mechanics problem. The present study investigates the motion of axisymmetric prolate spheroids and Cassini ovals of micro-scale through Newtonian and non-Newtonian fluids, bounded by a cylindrical pore. The drag force is numerically obtained over a range of Reynolds number, from creeping flow condition to Re = 40 (for steady state simulations). Both Newtonian and non-Newtonian fluid simulations are carried out, with power-law index values of 0.6, 0.8, 1.0, 1.2, and 1.4, while considering the wall effects due to the cylindrical pore confinement. CFD software package ANSYS CFX is used to model the steady motion of a particle translating in a quiescent fluid along the axis of a coaxial cylinder and to numerically solve the flow around the particle to calculate the coefficient of drag. It is shown that for the different values of power-law index, the drag coefficient increased with increased confinement and decreased with an increase in Reynolds number. The results for bounded creeping Newtonian flow were validated against analytical solutions in the literature. The results are found to be in accordance with the results available in the literature and based on theoretical expectations.

Search Terms: Non-Newtonian fluids, power law fluids, prolate spheroid, Cassini oval, drag force, wall effects

Table of Contents

List of Figures

List of Tables

Nomenclature

a	length of spheroid from the origin along the major axis (μm)
a/b	spheroid shape factor (dimensionless)
b	length of spheroid from the origin along the minor axis (μm)
b/R	confinement ratio (dimensionless)
c	Focus length of Cassini oval from the origin along the minor axis (μm)
Cd	coefficient of drag (dimensionless)
$(c/d)^2$	Cassini oval shape factor (dimensionless)
d	length of Cassini oval from the origin along the minor axis (μm)
F/Fo	normalized drag force (dimensionless)
K	consistency index for power law fluid ($Pa.s^n$)
n	power-law index (dimensionless)
R	radius of the cylindrical pore (μm)
Re	Reynolds number, Newtonian fluids (dimensionless)
Re_{CS}	Collins-Schowalter Reynolds number, non-Newtonian fluids (dimensionless)
Re_{MR}	Metzner and Reed Reynolds number, non-Newtonian fluids (dimensionless)
v	velocity of the particle (m/s)
Greek letters	
ρ	density of the fluid (kg/m^3)
ω	intermediate variable ω = log Re (dimensionless)
τ	shear stress (Pa)
$\dot{\gamma}$	shear rate (s^{-1})
ψ	stream function
λ	time constant for Bird Carreau and Carreau-Yasuda fluid models
μ	viscosity of the fluid (Pa.s)

Chapter 1. Introduction

1.1 Problem Statement

This thesis will investigate the effects of Newtonian and non-Newtonian properties of fluid, the effects of Reynolds number and the effects of flow confinement on the motion of particles of selected shapes. The study attempts to numerically investigate the translational motion of stationary axisymmetric prolate particles (spheroids and Cassini ovals), through Newtonian and non-Newtonian (shear-thinning and shear-thickening) fluids bounded by the walls of cylindrical pores.

Each prolate particle moves in the cylindrical pore through the fluid with a certain speed, while the cylindrical pore and the fluid are assumed to be stationary. As the particle moves through the fluid, it experiences a combination of drag forces, including pressure drag and friction drag. The total drag force is obtained using ANSY CFX to solve the equations governing the flow, i.e. the Navier-Stokes equations. The problem is normalized to get a dimensionless form by considering Reynolds number instead of velocity and coefficient of drag instead of drag force. This non-dimensionalization also takes into account the dimensions of the particle, the density and the viscosity of the fluid. The flow around the particle can also be visualized through velocity streamlines and pressure contours using built-in options in ANSYS CFX.

The axisymmetric prolate particles can be divided into two categories: spheroids and Cassini ovals. Each shape is defined by a unique equation where the shape of the particle varies with a shape factor. Each case will be solved for a range of shape parameters over a range of Reynolds number while varying the pore diameters with respect to the particle size.

1.2 Significance of the Research

The bounded and unbounded motion of small particles through a viscous fluid is of great practical importance in various fields of engineering and science, including applications in the fields of biomedical engineering, chemical and environmental engineering, and in interface and colloidal sciences.

In biomedical engineering, the motion of blood cells in plasma and other particles in the blood stream, such as vesicles and lipoproteins, is of great significance. The case of vesicles is of interest as these particles can be of various shapes depending on the external forces from the surrounding fluid. A vesicle can be modeled as a small sack of liquid enclosed in a membrane. The membrane is a plasma membrane and can be deformed easily. Vesicles can store or transport substances such as enzymes, digested cellular products and waste. They can also act as chemical reaction chambers. More importantly, artificially prepared vesicles, called liposomes, are of interest to modern biomedical engineers as they can be used for transportation of nutrients and pharmaceutical drugs through blood stream. It is reported that the vesicles, both natural and artificial, are affected by the flow [1] and the walls of the capillary [2]. Low density lipoproteins (LDLs) undergo similar shape shifting as they are also made of easily influenced proteins and lipids.

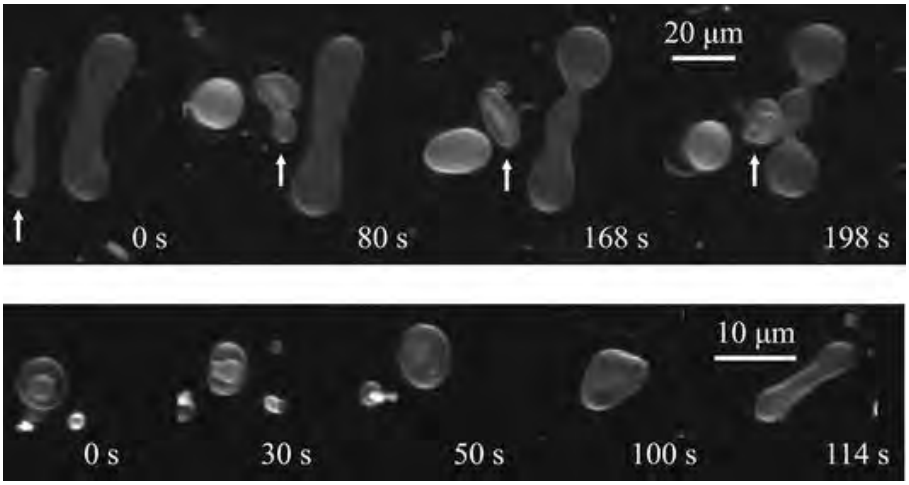

Figure 1: Vesicle of various shapes in blood [1]

Furthermore, blood behaves as a non-Newtonian fluid for shear stress values less than 100 s^{-1} as its viscosity is a function of the applied shear. In fact, blood is a shear-thinning fluid, i.e. its viscosity decreases with increase in shear rate.

Hong et al. [3] and Gijsen et al. [4] investigated the effects of non-Newtonian characteristics of plasma on LDL transportation in arterial wall. It was seen that for non-Newtonian flows, the filtration velocity was enhanced by the shear thinning effect when compared to Newtonian flows. The accumulation of macromolecules such as

low-density lipoprotein (LDL) in the intima layer is one of the risk factors for atherosclerosis. The increase in filtration velocity resulted in a higher LDL concentration, thus, elevating the risks of atherosclerosis. Therefore, it is important to model blood as a non-Newtonian fluid rather than a Newtonian fluid to properly evaluate risk factors.

Similarly, Wang and Bernsdorf [5] also suggested the use of more accurate rheology of blood and demonstrated the difference between Newtonian and non-Newtonian flow regimes using simulations for aneurysms. An aneurysm is the widening of a blood vessel to the point that, if ruptured, it can be life threatening. One of the solution is to divert the flow using a metal frame, medically known as a stent. Another solution, known as coiling, is to reinforce the vessel with wire. Both of these modifications can be studied extensively using computer simulations and their behavior can be predicted to ensure safety before installation. It was seen that for the case of non-Newtonian shear thinning blood model, the wall shear stress was lower when compared to the case of Newtonian fluid model. Therefore, it is important to model blood as non-Newtonian to avoid overestimation of wall stress as it can lead to adverse effects on the flow.

Other studies [4], [6]-[10] also concluded that non-Newtonian models of blood provide better results over Newtonian model when compared to experimental values especially for low shear rates. Other applications where the non-Newtonian properties of blood play an important role include the work of Sharma and Bhat [11], who performed experiments regarding non-Newtonian rheology of leukemic blood and plasma and found the power-law constants, n and K, to have different values when compared to the constants for healthy blood. In other words, these factors can be used as a measure of blood health.

In chemical engineering, microfluidics is an important field that deals with particles and flow on a micro scale. Microfluidics include microflows, microdrops, diffusion of nanoparticles, transport of nanoparticles, bioMEMS, reactions in biochips, micromechanical control of cells, and controlling the cellular environment [12]-[15]. It must be noted that most of the theory of macrofluidics, such as equations of motion, Navier-Stokes equations, etc., also apply to microfluidics. However, it is of interest to

investigate the non-Newtonian behavior of fluids in these micro systems. Another example in chemical engineering includes modeling the viscosity of emulsions which are often non-Newtonian in nature.

Wei et al. [16] studied the water-in-crude oil emulsions and developed a prediction model for the apparent viscosity of the non-Newtonian emulsions. Crude oil forms stable emulsions with water in presence of surface active components, namely asphaltenes and resins. These emulsions have higher apparent viscosity and exhibit non-Newtonian, shear-thinning behavior. This behavior affects most of the petroleum processes including exploitation, gathering and transportation. Therefore, it is important in chemical engineering to create accurate rheological models of such fluids by including non-Newtonian characteristics. Other applications can be found in transport phenomena. Examples include various studies in mass transport [17]-[20] and in heat transfer [21]-[23].

In environmental engineering, geophysical phenomena such as the flow of lava, snow avalanches, mud slides and debris flows, all have non-Newtonian characteristics. Lava is composed of molten rocks with silicate crystals and a microstructure of suspended bubbles. Although it can be up to 100,000 times more viscous than water, lava tends to flow great distances due to its non-Newtonian shear-thinning properties [24]. Lingyan Huang et al. demonstrated the effect of non-Newtonian rheology of mud flow [25].

A snow avalanche is the accelerating non-Newtonian flow of snow down a sloping surface, usually caused by mechanical failure in the snowpack. Bovet et al. [26] proposed a model for snow avalanche dynamics based on Bingham fluids model. Similar models can be used for mud avalanches. In debris flows, water-laden soil masses and rock fragments travel downhill as streams, carrying objects in their paths. Although they have higher overall densities compared to those of rock avalanches, due to the water content, the liquefaction of sediments as a result of high pore-fluid pressures, and the shear thinning effect, debris flows can flow almost as fluidly as water [27].

On micro level, environmental phenomena such as sedimentation and aerosol technology are of interest with regards to non-Newtonian characteristics of fluids in

environmental sciences. The settling of small particles in various non-Newtonian fluids has been studied thoroughly in various studies [28]-[31]. Similarly, aerosol technology applications also include the settling of particles in air. Some examples of aerosol technologies using non-Newtonian elements include biomedical technologies, microelectronics, occupational hygiene, pollution control, and coating of electronic chips. Certain types of particles tend to be micropolar fluids, such as polymers, lubricants, and paints, and cannot be modeled as Newtonian fluids without losing important non-Newtonian characteristics [32]. Therefore, non-Newtonian models should be used to describe the flow more accurately.

In interface and colloidal sciences, a colloid is defined as a heterogeneous system composed of nanoparticles dispersed throughout a continuous medium. Colloids are not like solutions, where one material is chemically dissolved in the other, as colloids are mechanical mixtures. Interface and colloid sciences have applications in nanotechnology, microfluidics, biotechnology, pharmaceuticals, minerals, and ceramics. The settling of particles in colloids is called flocculation. Although some studies [33], [34] exist that investigate the phenomenon by assuming Newtonian models, it must be noted that only few of the colloids can be modeled close to Newtonian behavior.

1.3 Objectives

The objectives of this study are to numerically investigate the effects of non-Newtonian characteristics, the effects of Reynolds number and on the translation of axisymmetric prolate particles in cylindrical pores for the following cases:

1. A Newtonian fluid model for creeping flow condition ($Re \ll 1$)
2. A Newtonian fluid model for low Reynolds number flows
3. A non-Newtonian fluid model for creeping flow condition
4. A non-Newtonian fluid model for low Reynolds number flows

1.4 Thesis Organization

The framework for the thesis report is given as follows:

- Chapter 1: Introduction, including problem statement, significance of the research, and objectives of the present study.
- Chapter 2: Review of the literature highlighting the effects of Newtonian and non-Newtonian characteristics, a review of non-Newtonian models, and the effect of Reynolds number.
- Chapter 3: Modelling, including problem formulation with the definitions of the cylindrical pore, the prolate particles (spheroids and Cassini ovals), the properties of the working fluid, the Reynolds number for Newtonian and non-Newtonian fluids, the boundary conditions, and the normalized Drag Force and coefficient of drag. This section also provides a brief introduction to CFD and how the fluid domain was solved using the CFD software package ANSYS CFX.
- Chapter 4: Results for creeping motion in Newtonian fluid (Case 1) including the effect of confinement ratio and the effect of particles shape for both spheroids and Cassini ovals.
- Chapter 5: Results for low Reynolds number motion in Newtonian fluid (Case 2) including the effect of Reynolds number, the effect of confinement ratio and the effect of particle shape for spheroids and Cassini ovals
- Chapter 6: Results for creeping motion in non-Newtonian fluid (Case 3) with similar analysis to Case 1.
- Chapter 7: Results for low Reynolds number motion in non-Newtonian fluid (Case 4) with similar analysis to Case 2. The effect of power-law index is also studied.
- Chapter 8: Conclusion highlighting the key findings of the study and ideas for future studies.

Chapter 2. Literature Review

2.1 Effects of Newtonian and non-Newtonian Flow Characteristics

Depending on the type of non-Newtonian fluid under study, non-Newtonian properties effect fluid behavior in various ways. This section reviews both the Newtonian model and the non-Newtonian fluid models.

2.1.1 Newtonian Flow Characteristics

The drag on particles moving in Newtonian fluids has been investigated thoroughly by various researchers. A variety of particles, including solids and liquids, have been studied in various fluids, using analytical methods for simplified models, numerical methods, and experimental procedures.

The most common problem of motion of a rigid sphere body in an unbounded Newtonian medium has been studied over the years since the works of Stokes [35]. Rewriting the non-dimensional momentum equation for spherical coordinates in terms of the stream function ψ, a highly non-linear equation is obtained, as follows:

$$\nabla^4\psi^* = \frac{\mathrm{Re}}{2}\left[\frac{\partial\psi^*}{\partial\theta}\frac{\partial}{\partial r^*}\left(\frac{\nabla^2\psi^*}{r^{*2}\sin^2\theta}\right) - \frac{\partial\psi^*}{\partial r^*}\frac{\partial}{\partial\theta}\left(\frac{\nabla^2\psi^*}{r^{*2}\sin^2\theta}\right)\right]\sin\theta \tag{1}$$

Where, ∇ is called the del operator. Since the above equation is highly non-linear, finding a general solution is not possible. However, approximate solution can be obtained for special cases. One such approximation is the creeping flow condition (Re = 0, or Re << 1) where the highly non-linear inertial terms on the right hand side of the equation are neglected. This yields what is known as the biharmonic equation:

$$\nabla^4\psi^* = 0 \tag{2}$$

Stokes solved the above fourth-order PDE and derived the expression for drag force F_D and the corresponding expression for coefficient of drag C_D are given as follows:

$$F_D = 6\pi\mu R v \tag{3}$$

$$C_D = \frac{24}{\mathrm{Re}} \tag{4}$$

Where μ is the viscosity, R is the radius of the sphere, v is the velocity of the fluid and Re is the Reynolds number. Note that the expression for drag is only valid for low Reynolds number flow. Experimentally, it is observed that the equations stay valid for flows with Reynolds number up to a value of 0.1. Beyond this value, the experimental results deviate from the Stokes solution.

Other researchers developed on the expression and increased the range of Reynolds number for which the expressions are valid. Oseen [36] came up with the following expression which is valid up to Reynolds number value of 1, with maximum 1% error from the experimental results:

$$C_D = \frac{24}{\mathrm{Re}}\left(1+\frac{3}{16}\mathrm{Re}\right) \tag{5}$$

Further improvements were made, first by Proudman and Pearson [37] and then by Ockendon and Evans (1972) [38] using series expansion, as follows:

$$C_D = \frac{24}{\mathrm{Re}}\left(1+\frac{3}{16}\mathrm{Re}+\frac{9}{160}\mathrm{Re}^2\log\frac{\mathrm{Re}}{2}+\frac{0.1879}{4}\mathrm{Re}^2+\ldots\right) \tag{6}$$

Similar extensions of the creeping flow solution can be found in the literature [39]-[42]. However, as the Reynolds number value increases above 1, these extensions of the creeping flow solution are no longer valid and the analytical solutions are not possible due to the increased significance of the non-linear inertial terms in the momentum equations. Therefore, to solve the momentum equation for Reynolds number higher than 1, the use of numerical methods is advised.

Jenson [43], using a finite difference method, obtain numerical results of drag coefficient for Reynolds number up to Re = 40. LeClair et al. [44] solved the Navier-Stokes equations numerically and obtained values of drag coefficient for Reynolds number up to Re = 400, while Fornberg [45] obtained values of drag coefficient for Reynolds number up to Re = 5000. A special case of finding the drag coefficient for the limit $\mathrm{Re}\rightarrow\infty$ was documented by Weisenborn and Bosch [46] using the method of induced forces. It was seen that over such large range of Reynolds number, the flow regimes for uniform flow over a sphere change drastically.

Johnson and Patel [47] and Cliffe et al. [48] studied, both numerically and experimentally, the various flow regimes including steady and unsteady laminar flow for Re < 300, while Mittal [49] studied the gradual changes in flow regime from steady axisymmetric flow, to steady non-axisymmetric flow, and then to unsteady non-axisymmetric. All these results can be collated in the form of a single curve relating the drag coefficient to the Reynolds number. This is referred to as the standard drag curve for translation of a sphere in an unbounded Newtonian fluid. Clift et al. [50] provides recommended drag correlations for the complete range of standard drag curve which are summarized in the Table 1.

Table 1: Drag correlations for standard drag curve, where ω = log Re [50]

Range	**Correlation**
Re < 0.01	$C_D = \frac{24}{\mathrm{Re}}\left(1+\frac{3}{16}\mathrm{Re}\right)$
0.01 < Re ≤ 20	$C_D = \frac{24}{\mathrm{Re}}\left(1+0.1315\,\mathrm{Re}^{(0.82-0.05\omega)}\right)$
20 ≤ Re ≤ 260	$C_D = \frac{24}{\mathrm{Re}}\left(1+0.1935\,\mathrm{Re}^{-0.6305}\right)$
260 ≤ Re ≤ 1500	$\log C_D = 1.6435 - 1.1242\omega + 0.1558\omega^2$
1500 ≤ Re ≤ 1.2 x 10^4	$\log C_D = -2.4571 + 2.5558\omega - 0.9295\omega^2 + 0.1049\omega^3$
1.2 x 10^4 ≤ Re ≤ 4.4 x 10^4	$\log C_D = -1.9181 + 0.637\omega - 0.0636\omega^2$
4.4 x 10^4 ≤ Re ≤ 3.38 x 10^5	$\log C_D = -4.339 + 1.5809\omega - 0.1546\omega^2$
3.38 x 10^5 ≤ Re ≤ 4 x 10^5	$C_D = 29.78 - 5.3\omega$
4 x 10^5 ≤ Re ≤ 10^6	$C_D = 0.1\omega - 0.49$
10^6 < Re	$C_D = 0.19 - \left(\frac{8\times10^4}{\mathrm{Re}}\right)$

As noted, the standard drag curve is valid for unbounded flows over a sphere only and cannot be used for cases of bounded flow or for different shape of solids. Yeh and Keh [51] did an analytical study of the drag on a prolate particle moving in a cylindrical pore through a Newtonian fluid for axisymmetric creeping flow conditions and developed expressions for the drag force experienced. It was found that the

normalized drag force is a function of the shape of the particles and the relative size of the particle with respect to the pore. These results will be used as the basis to compare the numerical results obtained using CFD analysis in this study to the analytical results for the case of creeping motion of axisymmetric prolate particle in Newtonian fluids. However, the effects of non-Newtonian properties of fluid and the effects of Reynolds number are to be investigated.

2.1.2 Non-Newtonian Flow Characteristics

Research on the drag experienced by particles in non-Newtonian fluids is scarce. Non-Newtonian fluids considered for the purpose of this thesis are shear-thinning and shear-thickening power-law fluids. Shear-thinning fluids have the property that their viscosity decreases with increase in shear rate. Shear-thickening fluids, on the other hand, have the property that their viscosity increases with increase in shear rate. The properties of non-Newtonian fluids will further be explained in section 2.2.

The efforts so far have been directed to establish a non-Newtonian standard drag curve equivalent to the Newtonian standard drag curve for spheres in unbounded domain. Starting with the creeping flow condition, the continuity and momentum equations are simplified by ignoring the inertial terms. However, unlike the case of Newtonian fluids with constant viscosity, the simplified equations are highly non-linear because of the viscosity being a function of the shear rate. Therefore, a solution similar to the aforementioned Stokes solution cannot be obtained for the case of non-Newtonian fluids.

Theoretical or numerical approximations are used instead to find solution to the governing equations. Theoretical methods such as forms of variational principle or linearization and perturbation methods can be used. Numerical methods such as finite element, finite volume, finite difference, boundary elements, and extended moment method are commonly used.

Analytical solutions for non-Newtonian flow over a sphere are very rare. Ceylan et al. [52] proposed a theoretical model for estimation of drag force on spherical solid particles flowing in weak non-Newtonian fluids only for a wide range of Reynolds

number, ranging from creeping flow to Re = 1000. Modifying Navier-Stokes equation using a stream function and the energy dissipation equation, analytical relations were derived for the drag coefficients.

Variational principles method is the most widely used in older research. Tomita [53] derived the fundamental equations of motion for shear thinning and shear thickening non-Newtonian fluids and proved that for a case where inertia terms are neglected, i.e. the creeping flow condition, and the external forces are derived from a potential or zero, the minimum energy dissipation equations are equivalent to the equations of motion. The solution was obtained using velocity variational principle. Wallick et al. [54] developed on these results and provided necessary corrections. Slattery [55], and Foster and Slattery [56] also used the velocity variational principle but for Reiner-Rivlin fluid model. These results are not considered accurate as certain assumptions were questioned by Leigh [57].

Other examples of velocity variational principle include works of Leonov (1988) [58] for power-law model, Ziegenhagen et al. [59] for truncated power-law model, Slattery [60] for power-law and Sisko fluid models, Ziegenhagen [61] for Powell-Eyring model, Mitsuishi et al. [62] for Sutterby model, Chhabra et al. [63] and Chhabra and Uhlherr [64] for power-law and Carreau viscosity model. Wasserman and Slattery [65] used velocity variational principles as well as stress variational principles for power-law model. The method calculates the upper and lower bounds of the drag coefficient. However, the results showed poor agreement with the experimental results and, hence, were later extended by Cho and Hartnett [66]. Hopke and Slattery [67] also used velocity and stress variational principles but for Ellis fluid model. The results of Hopke and Slattery were later extended by Chhabra et al. [68].

Linearization and perturbation methods are also used for non-Newtonian fluids. Acharya et al. [69] linearized momentum equations for power-law model fluids, resulting in an approximate closed from expression for drag coefficient. This expression was later corrected by Lockyear et al. [70] and further improved by Kawase and Ulbrecht [71]. In a separate work, Kawase and Ulbrecht [72] linearized the field equations for power-law model and studied the influence of power-law index on drag coefficient and on wall effects.

Rathna [73] used perturbation scheme for Reiner-Rivlin model fluids providing a first order correction for the Stokes drag. Yoshioka and Nakamura [74] used perturbation method for generalized Newtonian fluid observing that the predicted results provided very little deviation from the Stokes drag. Koizumi [75] used perturbation method for power-law model fluids and provided an approximate closed from expression for drag coefficient. A similar method was used by Kawase and Moo-Young [76]. Shmakov and Shamakova [77] evaluated drag on a sphere for shear-driven flow of power-law fluids using perturbation method.

With the advent of Computational Fluid Dynamics (CFD) solvers, numerical methods for solving have become more popular for finding solutions for the Navier-Stokes equations. Adachi et al. [78] provided numerical solution for power-law model fluids and provided results for drag coefficient for a range of power-law index between $0.8 < n < 1$ and for Reynolds number value $Re = 60$. Adachi et al. [79] also provided numerical solution for extended Williamson model. Crochet et al. [80] used finite element method and provided drag results for shear-thinning power-law fluids ($0.1 < n < 1$).

Gu and Tanner [81] provided solution for drag and wall effects using finite element method for power-law fluids with index between $0.1 < n < 1$. Tripathi et al. [82] and Tripathi and Chhabra [83] calculated drag on spheres and spheroids for power-law fluids using finite element method for index $0.4 \leq n \leq 1.8$ and Reynolds number $Re \leq 100$. Graham and Jones [84] provided drag values on spheres for $Re \leq 130$. Whitney and Rodin [85] provided drag correction factor for a sphere and a cylinder for power-law fluids. Kishore et al. [86] studied the drag on a single fluid sphere translating in non-Newtonian power-law fluids at moderate Reynolds numbers ($5<Re<500$).

Other studies of motion of particles in non-Newtonian medium are experimental. These are, however, very specific problems and do not directly contribute to the development of the non-Newtonian drag curve. Becker et al. [30] studied the free sedimentation of a rigid sphere near a single vertical plane wall in a non-Newtonian fluid. The sedimentation particles not only experience non-Newtonian effects while settling, they are also effected by fluid inertia and the presence of solid bounding surfaces. Examples include process such as the motion of drilling muds in boreholes,

gravity-driven drainage of paints, coating processes for thin films, falling-ball viscometry, and pumping of slurries.

The sedimentation process included the settling of the particle while simultaneously rotating. This process was studied using Deborah number for second order non-Newtonian fluids for Reynolds number of up to first order. It was found, both numerically and experimentally, that the shear-thinning effects of the fluid viscosity cause the sphere to rotate more slowly when compared to a Newtonian fluid. It was also found that for higher Deborah numbers, this effect may lead to anomalous rotation of the particle. The anomalous rotation referred to the observation that for low Reynolds number motion in non-Newtonian fluids, due to non-linearities, the spheres would drift towards the wall, opposite to the direction expected in Newtonian fluids. This effect was also observed earlier by Tanner [87]. Therefore, it can be seen that the behavior of particles Newtonian and non-Newtonian fluids can differ significantly. Shah et al. [31] also proposed a new model to find the drag and terminal velocity of spherical sedimentation particles.

Other similar cases in literature include the investigation of the drag to find the free settling velocity of cylinders and disks falling in non-Newtonian fluids by Rajitha et al. [88], the experimental and numerical investigation of the motion of spherical and cylindrical particles in non-Newtonian fluids inside a tube by Pereira [89], and the work of Sahu et al. [90] in study of two-dimensional laminar flow of power-law fluids across a square cylinder.

2.2 Review of non-Newtonian Models

Newtonian fluids are defined by a linear relationship between the shear stress and shear strain graph passing through the origin. If the graph in non-linear or if it doesn't pass though the origin, the fluid is regarded as non-Newtonian. In other words, the viscosity of a non-Newtonian fluid, measured as the slope of the shear stress-shear strain curve, is not constant like the viscosity of a Newtonian fluid. Non-Newtonian fluids can be divided into three main categories:

1. Viscoelastic fluids
2. Time-dependent non-Newtonian fluids
3. Time-independent non-Newtonian fluids

A viscoelastic fluid, as the name suggests, is a fluid that exhibits both viscous and the elastic properties when deformed. In other words, he fluid behaves both as a fluid due to its viscosity and as a solid due to its elasticity. Examples of viscoelastic fluids include polymeric solutions and polymeric melts, emulsions, foams, gels, soap solutions, and synovial fluid. The elastic properties of viscous fluids show similar behavior as the elastic properties of solid. When stress is applied, an elastic solid deforms elastically based on the linear slope of the stress-strain curve known as Young's modulus. Upon releasing the stress in the linear elastic region, the body deforms back to the original condition. This can be seen in Figure 2. However, if the applied stress exceeds the characteristic yield of the material, the material deforms plastically and upon releasing the stress, it is unable to restore to the original condition. The phenomenon of not achieving a complete recovery is known as creep. Similar analysis can be done for elasticity of viscoelastic fluids. When stress is applied and removed from a viscoelastic substance, it loses energy. Hysteresis, as seen in Figure 3, is observed in the stress-strain curve. The energy lost can be obtained by calculating the area of the hysteresis.

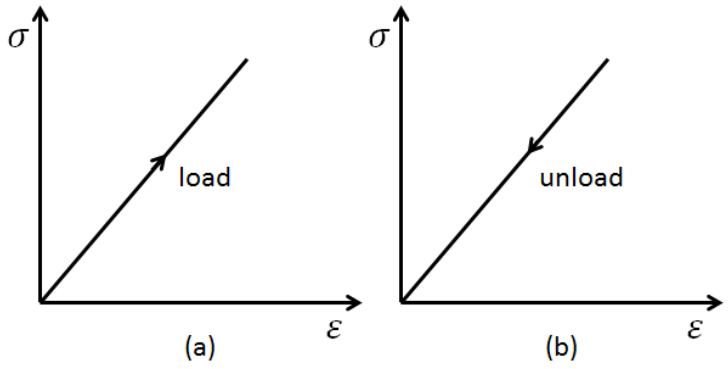

Figure 2: Stress-strain curves for purely elastic material for (a) loading (b) unloading

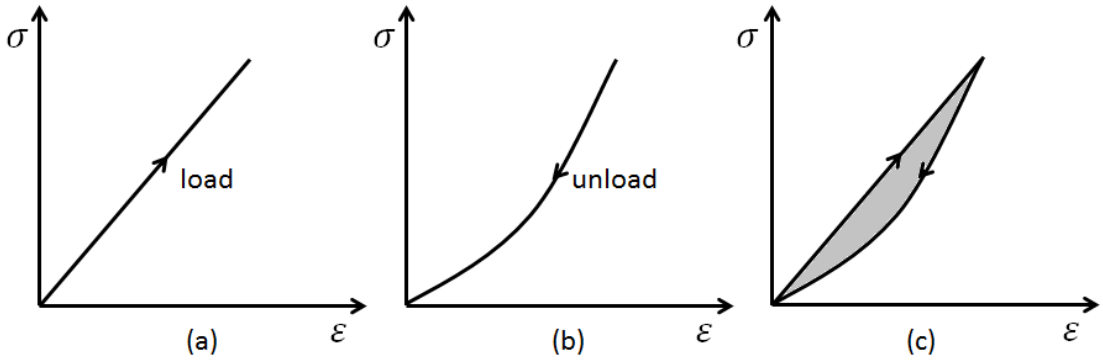

Figure 3: Stress-strain curves for viscoelastic material for (a) loading condition, (b) unloading condition, (c) hysteresis and energy lost (shaded)

Most substances like pharmaceuticals, personal care products and food items tend to change their properties over time. One such property is the change of viscosity of the fluid components with the passage of time. Examples include yogurt, gum solutions, various gels including iron oxide, gelatin, and pectin, castor oil, specific types of clay, some types of drilling mud, and many types of paint. A time-dependent fluid has a viscosity that is dependent on the shear rate and on the kinematic history of the shear rate for which the fluid has been under the application of a shear stress. Depending upon their response to shear over a period of time, time dependent behavior can be divided into two categories, thixotropy and rheopexy. Thixotropic behavior can be defined as when the apparent viscosity of a fluid decreases with the duration of stress. On the other hand, when the apparent viscosity of the fluid increases with the duration of stress, it is known as rheopecty.

Time-independent fluids are not affected by the prior history of the shear rate. The viscosity of these fluids depends only on the instantaneous shear rate and the corresponding shear stress value. In other words, such fluids do not have a memory of their past. Time-independent fluids may be divided into three further categories, Newtonian fluids, shear thinning fluids, and shear thickening fluids. Newtonian fluids, as discussed in earlier, exhibit a linear relationship between shear stress and shear strain rate. A fluid is called shear thinning, or pseudoplastic, when the apparent viscosity of the fluid increases with an increase in applied stress. Examples include blood, ketchup, syrups, whipped cream, paper pulp, nail polish, latex paint, and molasses. Conversely, a fluid is called shear thickening, or dilatant, when the apparent viscosity of the fluid

increases with an increase in applied stress. Examples include sand and water mixtures and corn starch suspensions in water. This study deals with the shear-thinning and shear-thickening effects of non-Newtonian fluids on the flow characteristics.

Although there is no general consensus among researchers and the CFD community about one standard model for numerically modeling non-Newtonian fluids, there are numerous models available in the literature to accomplish this task. Each model has its own advantages and disadvantages. Some of these models are already available in ANSYS CFX. The models that are not preprogrammed in ANSYS can, however, be programed by the users manually. Although case specific models can be developed, such as Cho and Kensey model, Walburn and Schneck model, model by Ballyk et al., and Fung model for modeling blood as a non-Newtonian fluid, this section summarizes the important models for general non-Newtonian fluids.

2.2.1 Power-law or Ostwald-de Waele model

Power-law [91], [92] is a generalized model for Newtonian and non-Newtonian fluids for which the shear stress can be given as follows:

$$\tau = K\left(\frac{\partial u}{\partial y}\right)^{n} \tag{7}$$

where τ is the shear stress, K is called the consistency index, $\partial u/\partial y$ is the velocity gradient or the shear rate, and n is called the power-law index and it depends on the type of fluid. For pseudoplastics (shear-thinning fluids), n is less than 1. For Newtonian fluids, n is equal to 1. For dilatants (shear-thickening fluids), n is greater than 1.

Rearranging the equation to get an equation similar to Newtonian fluids:

$$\tau = K\left(\frac{\partial u}{\partial y}\right)^{n-1}\frac{\partial u}{\partial y} \tag{8}$$

Comparing the above equation to the equation for Newtonian fluids given as:

$$\tau = \mu\frac{\partial u}{\partial y} \tag{9}$$

The effective viscosity (also known as the apparent viscosity), μ, for power-law fluids can be given as follows:

$$\mu_{eff} = K\left(\frac{\partial u}{\partial y}\right)^{n-1} \tag{10}$$

The Ostwald–de Waele power-law model is the most widely used viscosity model because of the simplicity of the mathematical relationship. However, it must be noted that this model, like all other models, only approximates the behavior of an actual non-Newtonian fluid, resulting in deviations from the real case. Here, the model behavior is not bounded on both the low and the high shear limits. In case of n being less than one, according to the power-law, increasing the shear rate would result in the effective viscosity decrease indefinitely. Such a fluid would, therefore, have infinite viscosity at rest and zero viscosity when the shear rate approaches infinity. This is not physically possible in real fluids where the minimum and the maximum effective viscosities of the fluid depend on the physical chemistry at the molecular level. Hence, the power-law is a good model for fluids only over a range of shear rates values.

Although other models exist that can model shear-dependent fluids over a broader range and are better at describing the entire flow behavior, they are more complex and come at the expense of simplicity. Experimental data for aqueous dispersion of polymer latex spheres, molten chocolate, and ball point pen ink can be fitted using the Ostwald–de Waele power law model. It must be noted that ANSYS CFX provides built-in support for power-law modeling of non-Newtonian fluids. For older versions of the software, the model is easy to program manually.

2.2.2 Bird Carreau model

The Bird Carreau model [93], or simply known as the Carreau model, is a constitutive model that models the entire shear history of the fluid. Most types of non-Newtonian fluids can be modeled using this model. However, it is more widely used for shear-thinning fluids.

$$\mu = \mu_{\infty} + \frac{\mu_0 - \mu_{\infty}}{\left(1 + (\lambda\dot{\gamma})^2\right)^{\frac{1-n}{2}}} \tag{11}$$

Where, μ_0 is low shear viscosity, μ_∞ is high shear viscosity, λ time constant, n is the power-law index and $\dot{\gamma}$ is the shear rate.

The Carreau model is better compared to power-law model as it takes into account the upper and lower boundaries μ_0 and μ_∞, respectively, in the model. At high shear rates the non-Newtonian fluid acts as a Newtonian fluid with viscosity μ_∞ and at low shear rates the non-Newtonian fluid acts as a Newtonian fluid with viscosity μ_0. However, it is more complex compared to power-law since it takes into account the shear history, introducing time constant λ into the model.

Experimental data for molten polystyrene, blood and other common shear-thinning fluids can be fitted using the Bird Carreau model. It must be noted that ANSYS CFX provides built-in support for Bird Carreau model for non-Newtonian fluids.

2.2.3 Carreau-Yasuda model

The Carreau-Yasuda model [94] for effective viscosity can be given as follows:

$$\mu = \mu_\infty + \frac{\mu_0 - \mu_\infty}{\left(1 + \left(\lambda\dot{\gamma}\right)^a\right)^{\frac{n-1}{a}}} \tag{12}$$

Where, μ_0 is low shear viscosity, μ_∞ is high shear viscosity, λ time constant, n is the power-law index, $\dot{\gamma}$ is the shear rate and a is called the Yasuda exponent.

Similar to the Carreau model, the Carreau-Yasuda model takes into account the upper and lower boundaries of viscosity μ_0 and μ_∞, respectively, in the model. At high shear rates the non-Newtonian fluid acts as a Newtonian fluid with viscosity μ_∞ and at low shear rates the non-Newtonian fluid acts as a Newtonian fluid with viscosity μ_0. Furthermore, the Yasuda exponent, a, provides a better model of non-Newtonian fluids. However, this model is more complex as it requires finding Yasuda exponent for the fluid empirically. It must be noted that ANSYS CFX provides built-in support for Carreau Yasuda model for non-Newtonian fluids.

2.2.4 Casson model

The Casson model [95] for effective viscosity can be given as follows:

$$\sqrt{\mu} = \sqrt{\frac{\tau_Y}{\dot{\gamma}}} + \sqrt{K} \tag{13}$$

Where τ_Y is the yield stress, K is called the consistency index, and $\dot{\gamma}$ is the shear rate.

The Casson model provides good curve fit for experimental data with shear rates greater than 1. However, the Casson model fails to fit the data over a wide range and is only valid over a small range of the shear rate values. Therefore, it is mostly assumed that the entire range of data can rather be fit by three separate Casson equations; first for the lowest range of data, second for the intermediate range and third for the highest range of shear rates. The first equation, with the lowest shear rate range, can be used to extrapolate to get the true yield stress from the zero shear rate condition. It must be noted that ANSYS CFX provides built-in support for Casson model for non-Newtonian fluids.

2.2.5 Cross model

The effective viscosity according to Cross model [96] is given as:

$$\mu = \mu_\infty + \frac{\mu_0 - \mu_\infty}{\left(1 + \alpha\dot{\gamma}^n\right)} \tag{14}$$

Where μ_0 is low shear viscosity, μ_∞ is high shear viscosity, n is the power-law index, $\dot{\gamma}$ is the shear rate and α is the model constant.

Cross model is based on the assumption that the non-Newtonian flow is associated with formation and rupture of structural links. Similar to the Carreau and the Carreau Yasuda model, Cross takes into account the upper and lower boundaries of viscosity μ_0 and μ_∞, respectively, in the model. At high shear rates the non-Newtonian fluid acts as a Newtonian fluid with viscosity μ_∞ and at low shear rates the non-Newtonian fluid acts as a Newtonian fluid with viscosity μ_0. Furthermore, the constant α relates to the rate of rupture of linkages is to be evaluated numerically. This adds to the complexity of the model. It must be noted that ANSYS CFX provides built-in support for Casson model for non-Newtonian fluids.

2.3 Effect of Reynolds number

It is known that the drag force on a body can be calculated using the following equation:

$$F_D = \frac{1}{2}\rho C_D A v^2 \tag{15}$$

Where F_D is the drag force which depends on the density ρ, the drag coefficient C_D, the area A, the velocity of the body v.

For a case where a one fluid is being studied, the density remains the same. Furthermore, when the same body is being studied, the drag coefficient remains constant since it is a geometric parameter, and the area remains the same. Therefore, the only factor that effects the drag is the velocity, or in more general terms, the Reynolds number.

As seen in section 2.1.1, solutions for unbounded flow over a sphere are have been obtained over a large range of Reynolds number starting from the Stokes solution for Newtonian creeping flow. It can be seen in section 2.1.2 that efforts to create a similar standard drag curve for non-Newtonian fluids are still very limited.

Chapter 3. Numerical Modelling of the Fluid Domain

3.1 Problem Formulation

The axisymmetric motion of a general prolate particle moving with a velocity U along the axis of a cylindrical pore through a motionless fluid, whether Newtonian or non-Newtonian, is modelled in this section by considering each element individually. The model can be divided into the cylindrical pore, the moving particle, the viscous fluid through which the particle is moving, and the velocity of the particle in terms of the Reynolds number. Figure 4 shows a general geometric sketch for the model. In theory, it is assumed that the cylinder of infinite length, i.e. the inlet and the outlet are far away from the particle. It is also known that the walls of the cylindrical pore are stationary.

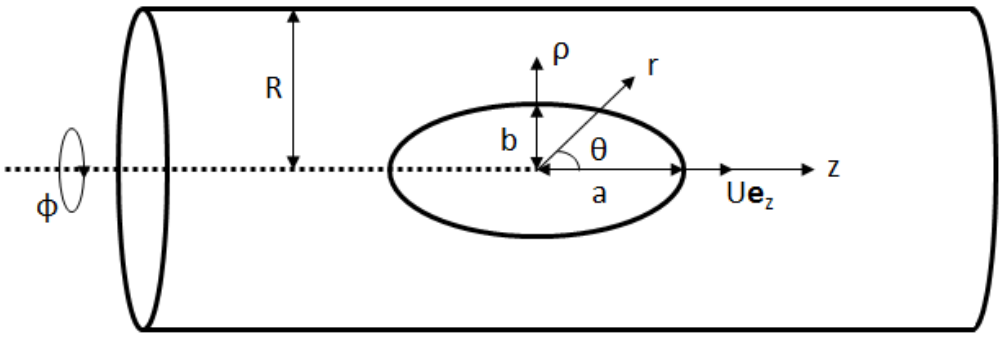

Figure 4: Model of the cylindrical pore and the prolate particle

3.1.1 Cylindrical Pore

The cylindrical pore that contains the fluid and particle is shown in Figure 4, where (ρ, ϕ, z) form the cylindrical coordinate system. The prolate particle, with length a in the major axis and length b in the minor axis, moves along the axis z with a velocity U. This direction is given in vector form as the unit vector e_z. The cylinder has a radius of R. As the radius R changes, while b remains constant, the ratio b/R changes and as a result, the drag force on the particle changes. This happens because the presence of the wall leads to the confinement of the flow near the particle. Therefore, the drag force is calculated for different b/R ratios (between 0.1 to 0.8). It is expected that the drag force in case of bounded flow is greater than the case unbounded flow.

3.1.2 Prolate particles

The types of prolate particles can be divided into two main categories: prolate spheroids and prolate Cassini ovals. This section provides a detailed description of each type.

3.1.2.1 Prolate Spheroid

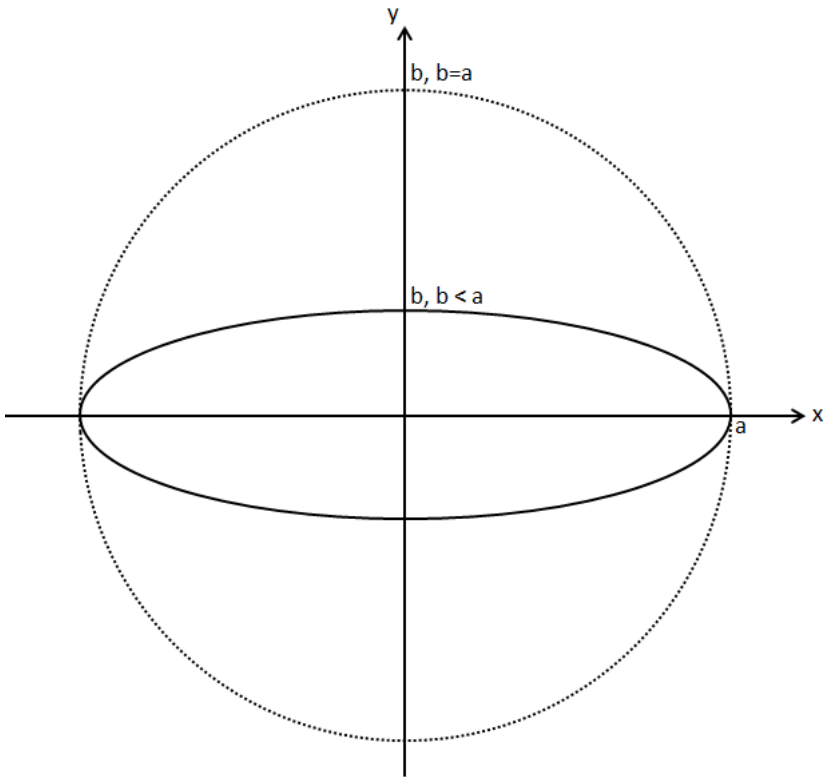

Figure 5: Prolate spheroid force case b < a and corresponding sphere when b = a

A spheroid, as seen in Figure 5, (also known as ellipsoid of revolution) is an axisymmetric surface which is obtained by rotating an ellipse about either its major axis or its minor axis. When the ellipse is rotated about its minor axis, the resulting spheroid is called an oblate spheroid. This can be seen in Figure 6. When the ellipse is rotated about its major axis, the resulting spheroid is called a prolate spheroid. This can be seen in Figure 7.

In blood, most of the particles are can be modeled as prolate spheroids instead of oblate spheroids. The ellipse, from which the prolate spheroid is constructed, takes different shapes based on the lengths of the two axes. The length from the origin to the

ellipse parameter along the major axis is usually donated by *a* whereas the length from the origin to the ellipse parameter along the minor axis is usually donated by *b*. The equation of the ellipse is given as follows:

$$\frac{x^2}{a^2}+\frac{y^2}{b^2}=1 \qquad \Rightarrow \qquad y=b\left[1-\left(\frac{x}{a}\right)^2\right]^{\frac{1}{2}} \tag{16}$$

Based on the ratio *a/b*, the ellipse changes from a sphere when *a/b* is 1 to a needle when *a/b* is ∞. As the *a/b* ratio changes, the drag force on the particle also changes. Therefore, the drag force is calculated for different *a/b* ratios.

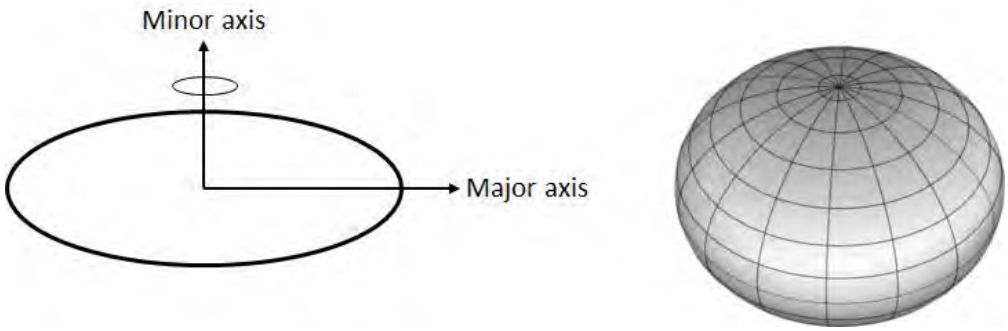

Figure 6: Oblate Spheroid

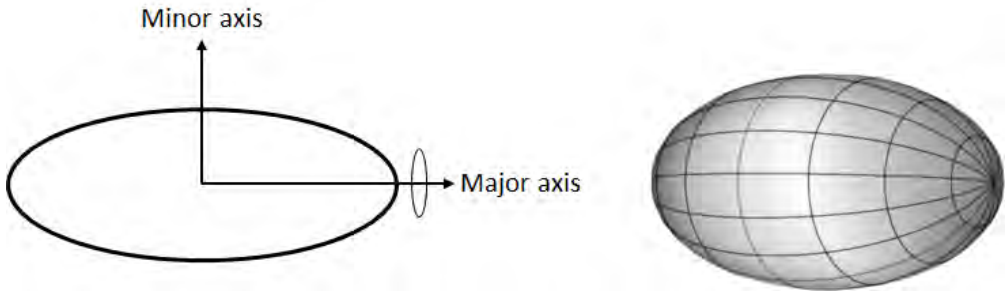

Figure 7: Prolate Spheroid

3.1.2.2 Prolate Cassini Oval

The Cassinian Ovals (also called Cassini ellipses and Ovals of Cassini) were first studied by Giovanni Domenico Cassini in 1680 as a proposed model for the then believed phenomenon of movement of the Sun around the Earth. A Cassini oval consists of two foci separated by a distance of *2c* (one foci at *+c* and other at *-c*) and

any point on the surface of the oval can be described such that the product of its distances from two foci, r_1 and r_2, is constant d^2. This can be seen in Figure 8.

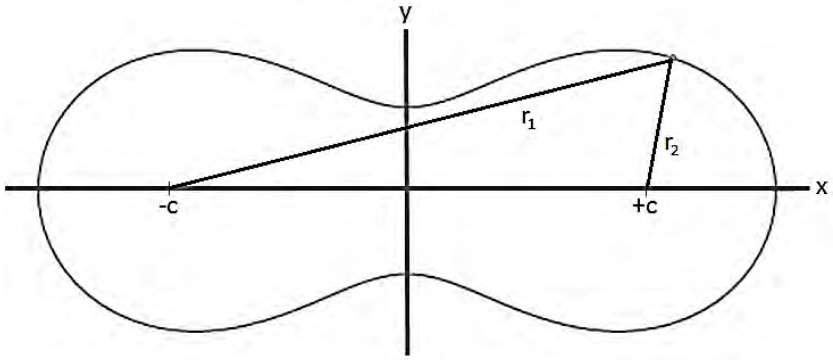

Figure 8: Cassini Oval

Mathematically, the surface of a Cassini oval can be defined as follows:

$$r_1 r_2 = d^2$$

$$\Rightarrow \quad \sqrt{(x+c)^2 + y^2}\sqrt{(x-c)^2 + y^2} = d^2$$

$$\Rightarrow \quad y = \left[\left(d^4 + 4c^2x^2\right)^{\frac{1}{2}} - x^2 - c^2\right]^{\frac{1}{2}} \tag{17}$$

The Cassini oval differs from a spheroid in the way that it can transform from a convex contour to a partially concave contour. The shape depends on the ratio $(c/d)^2$. As the ratio changes, the drag force experienced by the particle also changes. Hence, the drag force is calculated for different $(c/d)^2$ ratios. Some of the cases are shown in Figure 9.

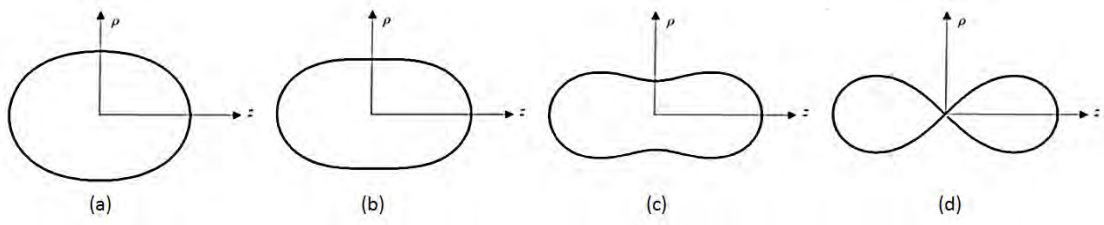

Figure 9: Cassini Ovals for $(c/d)^2$ ratios of (a) 0.3, (b) 0.5, (c) 0.8, (d) 1.0 [27]

Rotating the Cassini oval about its major axis results in a prolate oval, whereas rotating it about the minor axis results in an oblate oval. The prolate and oblate cases are shown in Figure 10 and Figure 11, respectively.

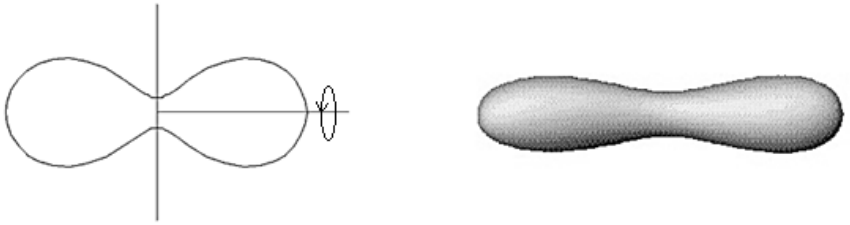

Figure 10: Prolate Cassini oval

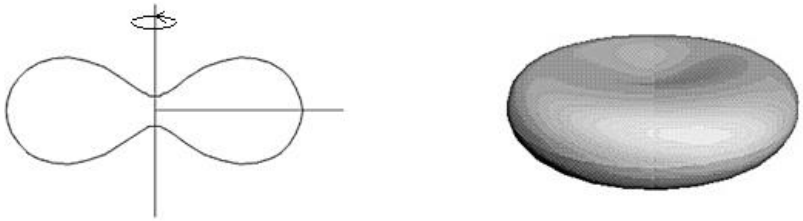

Figure 11: Oblate Cassini oval

3.1.3 Working fluid

The most important property that separates Newtonian and non-Newtonian fluids is the relationship of viscosity with the shear stress. When simple shear is applied, a Newtonian fluid responds linearly between the applied shear stress and the rate of shear. If the response is not characterized by such behavior, it is classified as a non-Newtonian fluid. It must be noted that sometimes non-Newtonian fluids can be modeled as a Newtonian fluid, especially for small shear rates, for simplification of problems.

3.1.3.1 Newtonian fluids

When modeling a Newtonian fluid, the viscosity is taken to be constant. Furthermore, as discussed in the literature review, for Newtonian fluids the viscous stresses due to the flow are directly proportional to the strain rate. In other words, they have a linear stress. Mathematically:

$$\tau = \mu \frac{du}{dy} \tag{18}$$

where τ is the shear stress, μ is the viscosity and du/dy is the rate of change of velocity u with respect to y.

Special cases exist where a non-Newtonian fluid may behave as a Newtonian fluid under certain conditions. For example, based on the work of Repogle et al. [97], it is widely accepted that blood acts as a Newtonian fluid, with constant viscosity for shear rates higher than 100 s^{-1}. This can be seen from Figure 12.

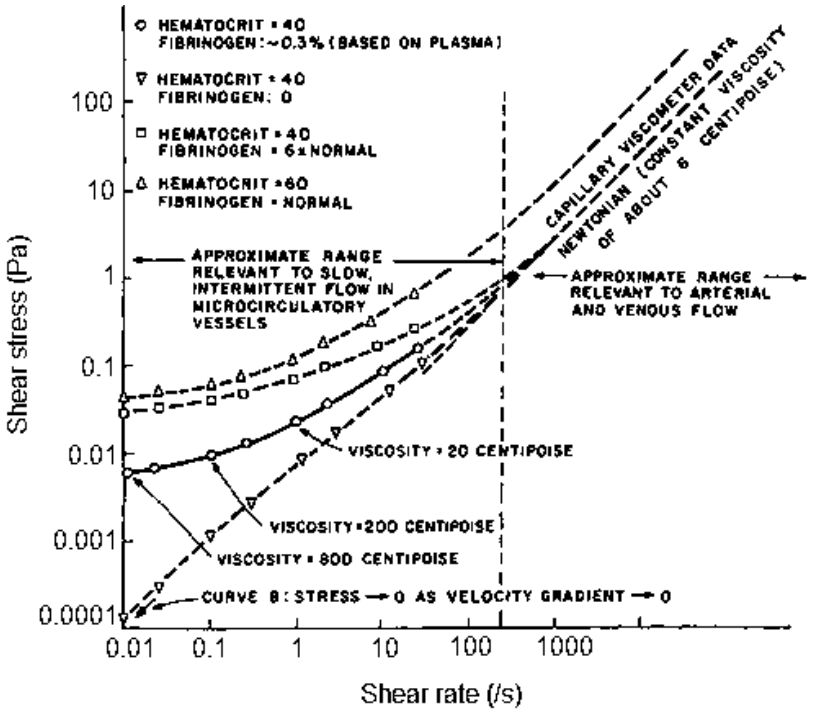

Figure 12: Shear stress versus shear rate for blood [97]

3.1.3.2 Non-Newtonian fluids

Of the various models for non-Newtonian fluids discussed in detail in the literature review section, the simplest model for the effective viscosity, μ, is the power law model. This can be given as follows:

$$\mu = K\left(\frac{\partial u}{\partial y}\right)^{n-1} \tag{19}$$

where K is the consistency factor and n is the power law index. For example, in the case of blood, K is equal to 0.0035 Pa.s [98], [99] and n is taken to be between 0.6-0.7 [100].

3.1.4 Reynolds Number

The Reynolds number of a particle moving though a Newtonian fluid can be calculated as follows:

$$\mathrm{Re} = \frac{\rho v D}{\mu} \tag{20}$$

where, ρ is the density of the fluid, v is the velocity of the particle, D is the length of the particle along the direction of flow and μ is the viscosity of the fluid. Referring to the general model in figure 4, D is given as 2a measured along the direction of flow, z-axis.

For non-Newtonian fluids, calculating the Reynolds number is not as trivial. As explained by Chhabra and Richardson [101], since the viscosity of non-Newtonian fluids is variable, it is difficult to correctly define a Reynolds number as the ratio of inertia forces to viscous forces. One of the most straightforward definition for Reynolds number of non-Newtonian fluids, based on a characteristic shear rate, is called the Collins-Schowalter Reynolds number and is defined as follows:

$$\mathrm{Re}_{CS} = \frac{\rho v^{2-n} D^n}{K} \tag{21}$$

where, n is the power-law index and K is called the consistency index. This relation is simply derived from simple dimensional analysis. Although Collins-Schowalter Reynolds number is simple and has been used almost exclusively in the past, it is known that it is not the best definition.

Alternatively, Metzner and Reed [102] correlated the pressure drop data for a fully-developed flow of non-Newtonian fluid in a pipe and derived the following definition for Reynolds number:

$$\mathrm{Re}_{MR} = \frac{\rho v^{2-n} D^n}{K} 8 \left(\frac{n}{6n+2} \right)^n \tag{22}$$

The definitions of Collins-Schowalter and Metzner and Reed Reynolds numbers can be related as follows:

$$\mathrm{Re}_{MR} = 8\left(\frac{n}{6n+2}\right)^{n} \mathrm{Re}_{CS} \tag{23}$$

For creeping motion, the velocity is selected such that the Reynolds number is very small, almost equal to zero. For cases with higher order Reynolds number, the velocity is calculated based on the Reynolds number.

3.1.5 Boundary Conditions

Based on the model definition, the particle moves with a velocity U through a stationary fluid and the pore walls are at rest as well. This can conversely be defined as the particle being stationary, and the fluid and wall moving at the velocity U. In this case the boundary conditions become:

1. Velocity U at the inlet
2. Static pressure at the outlet
3. Velocity U at the wall

3.1.6 Normalized Drag Force and Coefficient of Drag

The drag force for the creeping flow condition calculated from ANSYS is normalized using the following parameter as F/F_o [51]:

$$F_0 = -6\pi\eta b U\left\{\frac{3}{4}\left(\tau^2-1\right)^{\frac{1}{2}}\left[\left(\tau^2+1\right)\coth^{-1}\tau-\tau\right]\right\}^{-1} \tag{24}$$

$$where \quad \tau = \frac{a}{\sqrt{a^2-b^2}}$$

F_0 is the hydrodynamic drag force acting on a prolate spheroid translating in an unbounded fluid, η is the viscosity of the fluid, b is the length in the major axis, and U is the velocity of the particle. For all other cases, the drag coefficient is calculated:

$$C_D = \frac{F_D}{\frac{1}{2}\rho A v^2} \tag{25}$$

3.2 Modeling of the Fluid Domain using CFD

3.2.1 Introduction to CFD

Computers have been used to find solutions to fluid flow problems, especially when finding the analytical solution is not possible. This is regarded as Computational Fluid Dynamics or CFD. These computer programs can be written for specific problems or for specific classes of problems. Today with the advancement of technology, computers have better computing power and provide graphical user interface for 3D representation and manipulation of models that simplify the process of creating geometry, generating and visualizing the mesh, applying the boundary conditions and obtaining visual outputs by processing the results, thus, reducing set-up, computational and post-processing time, and hence, cost. Furthermore, CFD provides an accurate, time and cost-effective alternative to model testing.

Numerical methods gained popularity with the advent of CFD solvers. All CFD solvers are based on the Navier-Stokes equations. Upon ignoring the viscous terms, the Navier-Stokes equations can be simplified to a new set of equations, known as the Euler equations. Furthermore, upon ignoring the vorticity terms the Euler equations yield the full potential equations. These equations can be linearized for subsonic and supersonic flows with small perturbations. The earliest numerical methods developed were for solving the linearized potential equations using conformal transformations for flow over a cylinder and flow over an airfoil [103]. It is, however, the work of Richardson [104] that can be considered a predecessor of modern CFD as Richardson used finite differences method in his calculations by physically dividing the space in cells. Although the experiments were flawed and failed severely, there are a lot of similarities between early CFD calculations using ENIAC (Electronic Numerical Integrator and Computer) and in Richardson's 1922 book [105]. Soon after ENIAC, with the rapid development in computational power, it was possible to develop three-dimensional methods for solving more complex CFD problems.

The first CFD program to solve fluid flow model based on Navier Stokes equations was created by a group led by Francis H. Harlow at Los Alamos National Lab [106], [107]. During the late sixties, the group created a number of numerical methods to simulate 2D transient fluid flow, including the particle-in-cell method by

Harlow [108], the fluid-in-cell method by Gentry et al. [109], the vorticity-stream-function method by Fromm [110] and the marker-and-cell method by Harlow and Welch [111]. Among these methods, the vorticity-stream-function method by Fromm has since became the basis for most CFD programs as it was the first real effort in modeling incompressibility for 2D, transient flows, as opposed to the simpler case of compressible flows.

In 1967, Hess and Smith [112] published the first paper on solving a three-dimensional fluid domain outlining the method of discretizing the geometry's surface with panels. It must, however, be noted that the Panel method had its limitations as it was a simplified model and could not simulate lifting flows. Hence, the primary applications included motion of ship hulls and aircraft fuselages. In 1968, Rubbert and Saaris of Boeing Aircraft [113] published a paper for a lifting Panel code. Soon after, more advanced Panel codes for three-dimensional flows were developed at Boeing [114], Lockheed [115], Douglas [116], McDonnell Aircraft [117], NASA [118] and Analytical Methods [119]-[122].

For cases that can be solved as 2D problems, for example airfoils. Panel codes were developed. These codes also include boundary layer analysis to account for the viscous effects. Eppler's [124] program, named the PROFILE code, was made available in the early 1980s. The PROFILE code was followed by the XFOIL code [125]. Both are commercially used for airfoil design. Panel codes, however, have their limitations, the most prominent one being the failure to model non-linear flows at transonic speeds. For such purposes, Full Potential codes were developed based on the panel codes algorithm. Earliest form of the Full Potential equations was published by Murman and Cole [126] of Boeing in 1970. Bauer et al. [127] wrote several Full Potential codes for the case of two-dimensional airfoils, including the Program H code which was most widely used of the series. Melnik [128] developed on the Program H code, creating Grumfoil. Jameson and Caughey [129] developed a three-dimensional Full Potential code named FLO22. This code was of great importance as it directly led to the development of Boeing's Tranair code [130] which is still actively used in the industry.

For more accurate results for transonic flow solutions, developers turned to the Euler equations. Based on the work Jameson on his three-dimensional FLO57 code

[131] Lockheed developed the TEAM program [132], and IAI/Analytical Methods developed the MGAERO program [133]. MGAERO is of importance as the code was unique in utilizing a Cartesian mesh, when other similar softwares relied on structured body-fitted grids. Jameson's other work include development of three-dimensional code [134] which discretizes the fluid domain using a tetrahedral grid. This has become a standard for most modern CFD solvers like ANSYS CFX.

It is important to note that the Full Potential codes and the Euler codes are based on equations derived from simplification of Navier-Stokes equations. Therefore, these codes are valid for special cases only and can rarely capture the entirety of a flow described by the Navier-Stokes equations. Therefore, developers urged the ultimate need to create codes for solving the entire Navier-Stokes equations. First, simpler two-dimensional codes were created, including NASA Ames' ARC2D code, leading to development of a variety of three-dimensional codes, including NASA's ARC3D, OVERFLOW, and CFL3D. These codes then lead to development of various commercial CFD packages being used today.

3.2.2 ANSYS CFX

ANSYS CFX is one such CFD software package that is designed based on finite volume technique [135]. In fluid mechanics, the equations that describe the flow are known as the Navier-Stokes equations. The Navier-Stokes equations, in general terms, are given as:

$$\frac{\partial \rho}{\partial t} + \nabla.(\rho \boldsymbol{v}) = 0 \tag{26}$$

$$\rho\left(\frac{\partial \boldsymbol{v}}{\partial t} + \boldsymbol{v}.\nabla \boldsymbol{v}\right) = -\nabla p + \nabla \boldsymbol{T} + f \tag{27}$$

Where ρ is the fluid density, v is the velocity, p is the pressure, T is the stress tensor, f represents forces acting on the fluid and ∇ is the del operator.

These equations are partial differential equations that were derived in the early nineteenth century. It must be noted that the Navier-Stokes equations have no known general analytical solution. These equations can often be simplified to find analytical solutions only for special cases. However, for more general cases, the Navier-Stokes

equations can be discretized and solved numerically. The discretization is done using the aforementioned finite volume technique where the domain is divided into much smaller sub-regions, known as control volumes. The Navier-Stokes equations are discretized and solved iteratively for each individual control volume providing an approximation of the value of a particular variable at specific points throughout the domain. Combining the individual results, the overall results can be obtained.

In general, the steps of obtaining the solution can be divided into three main categories, which can further be divided into subcategories as follows:

1. Pre-processing
    a. Geometry: A 3D CAD model of the fluid domain is created. This can be achieved using the built in modeler or by importing the model from an external CAD software like Autodesk Inventor. It must be noted that the DesignModeler in ANSYS has limited capabilities and therefore, external softwares must be used when necessary. Since, the flow is axisymmetric, symmetry can be used to solve half or even quarter of the domain to in order to save solution time.
    b. Mesh generation: A finite volume mesh is generated using tetrahedral elements. It must be noted that the student version of ANSYS has limitations on the maximum number of elements. Therefore, the mesh should be generated such that it is fine close to the particle body to capture the boundary layer and boundary layer separation.
    c. Boundary conditions: The boundary conditions are defined including velocities at the inlet and the wall, static pressure at the outlet and symmetry if applicable.
    d. Material properties: A new material, with blank properties, was created. Material properties including density and viscosity were defined. The density was input as a constant value. The viscosity was set as a constant value for Newtonian fluid. An expression was created for the variable viscosity in the case of non-Newtonian fluids based on the power-law model.

e. Solver initialization: The solution scheme was selected as Advection Scheme and the convergence criteria was selected as 10^{-5}.

2. Solver
    a. ANSYS CFX solver: Once the initialization is completed in the pre-processing phase, the solver starts and iteratively solves the governing equations of the flow in the fluid domain based on the Advection scheme. The solver stops once the selected convergence criteria condition is met.
    b. Create result files: The output files are created from which the results can be derived in post-processing.
3. Post Processing
    a. Plot results: Various plots can be obtained, including velocity and pressure contours, streamlines, and velocity vs length in the wake region.
    b. Calculate function values: The drag force on the article was calculated using the function calculator option. The force was values can then be used to calculate the coefficient of drag.
    c. Export data: Data can be exported to be used in external programs. Tabular data can be exported as an Excel sheet. Similarly, images of plots and graphs can be transported in various formats.

A flowchart of the process can be found in Appendix A.

Chapter 4. Results for Creeping Motion in Newtonian Fluid

This section presents the numerical results for axisymmetric prolate spheroids and Cassini ovals for different shape factors and different confinement ratios, for the case of creeping motion in Newtonian fluid.

First, the results for the spheroids will be shown and the effect of confinement ratio and the effect of particle geometry will be examined. Five different shape factors *a/b* will be studied with values 1, 1.1, 2, 5 and 10. For each shape factor, confinement ratio *b/R* values of 0.1, 0.2, 0.3, 0.4, 0.5, 0.6, 0.7 and 0.8 will be studied. The results are shown in section 4.1.

Similar analysis will be repeated for the case of Cassini ovals. Six different shape factors $(c/d)^2$ will be studied with values 0.1, 0.3, 0.5, 0.7, 0.9, 0.95. For each shape factor, confinement ratio *b/R* values of 0.1, 0.2, 0.3, 0.4, 0.5, 0.6, 0.7 and 0.8 will be studied. The results are shown in section 4.2.

Sample velocity streamlines and pressure contours will be shown to help understand the flow dynamics. These results are shown in section 4.3.

4.1 Spheroid

4.1.1 Effect of Confinement Ratio

As seen from figures 13-17, as the confinement ratio increases, the normalized drag force also increases. These results were validated against analytical solutions available in the literature. The confinement ratio is defined as b/R, i.e. the ratio between the length of the particle in the minor axis measured from the axis of translation denoted as ‘b’ and the radius of the cylindrical pore denoted as ‘R’. The particle and the pore are coaxial, as explained previously. As the confinement ratio increases, for the same value of b, R decreases. Therefore, the area for the fluid to pass between the particle and the decreases. Physically, based on the continuity equation, the velocity in the confined region increases and the drag force also increases.

4.1.1.1 a/b = 1

Table 2: Numerical and analytical [51] results for Case 1, spheroid a/b = 1

b/R	F/Fo numerical	F/Fo analytical	%error
0.1000	1.3084	1.2632	3.5812
0.2000	1.6975	1.6795	1.0755
0.3000	2.3622	2.3701	0.3340
0.4000	3.5295	3.5914	1.7224
0.5000	5.7650	5.9474	3.0656
0.6000	10.9833	11.0919	0.9788
0.7000	23.9145	24.6759	3.0855
0.8000	73.2583	74.6687	1.8889

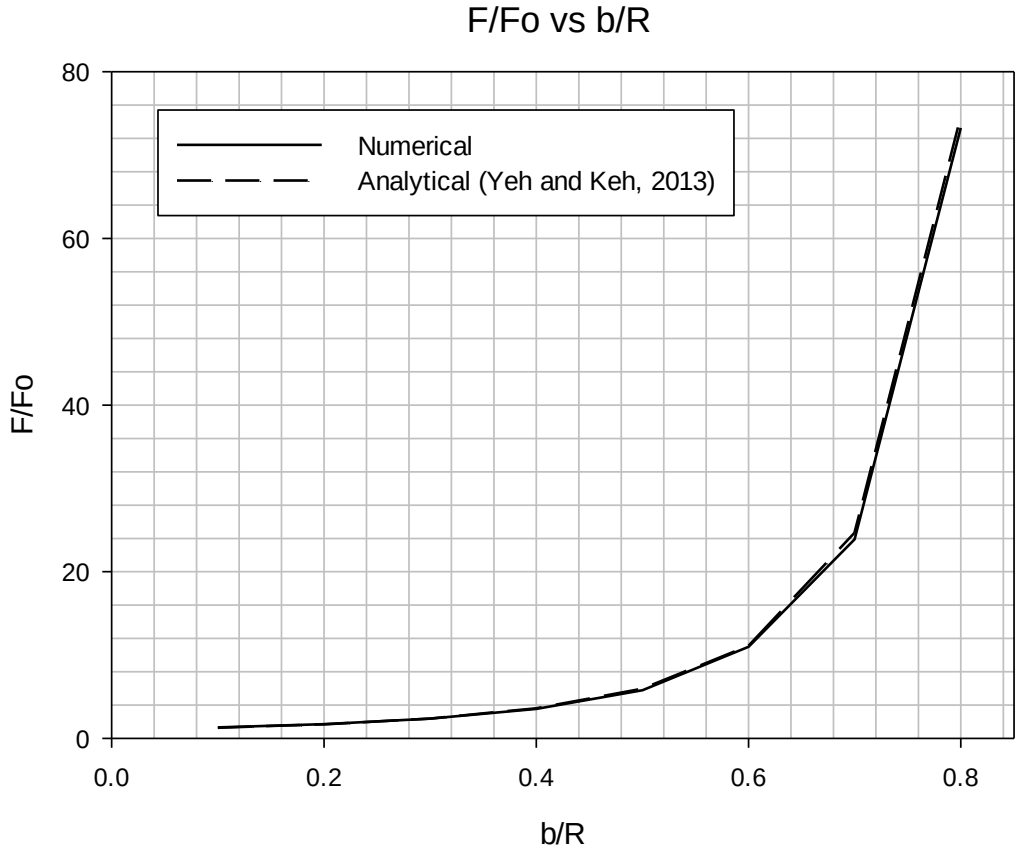

Figure 13: F/Fo vs b/R, numerical and analytical [51], for Case 1, spheroid a/b = 1

4.1.1.2 a/b = 1.1

Table 3: Numerical and analytical results [51] for Case 1, spheroid a/b = 1.1

b/R	F/Fo numerical	F/Fo analytical	%error
0.1000	1.2697	1.2697	5.2346e-3
0.2000	1.6792	1.6993	1.1838
0.3000	2.4239	2.4165	0.3035
0.4000	3.6621	3.6917	0.8002
0.5000	6.0361	6.1637	2.0711
0.6000	11.4181	11.5882	1.4679
0.7000	25.2353	25.9827	2.8765
0.8000	76.1410	79.2303	3.8992

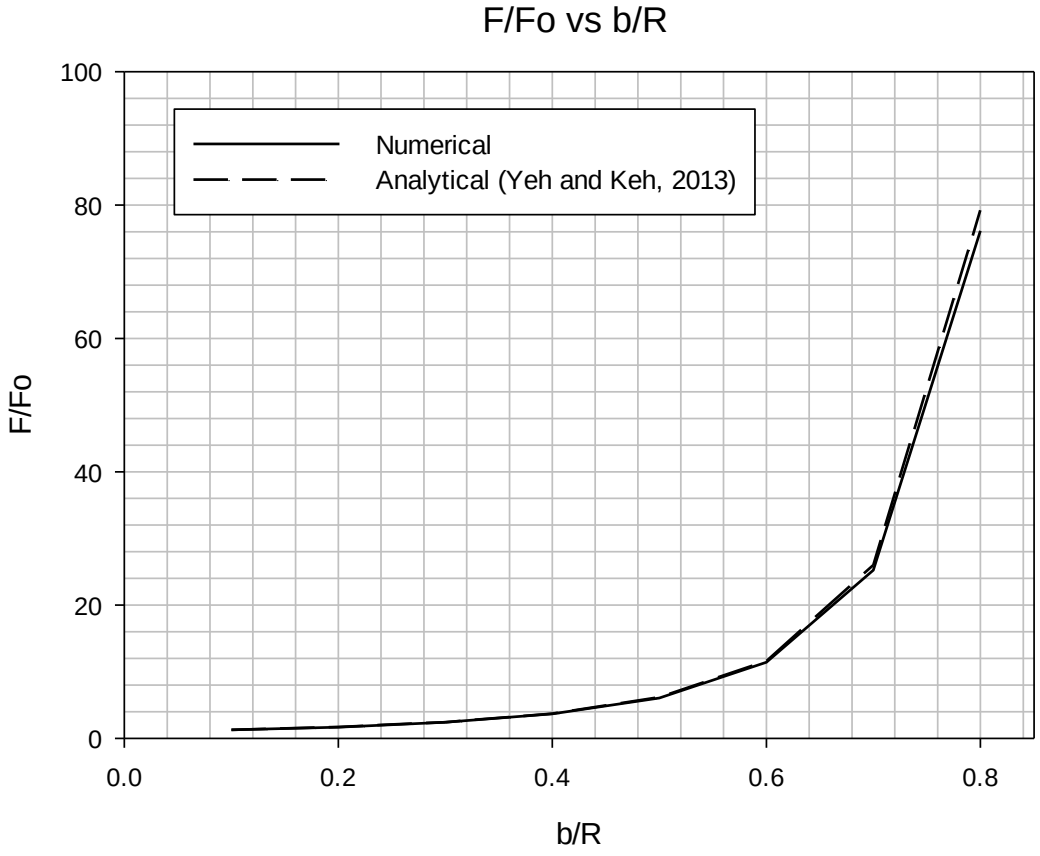

Figure 14: F/Fo vs b/R, numerical and analytical [51], for Case 1, spheroid a/b = 1.1

4.1.1.3 a/b = 2

Table 4: Numerical and analytical results [51] for Case 1, spheroid a/b = 2

b/R	F/Fo numerical	F/Fo analytical	%error
0.1000	1.3172	1.3302	0.9802
0.2000	1.8547	1.8831	1.5091
0.3000	2.8432	2.8334	0.3464
0.4000	4.5440	4.5595	0.3414
0.5000	7.9354	7.9760	0.5097
0.6000	15.2587	15.6331	2.3948
0.7000	35.2352	36.3869	3.1652
0.8000	110.7995	114.7770	3.4654

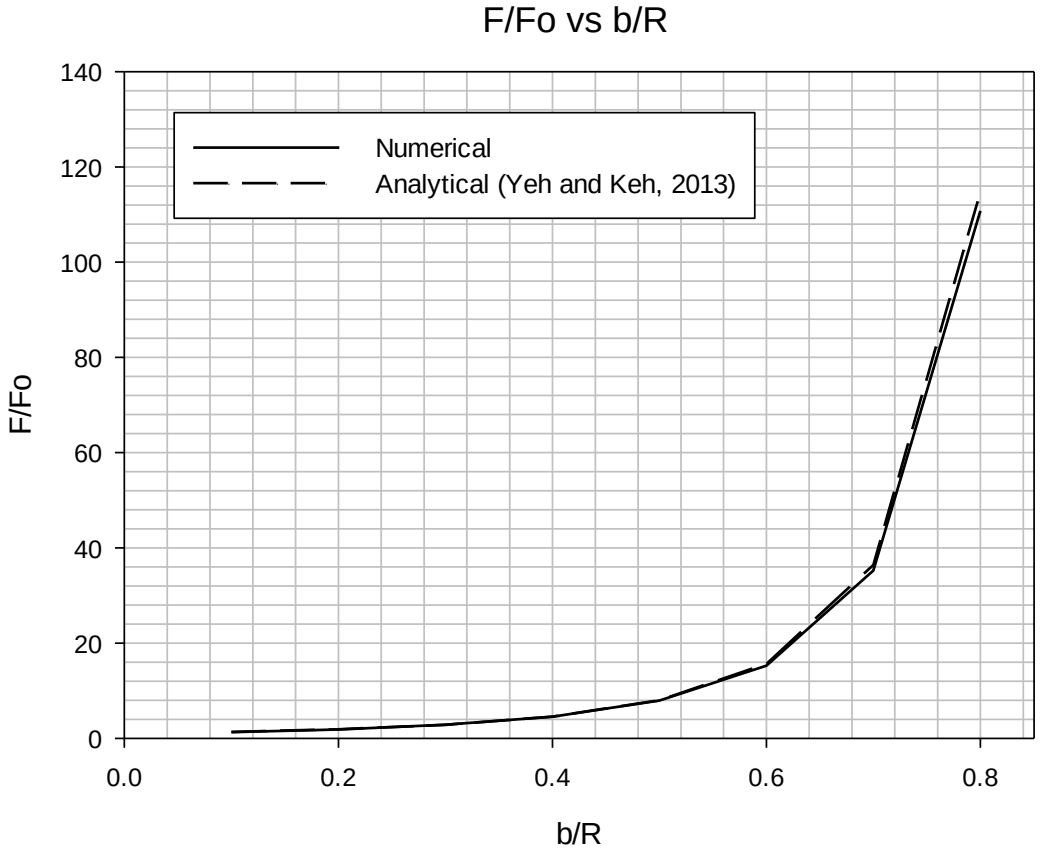

Figure 15: F/Fo vs b/R, numerical and analytical [51], for Case 1, spheroid a/b = 2

4.1.1.4 a/b = 5

Table 5: Numerical and analytical results [51] for Case 1, spheroid a/b = 5

b/R	F/Fo numerical	F/Fo analytical	%error
0.1000	1.5173	1.5280	0.7002
0.2000	2.3812	2.4210	1.6420
0.3000	3.8788	3.9294	1.2878
0.4000	6.5904	6.6712	1.2107
0.5000	11.9282	12.1464	1.7968
0.6000	24.0164	24.5529	2.1851
0.7000	56.4037	58.5477	3.6620
0.8000	178.9283	188.2540	4.9538

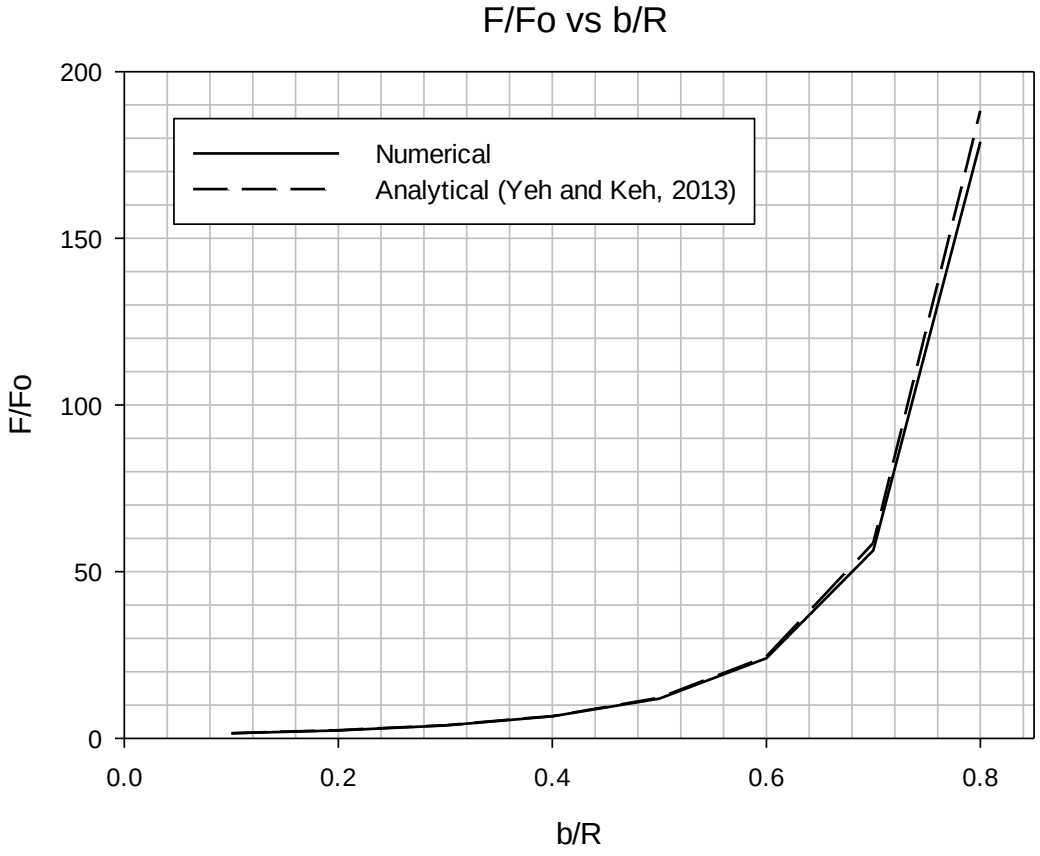

Figure 16: F/Fo vs b/R, numerical and analytical [51], for Case 1, spheroid a/b = 5

4.1.1.5 a/b = 10

Table 6: Numerical and analytical results [51] for Case 1, spheroid a/b = 10

b/R	F/Fo numerical	F/Fo analytical	%error
0.1000	1.7933	1.7935	0.0109
0.2000	3.0403	3.0200	0.6697
0.3000	5.0158	5.0436	0.5523
0.4000	8.7258	8.7088	0.1944
0.5000	15.9315	16.0329	0.6327
0.6000	32.2995	32.6570	1.0948
0.7000	76.7198	78.2899	2.0055
0.8000	232.7087	252.6770	7.9027

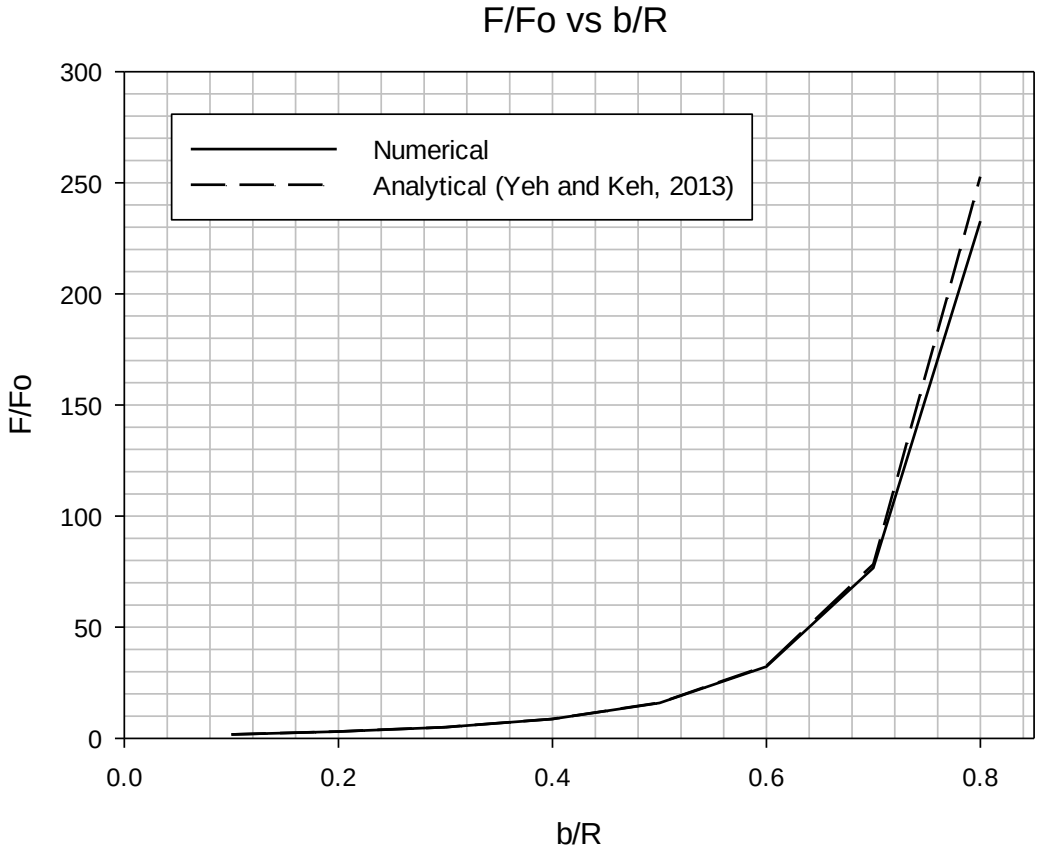

Figure 17: F/Fo vs b/R, numerical and analytical [51], for Case 1, spheroid a/b = 10

4.1.2 Effect of Particles Shape

As seen in figure 18, the normalized drag force F/Fo increases with increase in the shape factor a/b. The case of a/b = 1 represents the special case of spheroid, the sphere. As defined previously, ‘a’ is the length in the major axis and ‘b’ is the length in the minor axis. As the shape factor increases, for the same value of ‘a’, the value of ‘b’ decreases. The spheroid goes from a sphere at a/b = 1 to a needle as a/b approaches ∞. The increase in the drag force can be explained by the increase in surface area of the particle with the increase in shape factor. This becomes more prominent in the cases with more severe confinement.

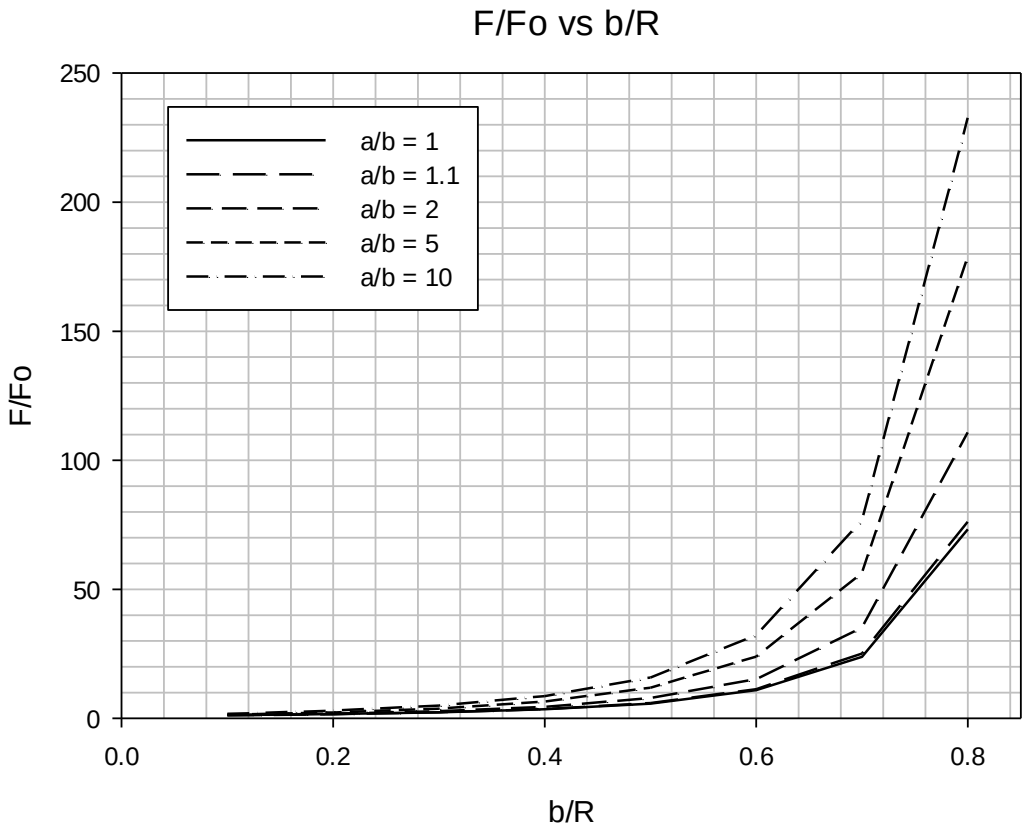

Figure 18: F/Fo vs b/R for different shape factors, numerical, for Case 1, spheroids

4.2 Cassini Oval

4.2.1 Effect of Confinement Ratio

As seen from figures 19-24, as the confinement ratio increases, the normalized drag force also increases. These results were validated against analytical solutions available in the literature. The confinement ratio is defined as b/R, i.e. the ratio between the maximum length of the particle in the minor axis measured from the axis of translation denoted as ‘b’ and the radius of the cylindrical pore denoted as ‘R’. The particle and the pore are coaxial, as explained previously. As the confinement ratio increases, for the same value of b, R decreases. Therefore, the area for the fluid to pass between the particle and the decreases. Physically, based on the continuity equation, the velocity in the confined region increases and the drag force also increases. The dynamics in the confinement region and the wake region as well can be observed by plotting the velocity streamlines and the pressure contours.

4.2.1.1 $(c/d)^2 = 0.1$

Table 7: Numerical and analytical results [51] for Case 1, Cassini oval $(c/d)^2 = 0.1$

b/R	F/Fo numerical	F/Fo analytical	%error
0.1000	1.5496	1.2705	21.9713
0.2000	1.7142	1.7017	0.7330
0.3000	2.4293	2.4223	0.2887
0.4000	3.7086	3.7045	0.1098
0.5000	6.1703	6.1925	0.3576
0.6000	11.5642	11.6571	0.7971
0.7000	25.8326	26.1741	1.3047
0.8000	77.0576	79.9433	3.6097

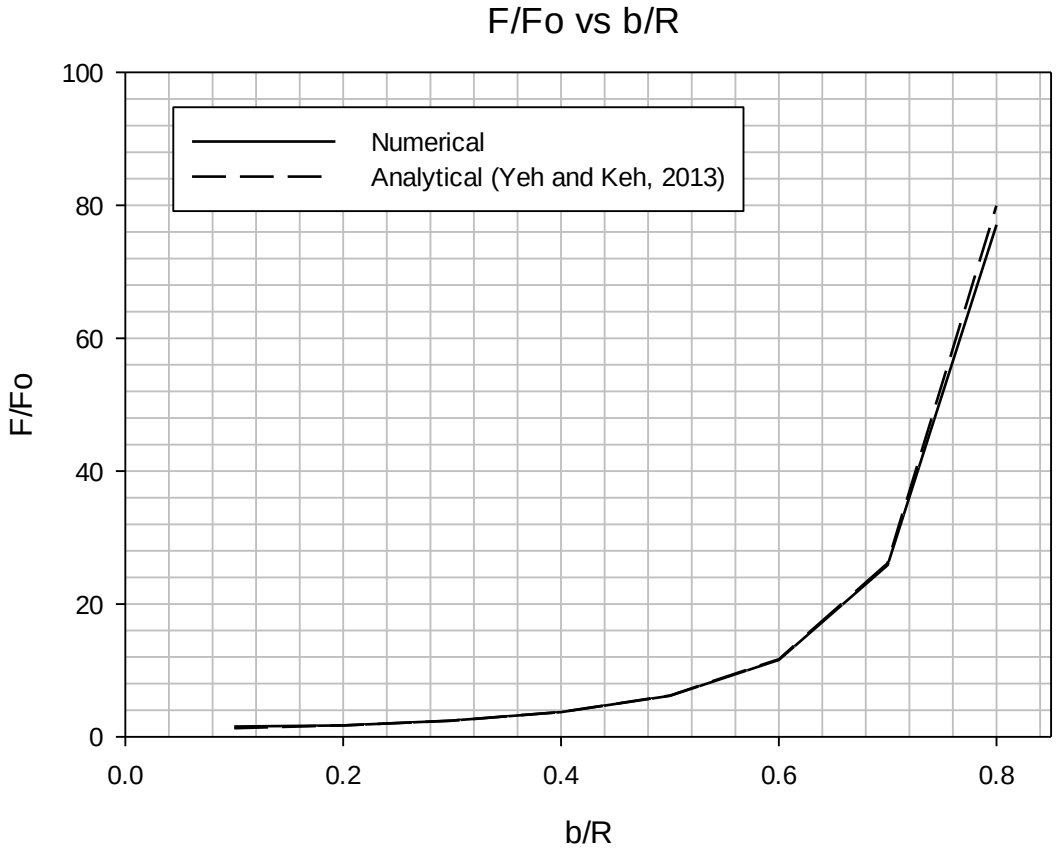

Figure 19: F/Fo vs b/R, numerical and analytical [51], for Case 1, Cassini oval $(c/d)^2 = 0.1$

4.2.1.2 $(c/d)^2 = 0.3$

Table 8: Numerical and analytical results [51] for Case 1, Cassini oval $(c/d)^2 = 0.3$

b/R	F/Fo numerical	F/Fo analytical	%error
0.1000	1.4117	1.2920	9.2630
0.2000	1.8088	1.7684	2.2851
0.3000	2.5927	2.5791	0.5261
0.4000	4.0483	4.0450	0.0811
0.5000	6.9328	6.9353	0.0367
0.6000	13.3261	13.3944	0.5100
0.7000	30.2628	30.8832	2.0087
0.8000	92.9081	97.0826	4.3000

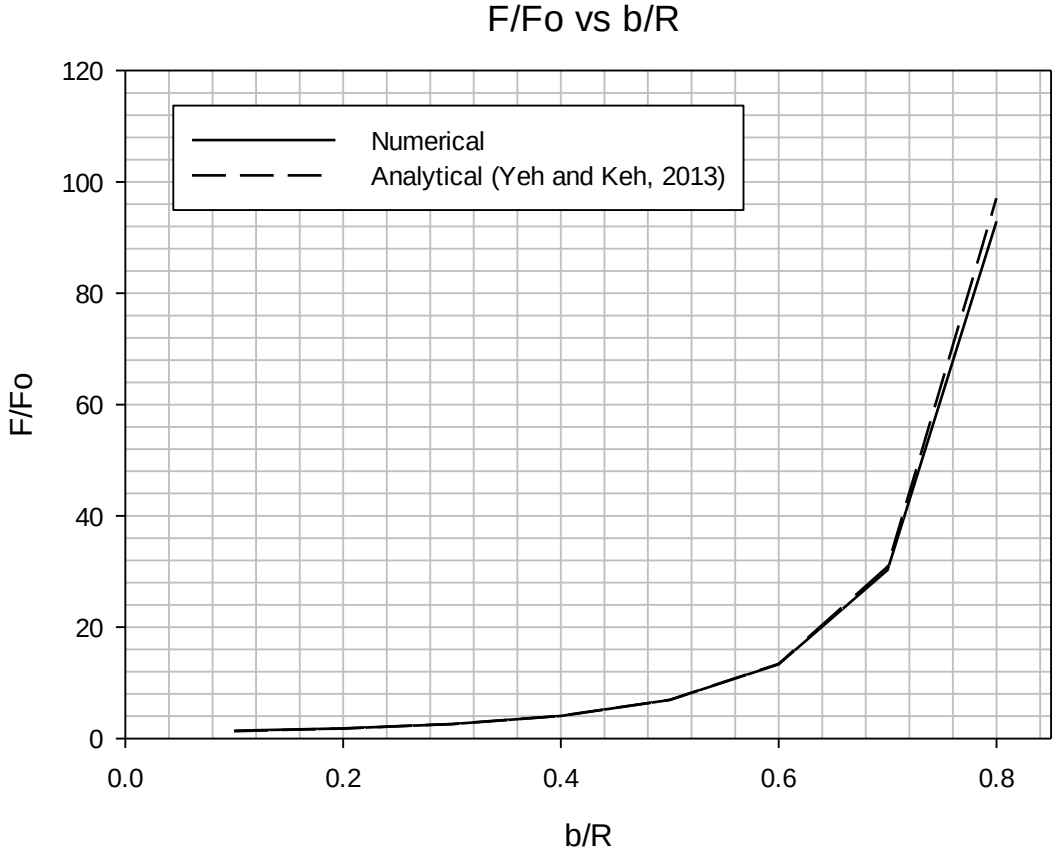

Figure 20: F/Fo vs b/R, numerical and analytical [51], for Case 1, Cassini oval $(c/d)^2 = 0.3$

4.2.1.3 $(c/d)^2 = 0.5$

Table 9: Numerical and analytical results [51] for Case 1, Cassini oval $(c/d)^2 = 0.5$

b/R	F/Fo numerical	F/Fo analytical	%error
0.1000	1.3490	1.3319	1.2814
0.2000	1.8974	1.8941	0.1789
0.3000	2.8754	2.8788	0.1177
0.4000	4.6695	4.7100	0.8597
0.5000	8.4234	8.4410	0.2092
0.6000	17.0225	17.1162	0.5475
0.7000	40.8695	41.8098	2.2491
0.8000	136.4038	141.9780	3.9261

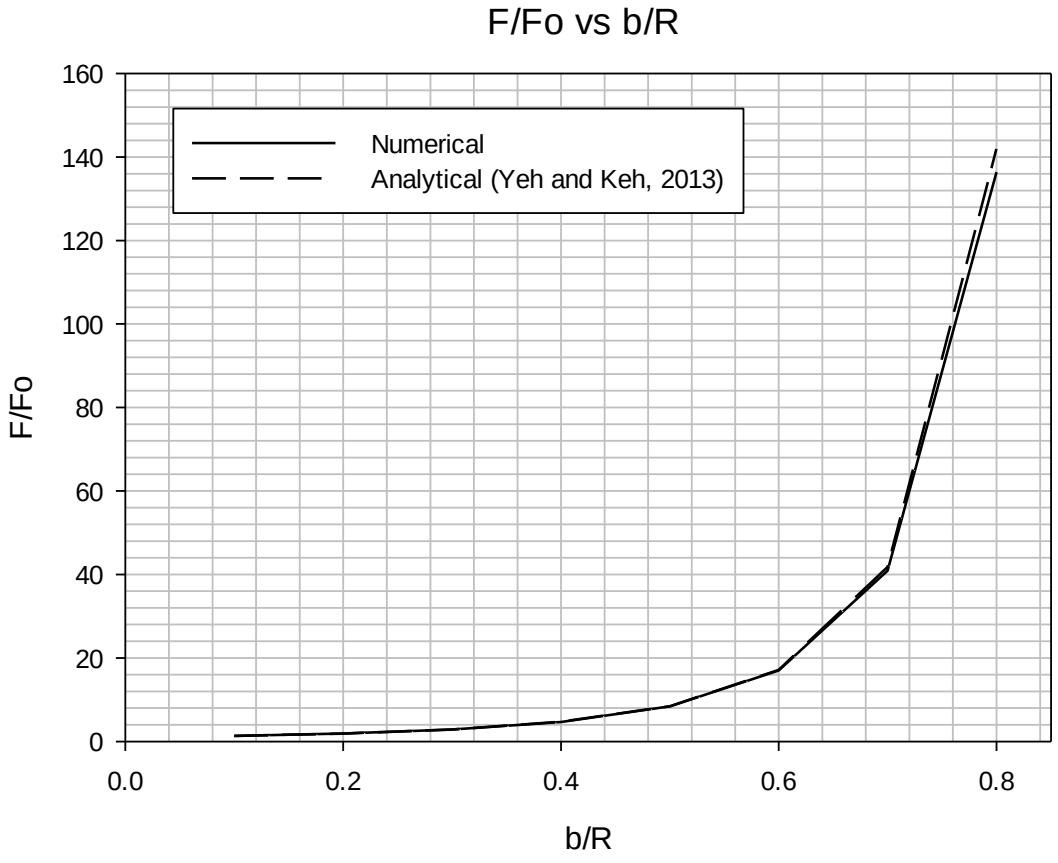

Figure 21: F/Fo vs b/R, numerical and analytical [51], for Case 1, Cassini oval $(c/d)^2 = 0.5$

4.2.1.4 $(c/d)^2 = 0.7$

Table 10: Numerical and analytical results [51] for Case 1, Cassini oval $(c/d)^2 = 0.7$

b/R	F/Fo numerical	F/Fo analytical	%error
0.1000	1.3888	1.3773	0.8384
0.2000	2.0322	2.0312	0.0500
0.3000	3.1828	3.1801	0.0860
0.4000	5.3124	5.3142	0.0341
0.5000	9.6563	9.6530	0.0343
0.6000	19.4978	19.6686	0.8683
0.7000	46.2972	47.6320	2.8024
0.8000	152.5172	155.9440	2.1974

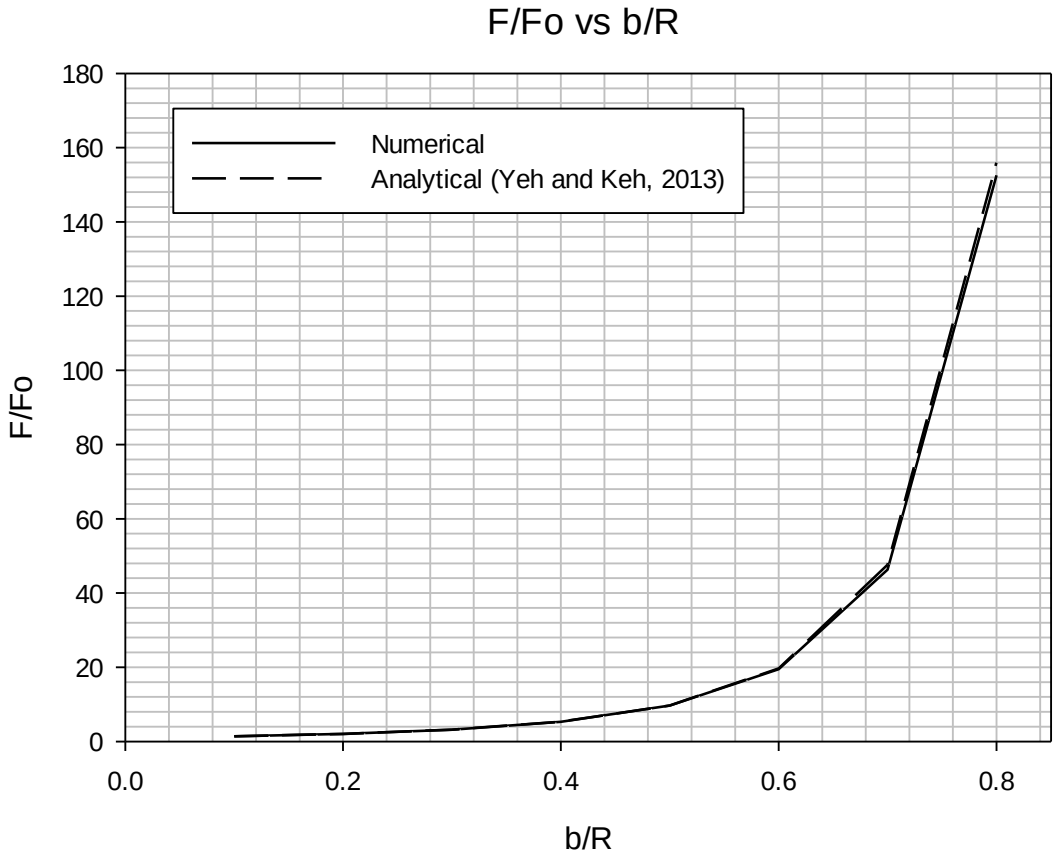

Figure 22: F/Fo vs b/R, numerical and analytical [51], for Case 1, Cassini oval $(c/d)^2 = 0.7$

4.2.1.5 $(c/d)^2 = 0.9$

Table 11: Numerical and analytical results [51] for Case 1, Cassini oval $(c/d)^2 = 0.9$

b/R	F/Fo numerical	F/Fo analytical	%error
0.1000	1.4173	1.4069	0.7395
0.2000	2.1042	2.0977	0.3068
0.3000	3.2503	3.2528	0.0785
0.4000	5.2723	5.2910	0.3539
0.5000	9.2157	9.2349	0.2079
0.6000	17.7385	17.8918	0.8567
0.7000	39.9164	40.8357	2.2512
0.8000	119.4542	125.3450	4.6996

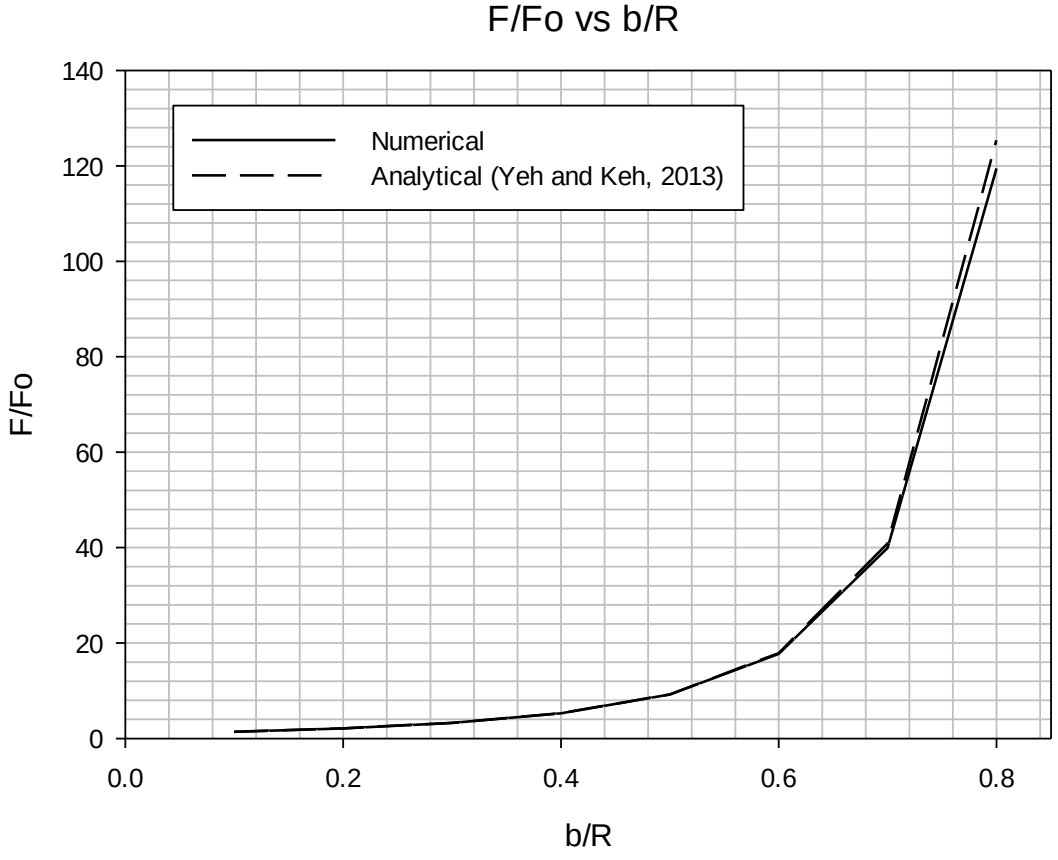

Figure 23: F/Fo vs b/R, numerical and analytical [51], for Case 1, Cassini oval $(c/d)^2 = 0.9$

4.2.1.6 $(c/d)^2 = 0.95$

Table 12: Numerical and analytical results [51] for Case 1, Cassini oval $(c/d)^2 = 0.95$

b/R	F/Fo numerical	F/Fo analytical	%error
0.1000	1.4213	1.4127	0.6059
0.2000	2.1143	2.1065	0.3701
0.3000	3.2537	3.2476	0.1893
0.4000	5.2028	5.2344	0.6032
0.5000	9.0150	9.0443	0.3229
0.6000	17.2282	17.3608	0.7636
0.7000	38.3850	39.3496	2.4514
0.8000	113.1589	120.3680	5.9892

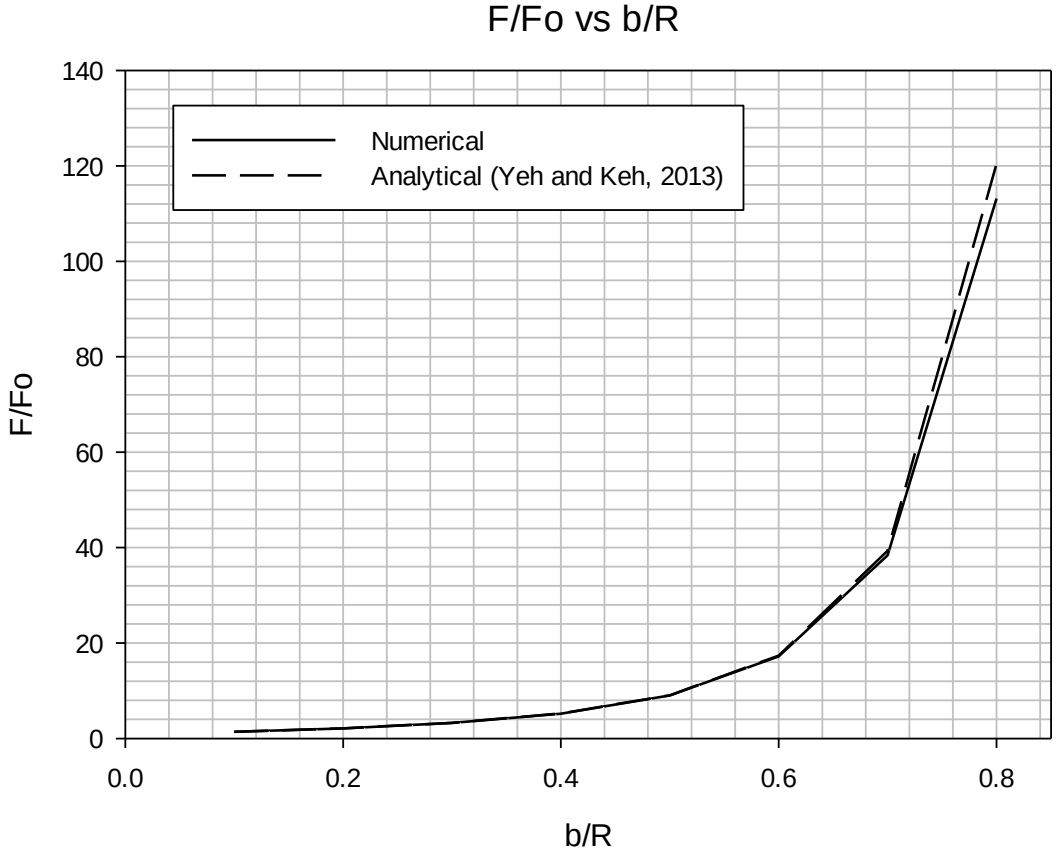

Figure 24: F/Fo vs b/R, numerical and analytical [51], for Case 1, Cassini oval $(c/d)^2 = 0.95$

4.2.2 Effect of Particle Shape

As seen in figure 25, the normalized drag force F/Fo increases with increase in the shape factor $(c/d)^2$. As explained earlier, the ratio $(c/d)^2$ changes the particle shape from a convex shape to a shape with a concave curve in the middle. This concavity effects the flow in different ways. The normalized drag force values increased in the following order. $(c/d)^2 = 0.1$, $(c/d)^2 = 0.3$, $(c/d)^2 = 0.95$, $(c/d)^2 = 0.9$, $(c/d)^2 = 0.5$ and $(c/d)^2 = 0.7$. It can be seen that for moderate concavity cases, $(c/d)^2 = 0.5$ and $(c/d)^2 = 0.7$, the drag force is higher compared to low concavity cases, $(c/d)^2 = 0.1$ and $(c/d)^2 = 0.3$, and high concavity cases, $(c/d)^2 = 0.95$ and $(c/d)^2 = 0.9$.

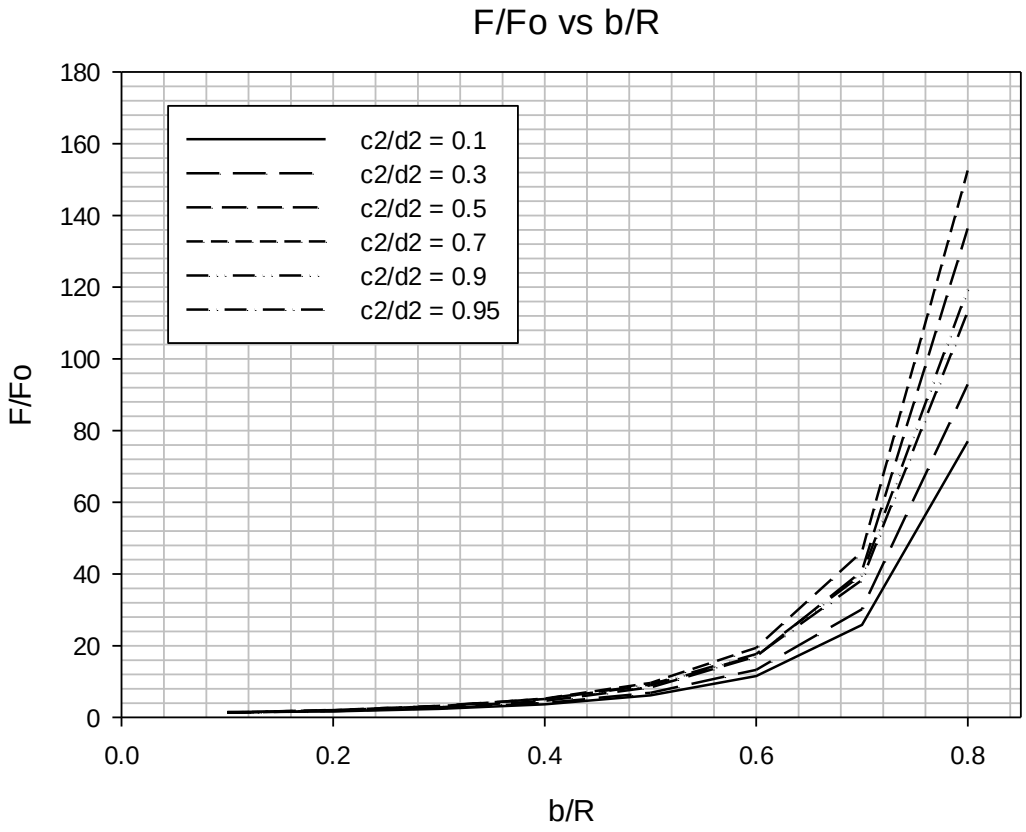

Figure 25: F/Fo vs b/R for different shape factors, numerical, for Case 1, Cassini ovals

4.3 Velocity Streamlines and Pressure Contours (Selected Cases)

As an example, the velocity streamlines and the pressure contours for the case of spheroid with shape factor a/b = 1.1 are shown here. The velocity streamlines are shown in figures 26-33 while the pressure contours are shown in figures 34-41. From the streamlines we can conclude that the flow is attached with no separation in the wake region. This is expected of creeping flows.

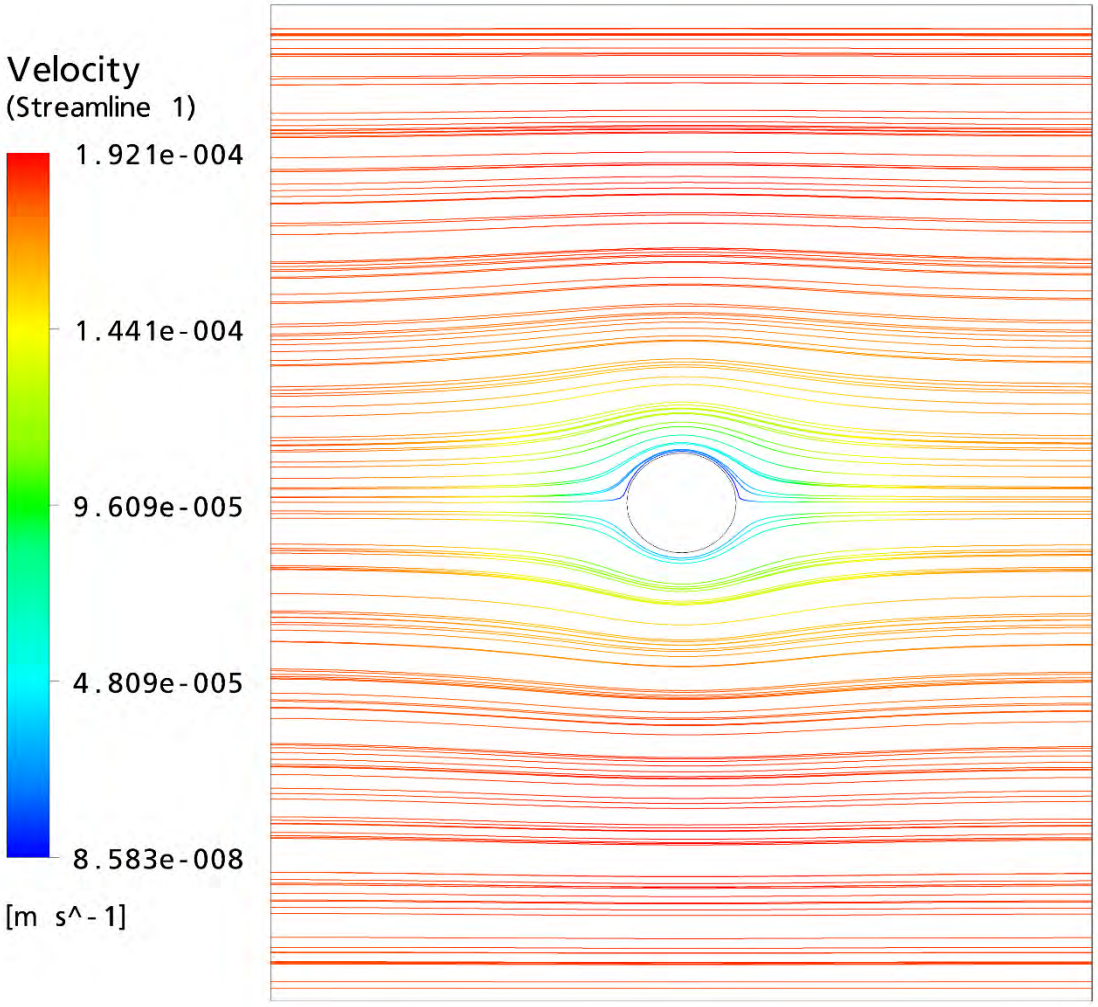

Figure 26: Velocity streamlines, case 1, spheroid a/b = 1.1, b/R = 0.1

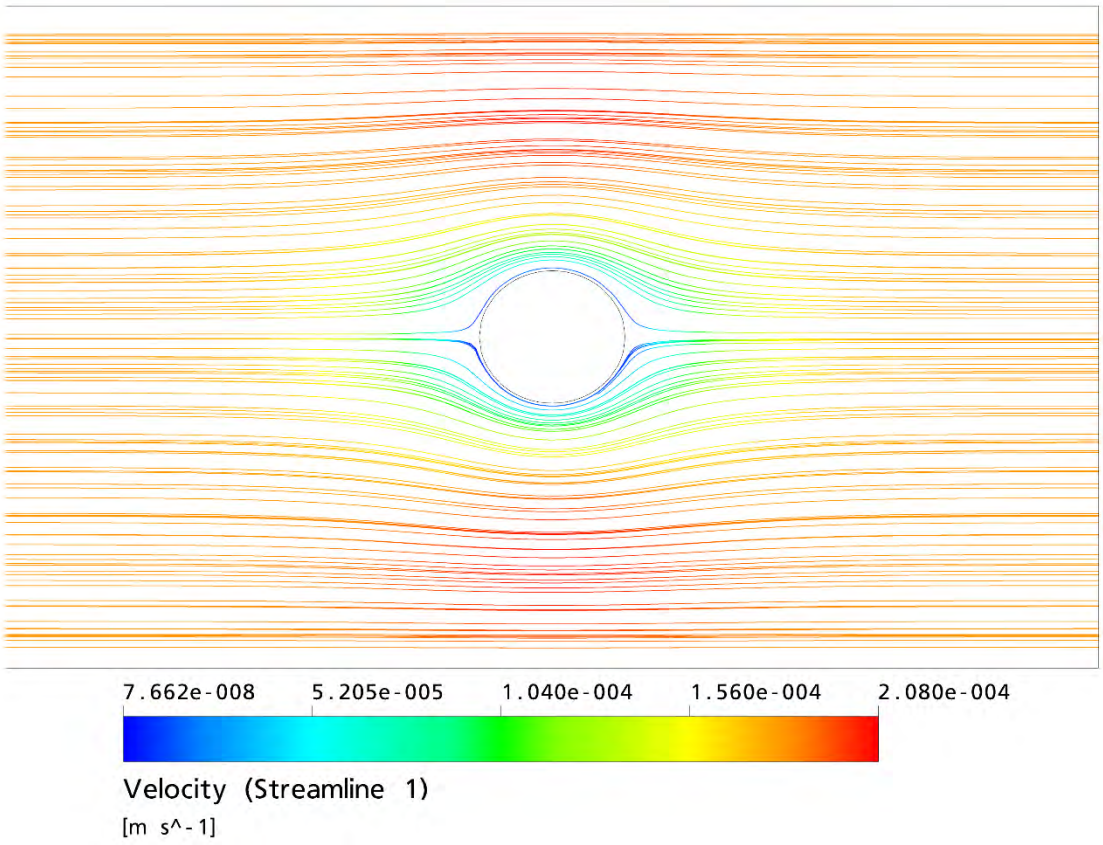

Figure 27: Velocity streamlines, case 1, spheroid a/b = 1.1, b/R = 0.2

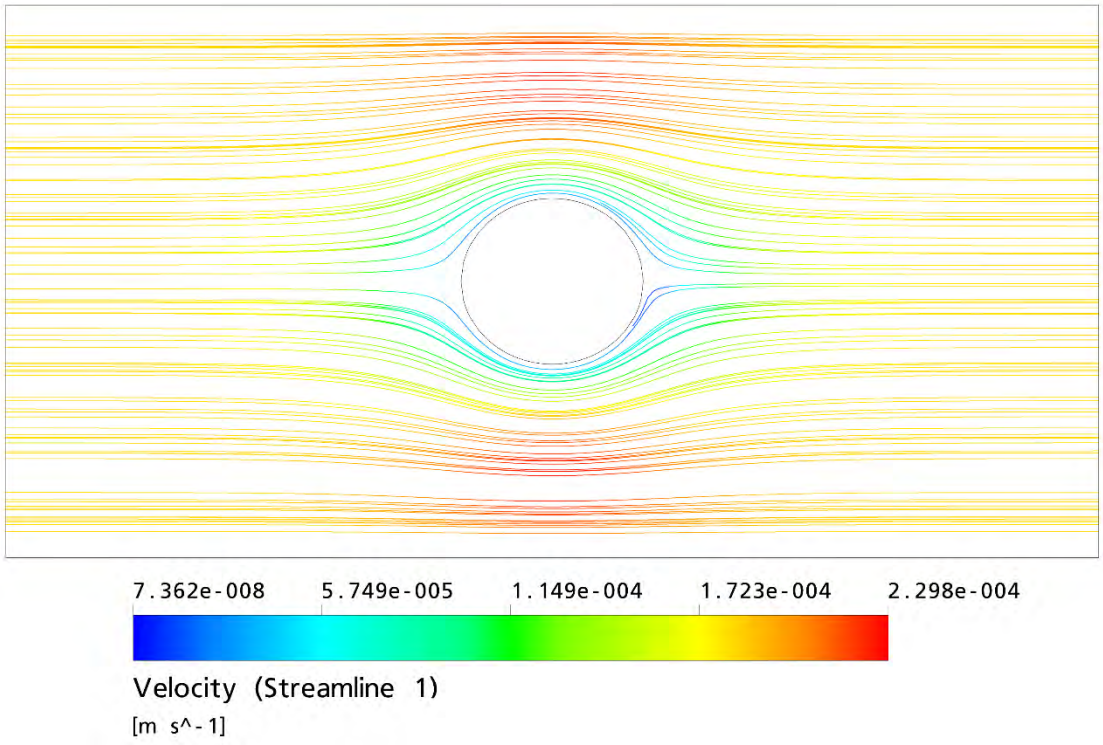

Figure 28: Velocity streamlines, case 1, spheroid a/b = 1.1, b/R = 0.3

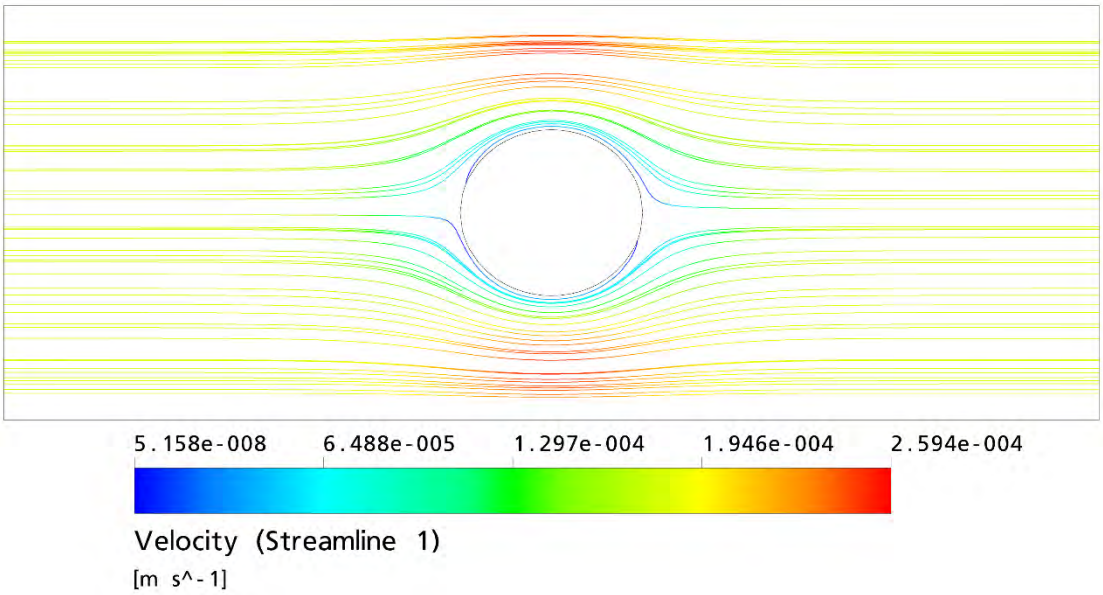

Figure 29: Velocity streamlines, case 1, spheroid a/b = 1.1, b/R = 0.4

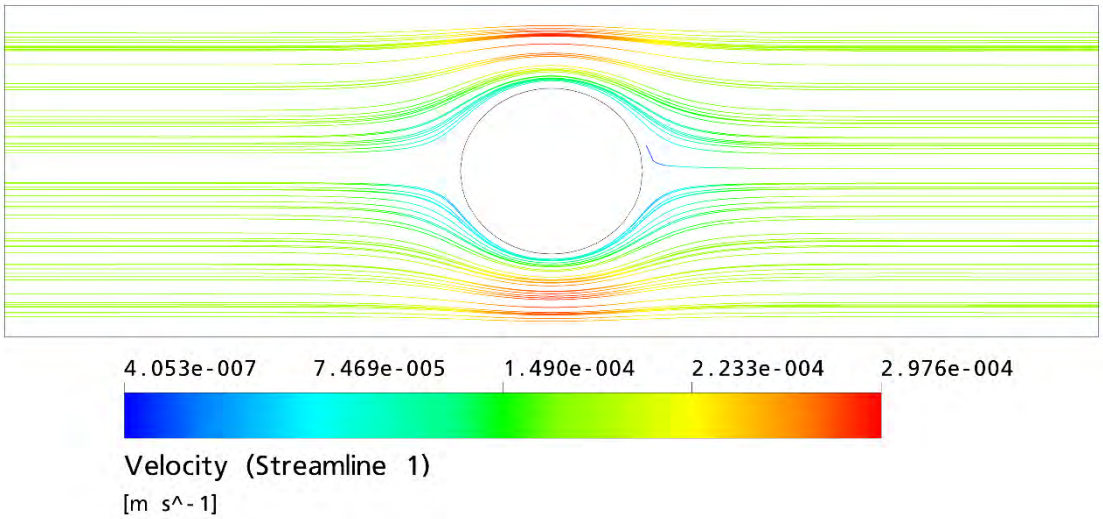

Figure 30: Velocity streamlines, case 1, spheroid a/b = 1.1, b/R = 0.5

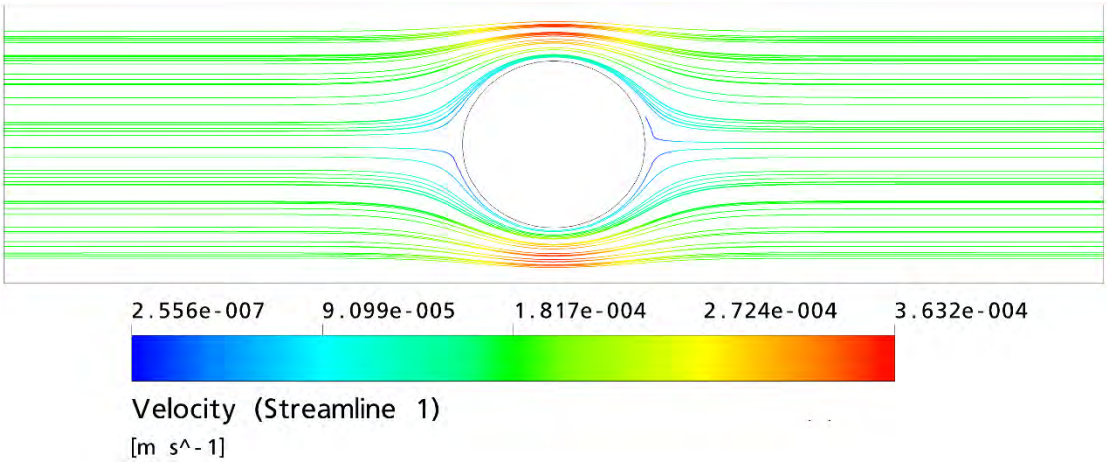

Figure 31: Velocity streamlines, case 1, spheroid a/b = 1.1, b/R = 0.6

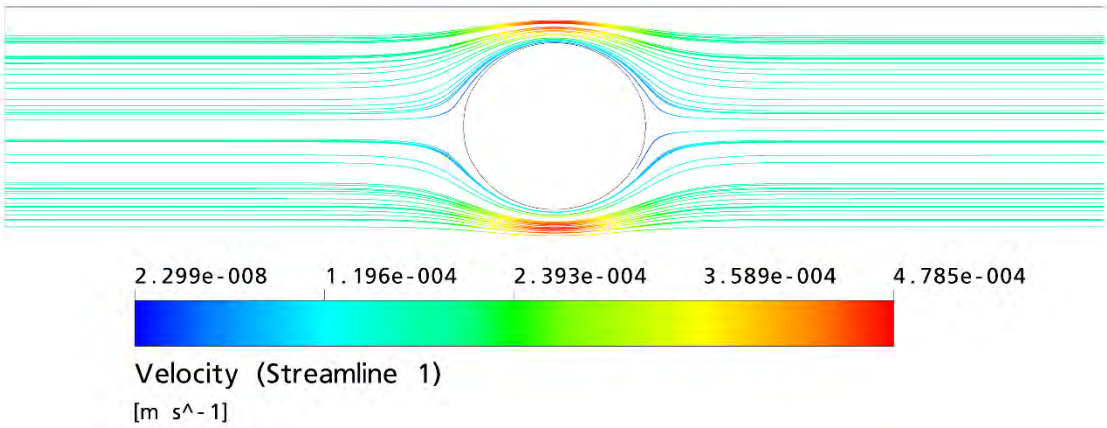

Figure 32: Velocity streamlines, case 1, spheroid a/b = 1.1, b/R = 0.7

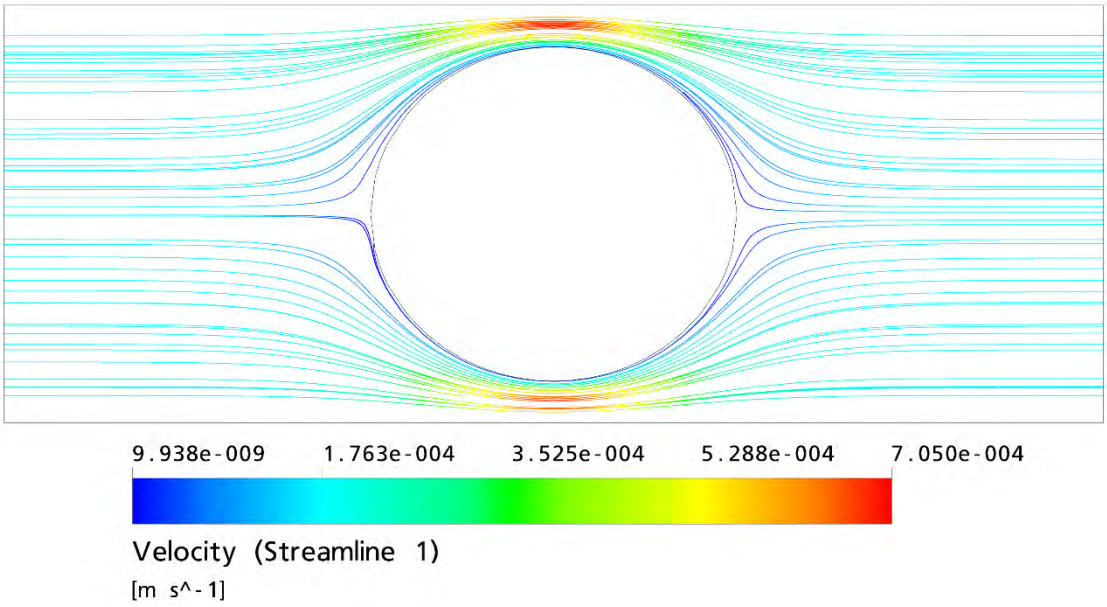

Figure 33: Velocity streamlines, case 1, spheroid a/b = 1.1, b/R = 0.8

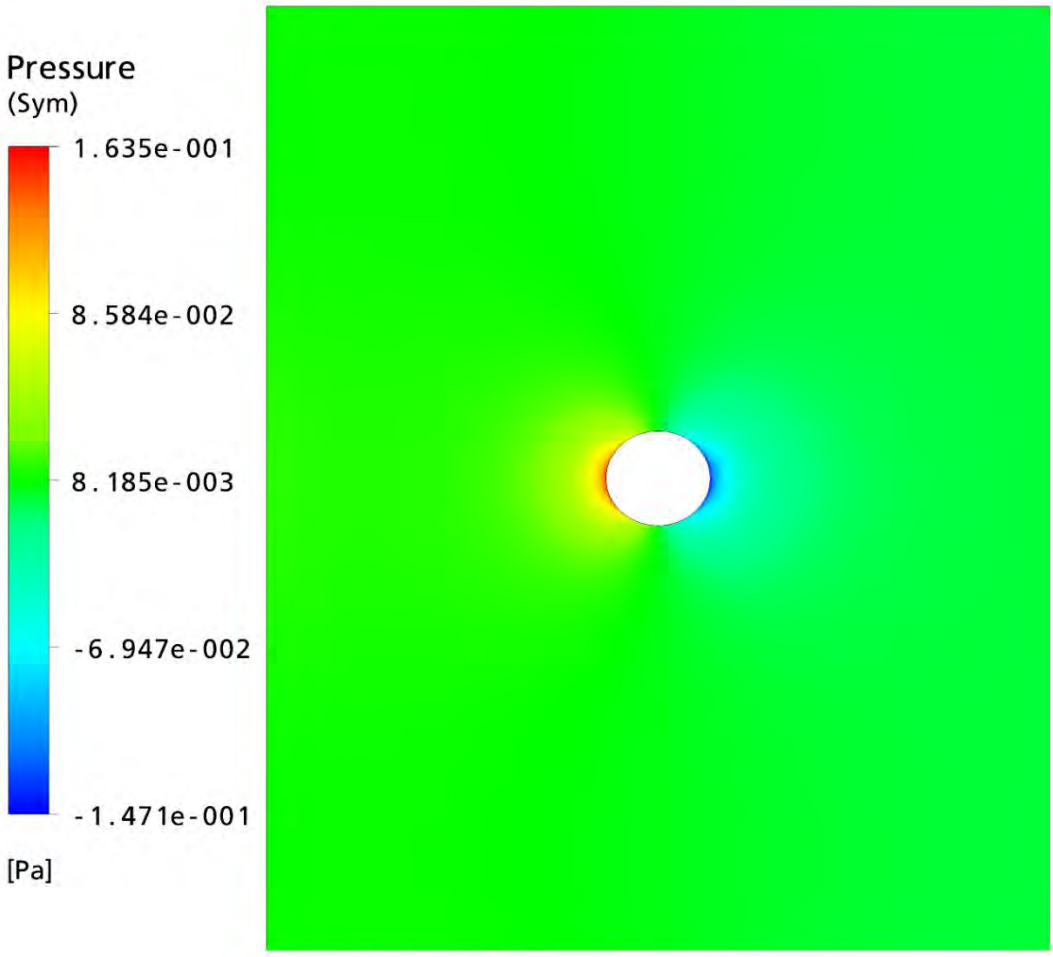

Figure 34: Pressure distribution, case 1, spheroid a/b = 1.1, b/R = 0.1

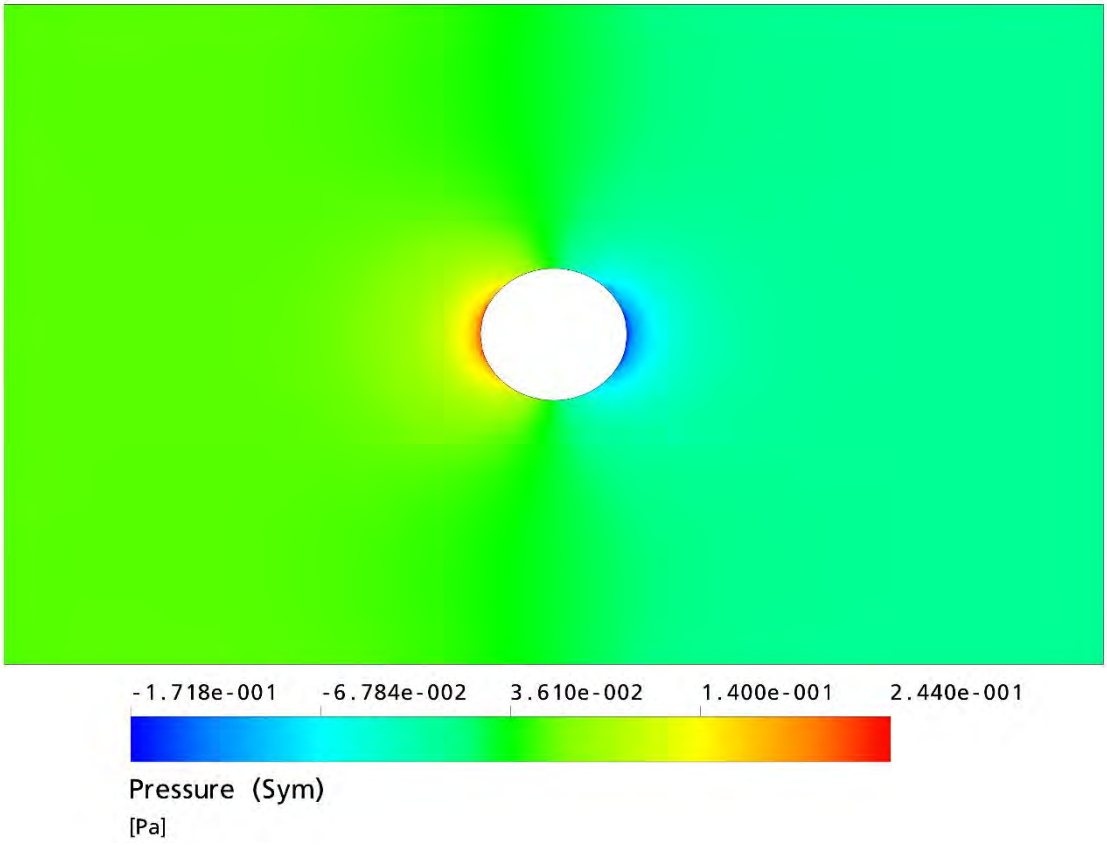

Figure 35: Pressure distribution, case 1, spheroid a/b = 1.1, b/R = 0.2

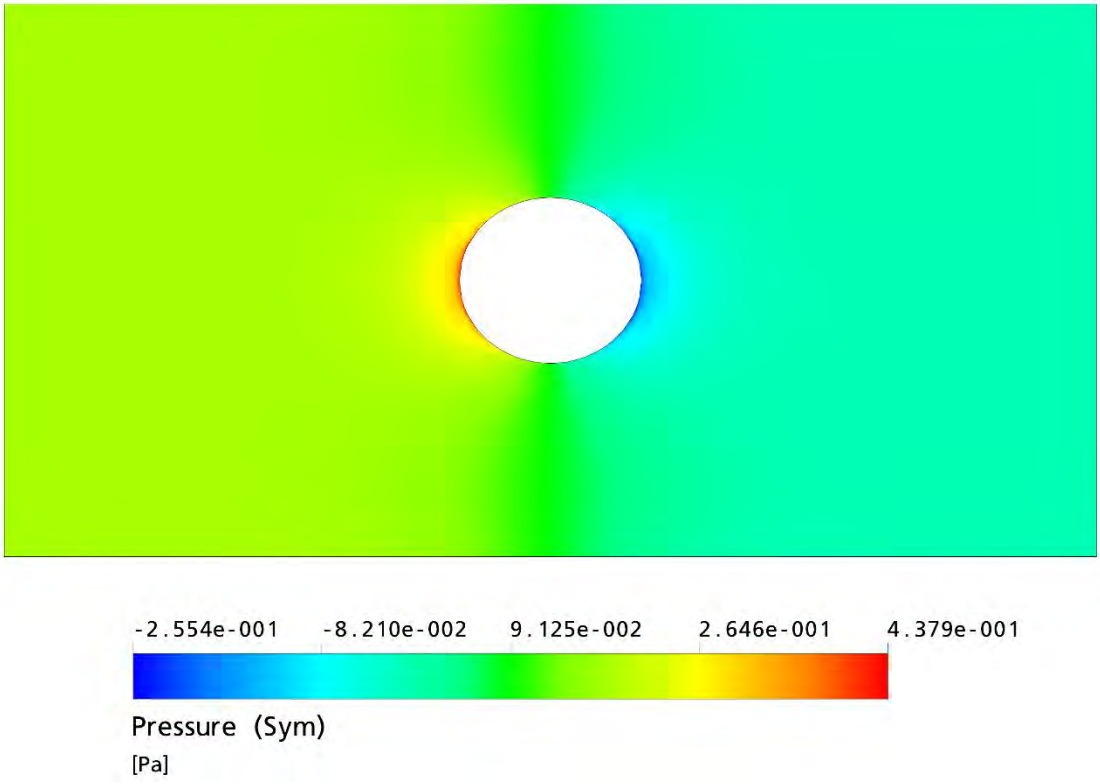

Figure 36: Pressure distribution, case 1, spheroid a/b = 1.1, b/R = 0.3

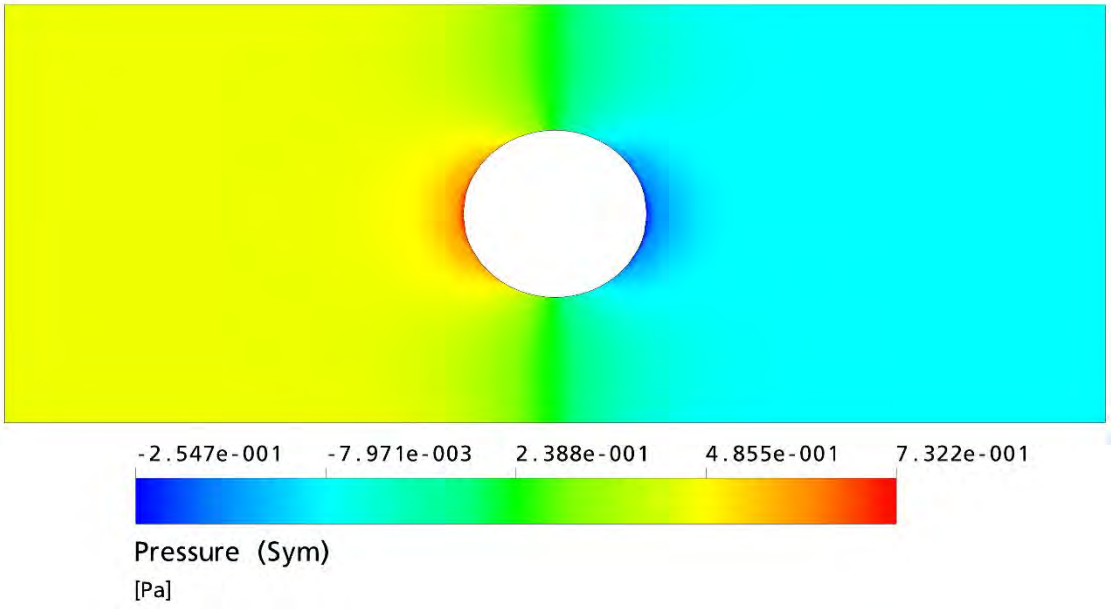

Figure 37: Pressure distribution, case 1, spheroid a/b = 1.1, b/R = 0.4

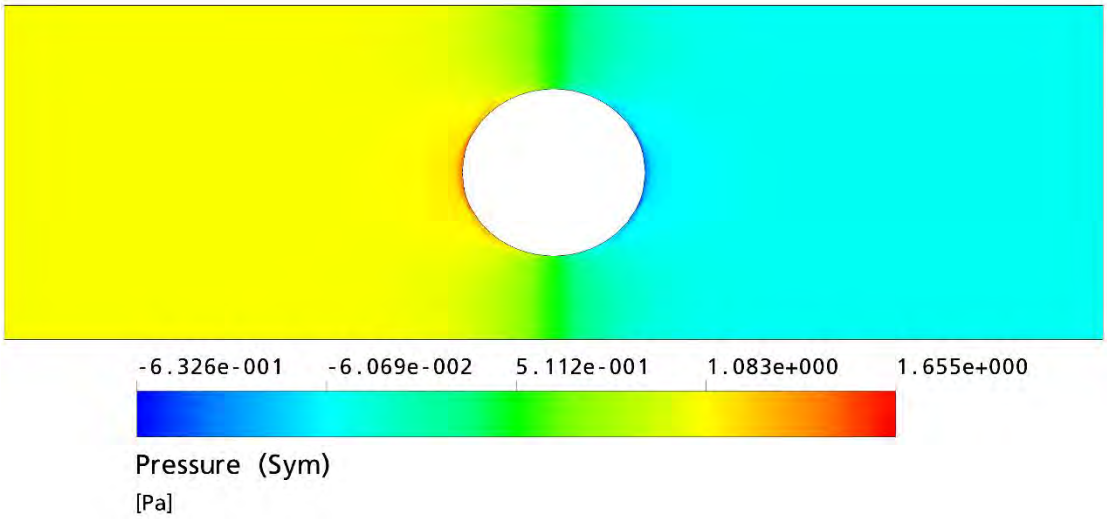

Figure 38: Pressure distribution, case 1, spheroid a/b = 1.1, b/R = 0.5

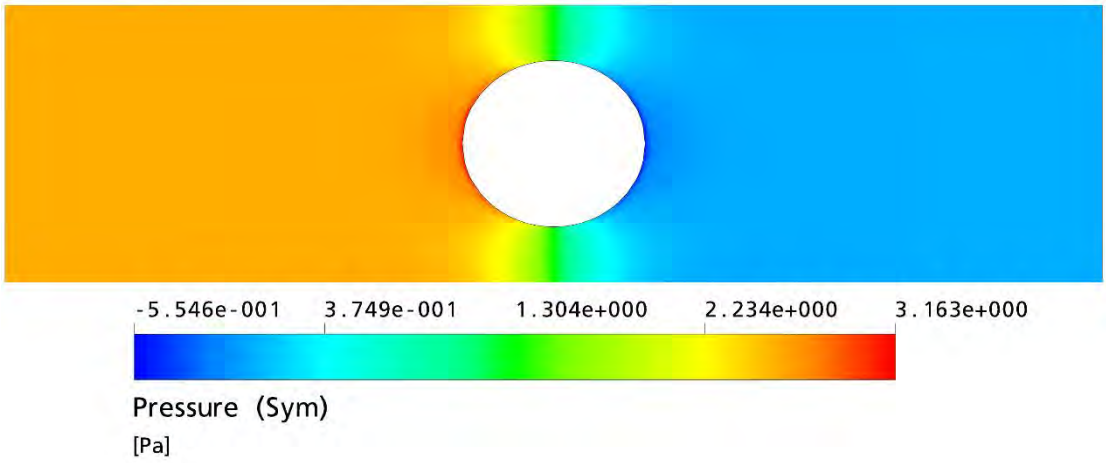

Figure 39: Pressure distribution, case 1, spheroid a/b = 1.1, b/R = 0.6

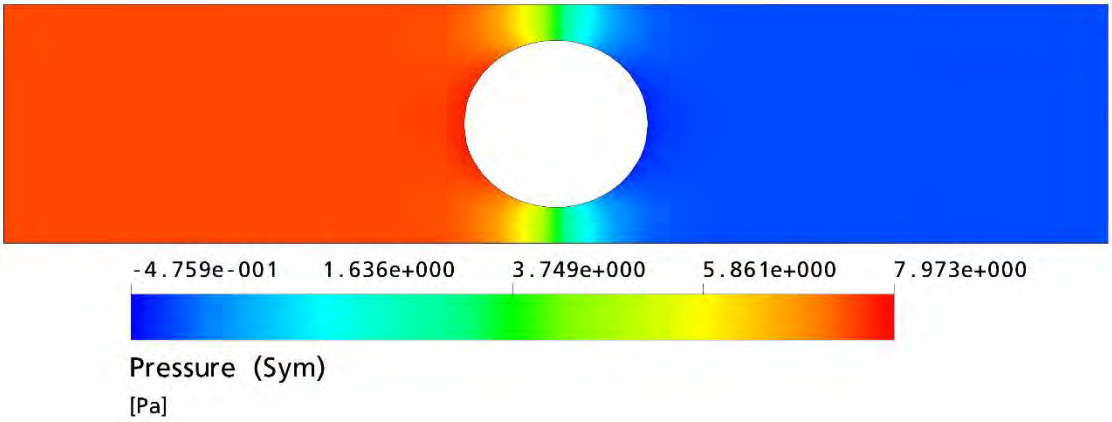

Figure 40: Pressure distribution, case 1, spheroid a/b = 1.1, b/R = 0.7

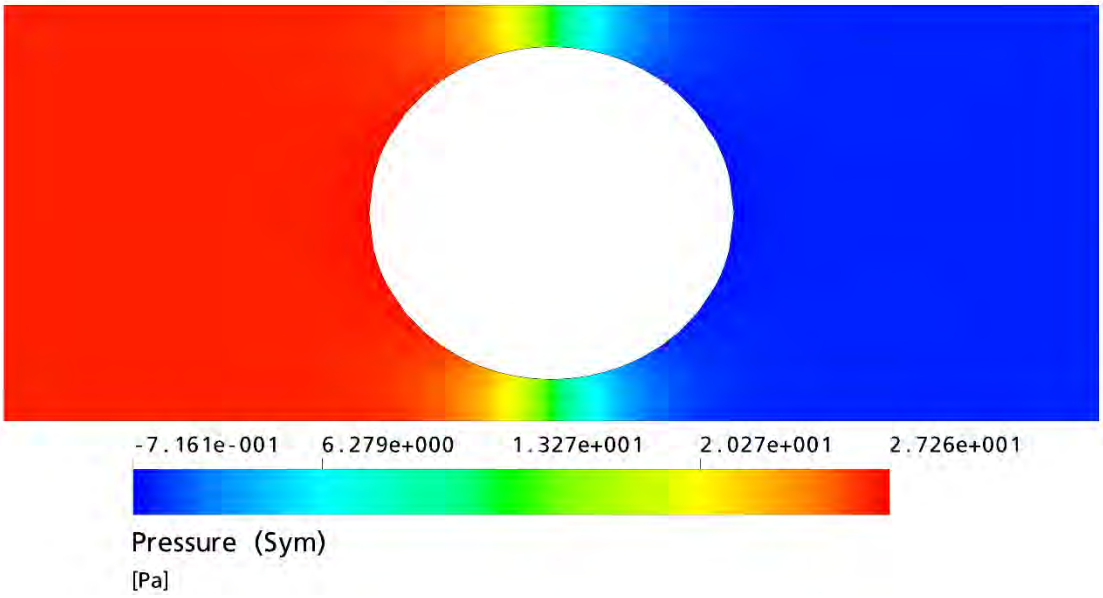

Figure 41: Pressure distribution, case 1, spheroid a/b = 1.1, b/R = 0.8

Chapter 5. Results for Low Reynolds Number Motion in Newtonian Fluid

This section presents the numerical results for axisymmetric prolate spheroids and Cassini ovals for different shape factors and different confinement ratios, for the case of low Reynolds number motion in Newtonian fluid.

First, the results for the spheroids will be shown and the effect of confinement ratio and the effect of particle geometry will be examined. Three different shape factors *a/b* will be studied with values 1, 2, and 10. For each shape factor, confinement ratio *b/R* values of 0.1, 0.3, 0.5, and 0.7 will be studied with the exception for the case of *a/b* = 1, for which confinement ratio *b/R* values of 0.1, 0.2, 0.3, 0.4, 0.5, 0.6, 0.7 and 0.8 will be studied. For each confinement ratio, six different values of Reynolds number will be studied. Re values of 0.01, 0.1, 1, 10, 20, 40 will be examined for steady cases. The results are shown in section 5.1.

Similar analysis will be repeated for the case of Cassini ovals. Three different shape factors $(c/d)^2$ will be studied with values 0.3, 0.7, and 0.95. For each shape factor, confinement ratio *b/R* values of 0.1, 0.3, 0.5, and 0.7 will be studied. For each confinement ratio, six different values of Reynolds number will be studied. Re values of 0.01, 0.1, 1, 10, 20, 40 will be examined for steady cases. The results are shown in section 5.2.

Sample velocity streamlines and pressure contours will be shown to help understand the flow dynamics. These results are shown in section 5.3.

5.1 Spheroid

5.1.1 Effect of Reynolds Number

As seen from figures 42-44, as the Reynolds number increases the coefficient of drag decreases. This is valid for all cases solved here. This follows the same pattern as the standard drag curve for unbounded flow over a sphere. Therefore, for bounded flows over spheroids, the drag coefficient is inversely proportional to the Reynolds number.

5.1.1.1 a/b = 1

Table 13: Numerical results for Case 2, spheroid a/b = 1

	Cd			
Re	**b/R = 0.1**	**b/R = 0.2**	**b/R = 0.3**	**b/R = 0.4**
0.0100	3221.7498	4063.3770	5709.0248	8569.6316
0.1000	322.4085	406.0134	570.1666	855.9470
1.0000	32.8640	40.8190	57.1231	85.6589
10.0000	4.6869	5.0692	6.3579	8.9945
20.0000	2.9315	3.0907	3.6772	4.9201
40.0000	1.9236	1.9977	2.2940	2.9202

	Cd			
Re	**b/R = 0.5**	**b/R = 0.6**	**b/R = 0.7**	**b/R = 0.8**
0.0100	14069.3050	25668.7678	54555.4516	166364.4618
0.1000	1405.2031	2564.5941	5453.3683	16633.7141
1.0000	140.5714	256.4339	544.9587	1663.2304
10.0000	14.3684	25.8365	54.4295	166.4676
20.0000	7.5346	13.1973	27.4264	83.5571
40.0000	4.2253	7.0381	14.1709	42.3617

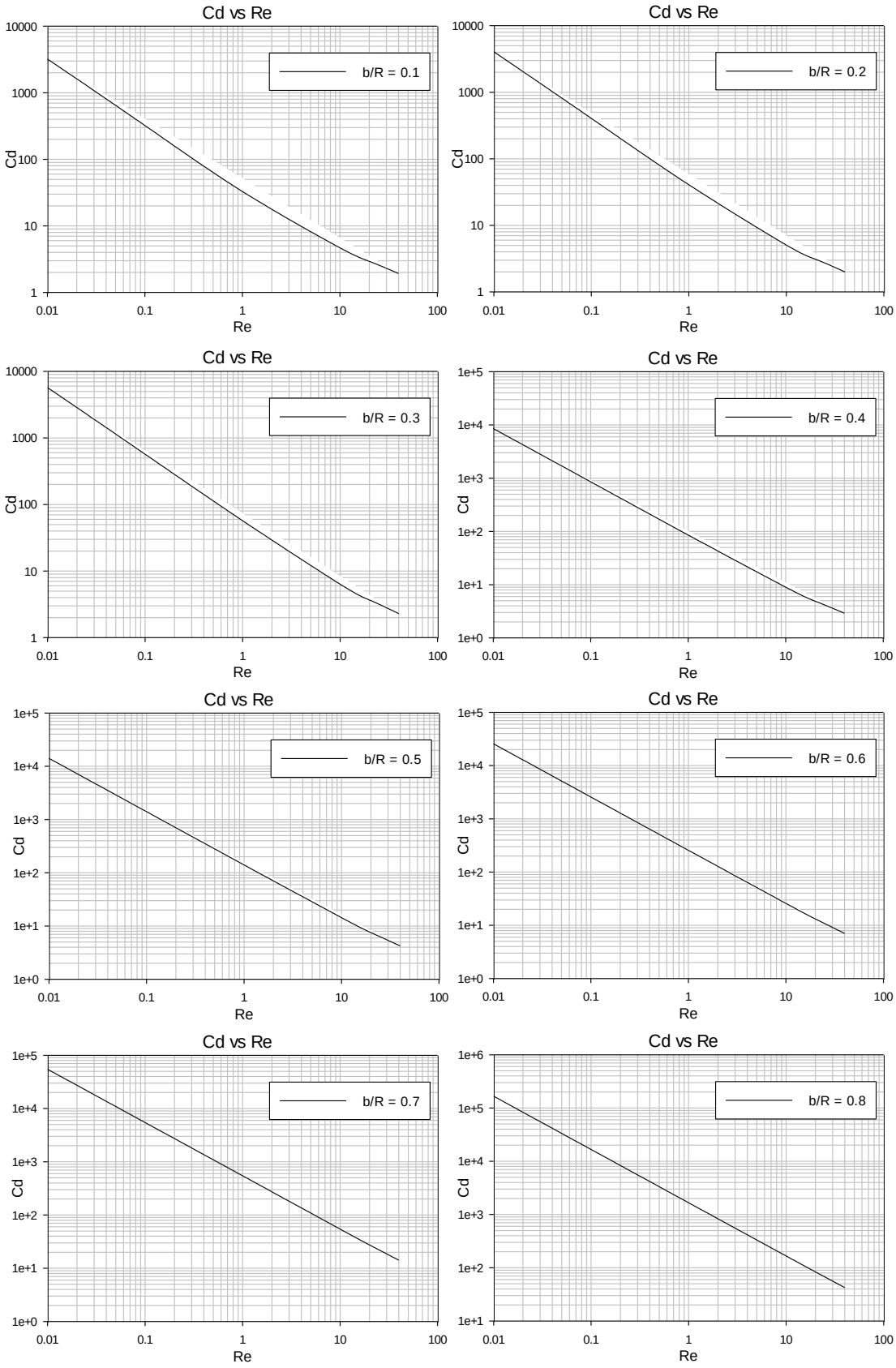

Figure 42: Cd vs Re for Case 2, spheroid a/b = 1 (individual cases)

5.1.1.2 a/b = 2

Table 14: Numerical results for Case 2, spheroid a/b = 2

	Cd			
Re	**b/R = 0.1**	**b/R = 0.3**	**b/R = 0.5**	**b/R = 0.7**
0.0100	3866.2063	8180.4150	22632.7239	95708.5421
0.1000	386.5845	817.5100	2262.2324	9570.7661
1.0000	39.3725	81.8240	226.2550	956.0101
10.0000	5.4526	8.6613	22.8332	95.0308
20.0000	3.3306	4.7514	11.6532	47.5105
40.0000	2.1130	2.7886	6.1487	23.9952

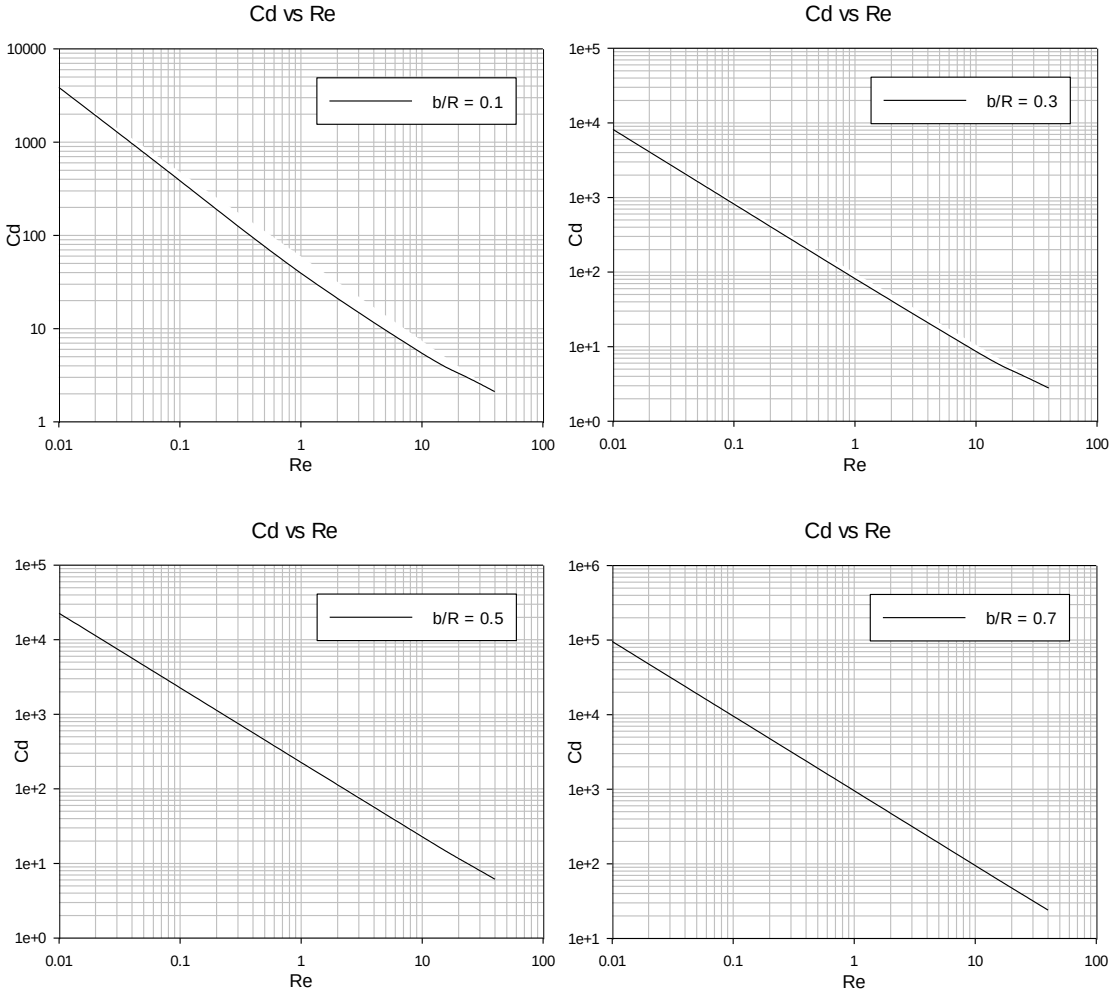

Figure 43: Cd vs Re for Case 2, spheroid a/b = 2 (individual cases)

5.1.1.3 a/b = 10

Table 15: Numerical results for Case 2, spheroid a/b = 10

	Cd			
Re	**b/R = 0.1**	**b/R = 0.3**	**b/R = 0.5**	**b/R = 0.7**
0.0100	11427.9461	31844.0586	97859.1374	462559.5568
0.1000	1142.8739	3183.6038	9786.9714	46255.8675
1.0000	114.8850	318.4661	978.0978	4644.1400
10.0000	13.4686	32.2001	97.7639	463.8199
20.0000	7.7165	16.4095	48.9948	231.9558
40.0000	4.5923	8.5592	24.6951	116.2313

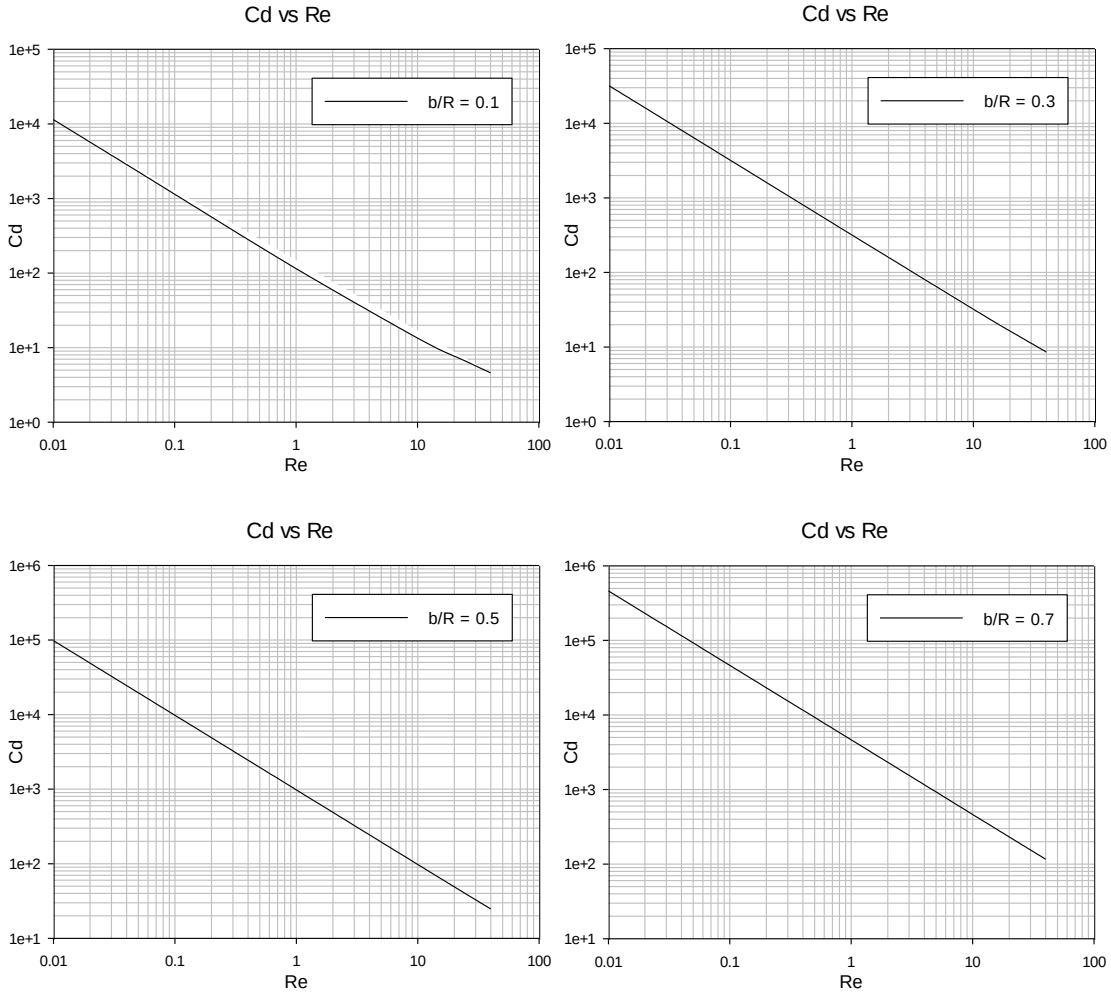

Figure 44: Cd vs Re for Case 2, spheroid a/b = 10 (individual cases)

5.1.2 Effect of Confinement Ratio

As seen from figures 45-47, the coefficient of drag increases with an increase in the confinement ratio following the same reasoning as for case 1, creeping Newtonian flow.

5.1.2.1 a/b = 1

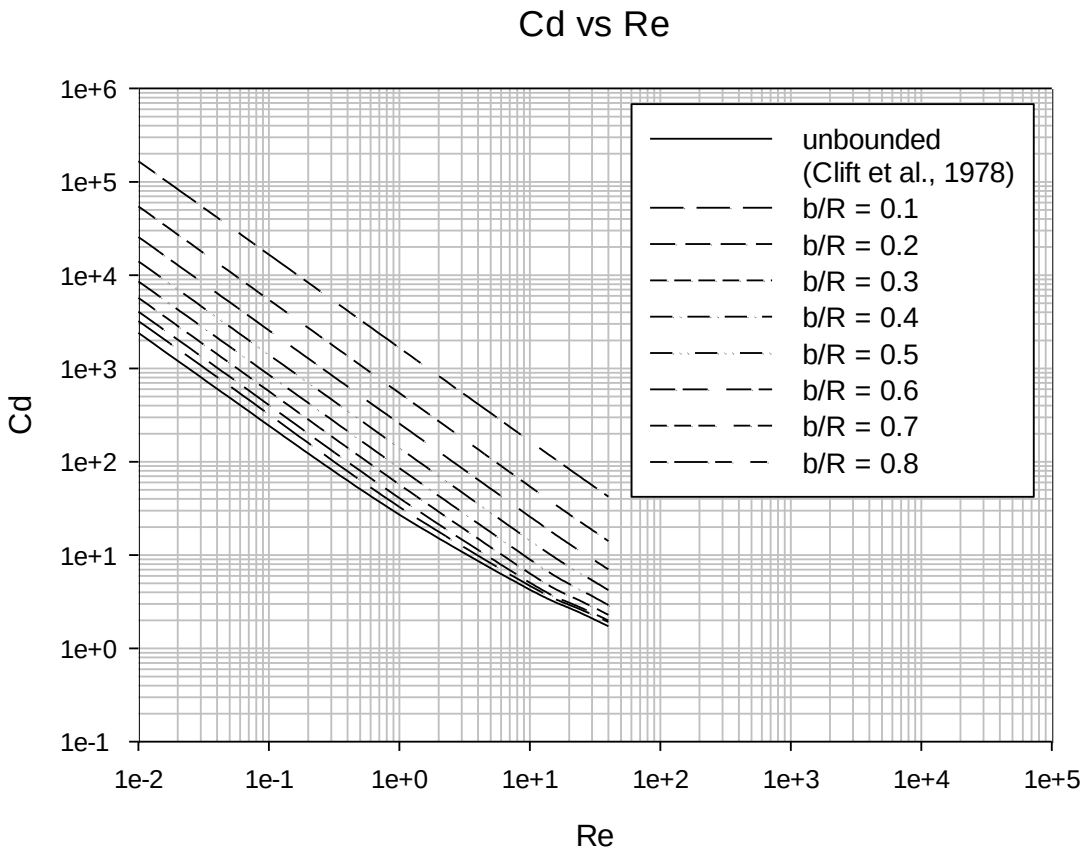

Figure 45: Cd vs Re for different confinement ratios, for Case 2, spheroid a/b = 1, all cases and unbounded [50]

5.1.2.2 a/b = 2

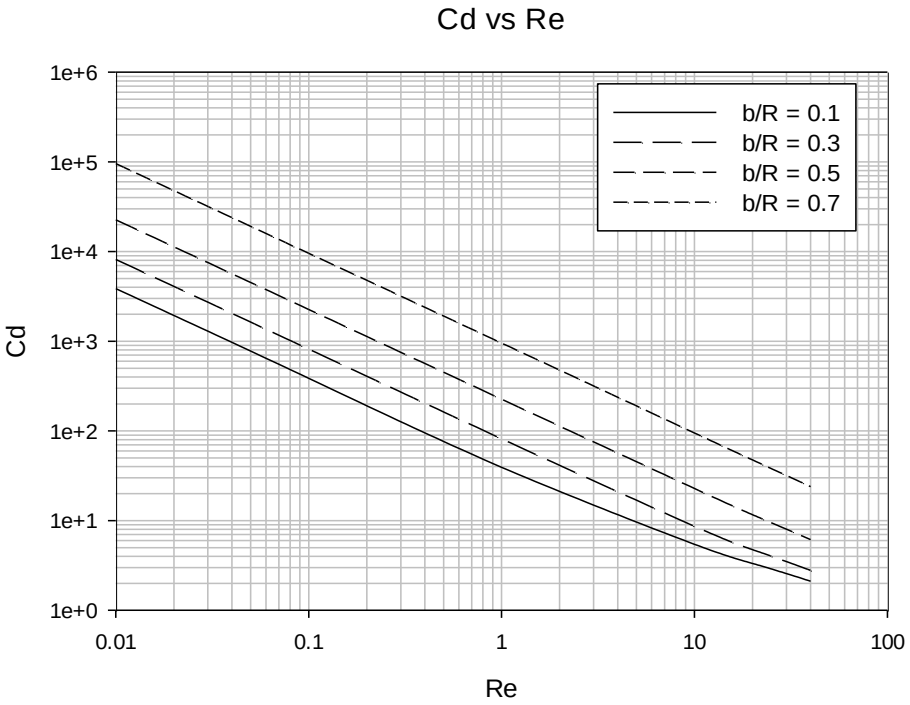

Figure 46: Cd vs Re for different confinement ratios, for Case 2, spheroid a/b = 2

5.1.2.3 a/b = 10

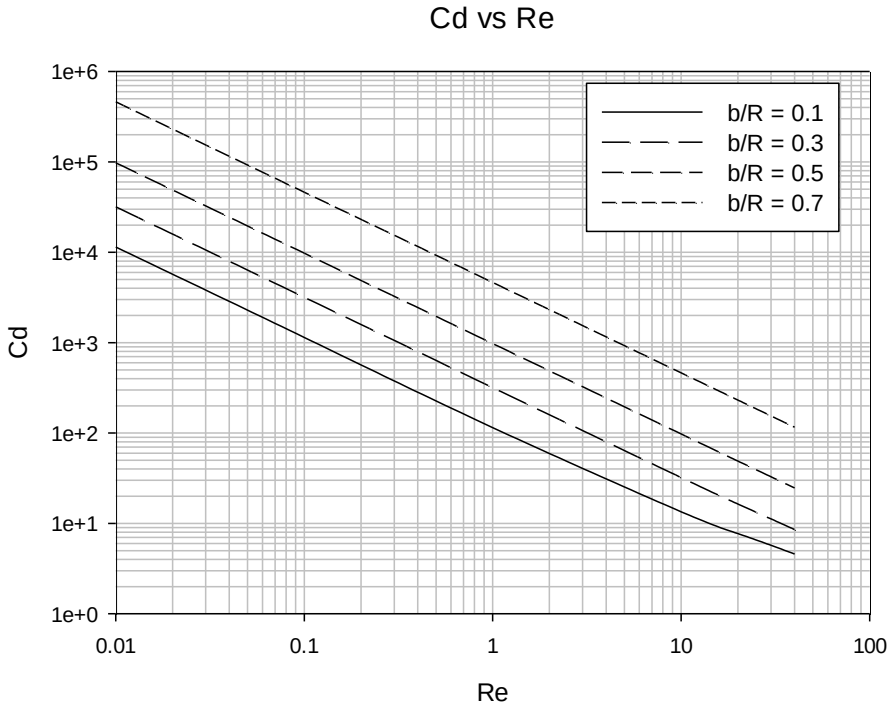

Figure 47: Cd vs Re for different confinement ratios, for Case 2, spheroid a/b = 10

5.1.3 Effect of Particle Shape

The effect of particle shape, figures 48-51, also follows the same reasoning as for case 1, creeping Newtonian flow.

5.1.3.1 b/R = 0.1

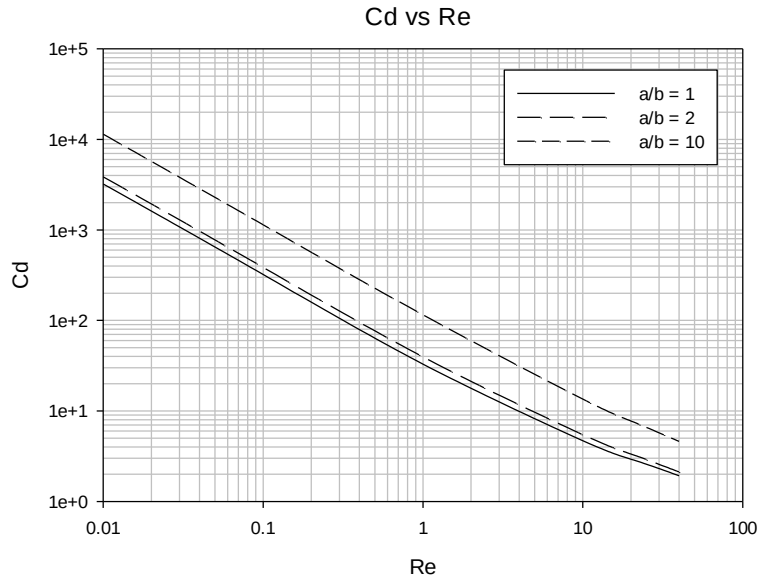

Figure 48: Cd vs Re for different shape factors ratios, for Case 2, spheroid b/R = 0.1

5.1.3.2 b/R = 0.3

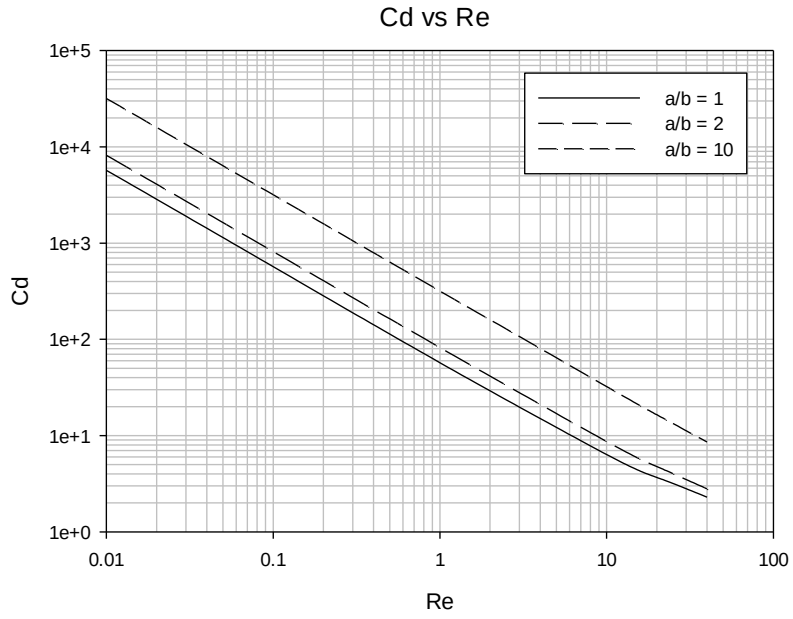

Figure 49: Cd vs Re for different shape factors ratios, for Case 2, spheroid b/R = 0.3

5.1.3.3 b/R = 0.5

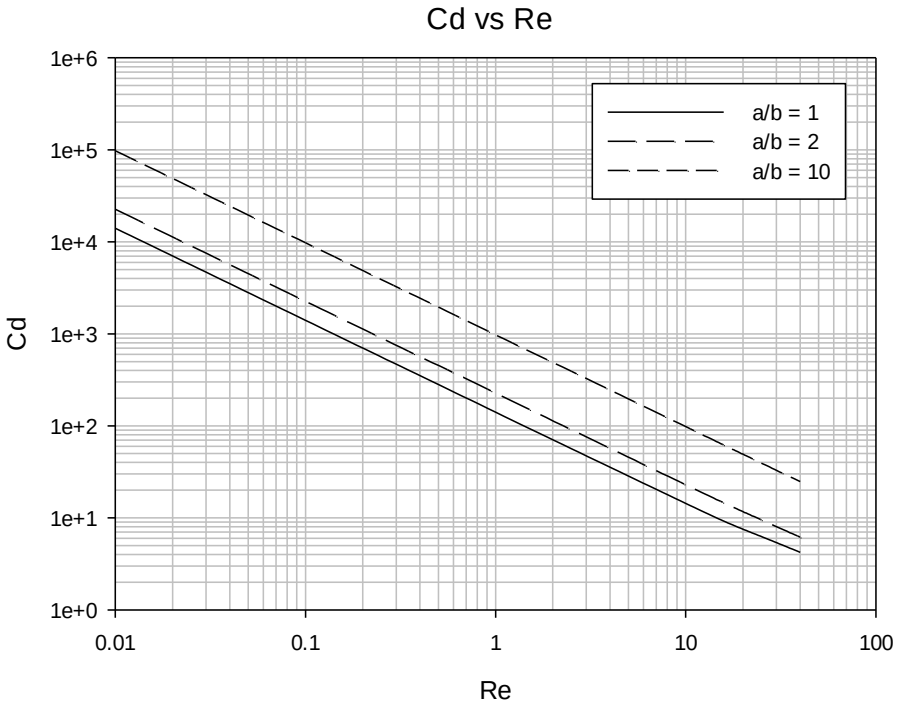

Figure 50: Cd vs Re for different shape factors ratios, for Case 2, spheroid b/R = 0.5

5.1.3.4 b/R = 0.7

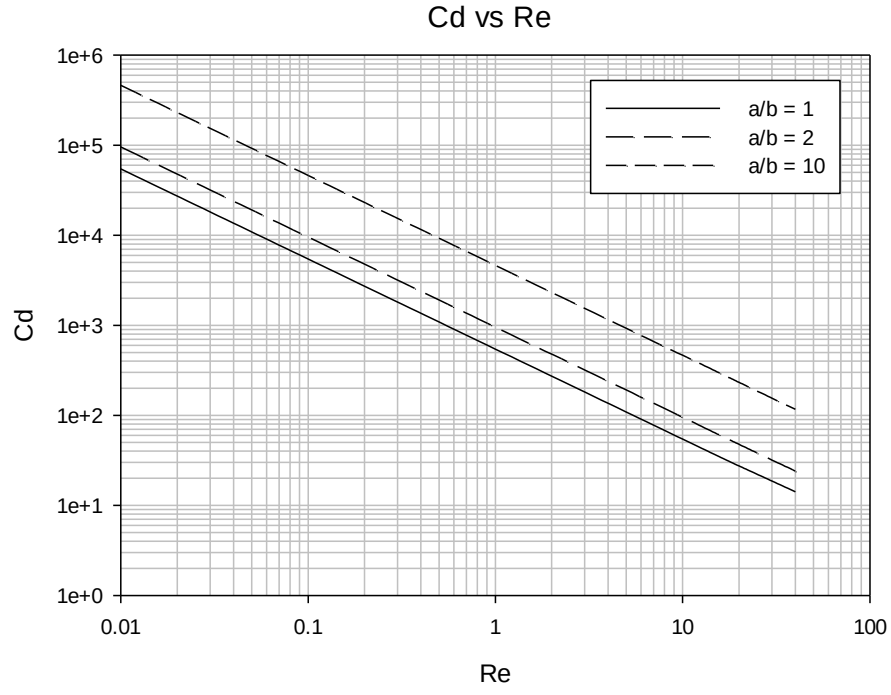

Figure 51: Cd vs Re for different shape factors ratios, for Case 2, spheroid b/R = 0.7

5.2 Cassini Oval

5.2.1 Effect of the Reynolds number

As seen from figures 52-54, similar to the case of spheroid, the coefficient of drag decreases with increase in Reynolds number.

5.2.1.1 $(c/d)^2 = 0.3$

Table 16: Numerical results for Case 2, Cassini oval $(c/d)^2 = 0.3$

	Cd			
Re	**b/R = 0.1**	**b/R = 0.3**	**b/R = 0.5**	**b/R = 0.7**
0.0100	3884.6663	6761.3296	17520.0496	75133.0825
0.1000	388.3193	675.5528	1750.3948	7510.2430
1.0000	39.4722	67.6501	175.0585	750.6679
10.0000	5.4266	7.3691	17.7471	74.9641
20.0000	3.3403	4.1740	9.1593	37.6200
40.0000	2.1450	2.5388	4.9676	19.1408

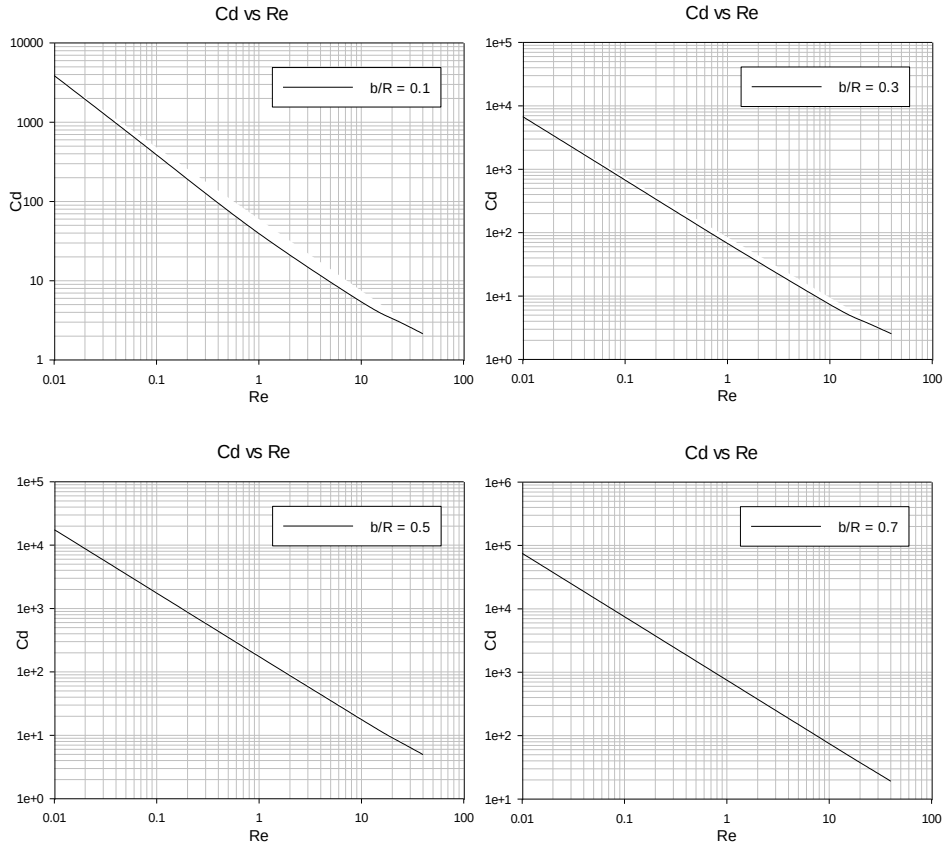

Figure 52: Cd vs Re for Case 2, Cassini oval $(c/d)^2 = 0.3$ (individual cases)

5.2.1.2 $(c/d)^2 = 0.7$

Table 17: Numerical results for Case 2, Cassini oval $(c/d)^2 = 0.7$

	Cd			
Re	**b/R = 0.1**	**b/R = 0.3**	**b/R = 0.5**	**b/R = 0.7**
0.0100	4555.8300	10163.4745	31221.0157	142498.5897
0.1000	455.4960	1015.2836	3014.4645	14246.1060
1.0000	46.3645	101.6200	301.4227	1423.9409
10.0000	6.3960	10.7041	30.3943	142.1138
20.0000	3.8996	5.8093	16.1067	71.1788
40.0000	2.4692	3.3648	8.1675	35.9466

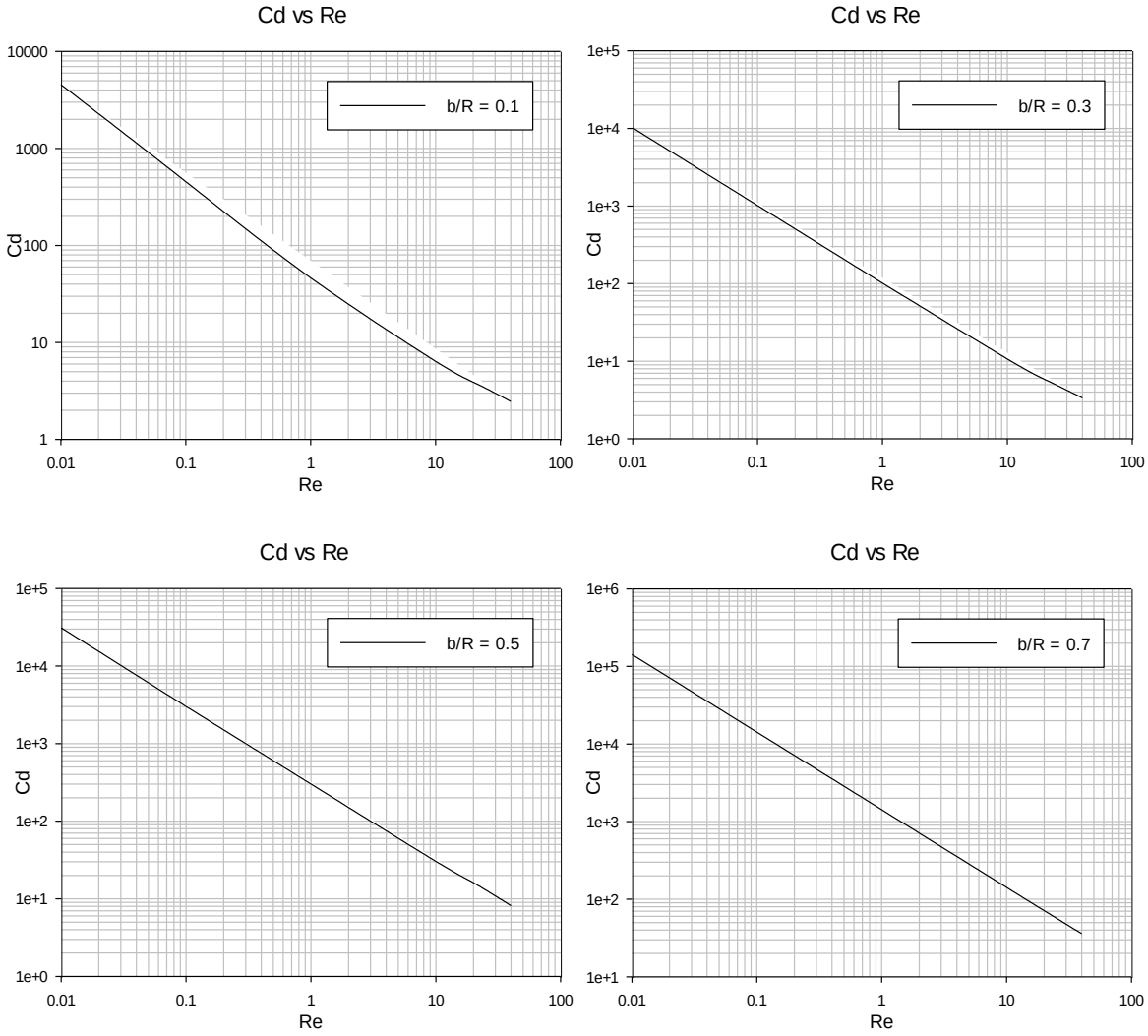

Figure 53: Cd vs Re for Case 2, Cassini oval $(c/d)^2 = 0.7$ (individual cases)

5.2.1.3 $(c/d)^2 = 0.95$

Table 18: Numerical results for Case 2, Cassini oval $(c/d)^2 = 0.95$

	Cd			
Re	**b/R = 0.1**	**b/R = 0.3**	**b/R = 0.5**	**b/R = 0.7**
0.0100	4965.1785	11320.8380	30601.5975	126037.8934
0.1000	496.3760	1131.1781	3058.8347	12603.5490
1.0000	50.4005	113.2403	305.8429	1259.4292
10.0000	6.8139	11.9614	30.9426	125.5304
20.0000	4.1384	6.4757	15.9168	63.0036
40.0000	2.6193	3.7332	8.5212	32.1455

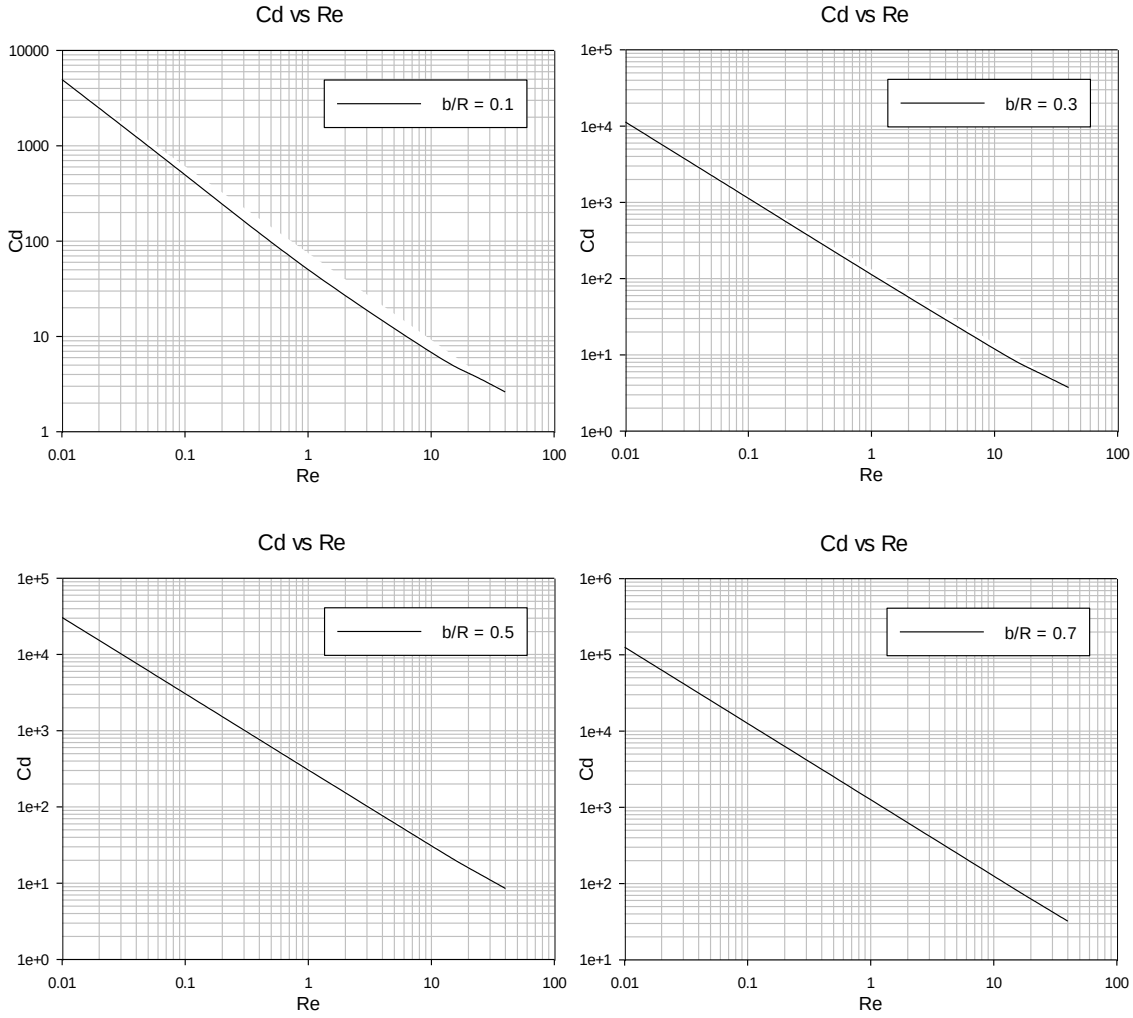

Figure 54: Cd vs Re for Case 2, Cassini oval $(c/d)^2 = 0.95$ (individual cases)

5.2.2 Effect of Confinement Ratio

As seen from figures 55-57, the coefficient of drag increases with the increase in the confinement ratio. This is similar to the previous cases.

5.2.2.1 $(c/d)^2 = 0.3$

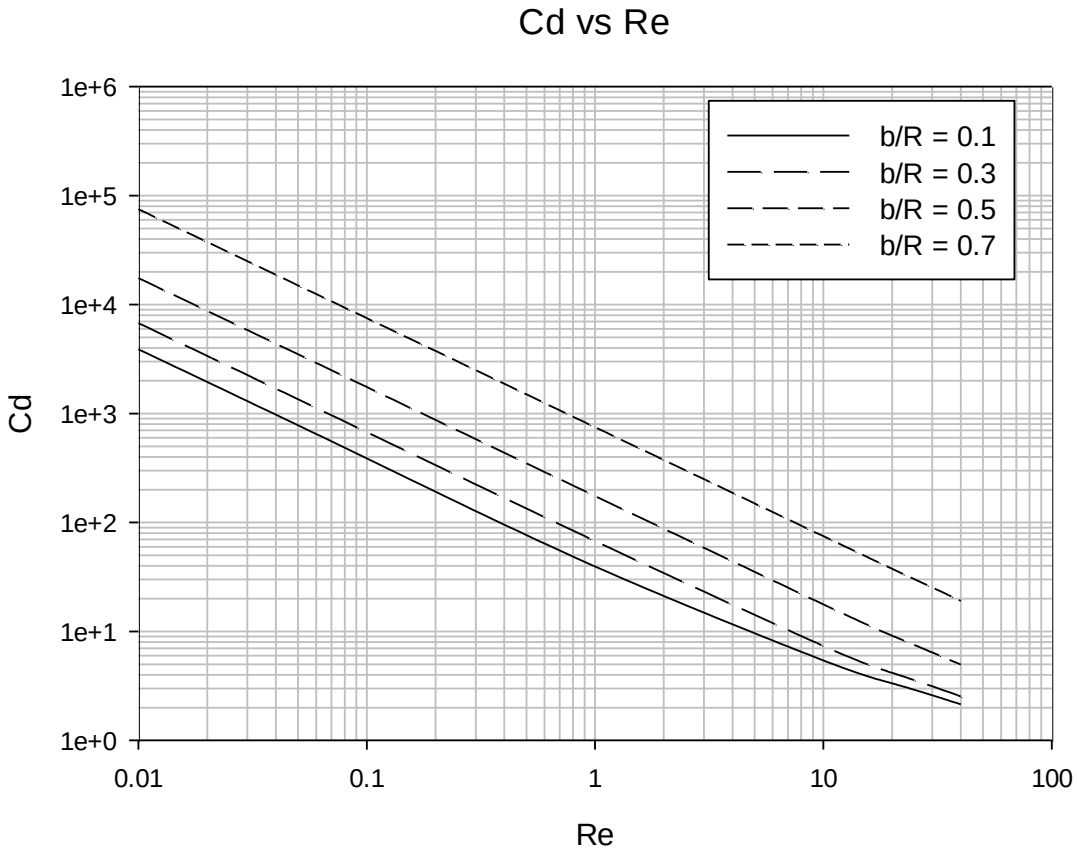

Figure 55: Cd vs Re for different confinement ratios, for Case 2, Cassini oval $(c/d)^2 = 0.3$

5.2.2.2 $(c/d)^2 = 0.7$

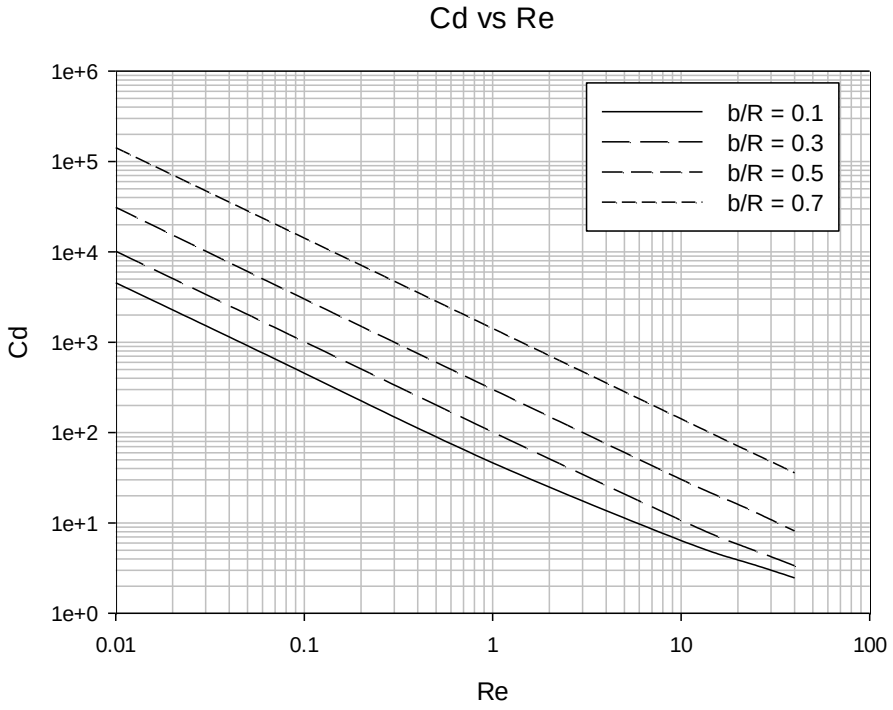

Figure 56: Cd vs Re for different confinement ratios, for Case 2, Cassini oval $(c/d)^2 = 0.7$

5.2.2.3 $(c/d)^2 = 0.95$

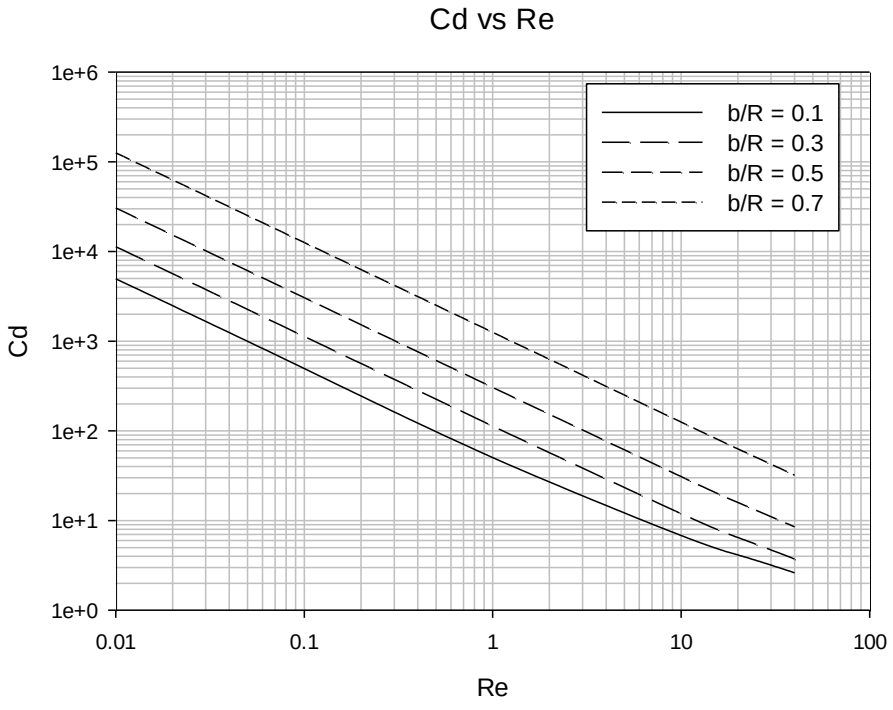

Figure 57: Cd vs Re for different confinement ratios, for Case 2, Cassini oval $(c/d)^2 = 0.95$

5.2.3 Effect of Particle Shape

The effect of particle shape, figures 58-61, also follows the same reasoning as for case 1, creeping Newtonian flow.

5.2.3.1 b/R = 0.1

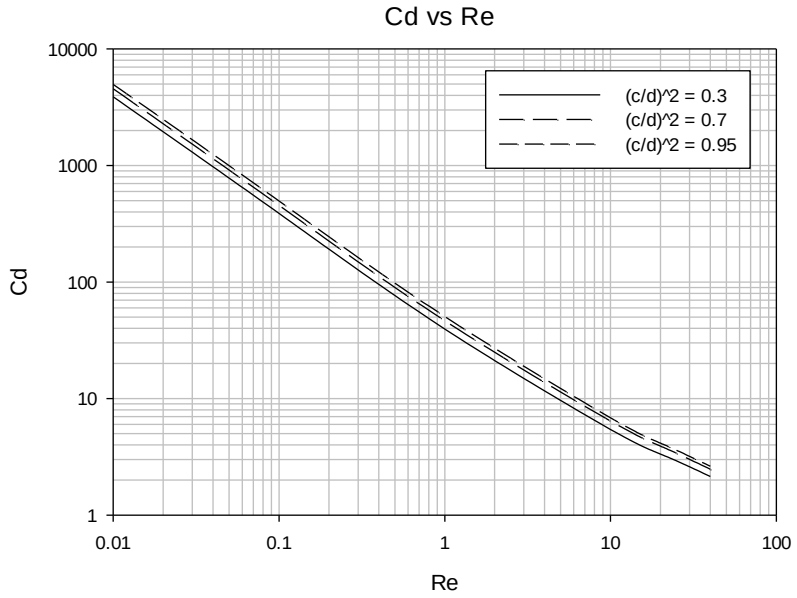

Figure 58: Cd vs Re for different shape factors, for Case 2, Cassini oval b/R = 0.1

5.2.3.2 b/R = 0.3

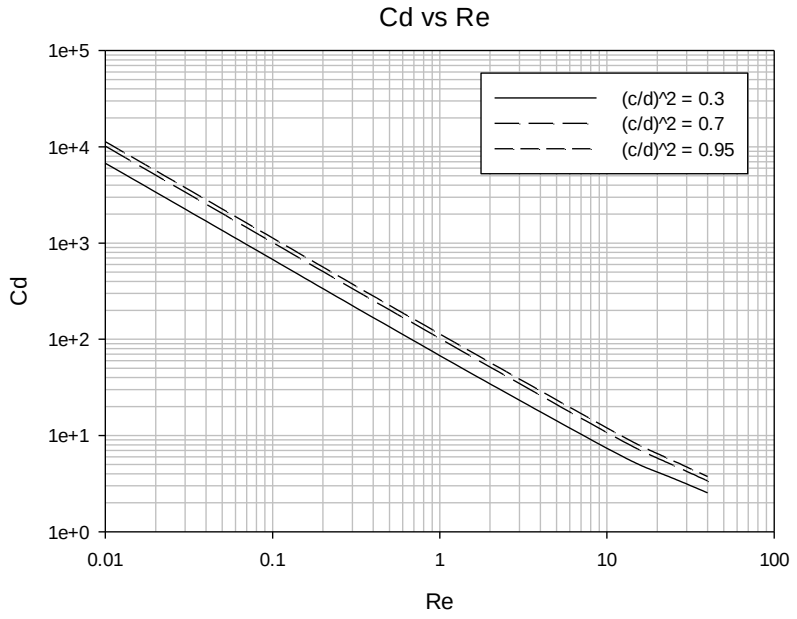

Figure 59: Cd vs Re for different shape factors, for Case 2, Cassini oval b/R = 0.3

5.2.3.3 b/R = 0.5

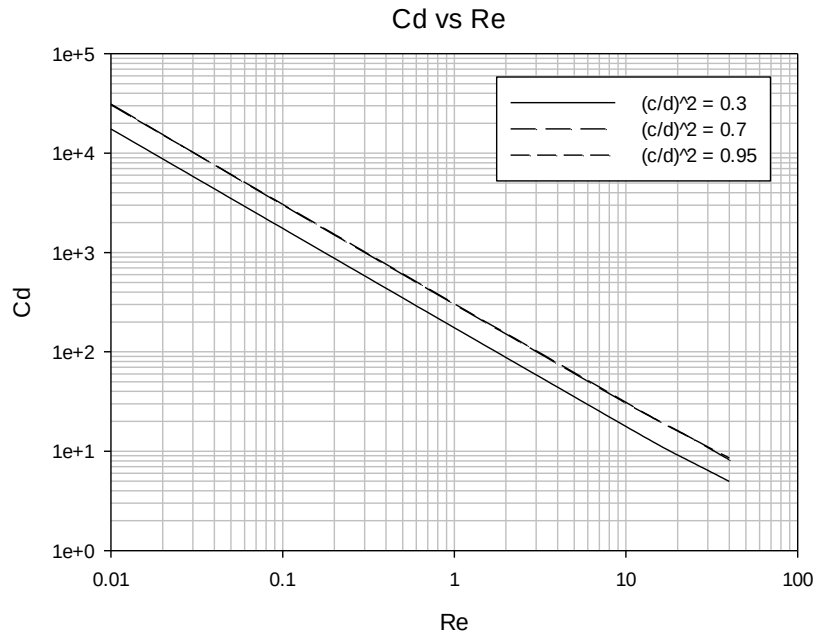

Figure 60: Cd vs Re for different shape factors, for Case 2, Cassini oval b/R = 0.5

5.2.3.4 b/R = 0.7

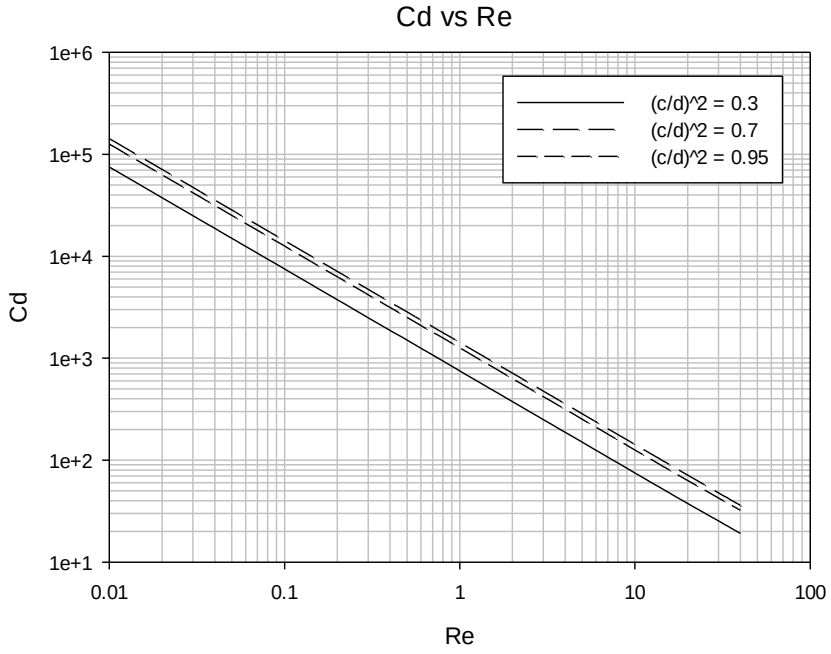

Figure 61: Cd vs Re for different shape factors, for Case 2, Cassini oval b/R = 0.7

5.3 Velocity Streamlines and Pressure Contours (Selected Cases)

As an example, the velocity streamlines and the pressure contours for the case of Cassini oval with shape factor $(c/d)^2 = 0.7$ with confinement ratio $b/R = 0.7$ are shown here. The velocity streamlines are shown in figures 62-67, while the pressure contours are shown in figures 68-73. From the streamlines we can conclude that the flow is attached with no separation in the wake region for lower Reynolds number values. For other cases, very small separation was seen at Re = 40 for some shapes.

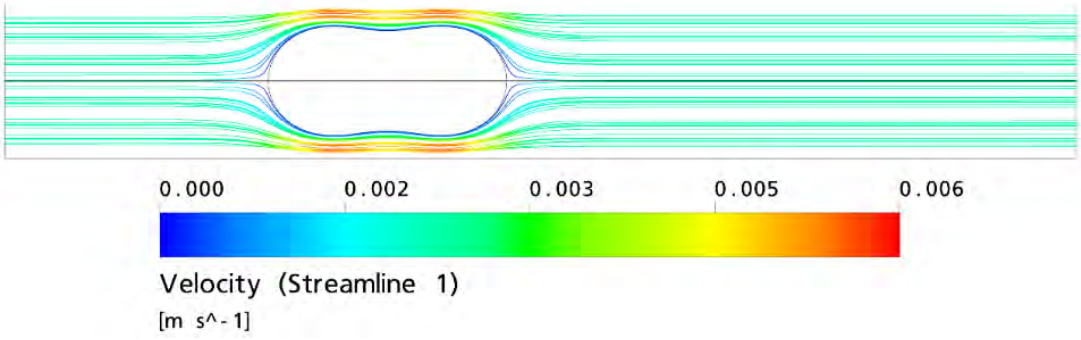

Figure 62: Velocity streamlines, Case 2, Cassini oval $(c/d)^2 = 0.7$, b/R = 0.7, Re = 0.01

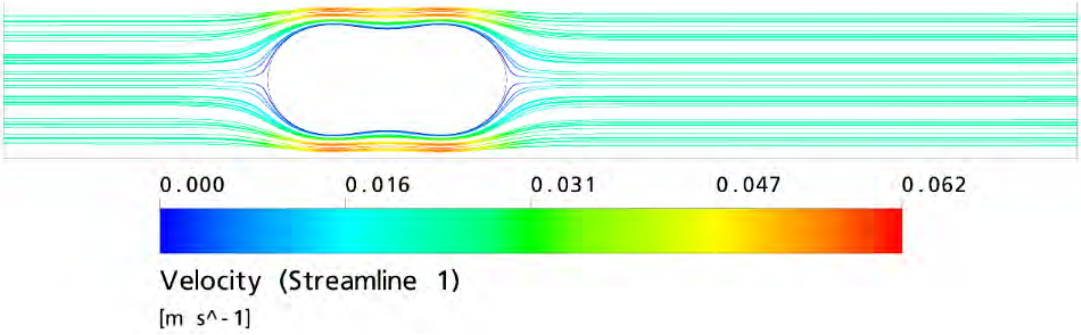

Figure 63: Velocity streamlines, Case 2, Cassini oval $(c/d)^2 = 0.7$, b/R = 0.7, Re = 0.1

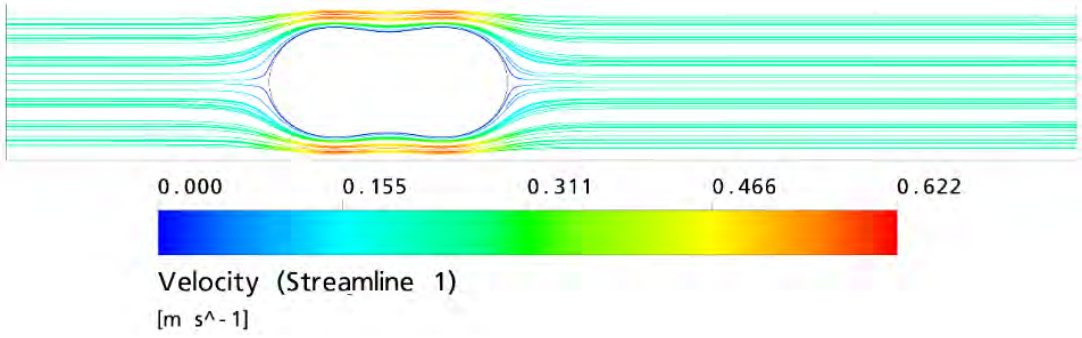

Figure 64: Velocity streamlines, Case 2, Cassini oval $(c/d)^2 = 0.7$, b/R = 0.7, Re = 1

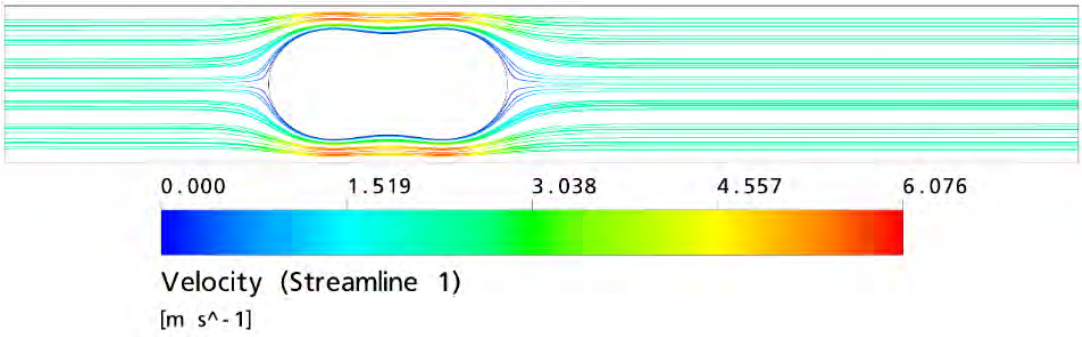

Figure 65: Velocity streamlines, Case 2, Cassini oval $(c/d)^2 = 0.7$, $b/R = 0.7$, Re = 10

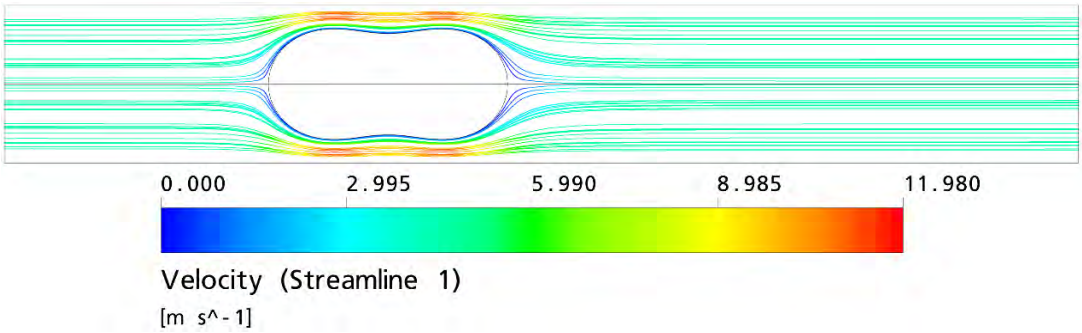

Figure 66: Velocity streamlines, Case 2, Cassini oval $(c/d)^2 = 0.7$, $b/R = 0.7$, Re = 20

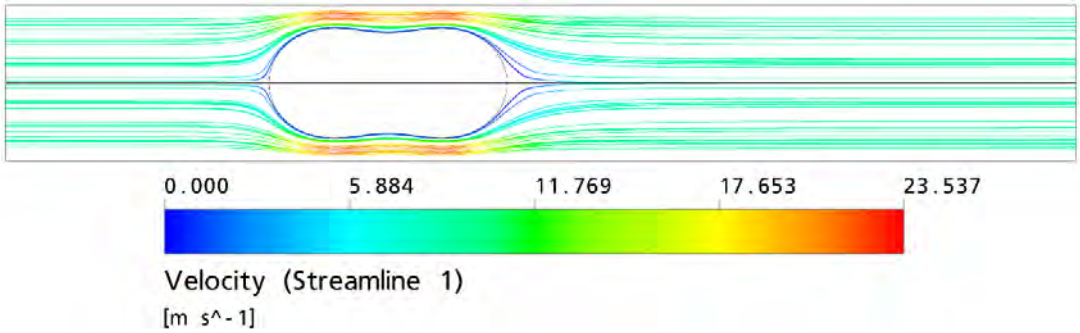

Figure 67: Velocity streamlines, Case 2, Cassini oval $(c/d)^2 = 0.7$, $b/R = 0.7$, Re = 40

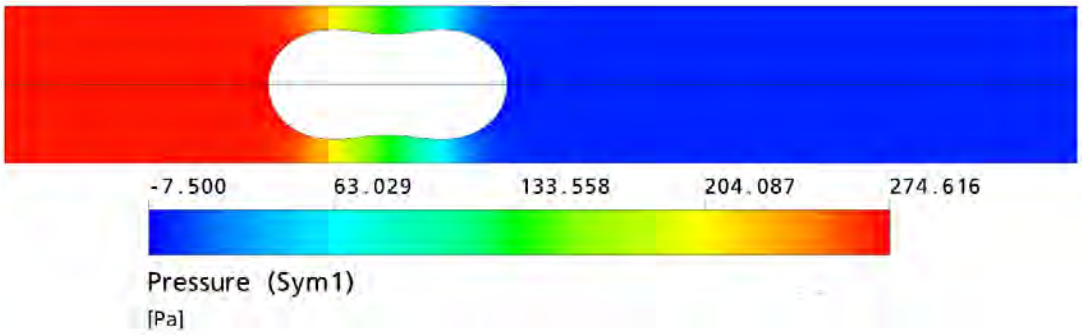

Figure 68: Pressure contour, Case 2, Cassini oval $(c/d)^2 = 0.7$, b/R = 0.7, Re = 0.01

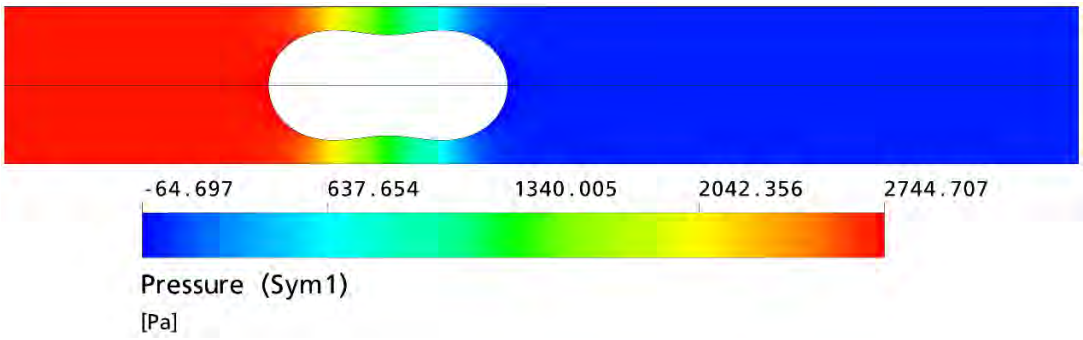

Figure 69: Pressure contour, Case 2, Cassini oval $(c/d)^2 = 0.7$, b/R = 0.7, Re = 0.1

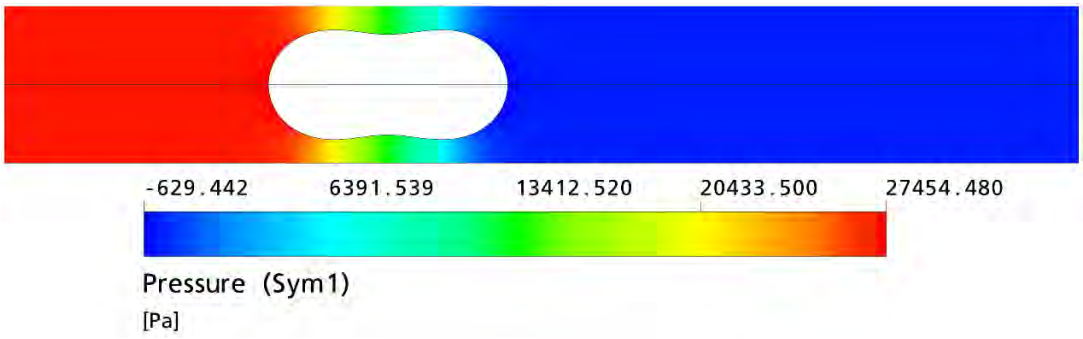

Figure 70: Pressure contour, Case 2, Cassini oval $(c/d)^2 = 0.7$, b/R = 0.7, Re = 1

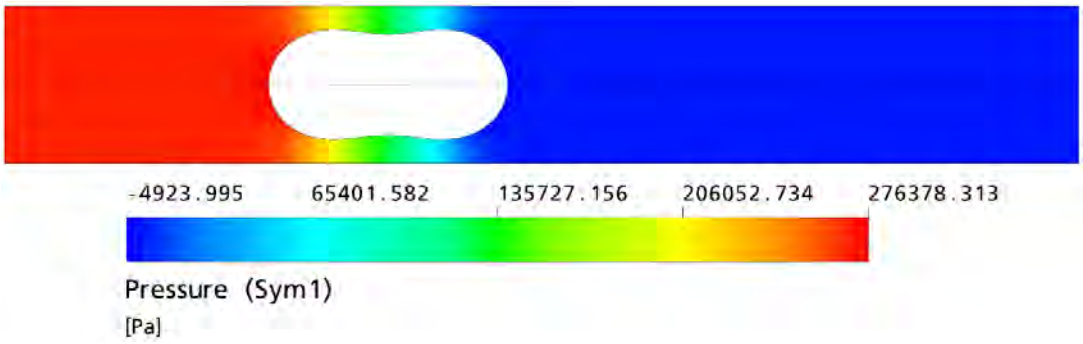

Figure 71: Pressure contour, Case 2, Cassini oval $(c/d)^2 = 0.7$, b/R = 0.7, Re = 10

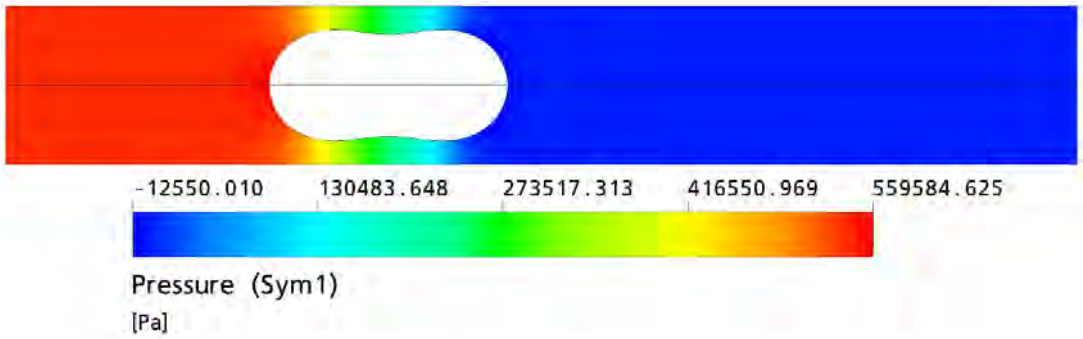

Figure 72: Pressure contour, Case 2, Cassini oval $(c/d)^2 = 0.7$, b/R = 0.7, Re = 20

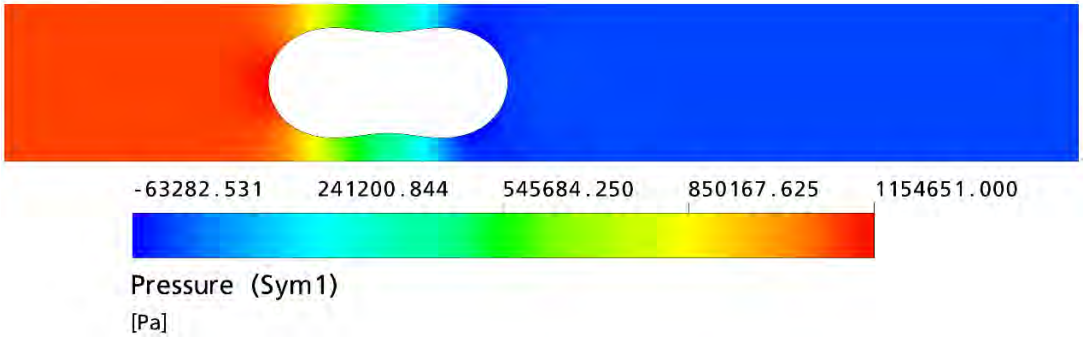

Figure 73: Pressure contour, Case 2, Cassini oval $(c/d)^2 = 0.7$, b/R = 0.7, Re = 40

Chapter 6. Results for Creeping Motion in non-Newtonian Fluid

This section presents the numerical results for axisymmetric prolate spheroids and Cassini ovals for different shape factors and different confinement ratios, for the case of creeping motion in non-Newtonian fluid.

First, the results for the spheroids will be shown and the effect of confinement ratio and the effect of particle geometry will be examined. Five different shape factors *a/b* will be studied with values 1, 1.1, 2, 5 and 10. For each shape factor, confinement ratio *b/R* values of 0.1, 0.2, 0.3, 0.4, 0.5, 0.6, and 0.7 will be studied. This will be repeated for four different values of power-law index *n* values including 0.6 and 0.8 for shear-thinning fluids and 1.2 and 1.4 for shear-thickening fluids. The results are shown in section 4.1.

Similar analysis will be repeated for the case of Cassini ovals. Six different shape factors $(c/d)^2$ will be studied with values 0.1, 0.3, 0.5, 0.7, 0.9, 0.95. For each shape factor, confinement ratio *b/R* values of 0.1, 0.2, 0.3, 0.4, 0.5, 0.6, and 0.7 will be studied. This will be repeated for four different values of power-law index *n* values including 0.6 and 0.8 for shear-thinning fluids and 1.2 and 1.4 for shear-thickening fluids. The results are shown in section 4.2.

Sample velocity streamlines and pressure contours will be shown to help understand the flow dynamics. These results are shown in section 4.3.

6.1 Spheroid

6.1.1 Effect of Confinement Ratio

As seen from figures 74-77, the drag coefficient increases with increase in the confinement ratio. This results is similar to the previous cases.

6.1.1.1 n = 0.6

Table 19: Numerical results for Case 3, spheroids, n = 0.6

	Cd				
b/R	**a/b = 1**	**a/b = 1.1**	**a/b = 2**	**a/b = 5**	**a/b = 10**
0.1	74912.45347	76720.93591	94478.36616	160388.9061	299110.968
0.2	82616.74028	84872.86575	108082.8994	198225.1147	420064.5961
0.3	96828.25201	99947.63474	133043.082	269212.6202	575921.9048
0.4	121208.017	126061.5639	175623.2615	399835.5967	1016573.226
0.5	162823.2718	170685.9576	248908.2792	655474.7848	1812087.064
0.6	237834.3517	252740.5051	399666.6974	1277423.512	3648623.879
0.7	398255.4573	427990.2407	794237.4199	2981360.7	8566352.736

Note that the coefficient of drag for a/b = 1, for n = 0.6 is given as 69468.40 [81].

6.1.1.2 n = 0.8

Table 20: Numerical results for Case 3, spheroids, n = 0.8

	Cd				
b/R	**a/b = 1**	**a/b = 1.1**	**a/b = 2**	**a/b = 5**	**a/b = 10**
0.1	48605.77553	49069.18318	60526.86231	104619.1436	202787.9718
0.2	57764.86885	58980.57203	76137.41809	148371.9109	324730.2583
0.3	73661.31018	76642.21456	104076.2835	227896.8916	468215.2779
0.4	100684.6361	105767.4676	150907.69	371466.6344	899275.0797
0.5	148555.5089	149896.363	242450.4094	664674.6461	1628276.47
0.6	248690.5698	263452.2509	440037.4559	1343012.124	3293935.672
0.7	482684.7274	495965.1136	993950.728	3168518.201	7742617.965

Note that the coefficient of drag for a/b = 1, for n = 0.8 is given as 42972.22 [81].

6.1.1.3 n = 1.2

Table 21: Numerical results for Case 3, spheroids, n = 1.2

	Cd				
b/R	**a/b = 1**	**a/b = 1.1**	**a/b = 2**	**a/b = 5**	**a/b = 10**
0.1	19720.61084	18948.97044	22289.87027	27070.46542	33815.74607
0.2	27739.73974	28070.53643	33585.30232	42676.42465	56955.36174
0.3	42646.91386	44620.35067	53010.33999	69331.96841	83193.21116
0.4	69703.64098	72943.73646	85770.9131	116950.237	161126.8866
0.5	121610.7519	127343.3191	150284.6389	211538.5747	291946.1301
0.6	243046.5145	246002.7134	290438.6949	428780.3197	590722.3859
0.7	536023.5007	550786.4621	675045.6296	1012368.196	1388588.899

6.1.1.4 n = 1.4

Table 22: Numerical results for Case 3, spheroids, n = 1.4

	Cd				
b/R	**a/b = 1**	**a/b = 1.1**	**a/b = 2**	**a/b = 5**	**a/b = 10**
0.1	11596.13108	10337.58313	6793.886823	3476.86584	2426.394561
0.2	16439.16431	15287.04251	9685.972787	5456.75221	4086.39735
0.3	24726.59475	23279.86488	14747.62847	8863.432176	5968.683209
0.4	38298.11895	35850.61553	23590.41454	14950.58056	11560.11705
0.5	62704.60417	59304.01359	41251.73501	27042.17993	20945.60888
0.6	120410.6467	111888.1856	79690.64295	54813.28437	42381.31521
0.7	262779.1273	249111.4913	185194.9913	129413.9422	99624.99895

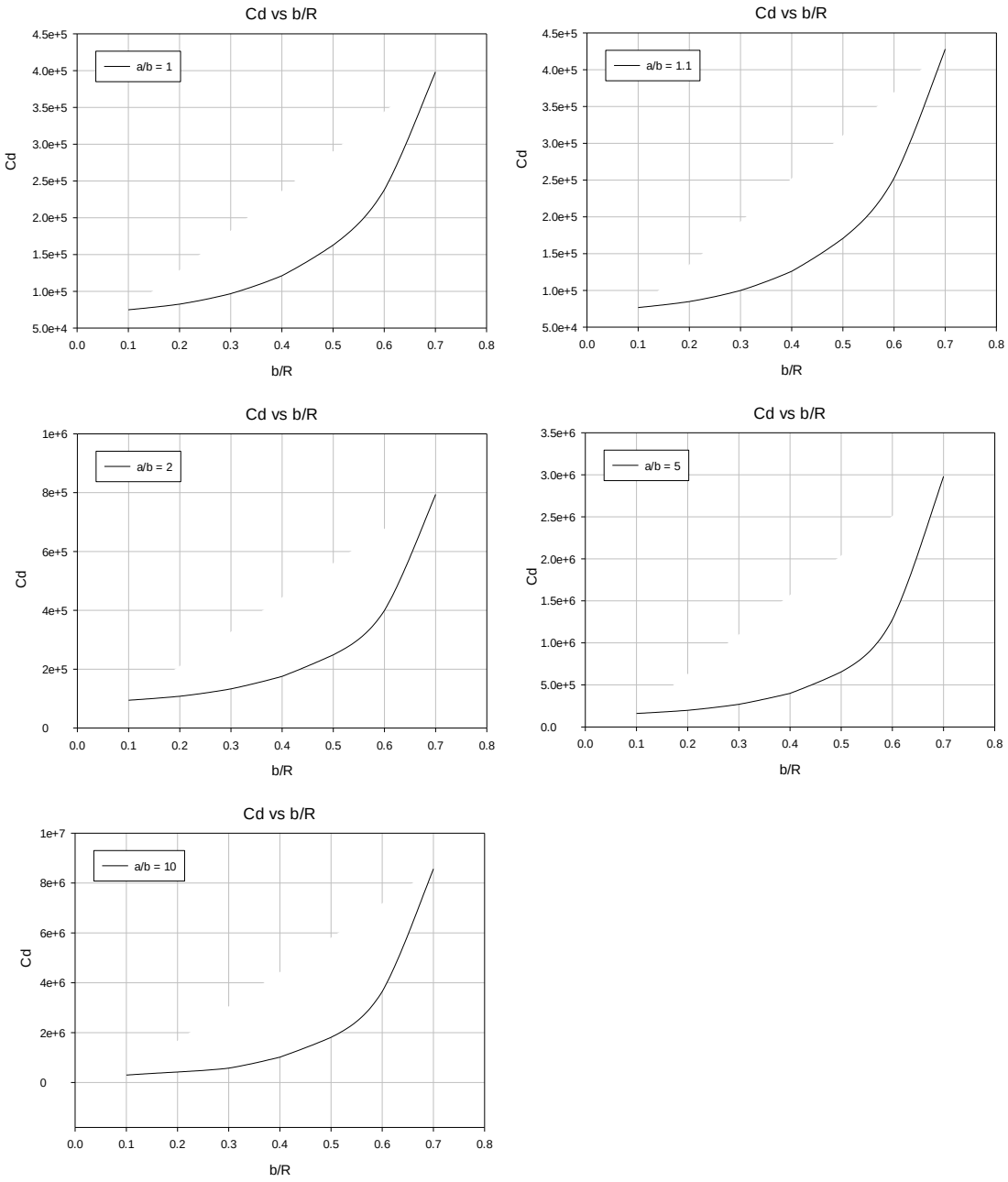

Figure 74: Cd vs b/R for Case 3, spheroids, n = 0.6 (individual cases)

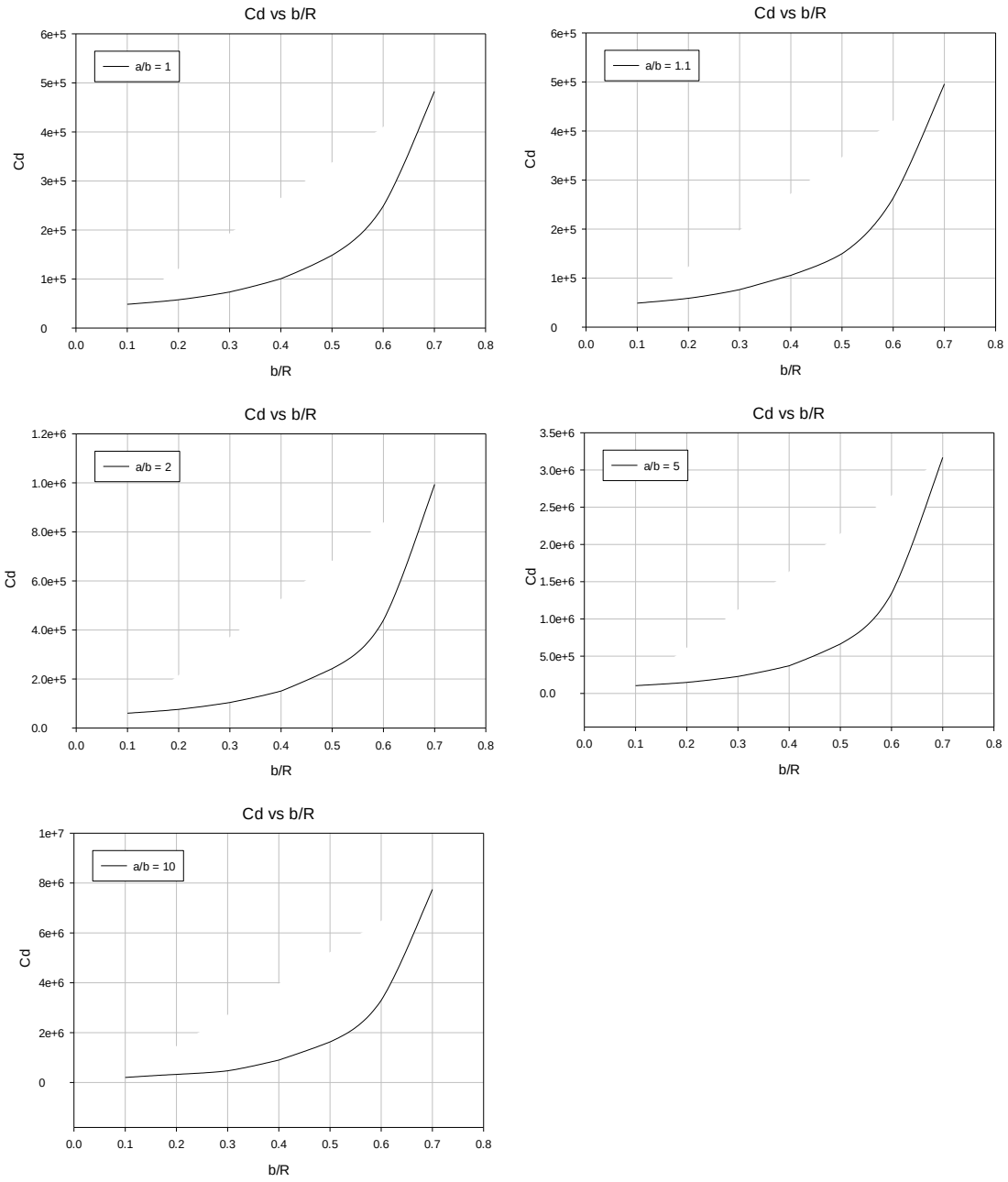

Figure 75: Cd vs b/R for Case 3, spheroids, n = 0.8 (individual cases)

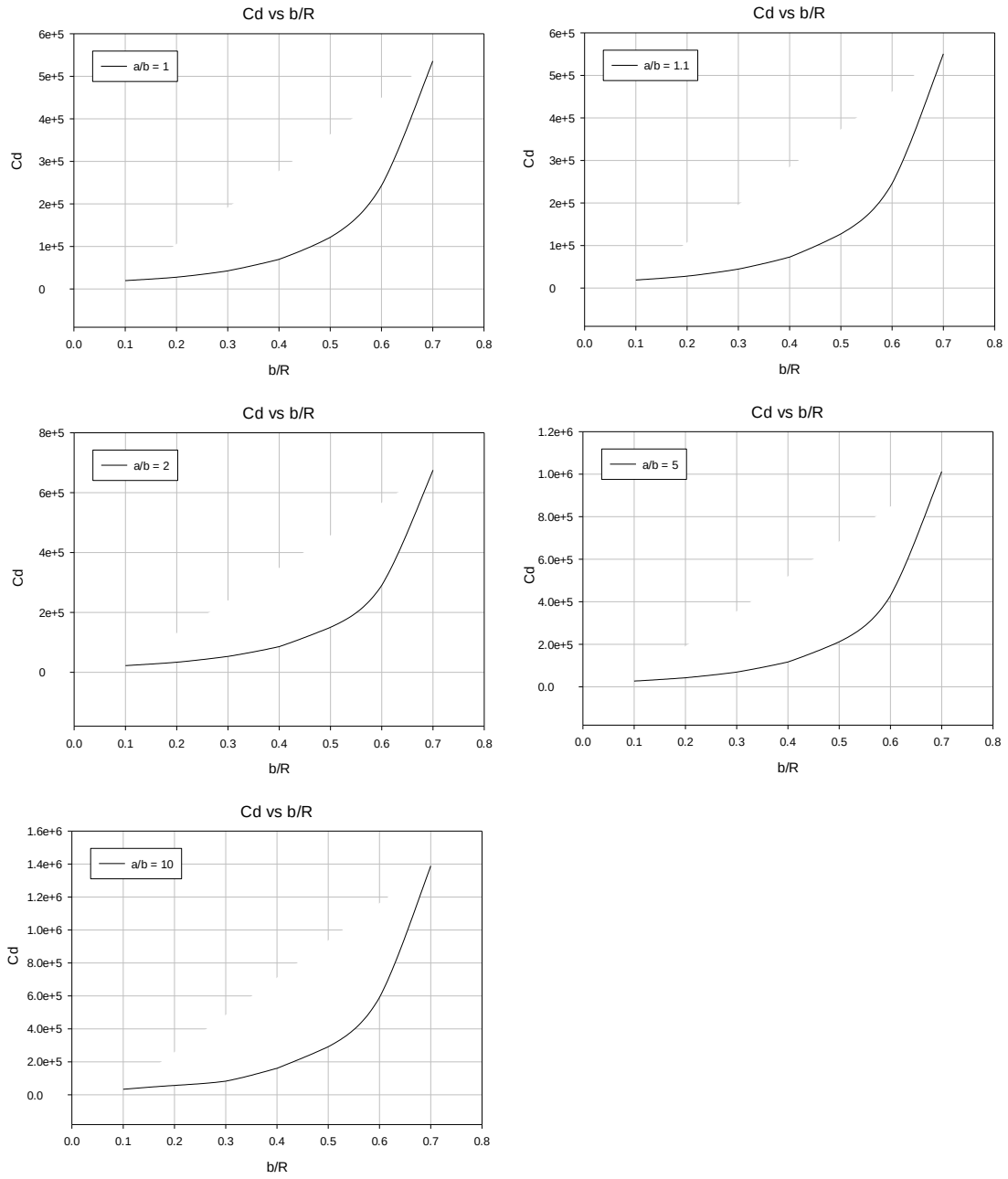

Figure 76: Cd vs b/R for Case 3, spheroids, n = 1.2 (individual cases)

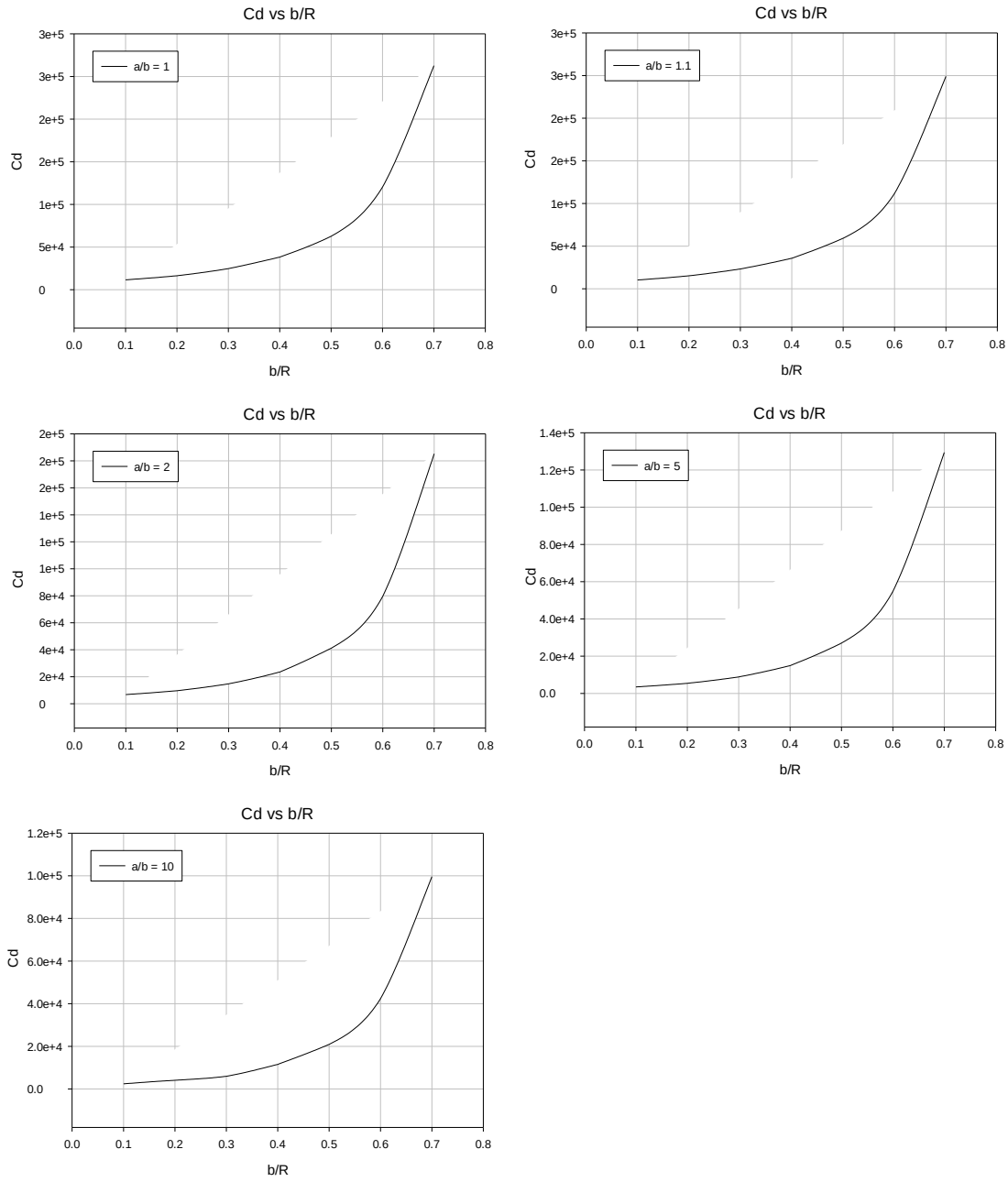

Figure 77: Cd vs b/R for Case 3, spheroids, n = 1.4 (individual cases)

6.1.2 Effect of Particle Shape

As seen from figures 78-81, the coefficient of drag increases with the increase in the shape factor value. This is similar to case 1 results, creeping Newtonian flow.

6.1.2.1 n = 0.6

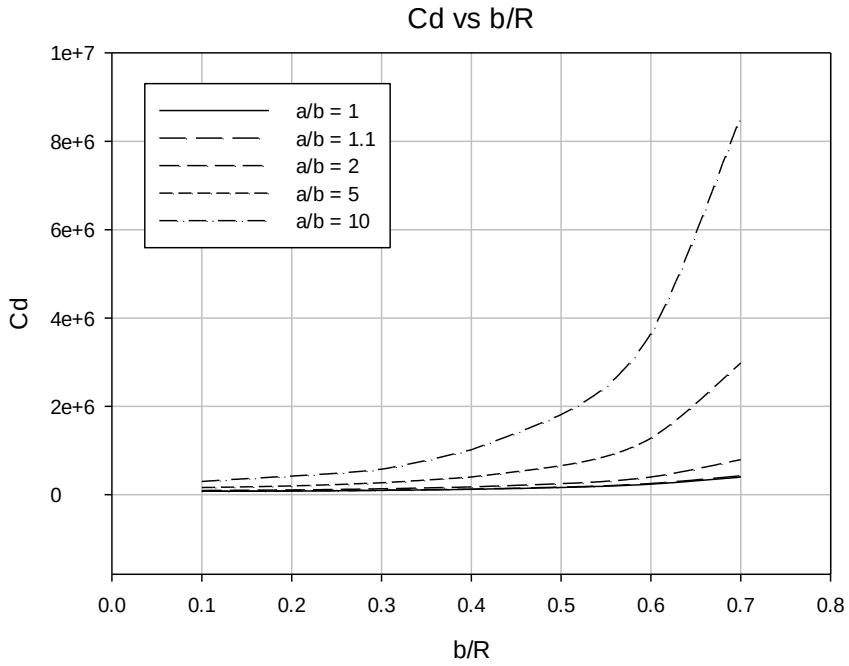

Figure 78: Cd vs b/R for different shape factor, for Case 3, spheroids, n = 0.6 (all cases)

6.1.2.2 n = 0.8

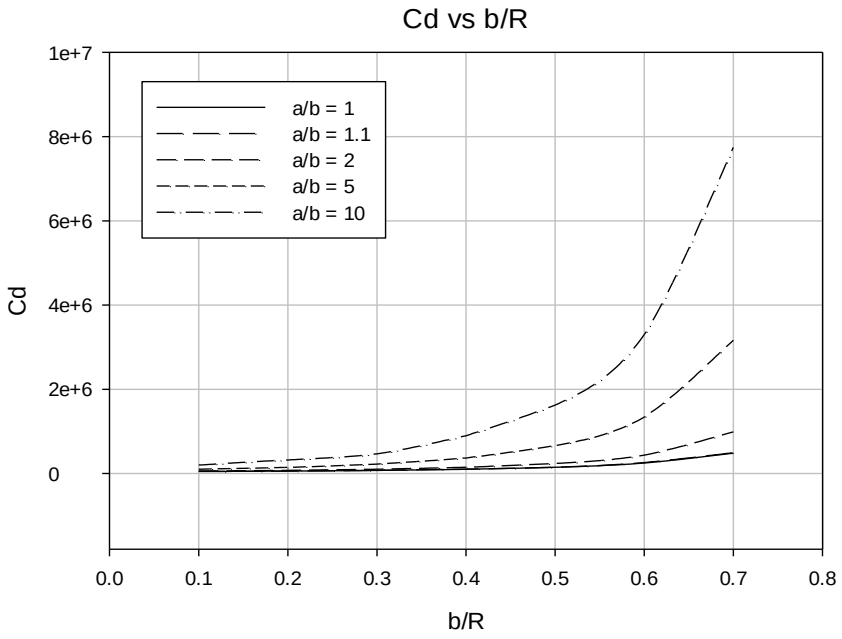

Figure 79: Cd vs b/R for different shape factor, for Case 3, spheroids, n = 0.8 (all cases)

6.1.2.3 n = 1.2

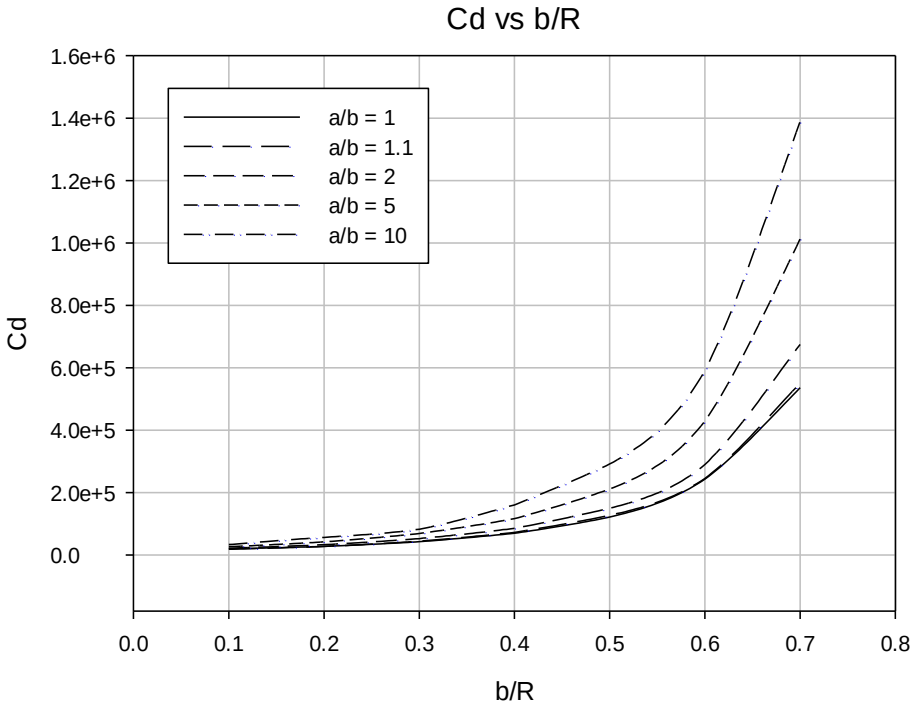

Figure 80: Cd vs b/R for different shape factor, for Case 3, spheroids, n = 1.2 (all cases)

6.1.2.4 n = 1.4

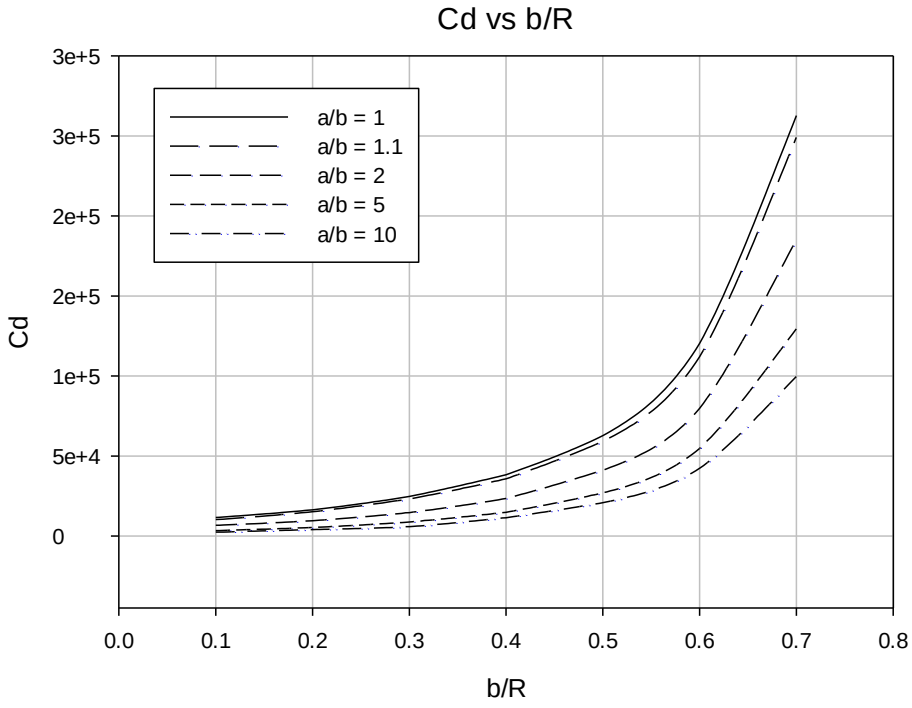

Figure 81: Cd vs b/R for different shape factor, for Case 3, spheroids, n = 1.4 (all cases)

6.2 Cassini Oval

6.2.1 Effect of Confinement Ratio

The effect of confinement ratio can be seen in figures 82-85. The results are in accordance with the previous cases.

6.2.1.1 n = 0.6

Table 23: Numerical results for Case 3, Cassini ovals, n = 0.6

	Cd		
b/R	**$(c/d)^2$ = 0.1**	**$(c/d)^2$ = 0.3**	**$(c/d)^2$ = 0.5**
0.1	76725.7466	83875.6777	95748.5272
0.2	84852.9341	93070.7682	109542.9286
0.3	100229.1182	111883.4751	135466.5101
0.4	126553.1259	143893.3930	180193.7088
0.5	171632.3860	199213.9993	258175.3588
0.6	253866.9163	301749.7108	406946.6986
0.7	425626.9645	519798.0782	751794.0277

	Cd		
b/R	**$(c/d)^2$ = 0.7**	**$(c/d)^2$ = 0.9**	**$(c/d)^2$ = 0.95**
0.1	109878.1546	119813.1010	121934.0468
0.2	129546.6447	142903.3492	144845.6256
0.3	164750.3555	182108.6838	183862.3334
0.4	222876.1687	242671.4616	245416.6975
0.5	325922.3598	346246.7704	348022.2965
0.6	525043.4267	548444.3847	548656.4701
0.7	1015108.3449	1033041.9530	1032705.4627

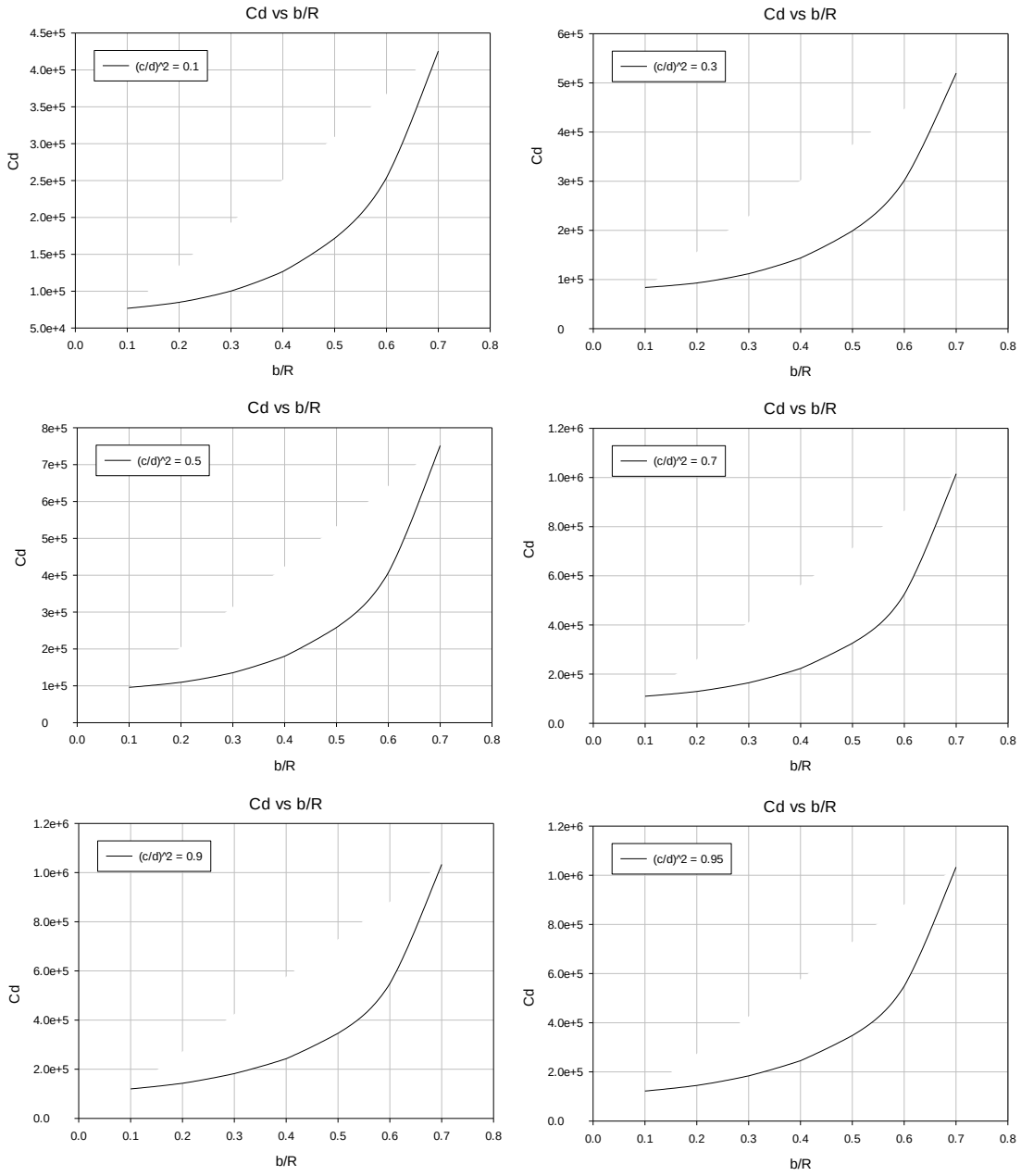

Figure 82: Cd vs b/R for Case 3, Cassini ovals, n = 0.6 (individual cases)

6.2.1.2 n = 0.8

Table 24: Numerical results for Case 3, Cassini ovals, n = 0.8

	Cd		
b/R	**$(c/d)^2 = 0.1$**	**$(c/d)^2 = 0.3$**	**$(c/d)^2 = 0.5$**
0.1	50298.4635	56322.6485	61979.9424
0.2	59940.2970	66429.9605	78080.0975
0.3	77348.6714	87077.1405	106464.4619
0.4	107196.0921	123259.7780	156132.9077
0.5	160756.7588	189495.5220	250496.9386
0.6	267010.7001	322809.5650	446985.4380
0.7	515951.2601	637805.8527	964615.3530

	Cd		
b/R	**$(c/d)^2 = 0.7$**	**$(c/d)^2 = 0.9$**	**$(c/d)^2 = 0.95$**
0.1	70967.0914	77440.2171	78766.4550
0.2	92489.7443	102190.0101	103683.4294
0.3	130134.6893	142826.3729	144410.6308
0.4	195066.3614	209552.7877	211113.0915
0.5	318158.6311	334955.3063	335489.1809
0.6	585037.3881	597864.9991	596492.4512
0.7	1306775.8486	1294237.8228	1282932.8172

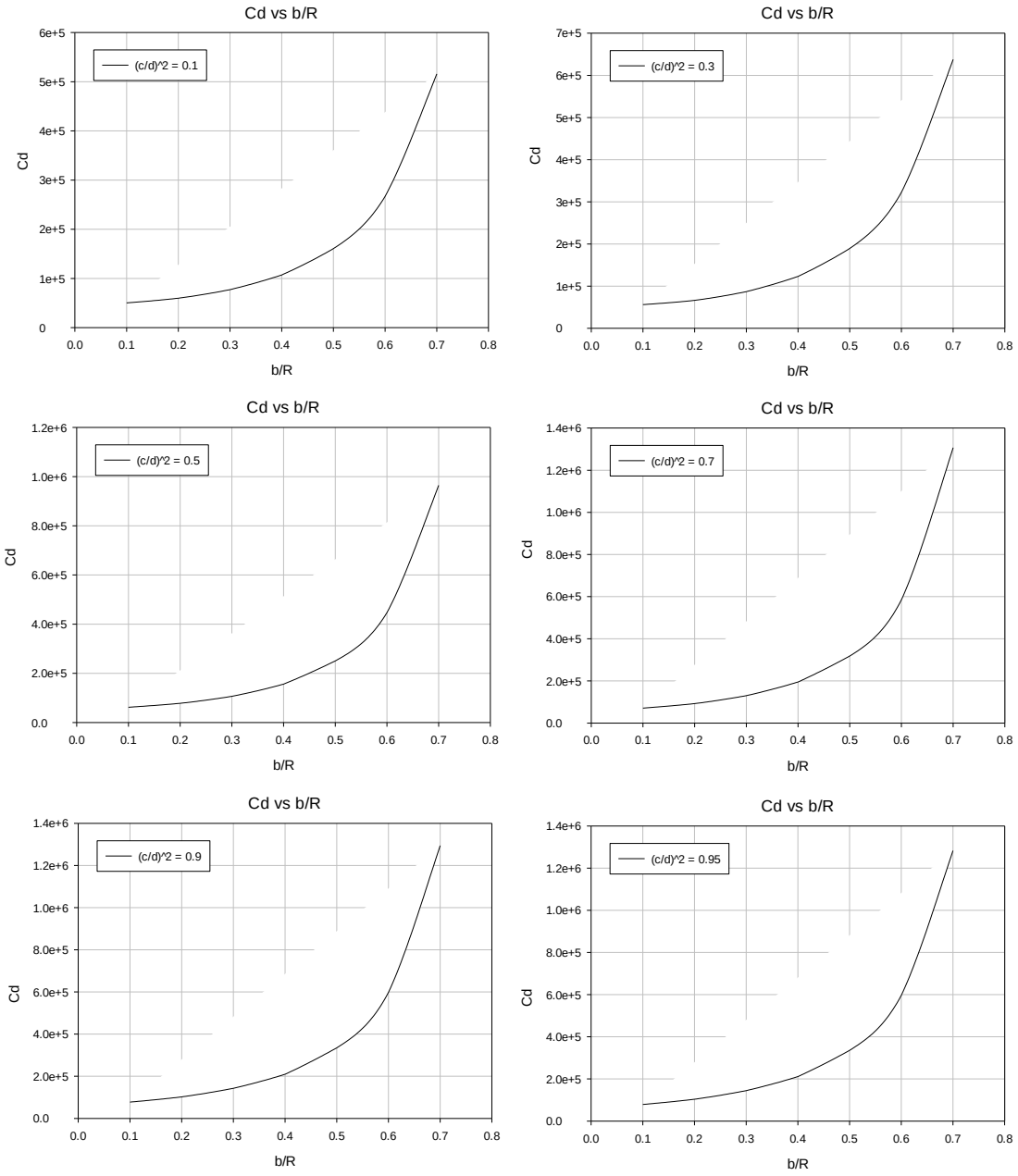

Figure 83: Cd vs b/R for Case 3, Cassini ovals, n = 0.8 (individual cases)

6.2.1.3 n = 1.2

Table 25: Numerical results for Case 3, Cassini ovals, n = 1.2

	Cd		
b/R	**$(c/d)^2 = 0.1$**	**$(c/d)^2 = 0.3$**	**$(c/d)^2 = 0.5$**
0.1	20620.3649	24560.4240	24136.1627
0.2	29092.9268	33018.6146	38244.2775
0.3	45602.6233	52125.2371	64683.9544
0.4	77061.6239	90427.8546	114800.5214
0.5	142983.4526	173415.8391	221010.6105
0.6	303548.5994	370519.6597	458272.6903
0.7	786536.0444	895034.2721	1109432.4790

	Cd		
b/R	**$(c/d)^2 = 0.7$**	**$(c/d)^2 = 0.9$**	**$(c/d)^2 = 0.95$**
0.1	27412.2229	29372.1567	29564.3185
0.2	45114.3511	47411.7988	47471.8443
0.3	76022.2768	76022.7214	75715.3305
0.4	132745.8153	125822.6452	122791.0516
0.5	244960.3272	220900.0218	213362.7861
0.6	496742.6978	425437.6371	407705.1706
0.7	1180237.2934	956962.4106	907972.0999

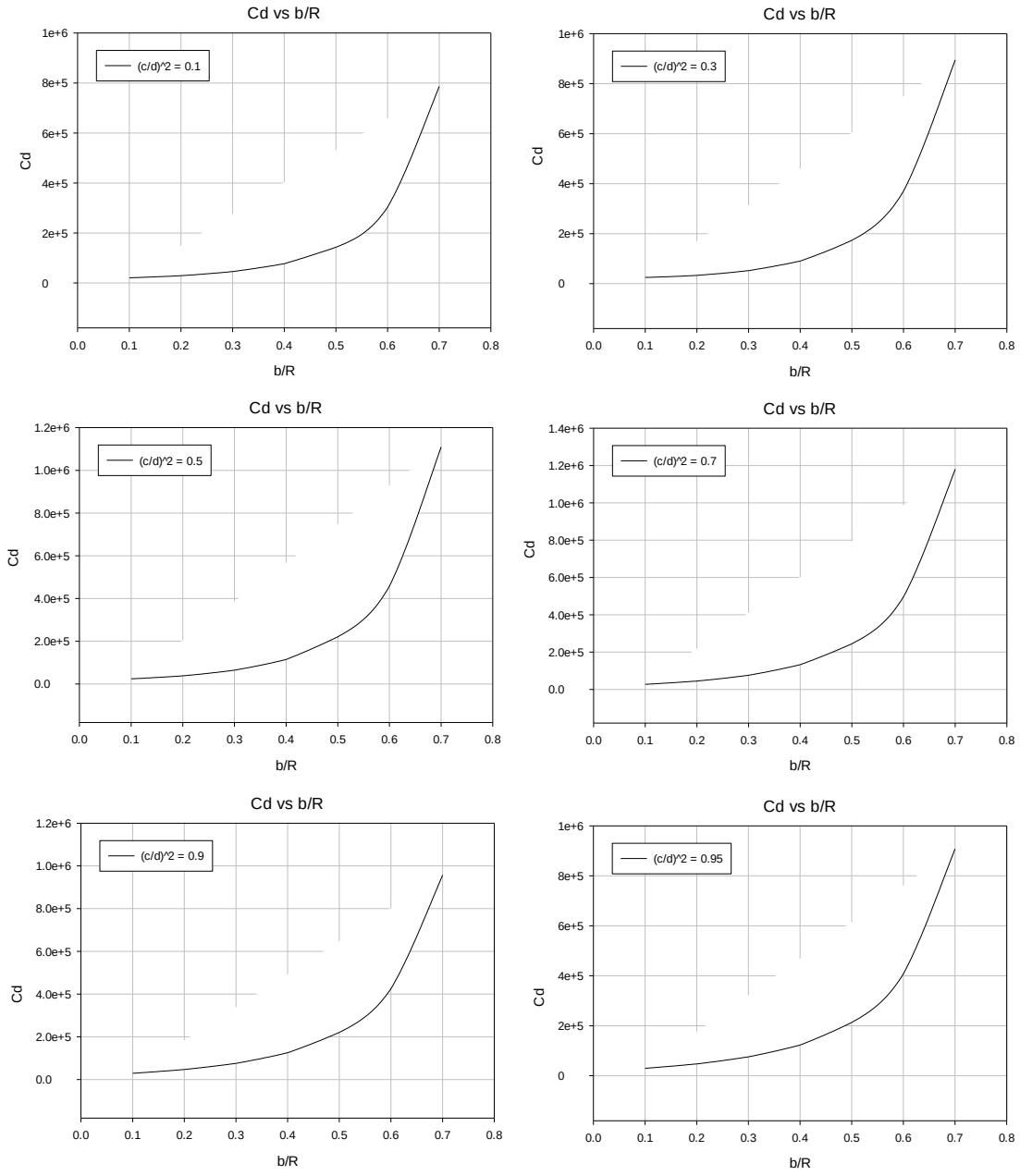

Figure 84: Cd vs b/R for Case 3, Cassini ovals, n = 1.2 (individual cases)

6.2.1.4 n = 1.4

Table 26: Numerical results for Case 3, Cassini ovals, n = 1.4

	Cd		
b/R	**$(c/d)^2 = 0.1$**	**$(c/d)^2 = 0.3$**	**$(c/d)^2 = 0.5$**
0.1	13009.4566	16119.3038	13999.9763
0.2	20033.9181	23069.4933	22679.1315
0.3	34866.6582	40029.6636	37027.9062
0.4	65425.9938	73168.6731	61676.2944
0.5	135700.5004	139016.0716	111716.7941
0.6	327186.7799	277615.2504	226000.4381
0.7	982183.5127	636982.6875	543212.2842

	Cd		
b/R	**$(c/d)^2 = 0.7$**	**$(c/d)^2 = 0.9$**	**$(c/d)^2 = 0.95$**
0.1	12158.0355	9974.5456	9485.8136
0.2	18854.6010	15102.7233	14289.5580
0.3	29882.3293	23338.2087	22016.4980
0.4	49934.4316	37841.2830	35258.1410
0.5	90850.5804	66215.5505	61123.7372
0.6	183640.6522	127449.2813	116743.2234
0.7	435941.0882	286621.1466	259961.6409

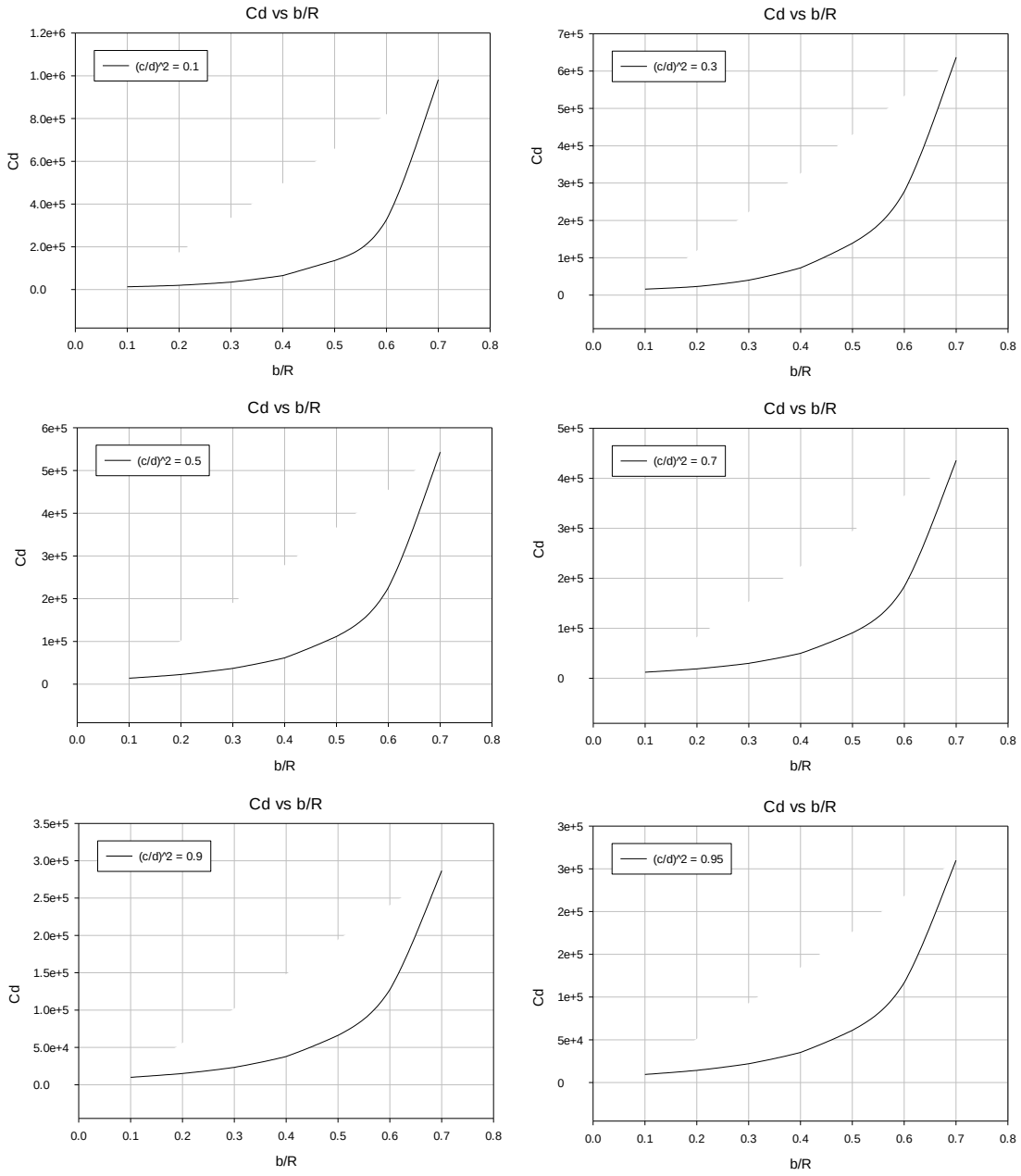

Figure 85: Cd vs b/R for Case 3, Cassini ovals, n = 1.4 (individual cases)

6.2.2 Effect of Particle Shape

The coefficient of drag changes with the change in the shape factor as shown in figures 86-89 for different power law index values. The trend between the drag coefficient and the confinement differs for each power law index value.

6.2.2.1 n = 0.6

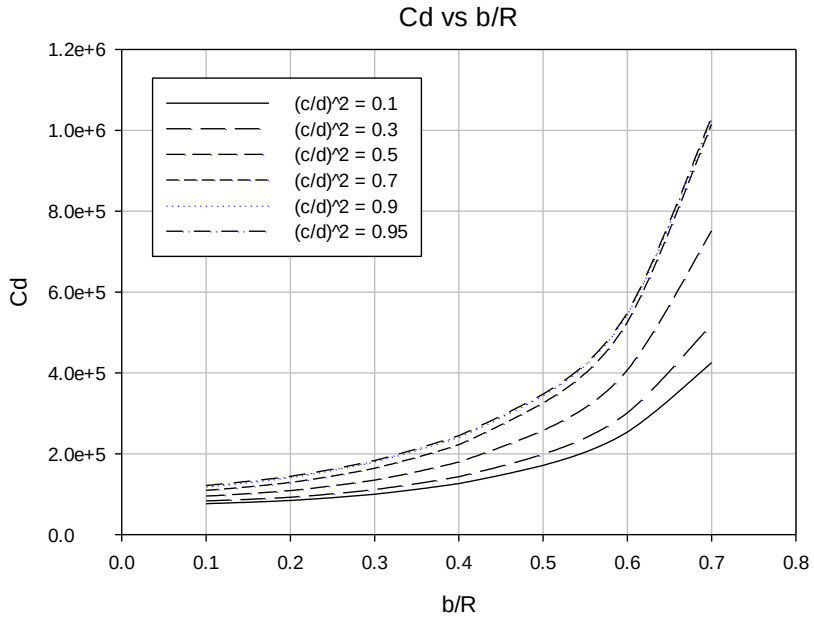

Figure 86: Cd vs b/R for different shape factor, for Case 3, Cassini ovals, n = 0.6 (all cases)

6.2.2.2 n = 0.8

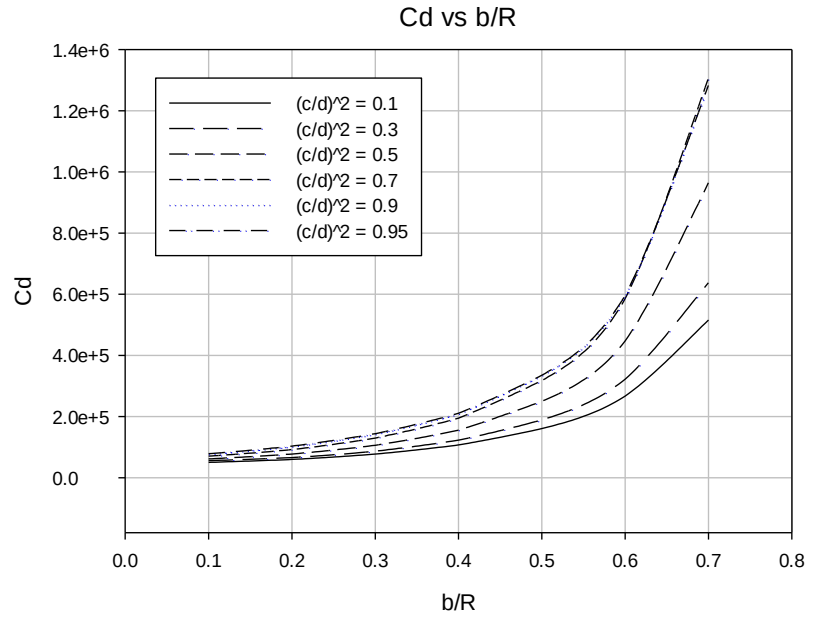

Figure 87: Cd vs b/R for different shape factor, for Case 3, Cassini ovals, n = 0.8 (all cases)

6.2.6.3 n = 1.2

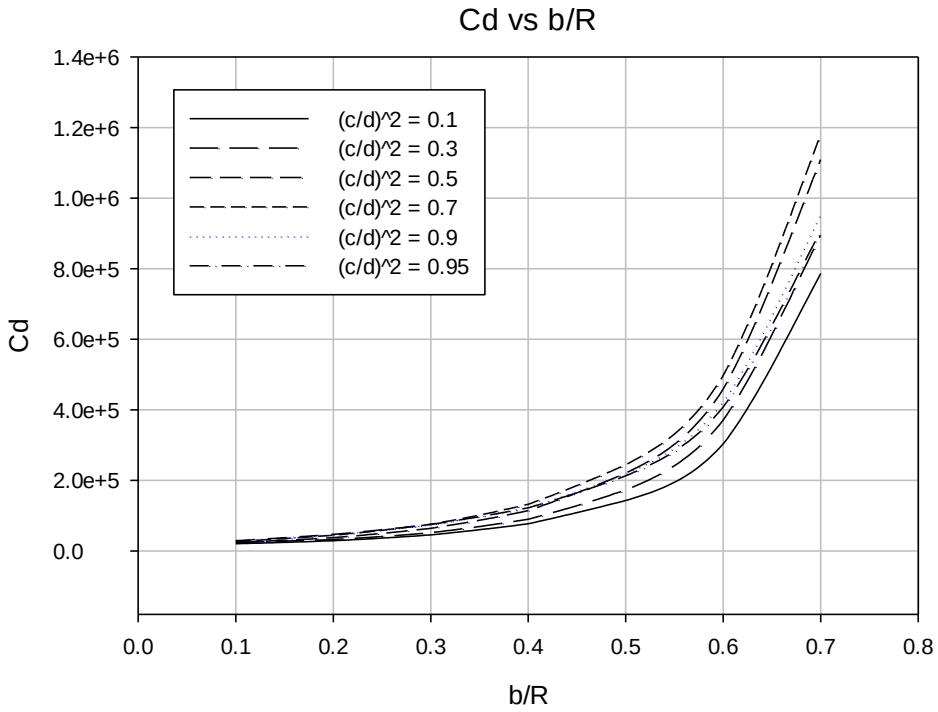

Figure 88: Cd vs b/R for different shape factor, for Case 3, Cassini ovals, n = 1.2 (all cases)

6.2.2.4 n = 1.4

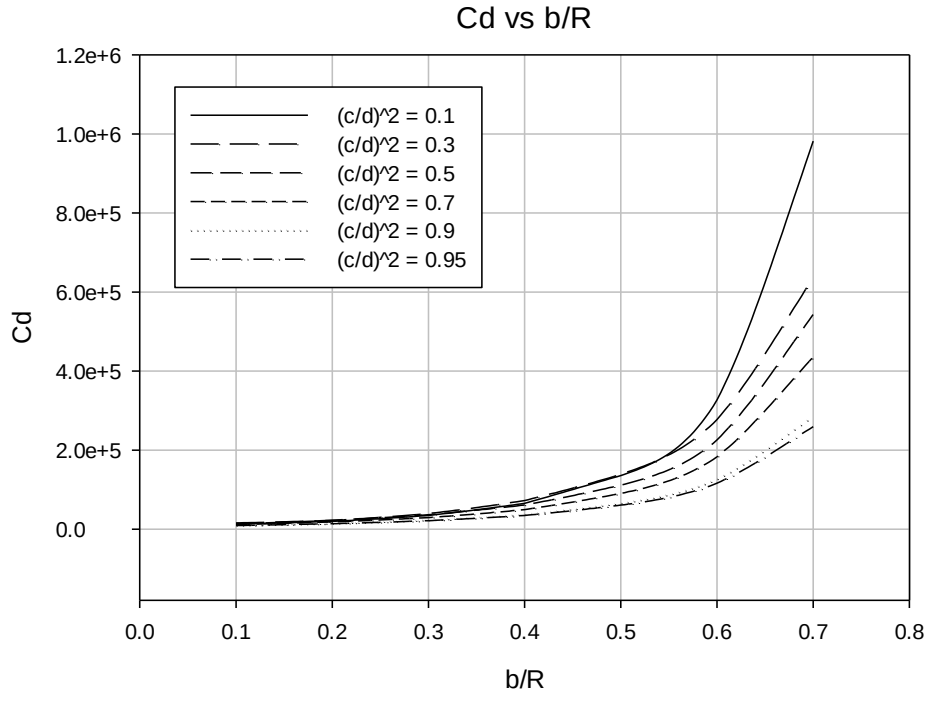

Figure 89: Cd vs b/R for different shape factor, for Case 3, Cassini ovals, n = 1.4 (all cases)

6.3 Velocity Streamlines and Pressure Contours (Selected Cases)

As an example, the velocity streamlines and the pressure contours for the case spheroid a/b = 1.1 with confinement ratio b/R = 0.7 are shown here. The velocity streamlines are shown in figures 90-93, while the pressure contours are shown in figures 94-97. From the streamlines we can conclude that the flow is attached with no separation in the wake region. This is expected of creeping flows.

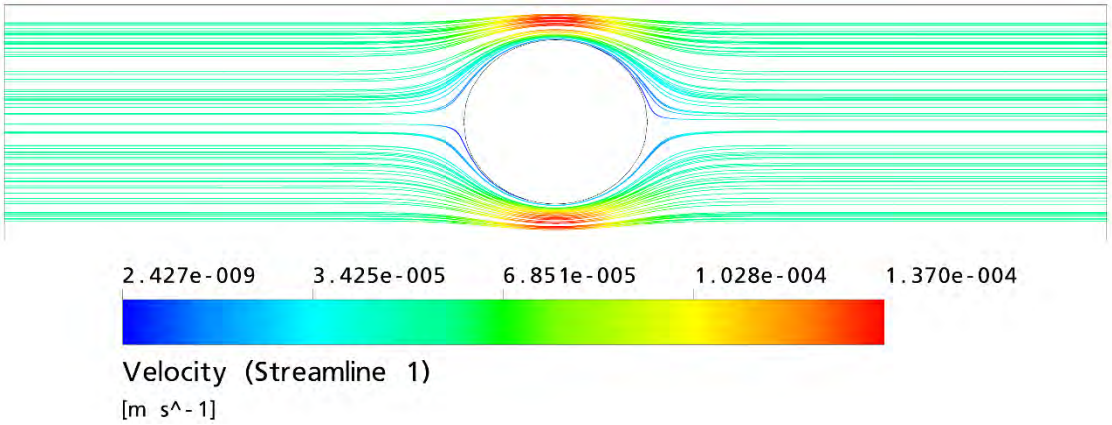

Figure 90: Velocity streamlines, Case 3, spheroid a/b = 1.1, b/R = 0.7, n = 0.6

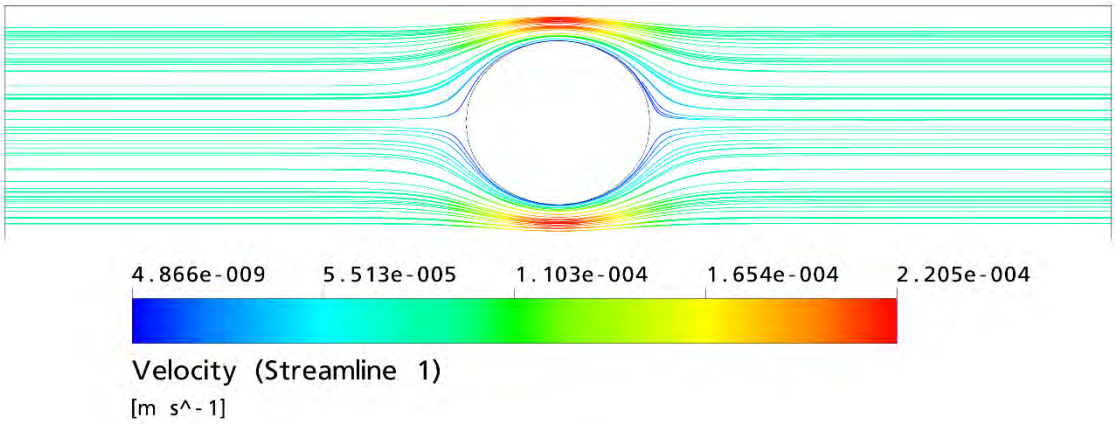

Figure 91: Velocity streamlines, Case 3, spheroid a/b = 1.1, b/R = 0.7, n = 0.8

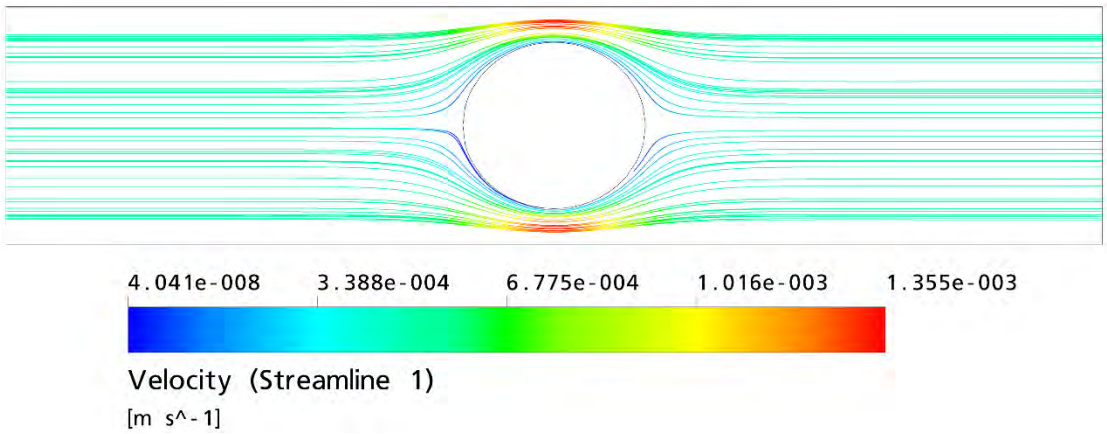

Figure 92: Velocity streamlines, Case 3, spheroid a/b = 1.1, b/R = 0.7, n = 1.2

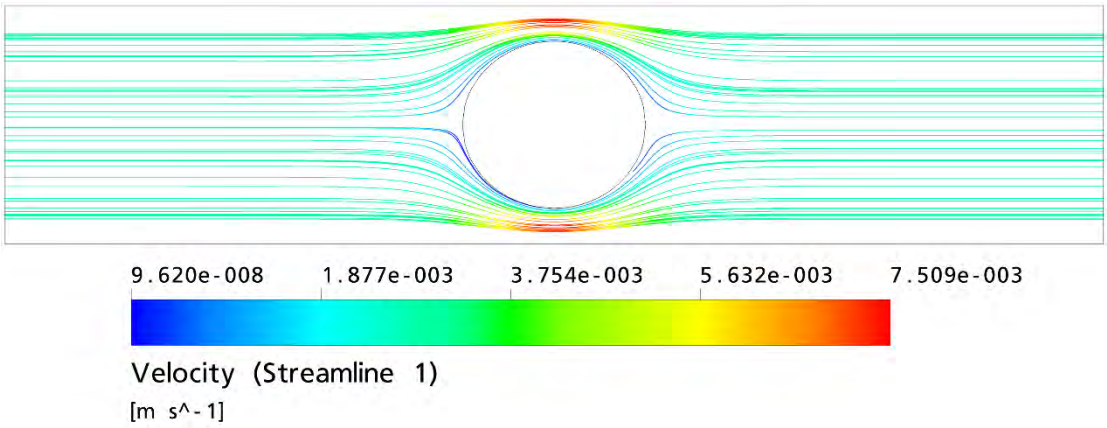

Figure 93: Velocity streamlines, Case 3, spheroid a/b = 1.1, b/R = 0.7, n = 1.4

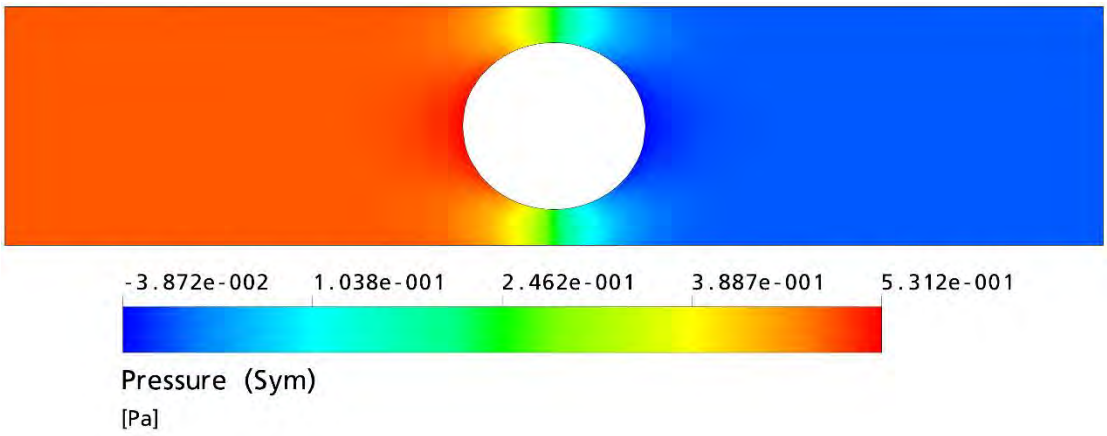

Figure 94: Pressure contours, Case 3, spheroid a/b = 1.1, b/R = 0.7, n = 0.6

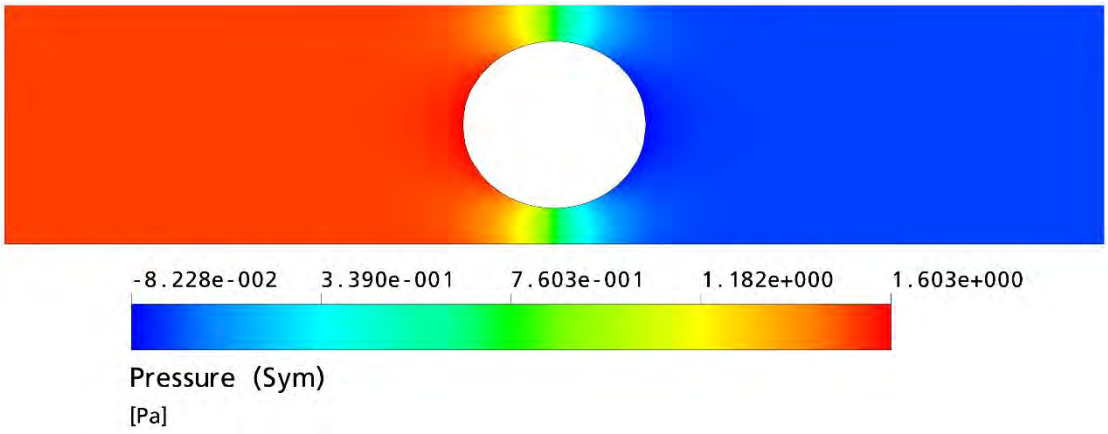

Figure 95: Pressure contours, Case 3, spheroid a/b = 1.1, b/R = 0.7, n = 0.8

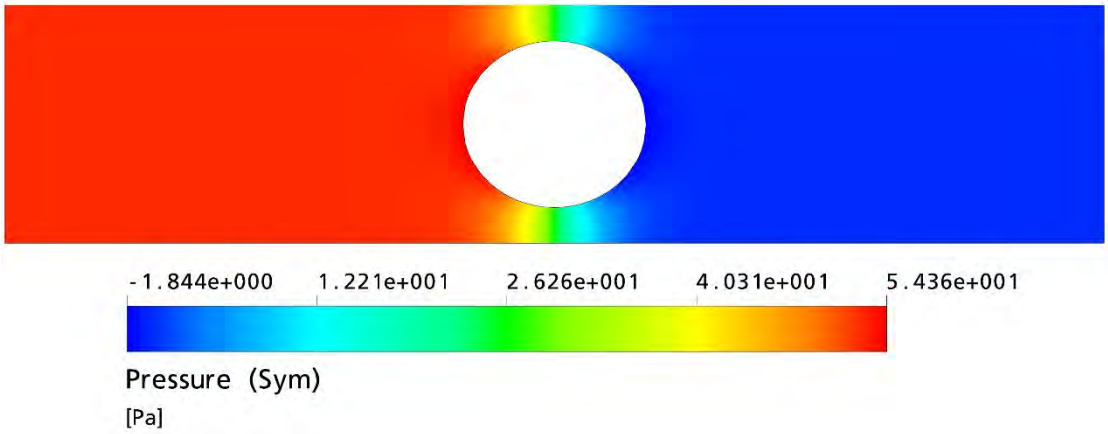

Figure 96: Pressure contours, Case 3, spheroid a/b = 1.1, b/R = 0.7, n = 1.2

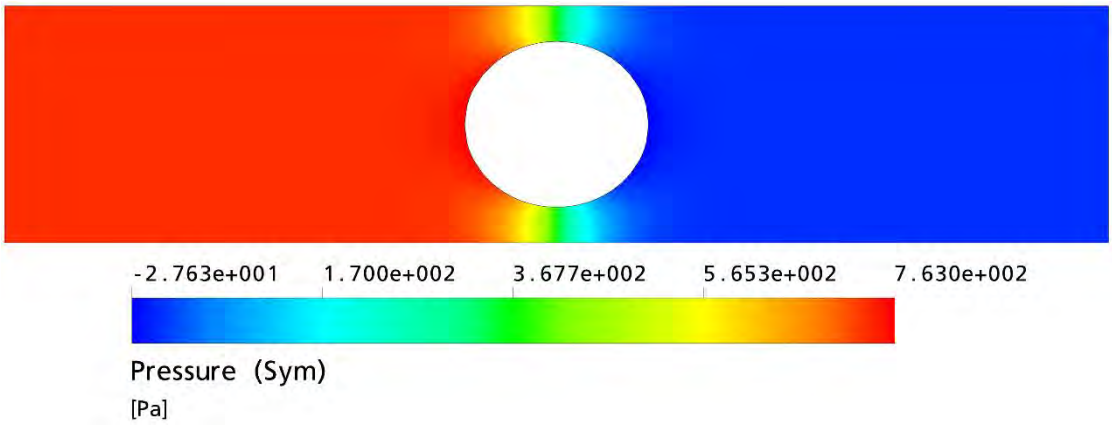

Figure 97: Pressure contours, Case 3, spheroid a/b = 1.1, b/R = 0.7, n = 1.4

Chapter 7. Results for Low Reynolds Number Motion in Non-Newtonian Fluid

This section presents the numerical results for axisymmetric prolate spheroids and Cassini ovals for different shape factors and different confinement ratios, for the case of low Reynolds number motion in non-Newtonian fluids.

First, the results for the spheroids will be shown and the effect of the power-law index, the effect of the confinement ratio, and the effect of particle geometry will be examined. Three different shape factors *a/b* will be studied with values 1, 2, and 10. For each shape factor, confinement ratio *b/R* values of 0.1, 0.3, 0.5, and 0.7 will be studied. For each confinement ratio, six different values of Reynolds number will be studied. Re values of 0.01, 0.1, 1, 10, 20, 40 will be examined for steady cases. This will be repeated for power-law index *n* values of 0.6 and 0.8 for shear-thinning fluids and 1.2 and 1.4 for shear-thickening fluids. The results are shown in section 5.1.

Similar analysis will be repeated for the case of Cassini ovals. Three different shape factors $(c/d)^2$ will be studied with values 0.3, 0.7, and 0.95. For each shape factor, confinement ratio *b/R* values of 0.1, 0.3, 0.5, and 0.7 will be studied. For each confinement ratio, six different values of Reynolds number will be studied. Re values of 0.01, 0.1, 1, 10, 20, 40 will be examined for steady cases. This will be repeated for power-law index *n* values of 0.6 and 0.8 for shear-thinning fluids and 1.2 and 1.4 for shear-thickening fluids. The results are shown in section 5.2.

Sample velocity streamlines and pressure contours will be shown to help understand the flow dynamics. These results are shown in section 5.3.

7.1 Spheroid

7.1.1 Effect of Reynolds number

The effect of Reynolds number follows the same trend as case 2, i.e. the drag coefficient decreases with increase in Reynolds number. This can be seen in figures 98-109.

7.1.1.1 n = 0.6

7.1.1.1.1 a/b = 1

Table 27: Numerical results for Case 4, n = 0.6, spheroid a/b = 1

	Cd			
Re	**b/R = 0.1**	**b/R = 0.3**	**b/R = 0.5**	**b/R = 0.7**
0.0100	7491.2533	9688.4568	16819.5658	55644.7747
0.1000	814.3759	1166.5181	2528.4635	10486.9228
1.0000	119.2933	198.9503	484.0174	2023.5579
10.0000	22.3229	38.4286	93.5131	390.8467
20.0000	14.2048	23.5575	57.0646	238.2991
40.0000	9.3178	14.5635	34.8779	145.3226

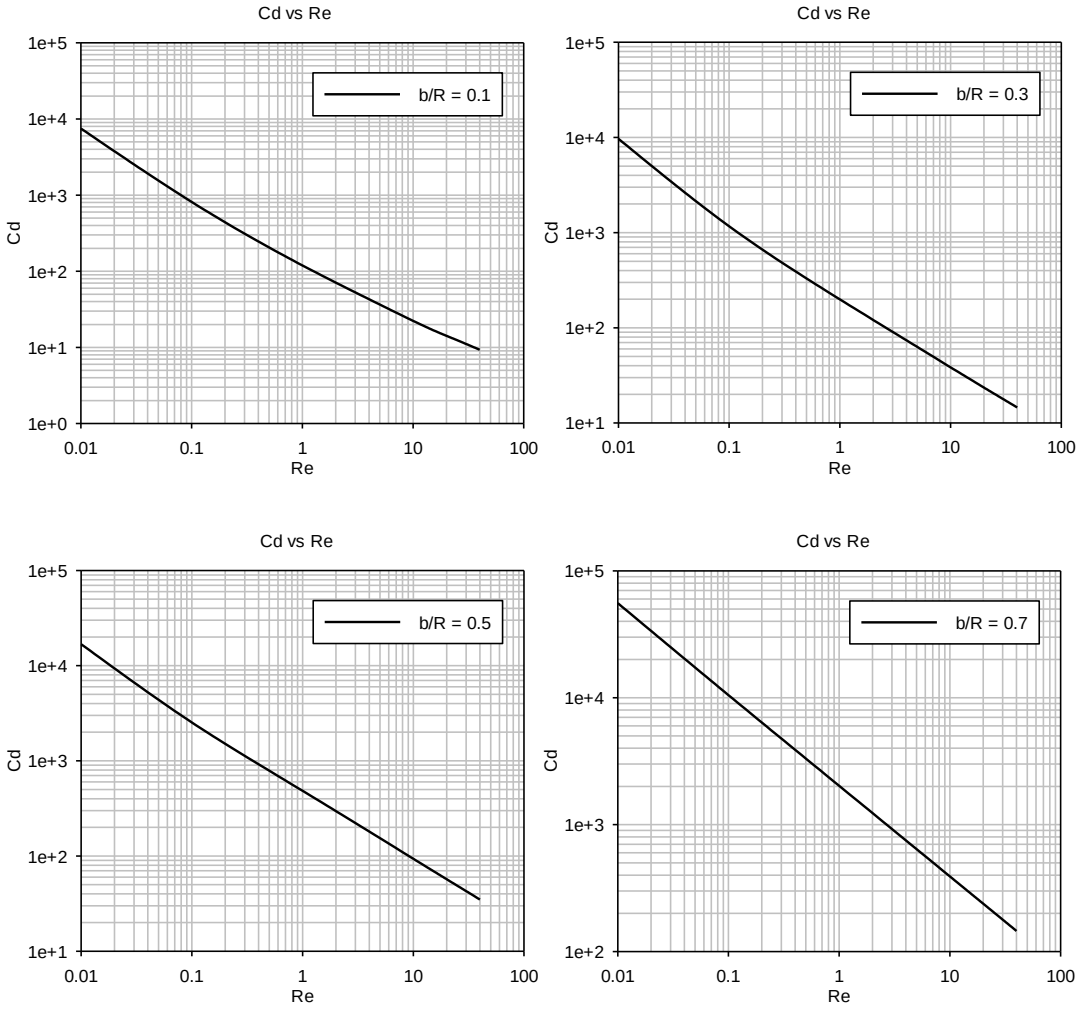

Figure 98: Cd vs Re for Case 4, n = 0.6, spheroid a/b = 1 (individual cases)

7.1.1.1.2 a/b = 2

Table 28: Numerical results for Case 4, n = 0.6, spheroid a/b = 2

	Cd			
Re	**b/R = 0.1**	**b/R = 0.3**	**b/R = 0.5**	**b/R = 0.7**
0.0100	9521.3802	14491.6260	33125.0654	143506.9110
0.1000	1247.7230	2230.6835	6164.9103	27659.9305
1.0000	205.1134	425.4163	1189.5087	5339.9911
10.0000	39.1112	82.1865	229.7263	1031.0587
20.0000	24.4226	50.1626	140.0655	628.4739
40.0000	15.5914	30.6809	85.4305	383.1205

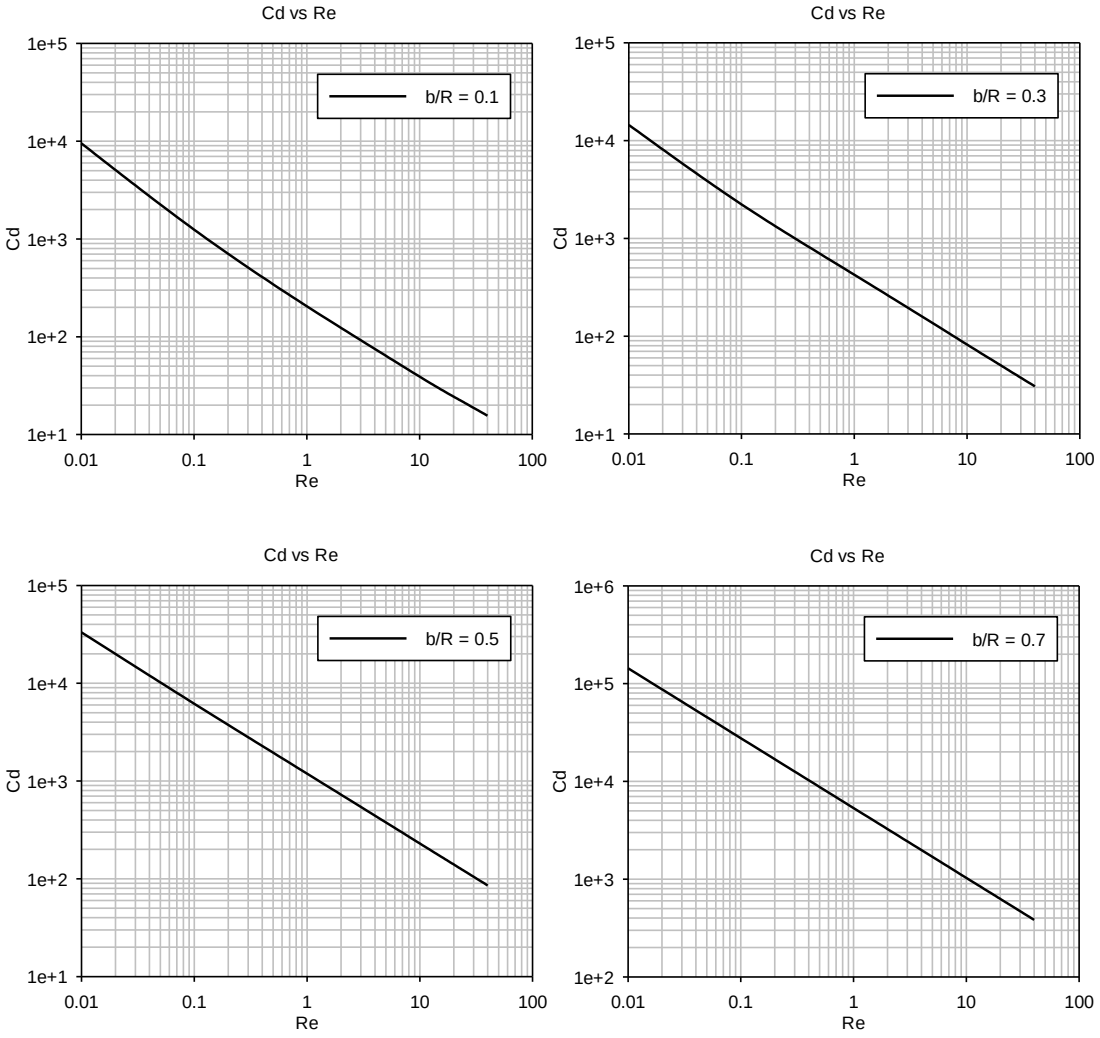

Figure 99: Cd vs Re for Case 4, n = 0.6, spheroid a/b = 2 (individual cases)

7.1.1.1.3 a/b = 10

Table 29: Numerical results for Case 4, n = 0.6, spheroid a/b = 10

	Cd			
Re	**b/R = 0.1**	**b/R = 0.3**	**b/R = 0.5**	**b/R = 0.7**
0.0100	43785.6071	99353.4743	347517.5898	1652728.3143
0.1000	7797.7200	19118.1024	67085.8785	319086.9758
1.0000	1500.5901	3690.8071	12952.1725	61606.0612
10.0000	290.0131	712.4433	2500.6080	11895.0633
20.0000	177.0333	434.2052	1524.1077	7250.3797
40.0000	108.3052	264.6286	928.9592	4419.5353

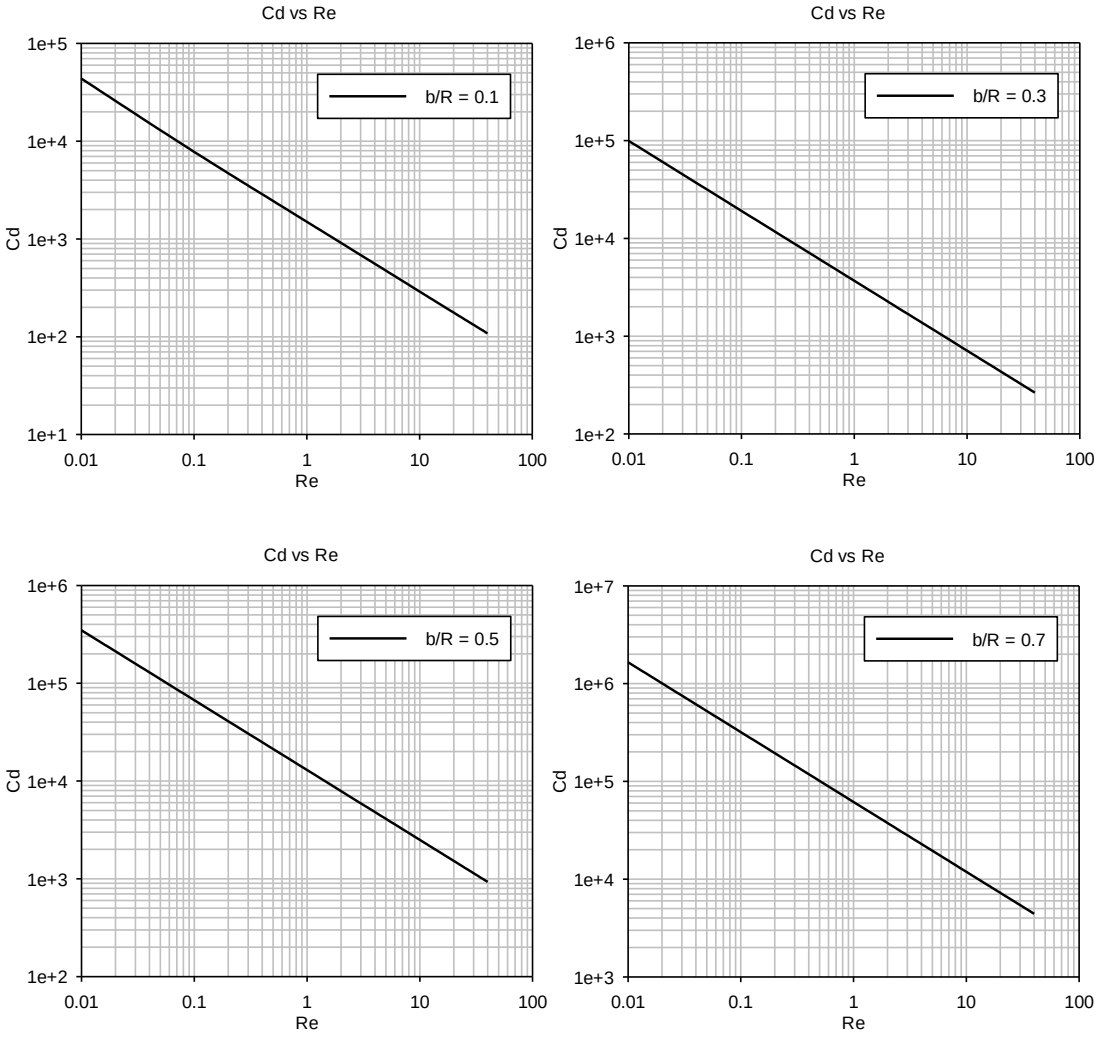

Figure 100: Cd vs Re for Case 4, n = 0.6, spheroid a/b = 10 (individual cases)

7.1.1.2 n = 0.8

7.1.1.2.1 a/b = 1

Table 30: Numerical results for Case 4, n = 0.8, spheroid a/b = 1

	Cd			
Re	**b/R = 0.1**	**b/R = 0.3**	**b/R = 0.5**	**b/R = 0.7**
0.0100	4862.7808	7471.4562	16009.0649	64704.3395
0.1000	553.3353	934.9724	2267.6262	9479.6710
1.0000	76.5250	136.3942	332.7616	1391.4571
10.0000	12.4146	20.2684	48.9740	204.4146
20.0000	7.7025	11.6436	27.6124	114.8255
40.0000	4.9753	6.9067	15.6895	64.6040

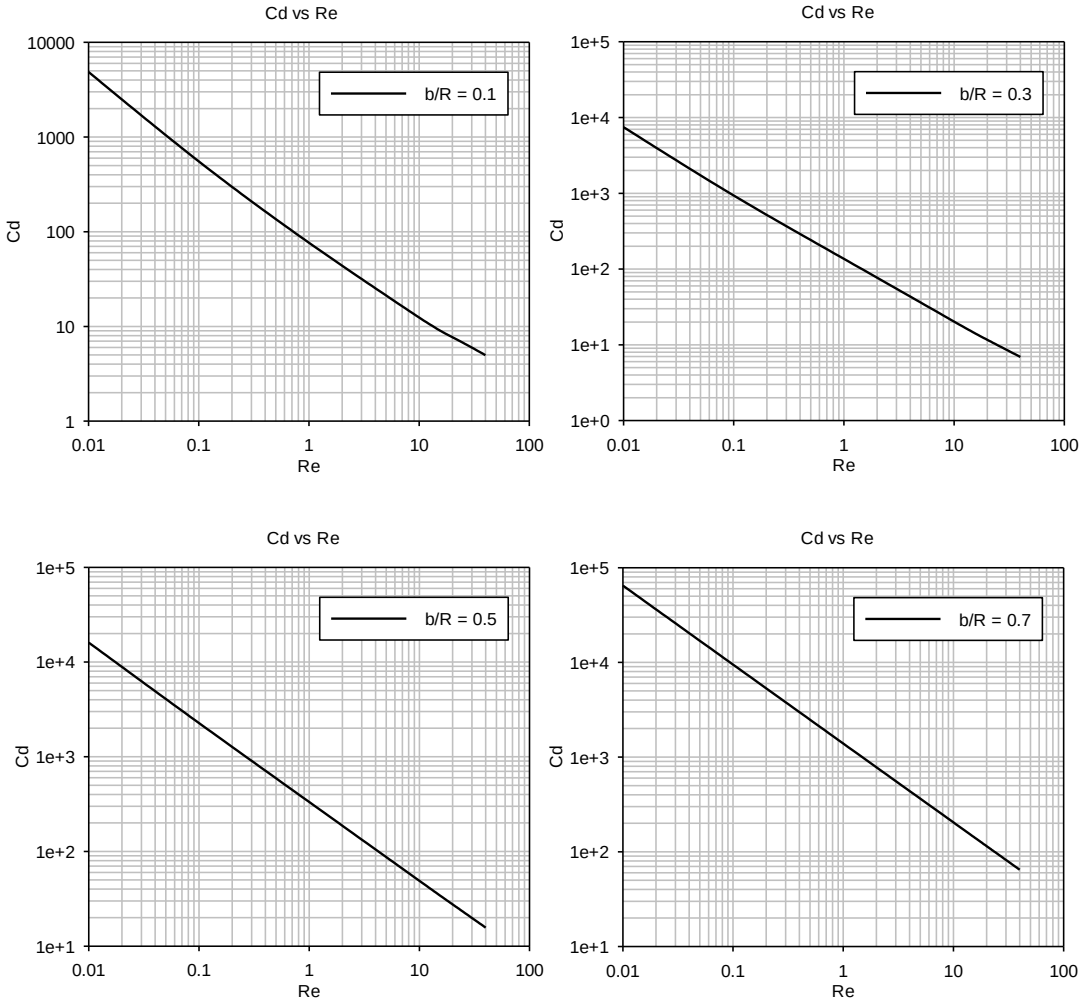

Figure 101: Cd vs Re for Case 4, n = 0.8, spheroid a/b = 1 (individual cases)

7.1.1.2.2 a/b = 2

Table 31: Numerical results for Case 4, n = 0.8, spheroid a/b = 2

	Cd			
Re	**b/R = 0.1**	**b/R = 0.3**	**b/R = 0.5**	**b/R = 0.7**
0.0100	6316.2012	11885.5949	32239.0349	144520.2574
0.1000	810.5086	1689.7525	4724.5763	21211.5778
1.0000	116.1860	247.9765	693.5198	3113.1637
10.0000	18.2409	36.5461	101.8947	457.0719
20.0000	11.0538	20.6664	57.2696	256.5828
40.0000	6.9467	11.8450	32.2550	144.0685

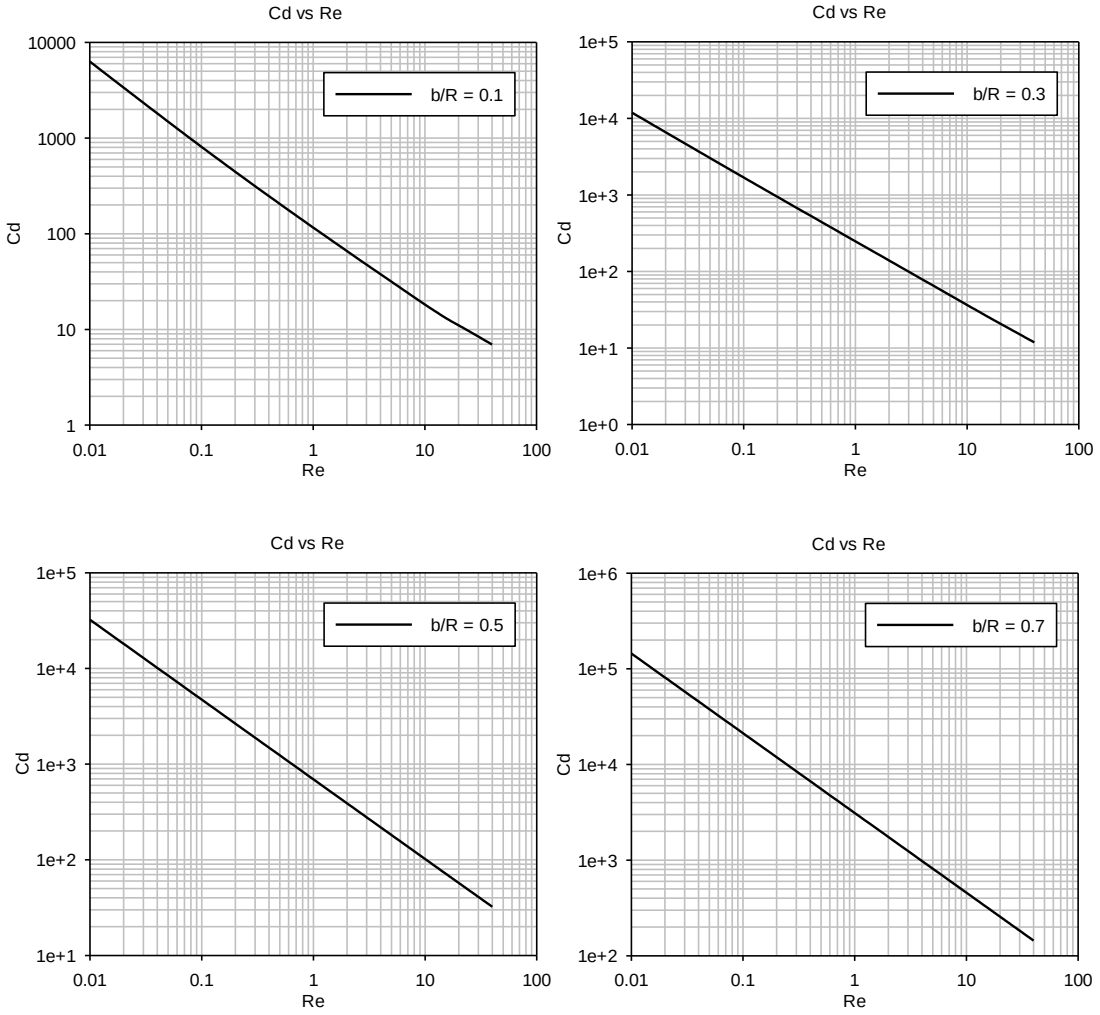

Figure 102: Cd vs Re for Case 4, n = 0.8, spheroid a/b = 2 (individual cases)

7.1.1.2.3 a/b = 10

Table 32: Numerical results for Case 4, n = 0.8, spheroid a/b = 10

	Cd			
Re	**b/R = 0.1**	**b/R = 0.3**	**b/R = 0.5**	**b/R = 0.7**
0.0100	27784.3538	68093.4362	238931.3130	1136454.1683
0.1000	4062.6355	9993.6572	35070.0444	166805.7816
1.0000	596.4993	1466.6810	5147.5070	24484.3901
10.0000	88.3313	215.2215	755.5205	3594.5997
20.0000	50.3209	120.8136	424.0160	2017.8183
40.0000	29.1987	67.8938	237.9872	1132.9301

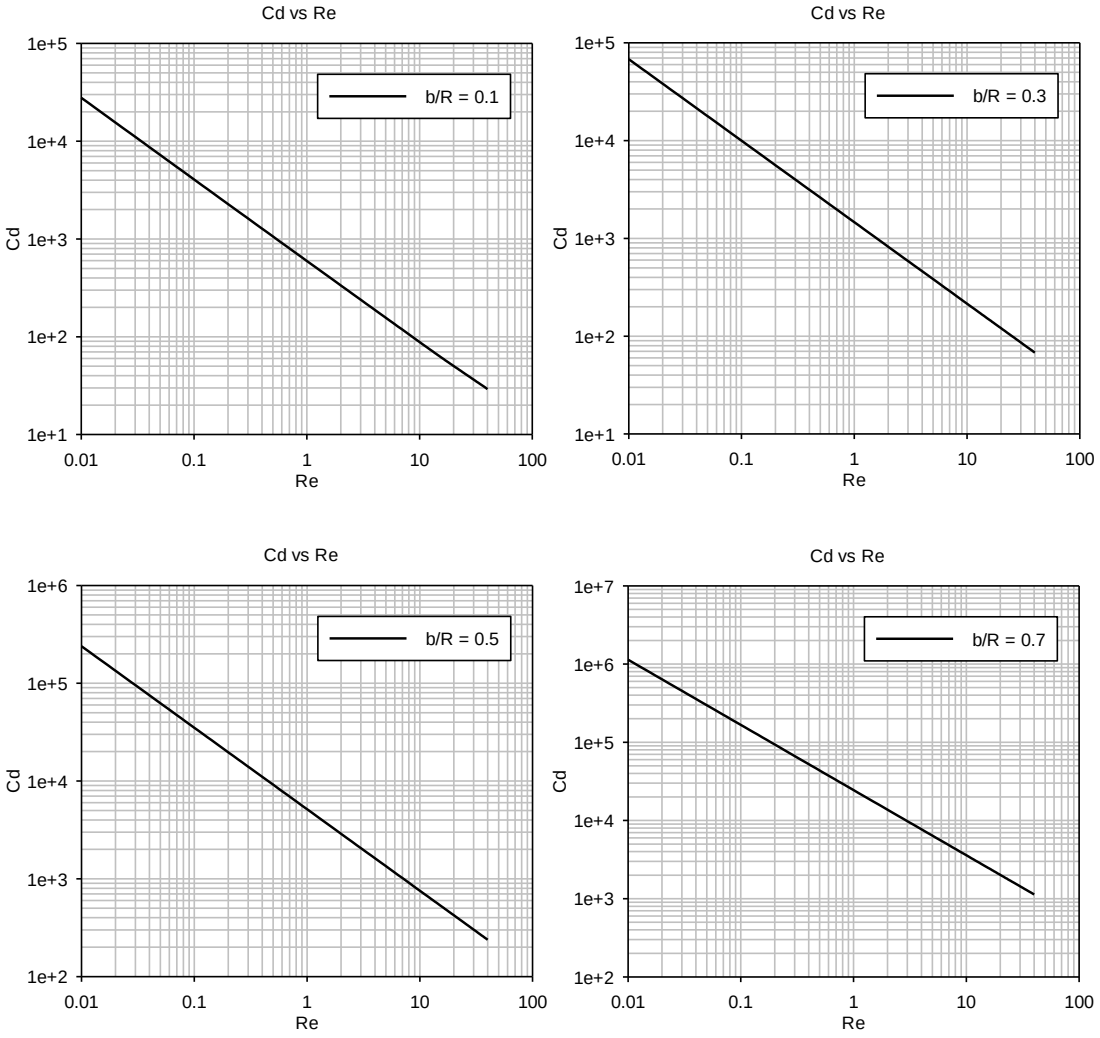

Figure 103: Cd vs Re for Case 4, n = 0.8, spheroid a/b = 10 (individual cases)

7.1.1.3 n = 1.2

7.1.1.3.1 a/b = 1

Table 33: Numerical results for Case 4, n = 1.2, spheroid a/b = 1

	Cd			
Re	**b/R = 0.1**	**b/R = 0.3**	**b/R = 0.5**	**b/R = 0.7**
0.0100	1602.1326	2959.0390	7228.4025	30236.3071
0.1000	92.9612	166.6255	406.5770	1700.5627
1.0000	6.6863	9.8390	23.0938	95.8295
10.0000	1.1405	1.3111	2.2163	6.8837
20.0000	0.7289			
40.0000	0.5044			

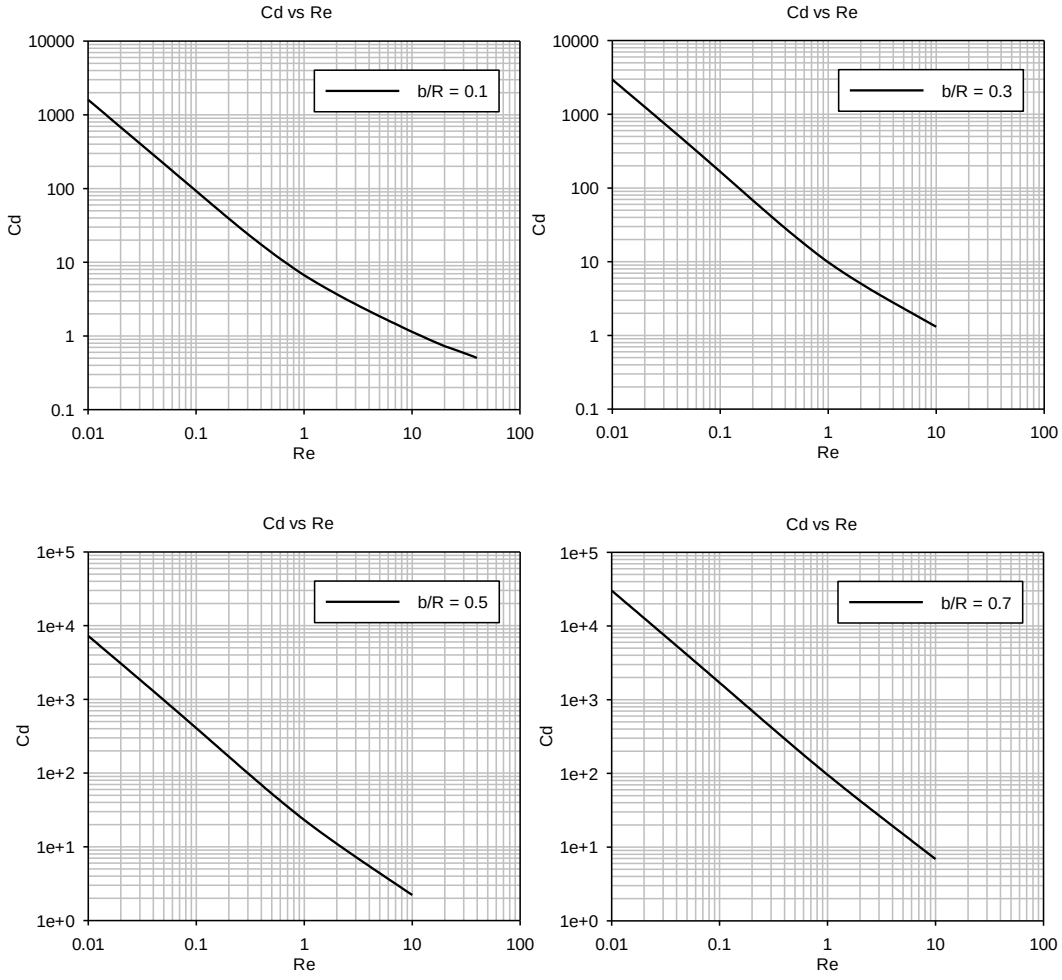

Figure 104: Cd vs Re for Case 4, n = 1.2, spheroid a/b = 1 (individual cases)

7.1.1.3.2 a/b = 2

Table 34: Numerical results for Case 4, n = 1.2, spheroid a/b = 2

	Cd			
Re	**b/R = 0.1**	**b/R = 0.3**	**b/R = 0.5**	**b/R = 0.7**
0.0100	1411.7031	3023.4651	8456.3750	37963.5366
0.1000	79.8524	170.0729	475.6134	2135.1737
1.0000	6.0462	9.9936	26.9623	120.2223
10.0000	0.9965	1.1858	2.2576	7.8633
20.0000	0.6058	0.7775		
40.0000	0.3421			

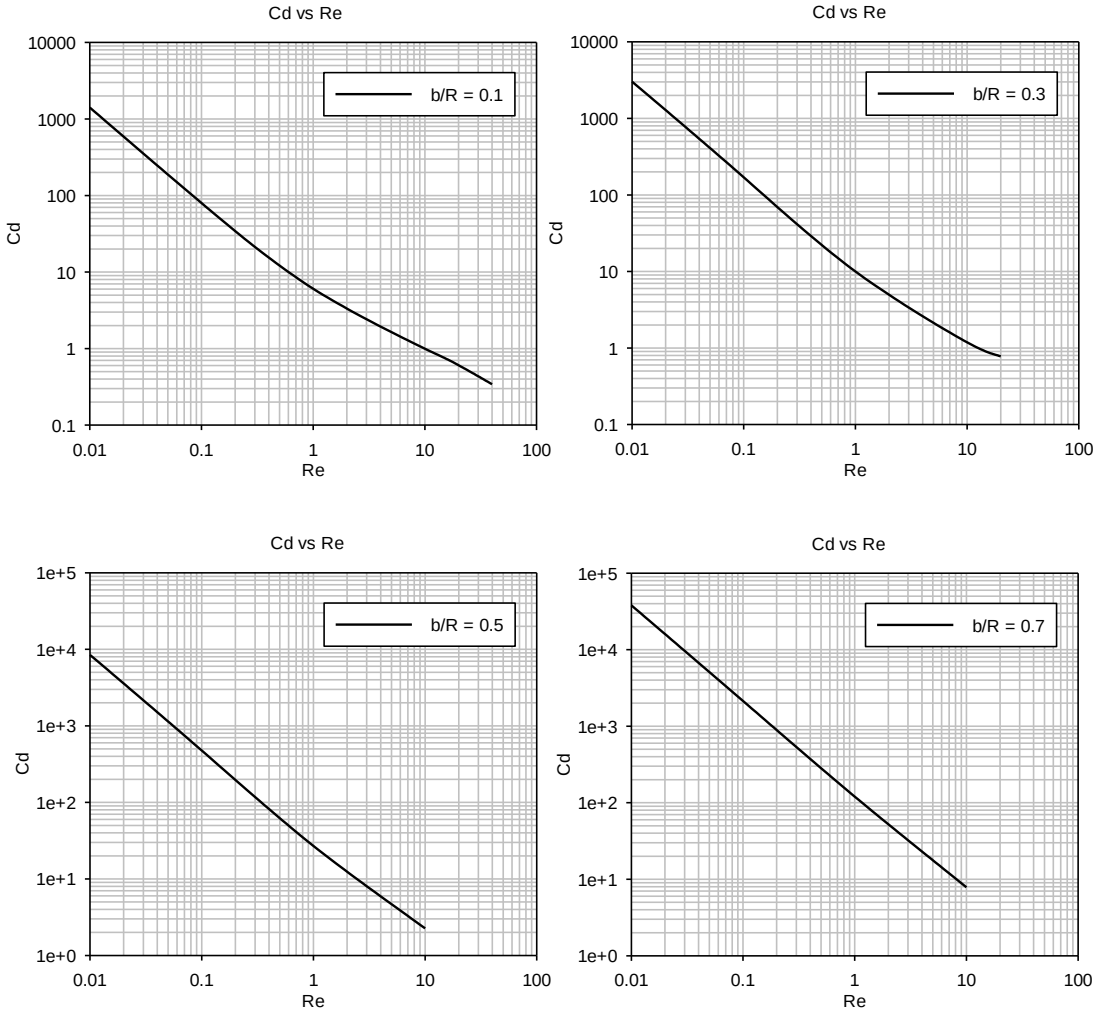

Figure 105: Cd vs Re for Case 4, n = 1.2, spheroid a/b = 2 (individual cases)

7.1.1.3.3 a/b = 10

Table 35: Numerical results for Case 4, n = 1.2, spheroid a/b = 10

	Cd			
Re	**b/R = 0.1**	**b/R = 0.3**	**b/R = 0.5**	**b/R = 0.7**
0.0100	1901.8555	4678.2297	16417.2158	78086.9486
0.1000	107.6381	262.9725	923.1730	4391.9957
1.0000	8.0228	15.2376	52.0870	248.1606
10.0000	1.1543	1.5943	3.5103	15.8098
20.0000	0.7686	0.8041		
40.0000				

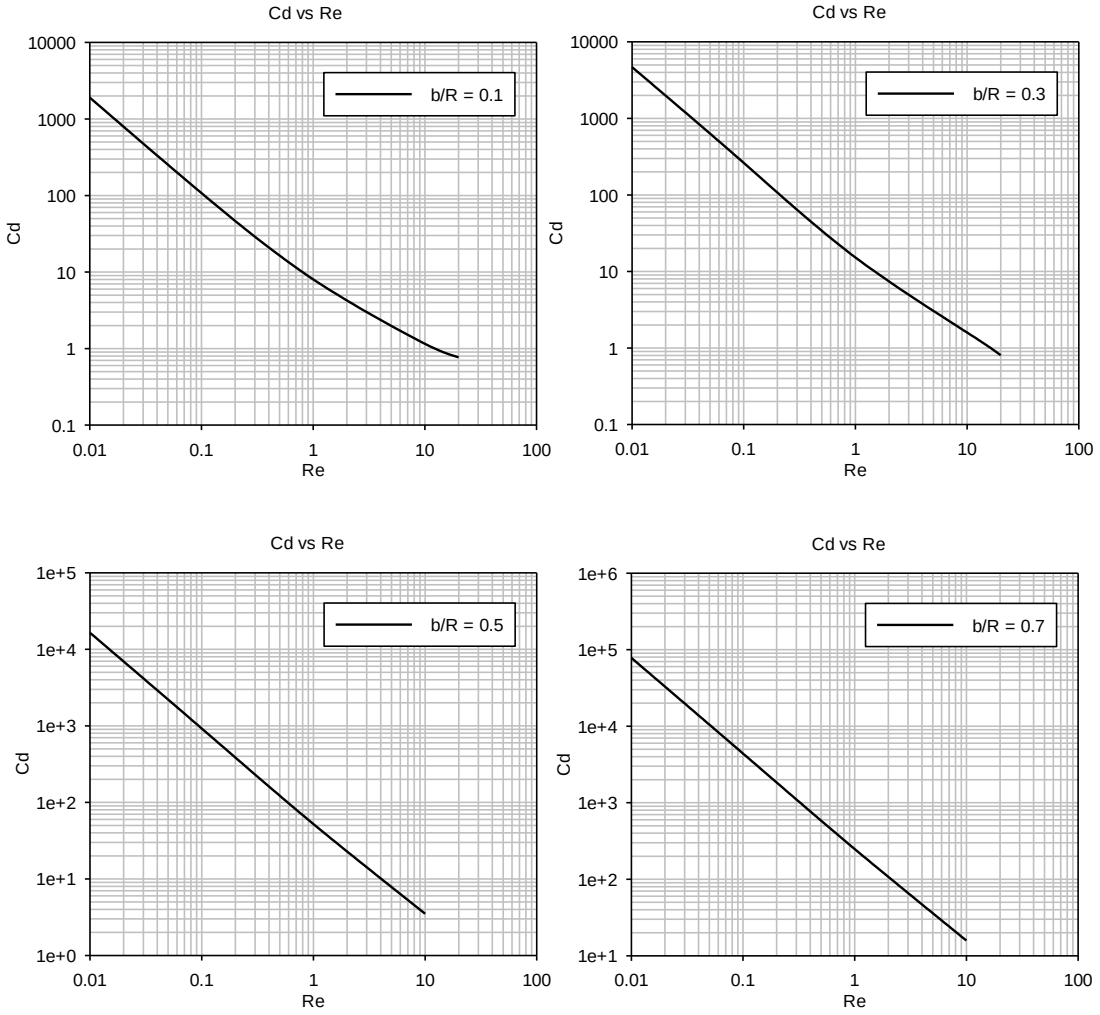

Figure 106: Cd vs Re for Case 4, n = 1.2, spheroid a/b = 10 (individual cases)

7.1.1.4 n = 1.4

7.1.1.4.1 a/b = 1

Table 36: Numerical results for Case 4, n = 1.4, spheroid a/b = 1

	Cd			
Re	**b/R = 0.1**	**b/R = 0.3**	**b/R = 0.5**	**b/R = 0.7**
0.0100	308.2095	554.7414	1353.7936	5662.8573
0.1000	8.0927	12.3451	29.3626	122.1775
1.0000	0.7880	0.9334	1.4997	
10.0000	0.1114	0.0822	0.1018	
20.0000				
40.0000				

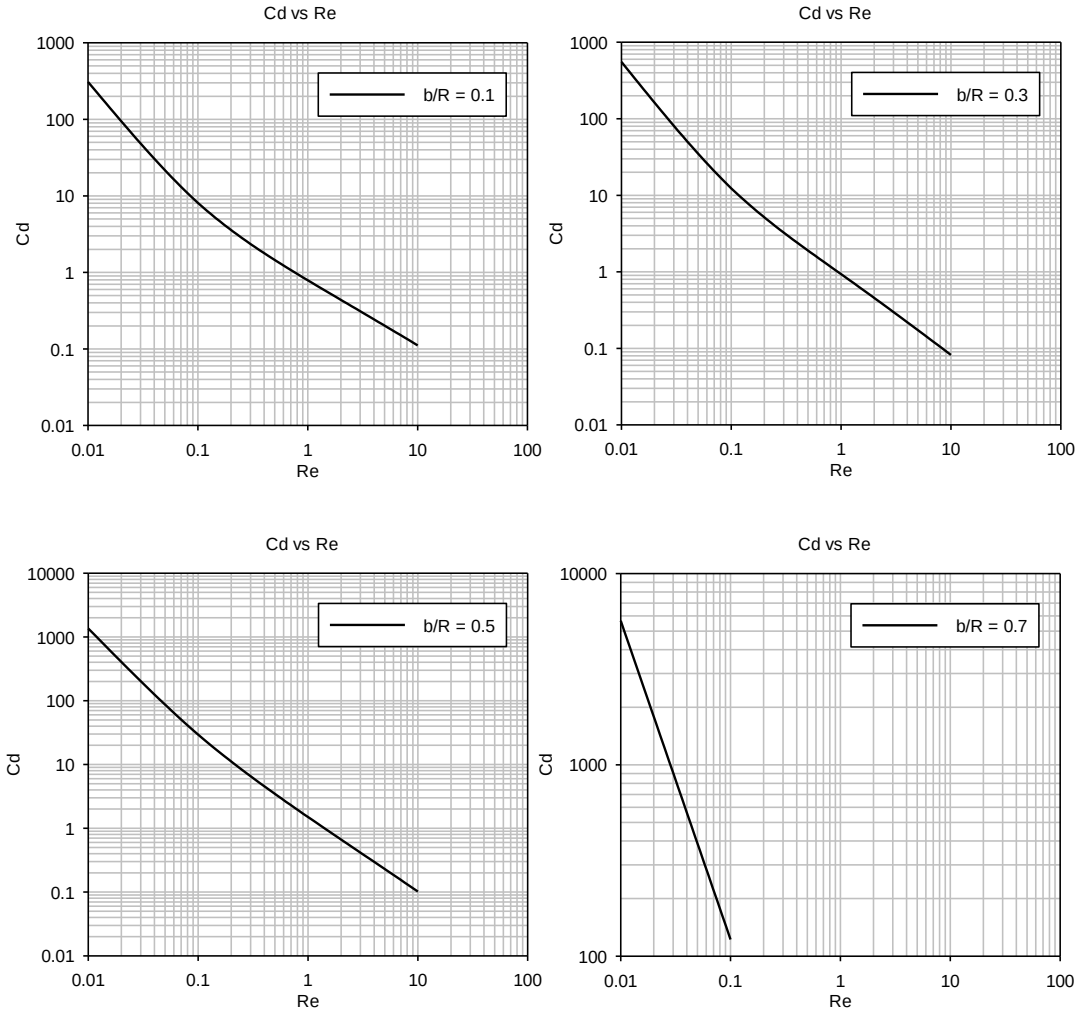

Figure 107: Cd vs Re for Case 4, n = 1.4, spheroid a/b = 1 (individual cases)

7.1.1.4.2 a/b = 2

Table 37: Numerical results for Case 4, n = 1.4, spheroid a/b = 2

	Cd			
Re	**b/R = 0.1**	**b/R = 0.3**	**b/R = 0.5**	**b/R = 0.7**
0.0100	148.7456	317.8037	888.8304	3990.4928
0.1000	4.7218	7.3727	19.4122	86.1549
1.0000	0.4630			
10.0000				
20.0000				
40.0000				

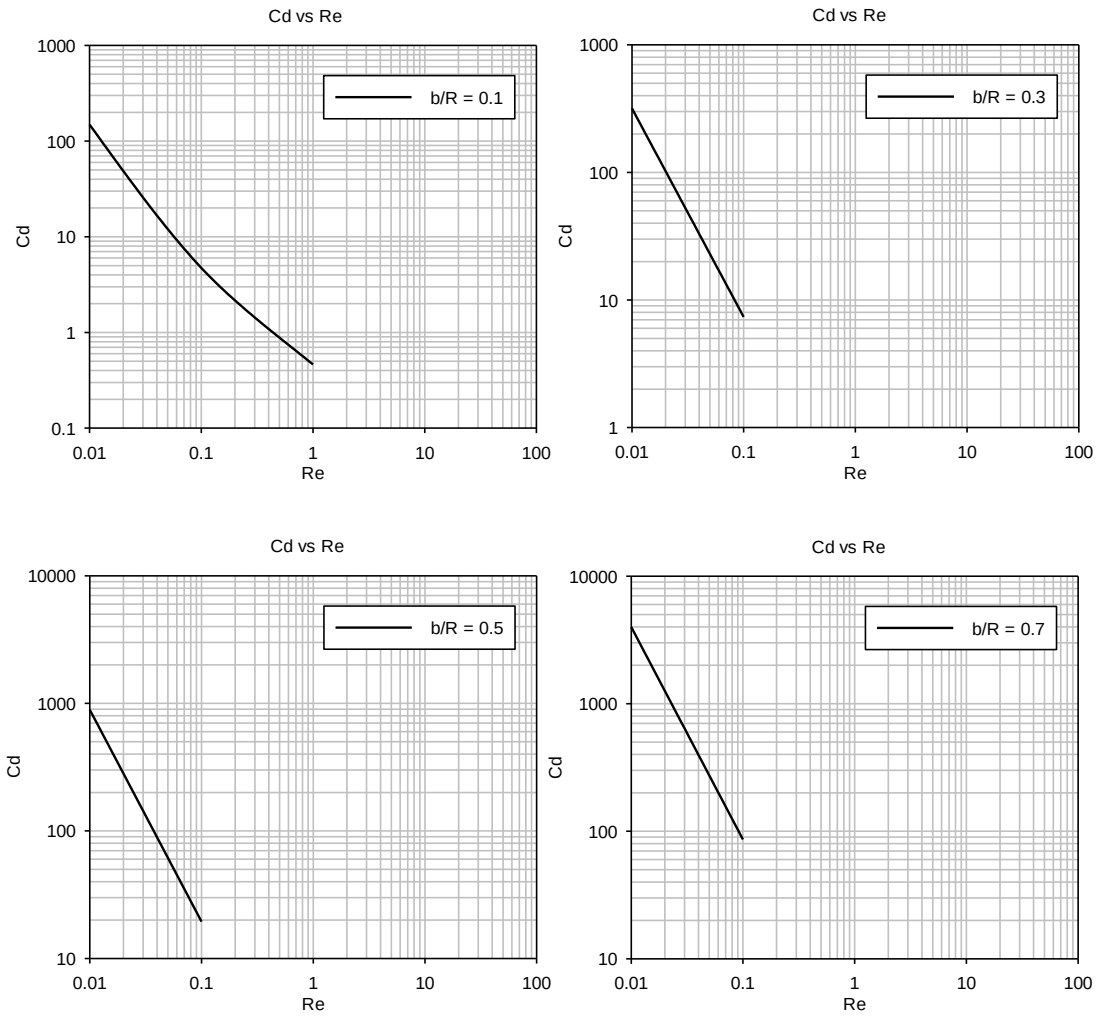

Figure 108: Cd vs Re for Case 4, n = 1.4, spheroid a/b = 2 (individual cases)

7.1.1.4.3 a/b = 10

Table 38: Numerical results for Case 4, n = 1.4, spheroid a/b = 10

	Cd			
Re	**b/R = 0.1**	**b/R = 0.3**	**b/R = 0.5**	**b/R = 0.7**
0.0100	53.4275	128.5601	451.2284	2147.2723
0.1000	2.4032	3.6343	10.1622	47.9848
1.0000				
10.0000				
20.0000				
40.0000				

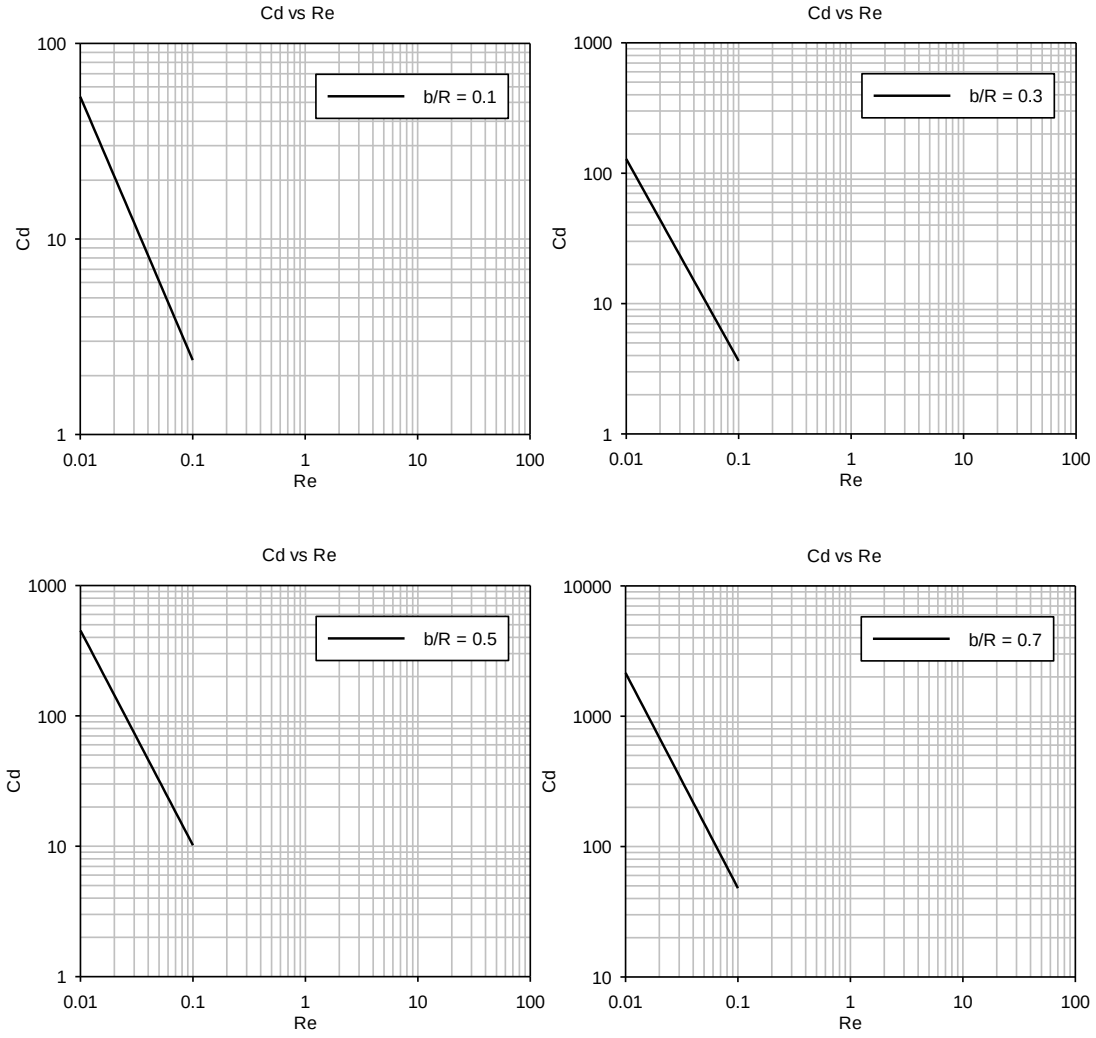

Figure 109: Cd vs Re for Case 4, n = 1.4, spheroid a/b = 10 (individual cases)

7.1.2 Effect of Confinement Ratio

The trend for coefficient of drag versus Reynolds number is similar to the previous cases, i.e. the drag coefficient increases with increase in confinement ratio. This can be seen from figures 110-121.

7.1.2.1 n = 0.6

7.1.2.1.1 a/b = 1

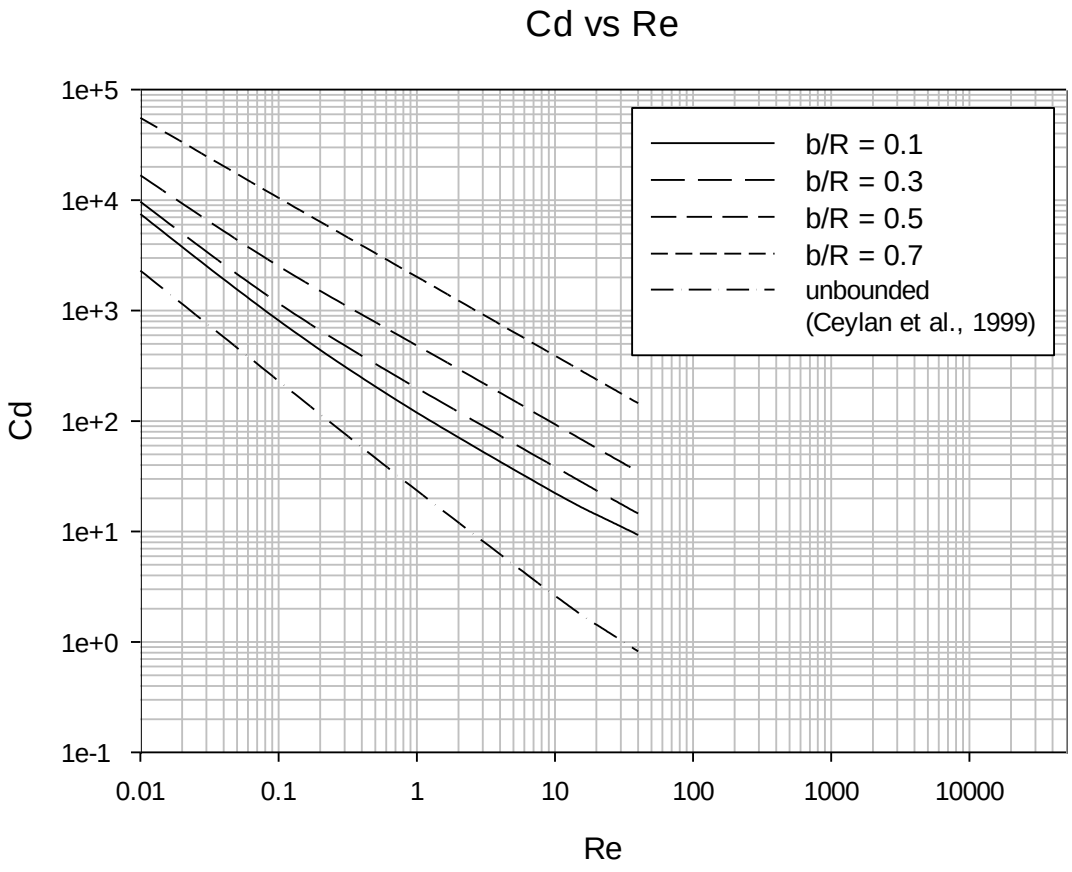

Figure 110: Cd vs Re for different confinement ratios, for Case 4, n = 0.6, spheroid a/b = 1 (all cases and unbounded [52])

.

7.1.2.1.2 a/b = 2

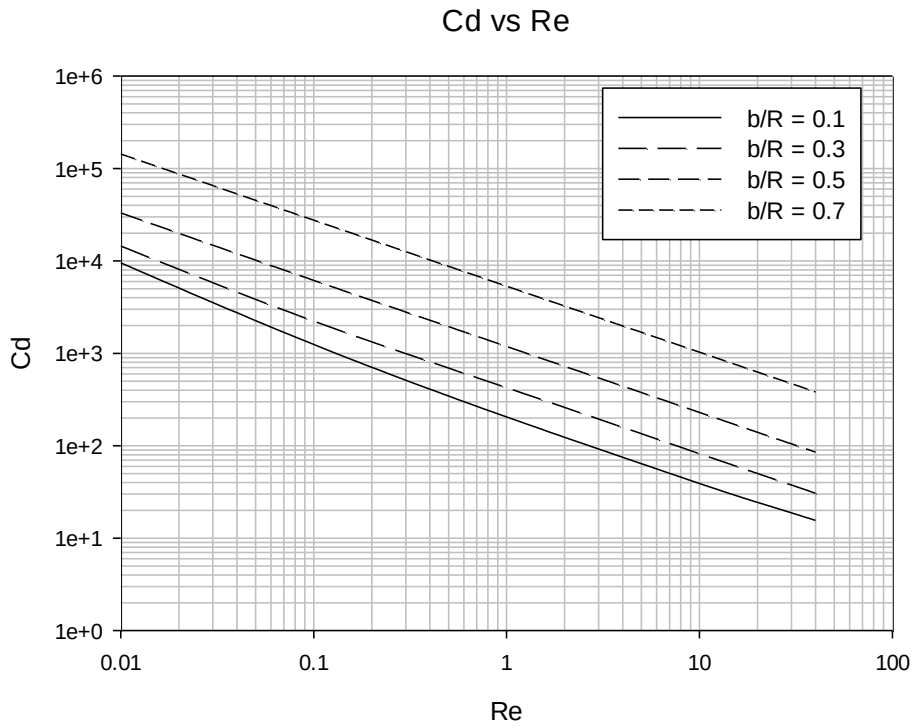

Figure 111: Cd vs Re for different confinement ratios, for Case 4, n = 0.6, spheroid a/b = 2

7.1.2.1.3 a/b = 10

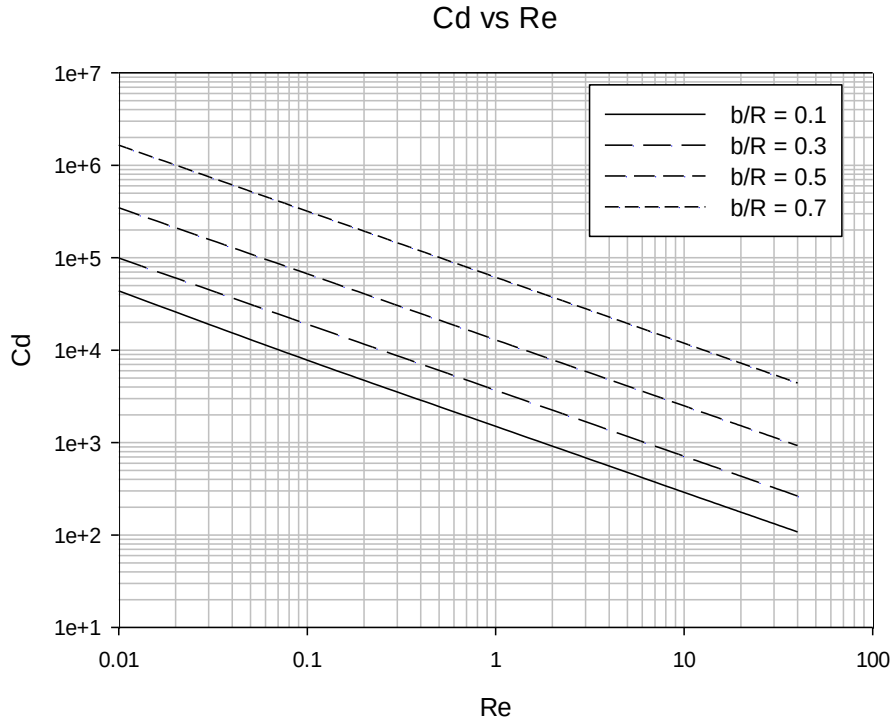

Figure 112: Cd vs Re for different confinement ratios, for Case 4, n = 0.6, spheroid a/b = 10

7.1.2.2 n = 0.8

7.1.2.2.1 a/b = 1

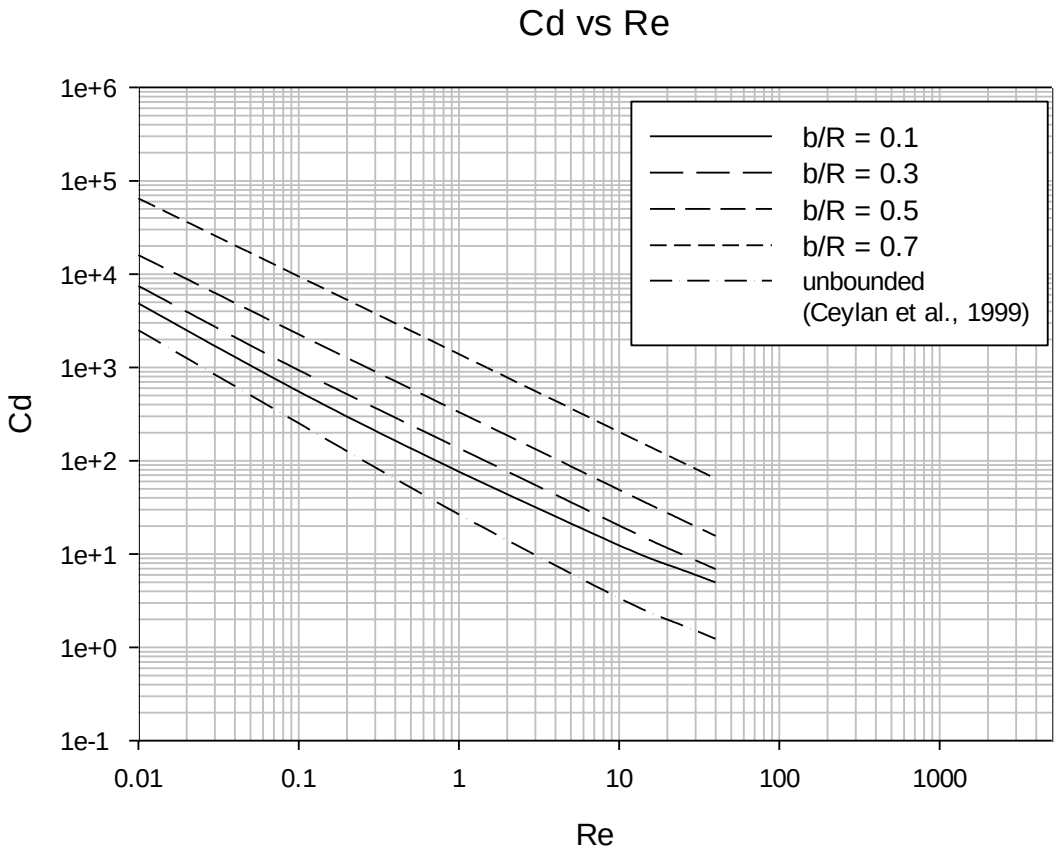

Figure 113: Cd vs Re for different confinement ratios, for Case 4, n = 0.8, spheroid a/b = 1 (all cases and unbounded [52])

7.1.2.2.2 a/b = 2

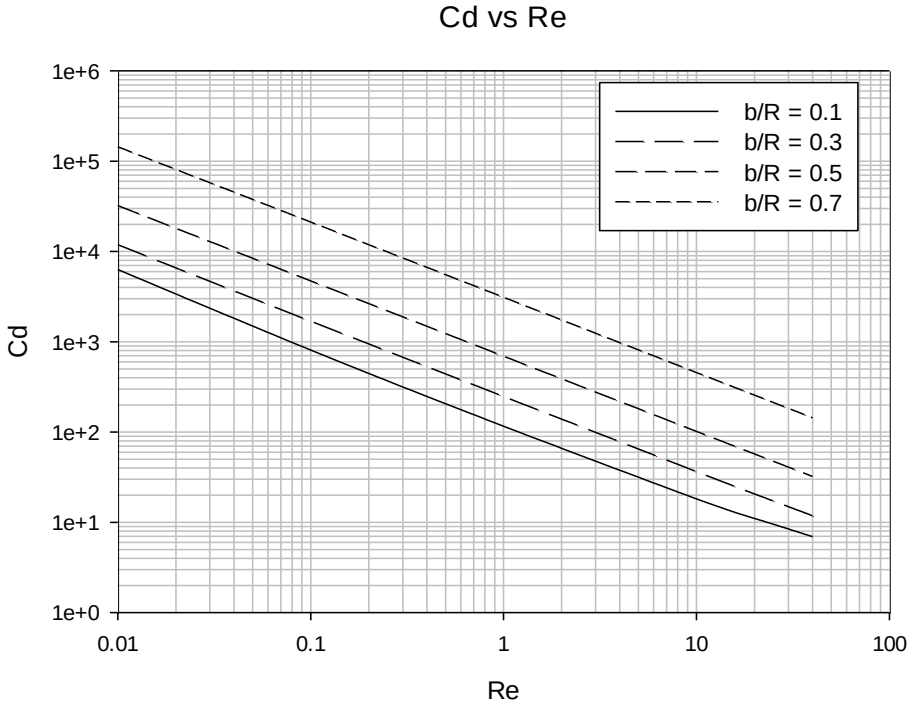

Figure 114: Cd vs Re for different confinement ratios, for Case 4, n = 0.8, spheroid a/b = 2

7.1.2.2.3 a/b = 10

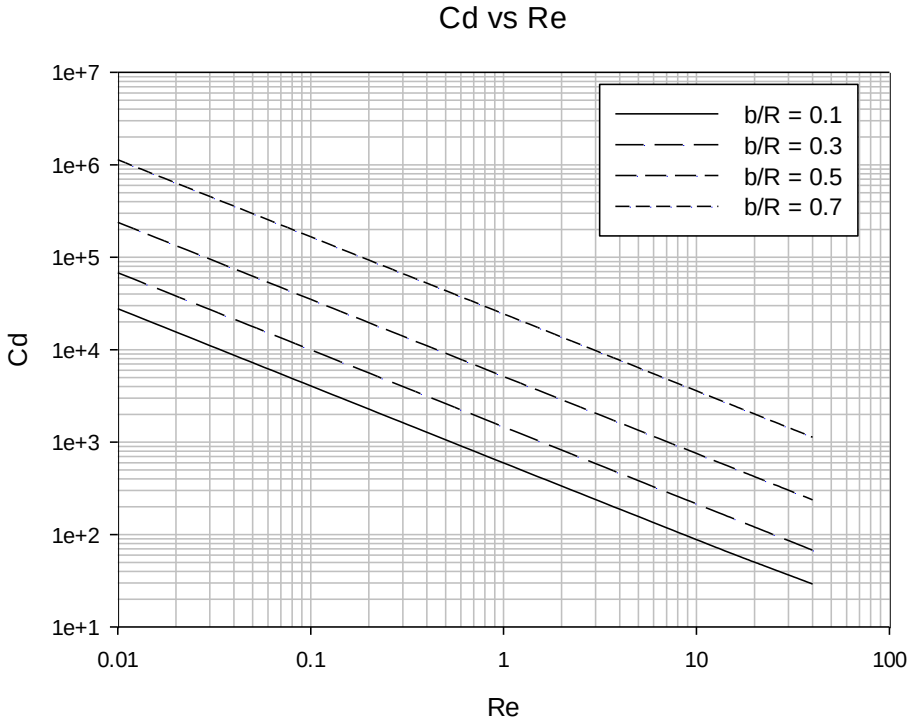

Figure 115: Cd vs Re for different confinement ratios, for Case 4, n = 0.8, spheroid a/b = 10

7.1.2.3 n = 1.2

7.1.2.3.1 a/b = 1

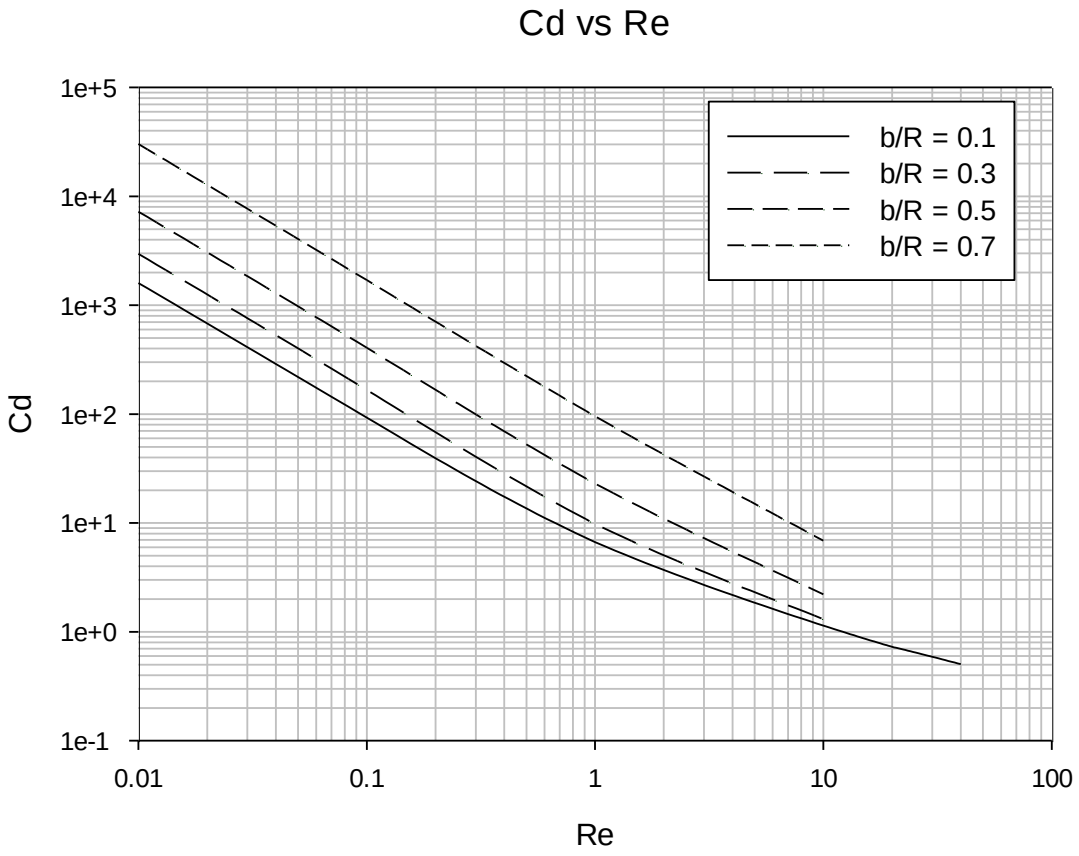

Figure 116: Cd vs Re for different confinement ratios, for Case 4, n = 1.2, spheroid a/b = 1

7.1.2.3.2 a/b = 2

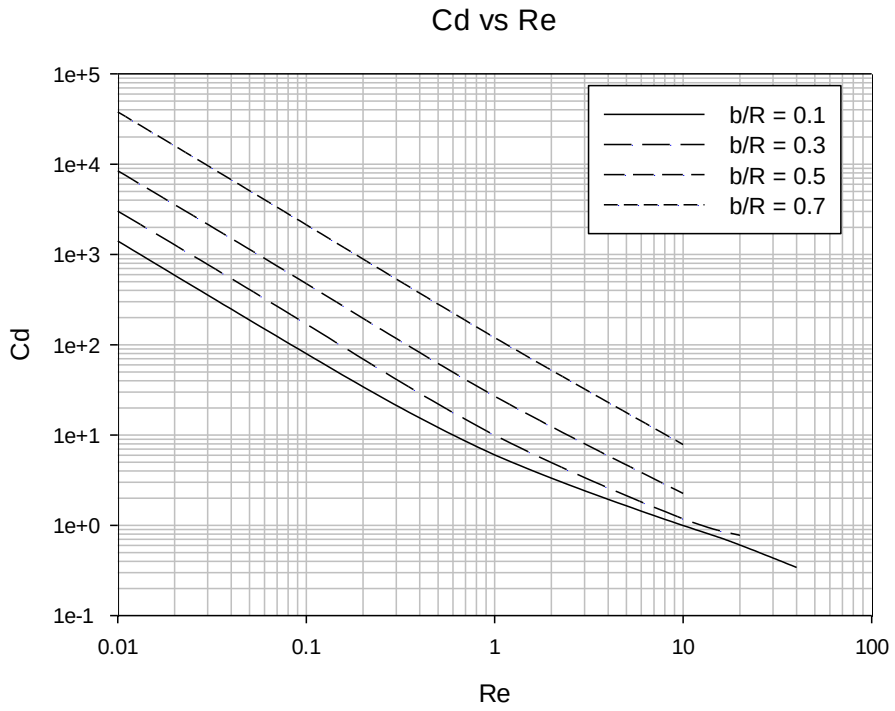

Figure 117: Cd vs Re for different confinement ratios, for Case 4, n = 1.2, spheroid a/b = 2

7.1.2.3.3 a/b = 10

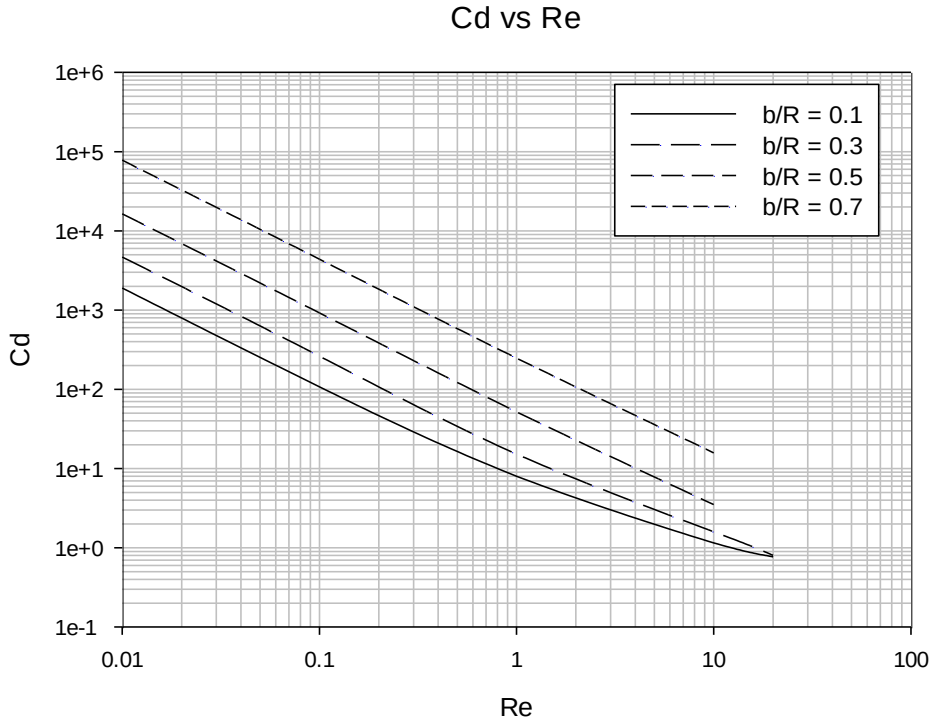

Figure 118: Cd vs Re for different confinement ratios, for Case 4, n = 1.2, spheroid a/b = 10

7.1.2.4 n = 1.4

7.1.2.4.1 a/b = 1

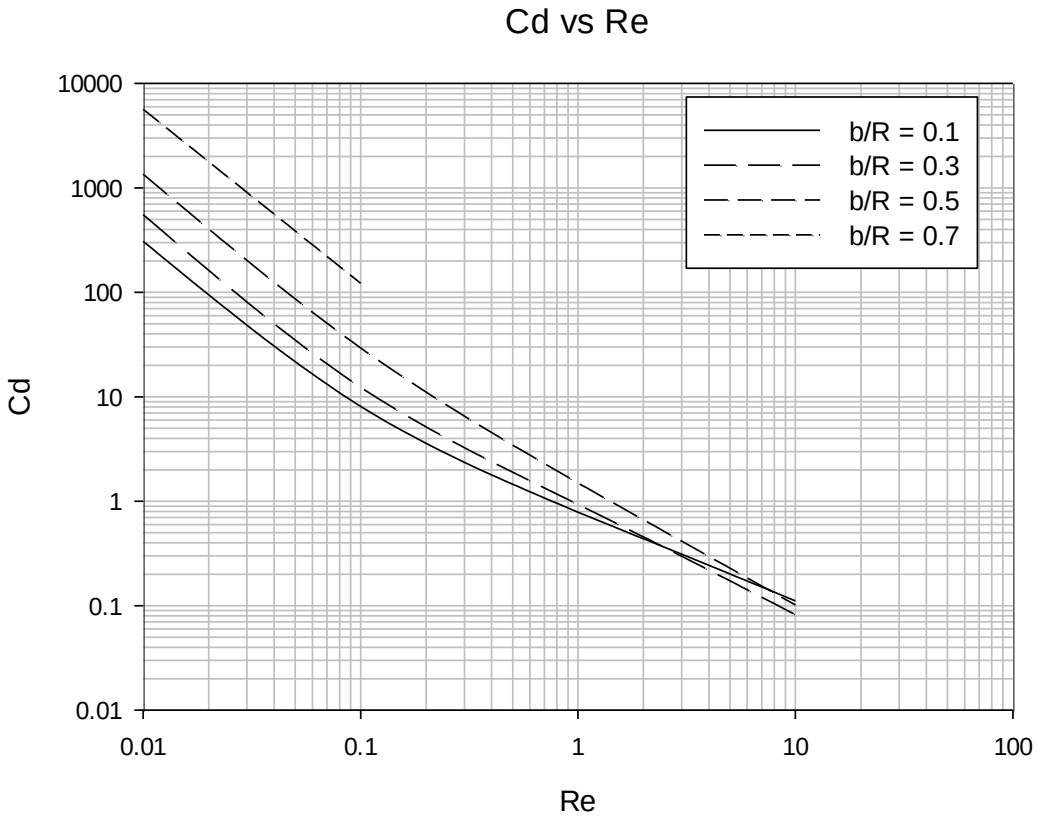

Figure 119: Cd vs Re for different confinement ratios, for Case 4, n = 1.4, spheroid a/b = 1

7.1.2.4.2 a/b = 2

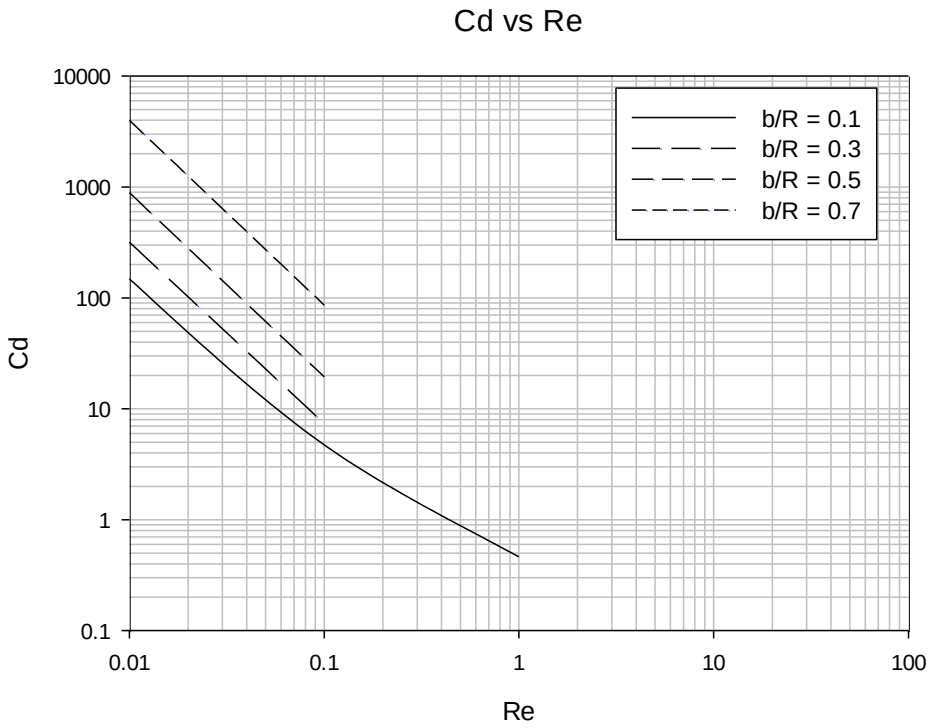

Figure 120: Cd vs Re for different confinement ratios, for Case 4, n = 1.4, spheroid a/b = 2

7.1.2.4.1 a/b = 10

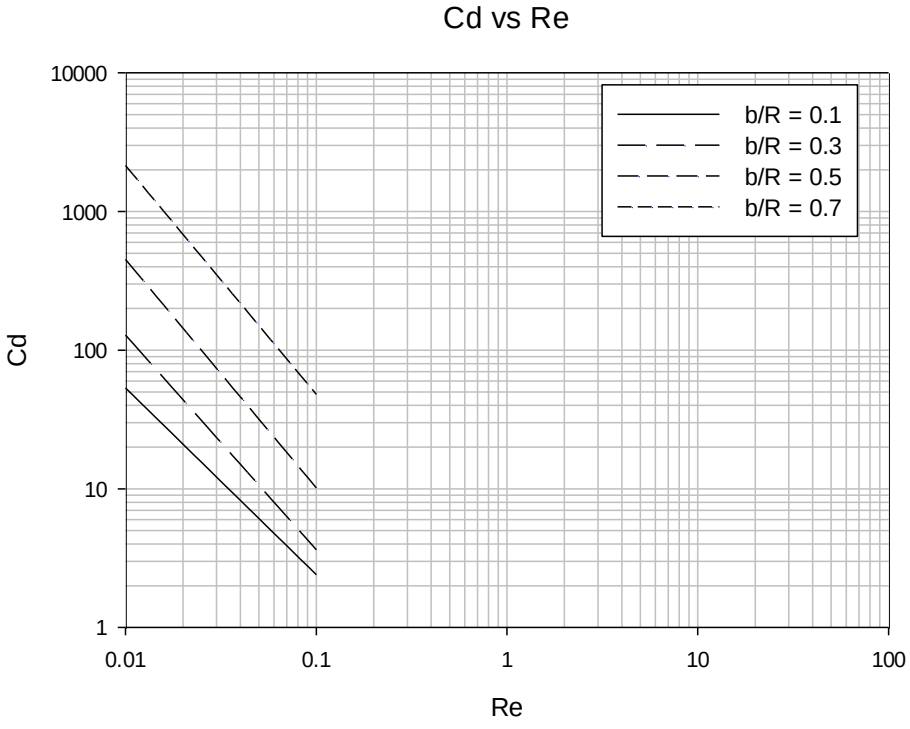

Figure 121: Cd vs Re for different confinement ratios, for Case 4, n = 0.6, spheroid a/b = 10

7.1.3 Effect of Particle Shape

The effect of particle shape can be seen in figures 122-137. For lower n values, Cd increases with increase in a/b. For higher n, Cd decreases with increase in a/b.

7.1.3.1 n = 0.6

7.1.3.1.1 b/R = 0.1

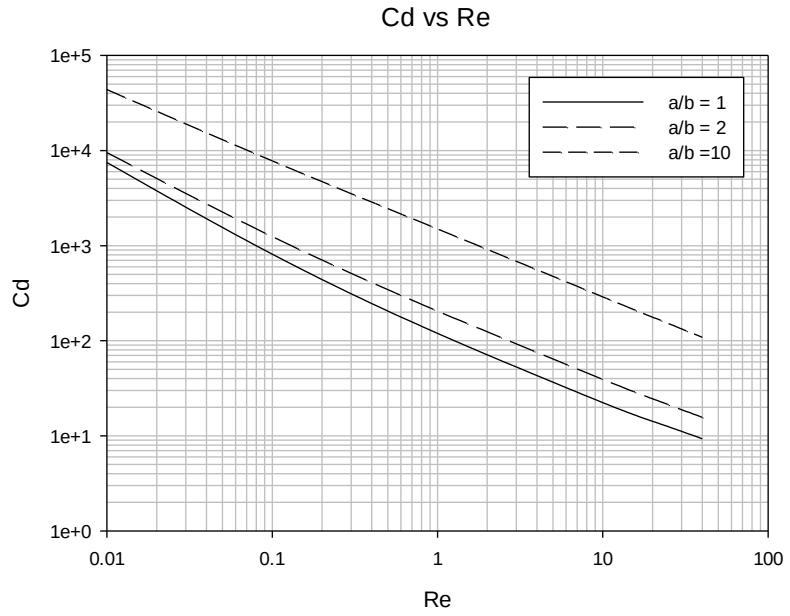

Figure 122: Cd vs Re for different shape factors, for Case 4, n = 0.6, spheroid b/R = 0.1

7.1.3.1.2 b/R = 0.3

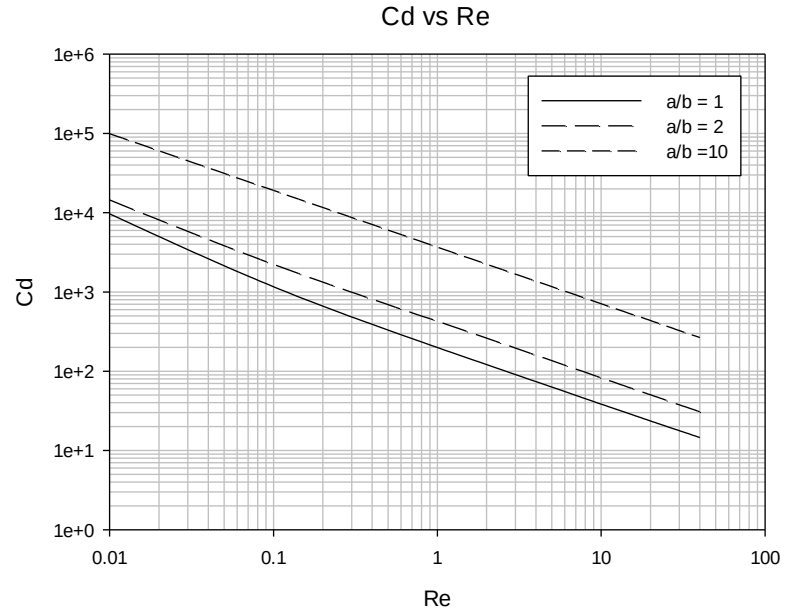

Figure 123: Cd vs Re for different shape factors, for Case 4, n = 0.6, spheroid b/R = 0.3

7.1.3.1.3 b/R = 0.5

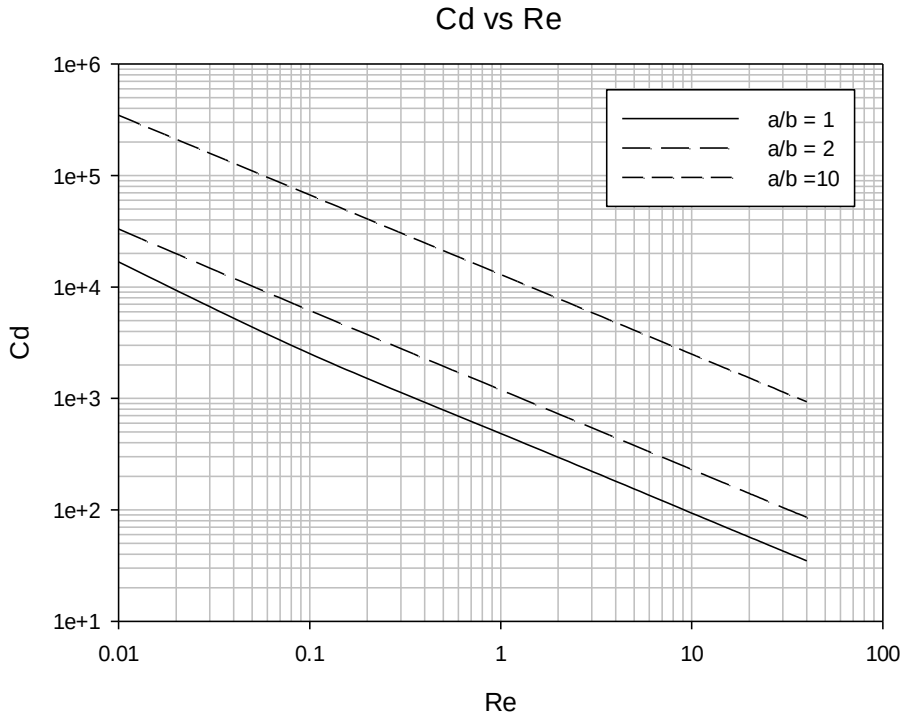

Figure 124: Cd vs Re for different shape factors, for Case 4, n = 0.6, spheroid b/R = 0.5

7.1.3.1.4 b/R = 0.7

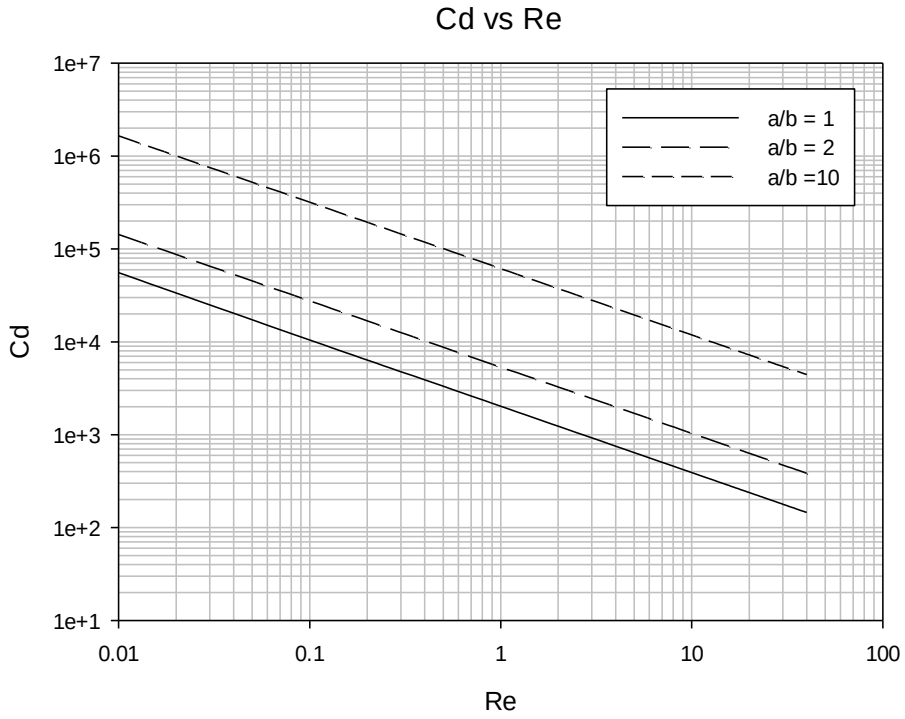

Figure 125: Cd vs Re for different shape factors, for Case 4, n = 0.6, spheroid b/R = 0.7

7.1.3.2 n = 0.8

7.1.3.2.1 b/R = 0.1

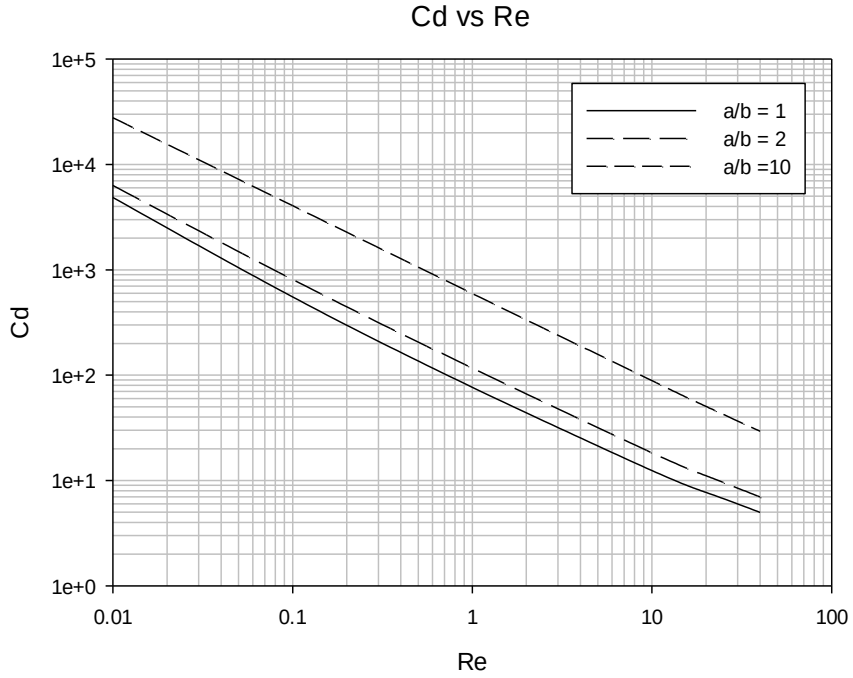

Figure 126: Cd vs Re for different shape factors, for Case 4, n = 0.8, spheroid b/R = 0.1

7.1.3.2.2 b/R = 0.3

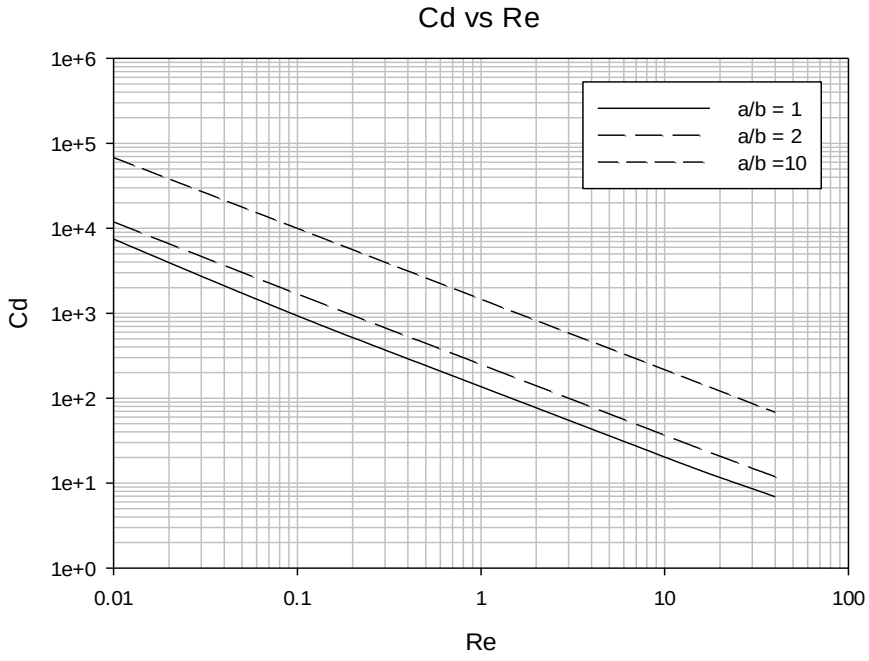

Figure 127: Cd vs Re for different shape factors, for Case 4, n = 0.8, spheroid b/R = 0.3

7.1.3.2.3 b/R = 0.5

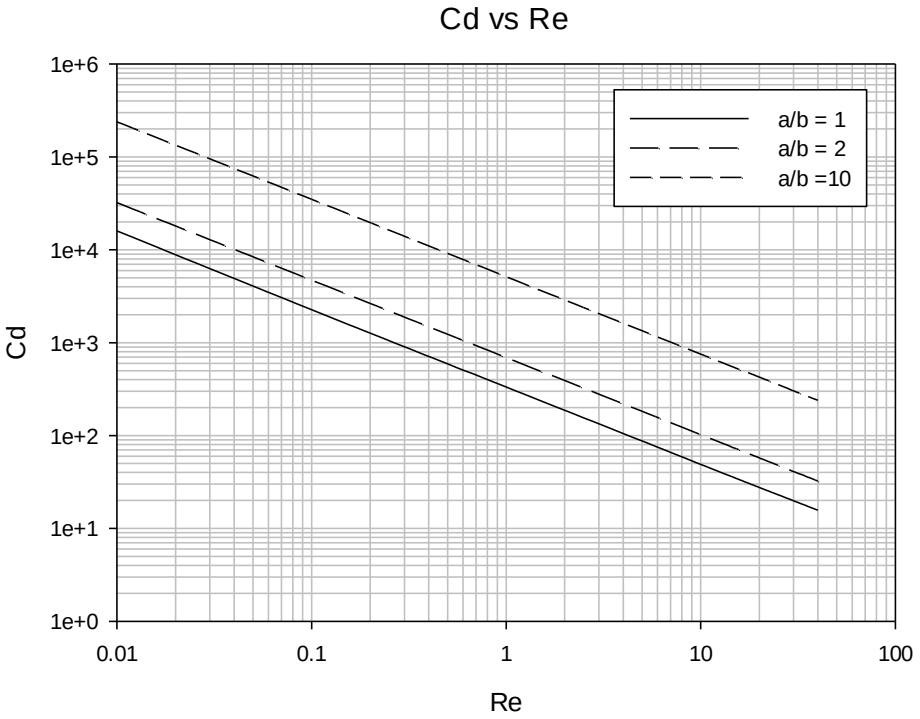

Figure 128: Cd vs Re for different shape factors, for Case 4, n = 0.8, spheroid b/R = 0.5

7.1.3.2.4 b/R = 0.7

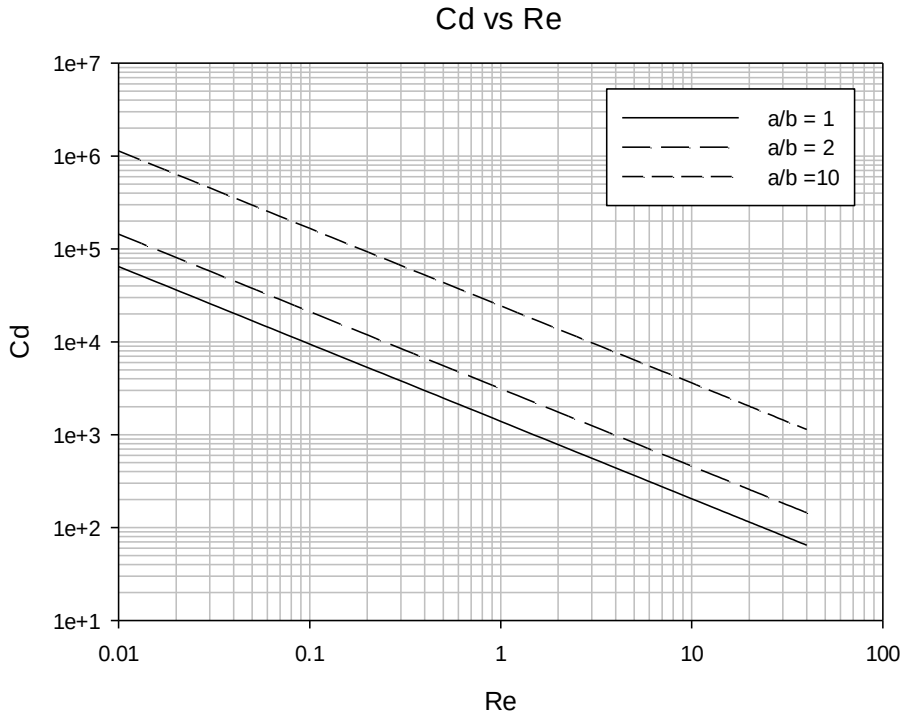

Figure 129: Cd vs Re for different shape factors, for Case 4, n = 0.8, spheroid b/R = 0.7

7.1.3.3 n = 1.2

7.1.3.3.1 b/R = 0.1

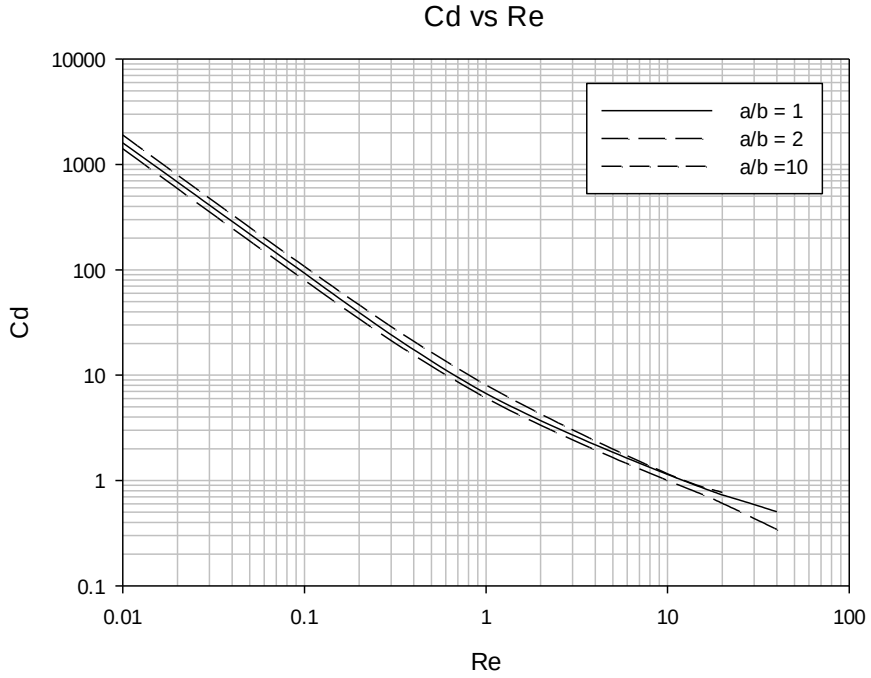

Figure 130: Cd vs Re for different shape factors, for Case 4, n = 1.2, spheroid b/R = 0.1

7.1.3.3.2 b/R = 0.3

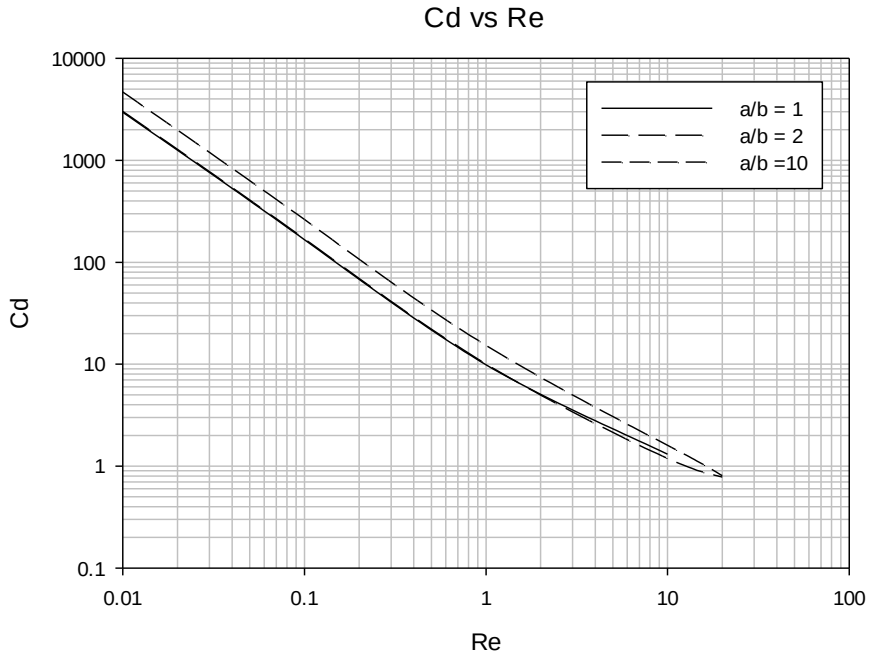

Figure 131: Cd vs Re for different shape factors, for Case 4, n = 1.2, spheroid b/R = 0.3

7.1.3.3.3 b/R = 0.5

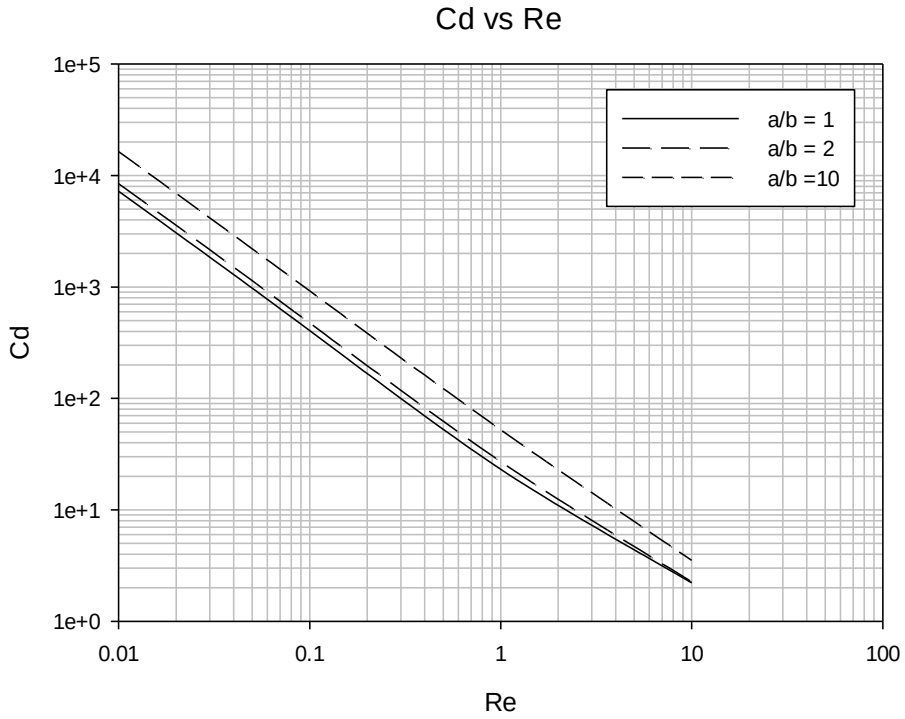

Figure 132: Cd vs Re for different shape factors, for Case 4, n = 1.2, spheroid b/R = 0.5

7.1.3.3.4 b/R = 0.7

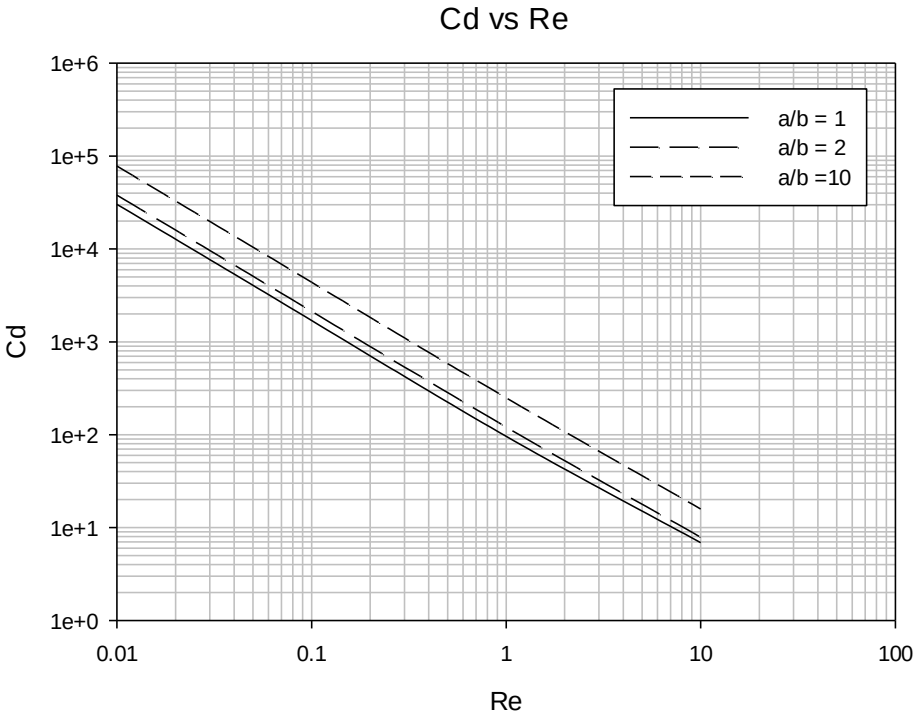

Figure 133: Cd vs Re for different shape factors, for Case 4, n = 1.2, spheroid b/R = 0.7

7.1.3.4 n = 1.4

7.1.3.4.1 b/R = 0.1

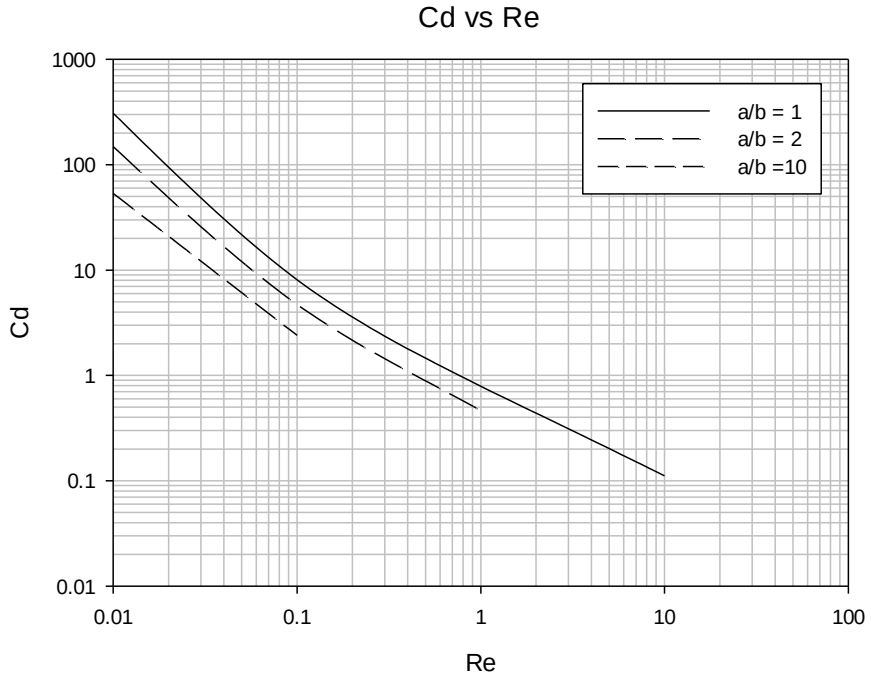

Figure 134: Cd vs Re for different shape factors, for Case 4, n = 1.4, spheroid b/R = 0.1

7.1.3.4.2 b/R = 0.3

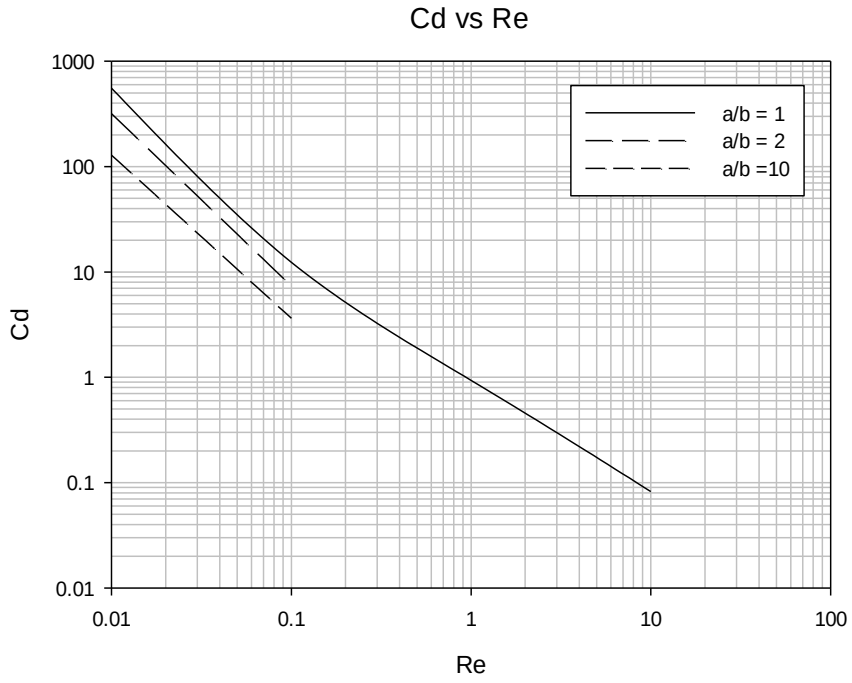

Figure 135: Cd vs Re for different shape factors, for Case 4, n = 1.4, spheroid b/R = 0.3

7.1.3.4.3 b/R = 0.5

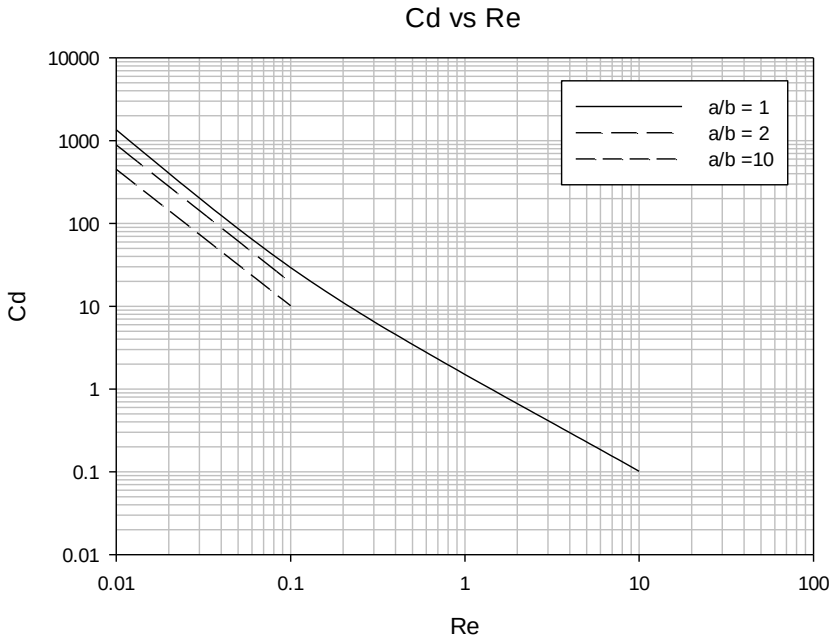

Figure 136: Cd vs Re for different shape factors, for Case 4, n = 1.4, spheroid b/R = 0.5

7.1.3.4.4 b/R = 0.7

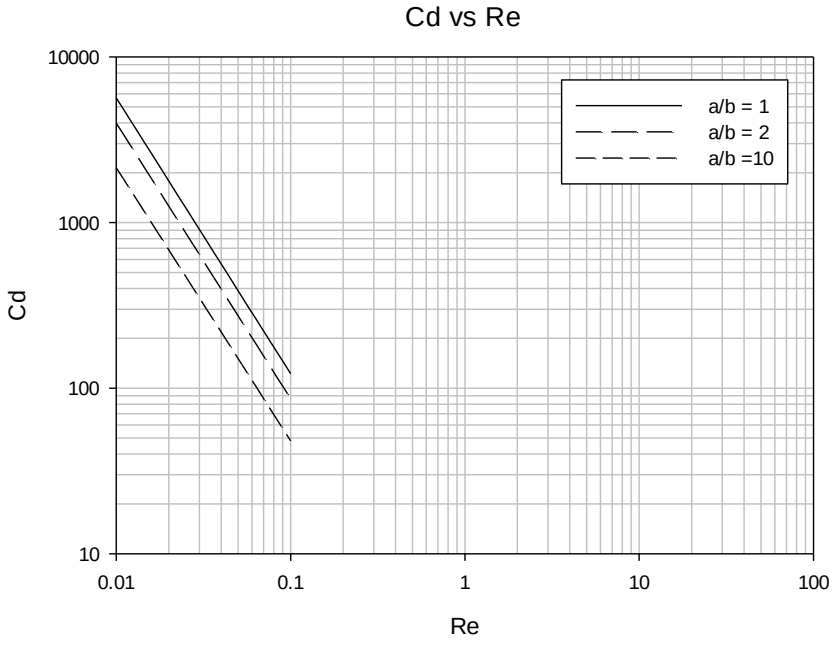

Figure 137: Cd vs Re for different shape factors, for Case 4, n = 1.4, spheroid b/R = 0.7

7.1.4 Effect of Power-Law Index

For all cases, Cd decreases with increase in the power law index value, as seen in figures 138-149.

7.1.4.1 a/b = 1

7.1.4.1.1 b/R = 0.1

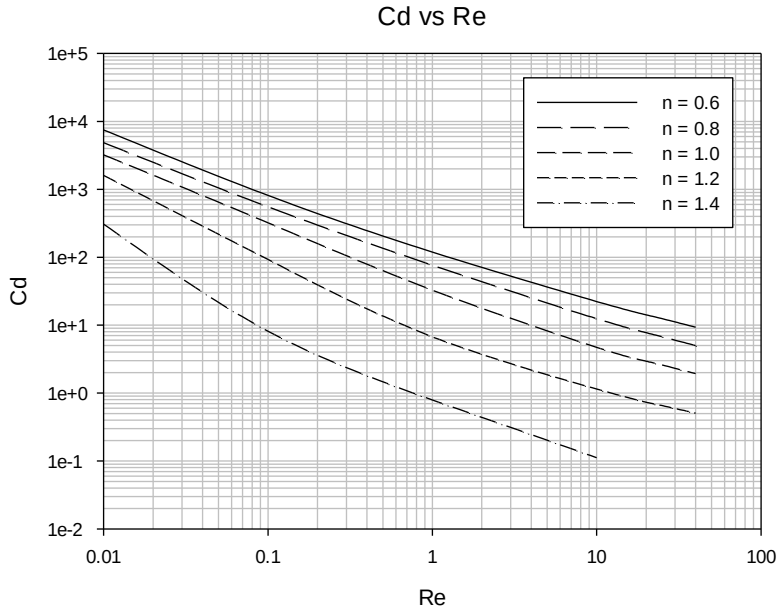

Figure 138: Cd vs Re for different power law values, Case 4, spheroid a/b = 1, b/R = 0.1

7.1.4.1.2 b/R = 0.3

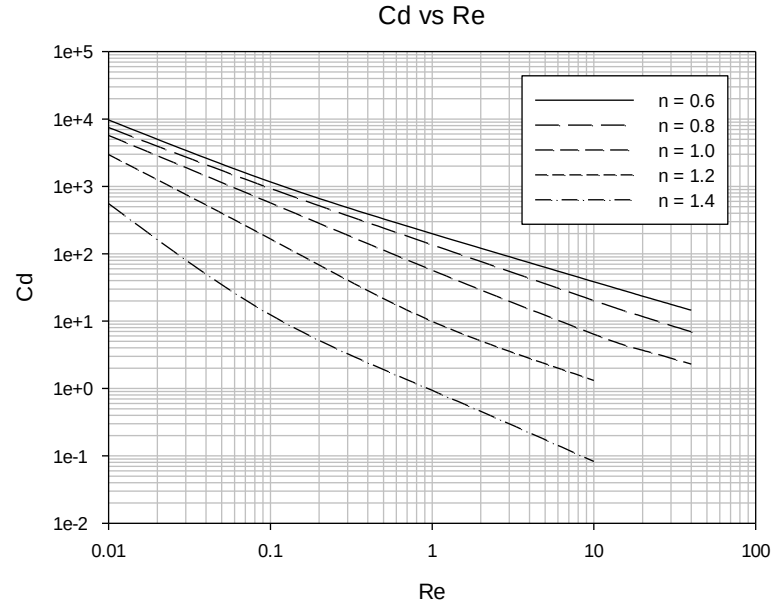

Figure 139: Cd vs Re for different power law values, Case 4, spheroid a/b = 1, b/R = 0.3

7.1.4.1.3 b/R = 0.5

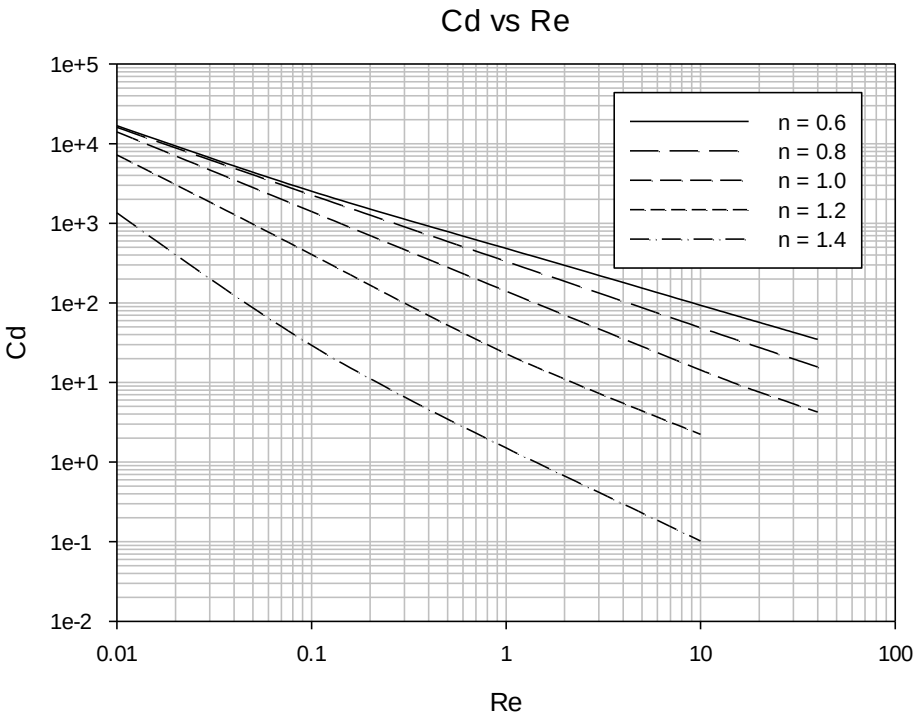

Figure 140: Cd vs Re for different power law values, Case 4, spheroid a/b = 1, b/R = 0.5

7.1.4.1.4 b/R = 0.7

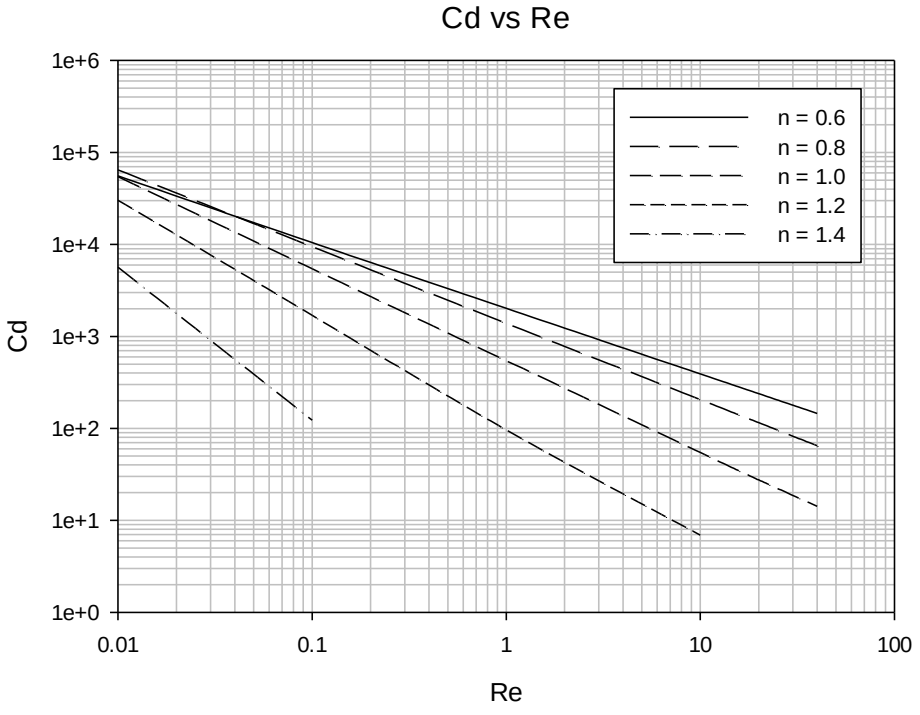

Figure 141: Cd vs Re for different power law values, Case 4, spheroid a/b = 1, b/R = 0.7

7.1.4.2 a/b = 2

7.1.4.2.1 b/R = 0.1

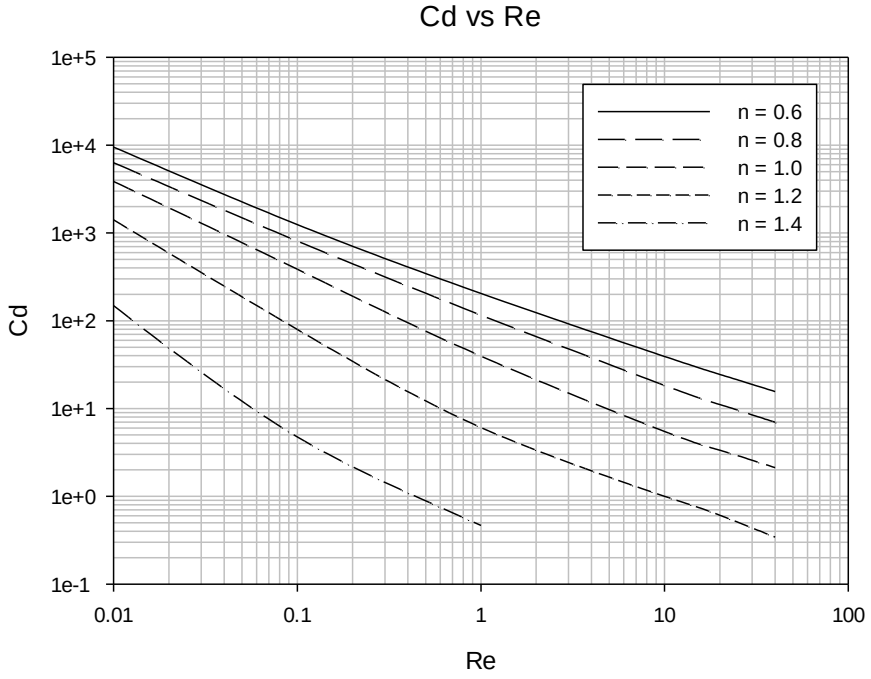

Figure 142: Cd vs Re for different power law values, Case 4, spheroid a/b = 2, b/R = 0.1

7.1.4.2.2 b/R = 0.3

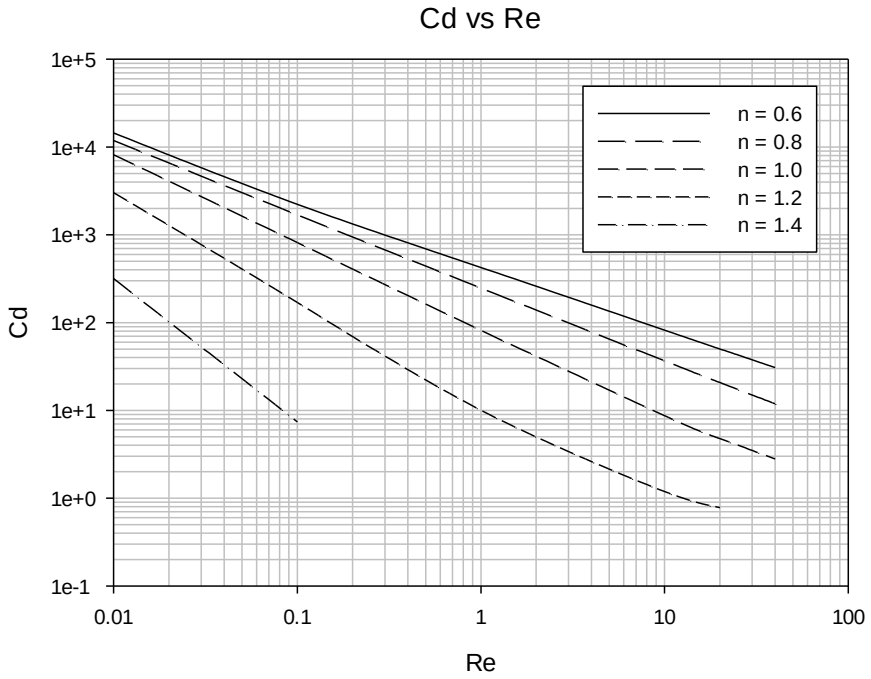

Figure 143: Cd vs Re for different power law values, Case 4, spheroid a/b = 2, b/R = 0.3

7.1.4.2.3 b/R = 0.5

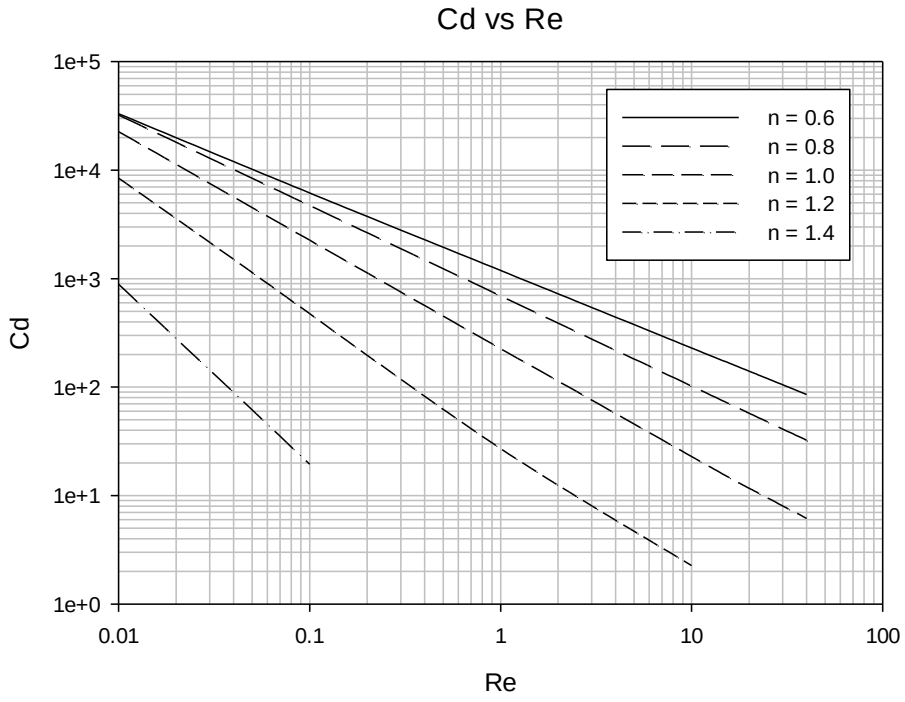

Figure 144: Cd vs Re for different power law values, Case 4, spheroid a/b = 2, b/R = 0.5

7.1.4.2.4 b/R = 0.7

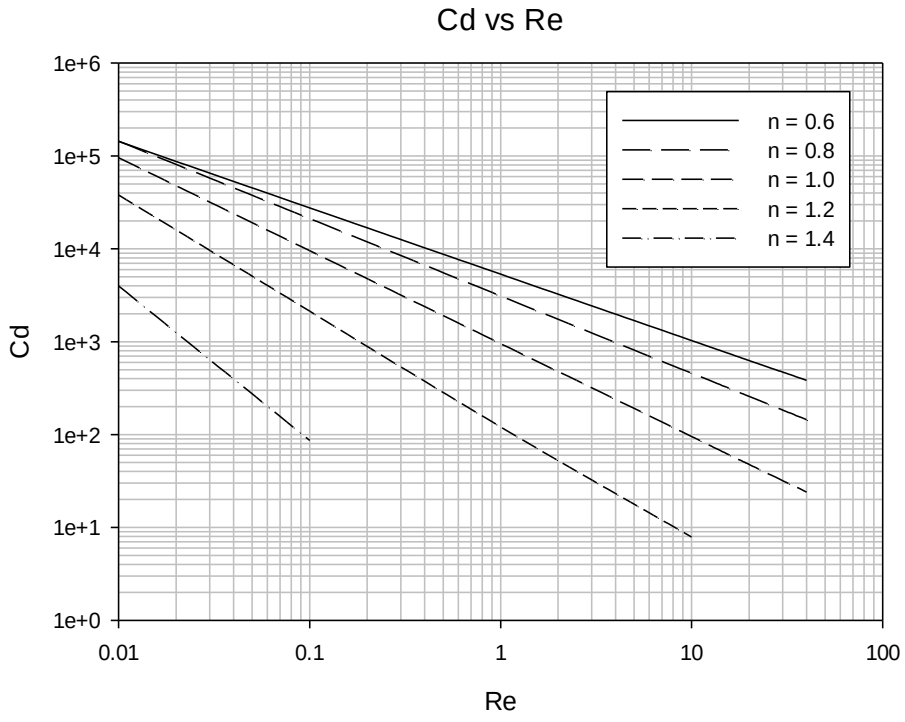

Figure 145: Cd vs Re for different power law values, Case 4, spheroid a/b = 2, b/R = 0.7

7.1.4.3 a/b = 10

7.1.4.3.1 b/R = 0.1

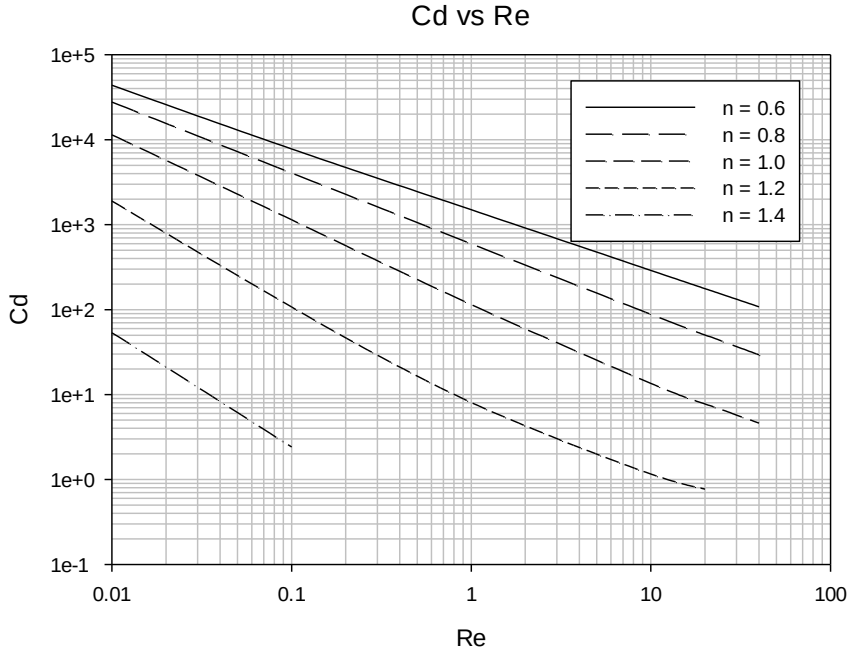

Figure 146: Cd vs Re for different power law values, Case 4, spheroid a/b = 10, b/R = 0.1

7.1.4.3.2 b/R = 0.3

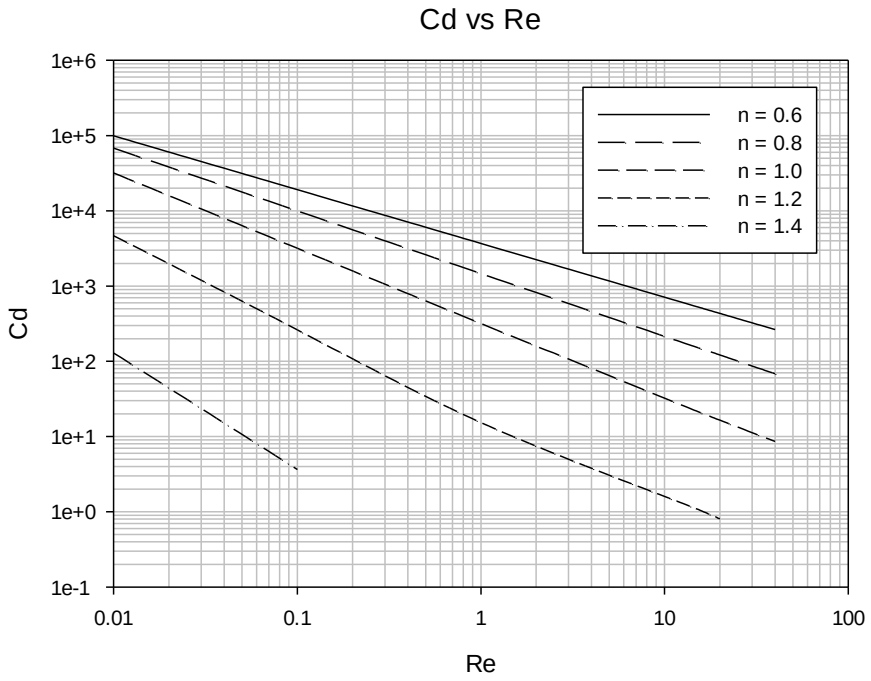

Figure 147: Cd vs Re for different power law values, Case 4, spheroid a/b = 10, b/R = 0.3

7.1.4.3.3 b/R = 0.5

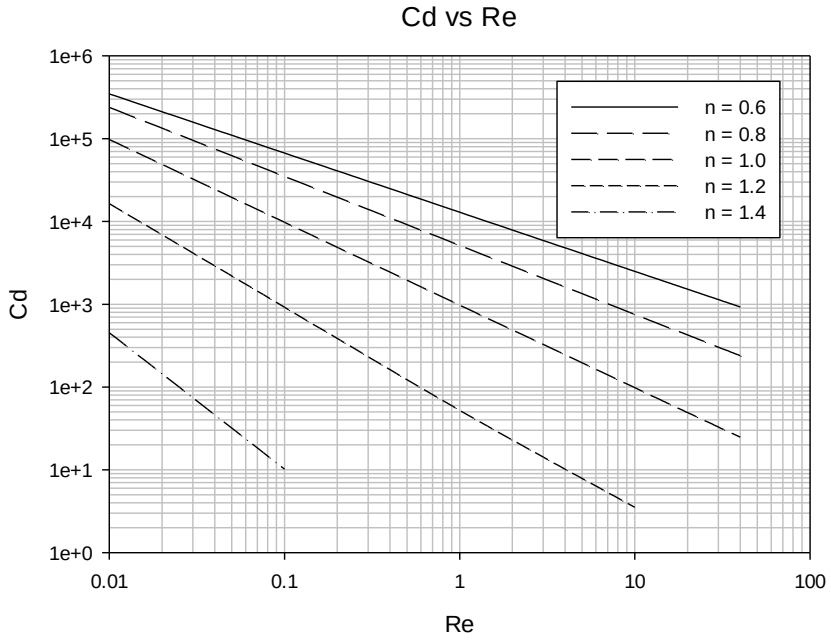

Figure 148: Cd vs Re for different power law values, Case 4, spheroid a/b = 10, b/R = 0.5

7.1.4.3.4 b/R = 0.7

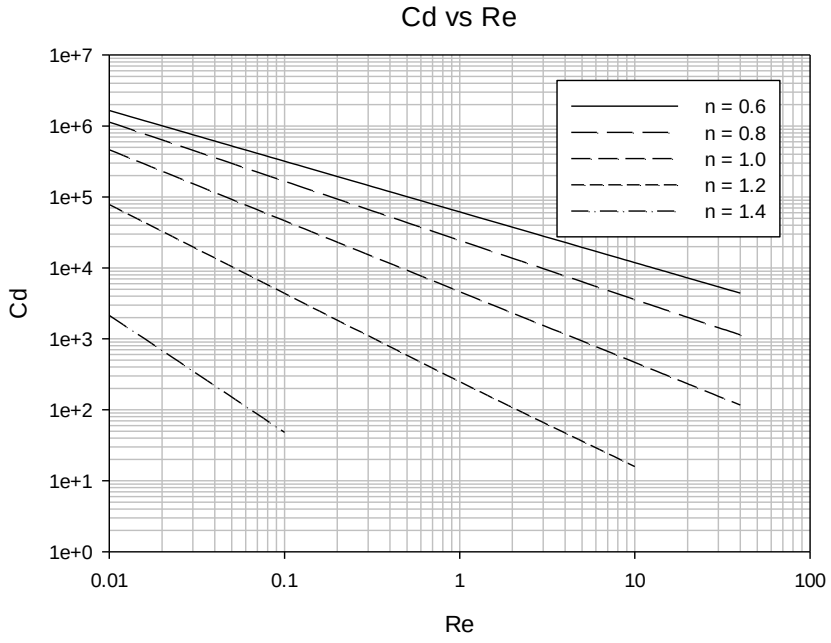

Figure 149: Cd vs Re for different power law values, Case 4, spheroid a/b = 10, b/R = 0.7

7.2 Cassini Oval

7.2.1 Effect of Reynolds number

As seen from figures 150-161, the drag coefficient decreases with increase in Reynolds number. This follows the same trend as the previous cases.

7.2.1.1 n = 0.6

7.2.1.1.1 $(c/d)^2 = 0.3$

Table 39: Numerical results for Case 4, n = 0.6, Cassini Oval $(c/d)^2 = 0.3$

	Cd			
Re	**b/R = 0.1**	**b/R = 0.3**	**b/R = 0.5**	**b/R = 0.7**
0.0100	16767.2075	22365.7277	40267.0997	126215.4265
0.1000	1740.9470	2458.0664	5363.7960	22758.7975
1.0000	232.9199	378.1367	1004.2610	4386.7720
10.0000	43.0268	72.5860	193.8800	847.0848
20.0000	27.5512	44.5344	118.2683	516.4241
40.0000	18.2159	27.5861	72.2444	314.9310

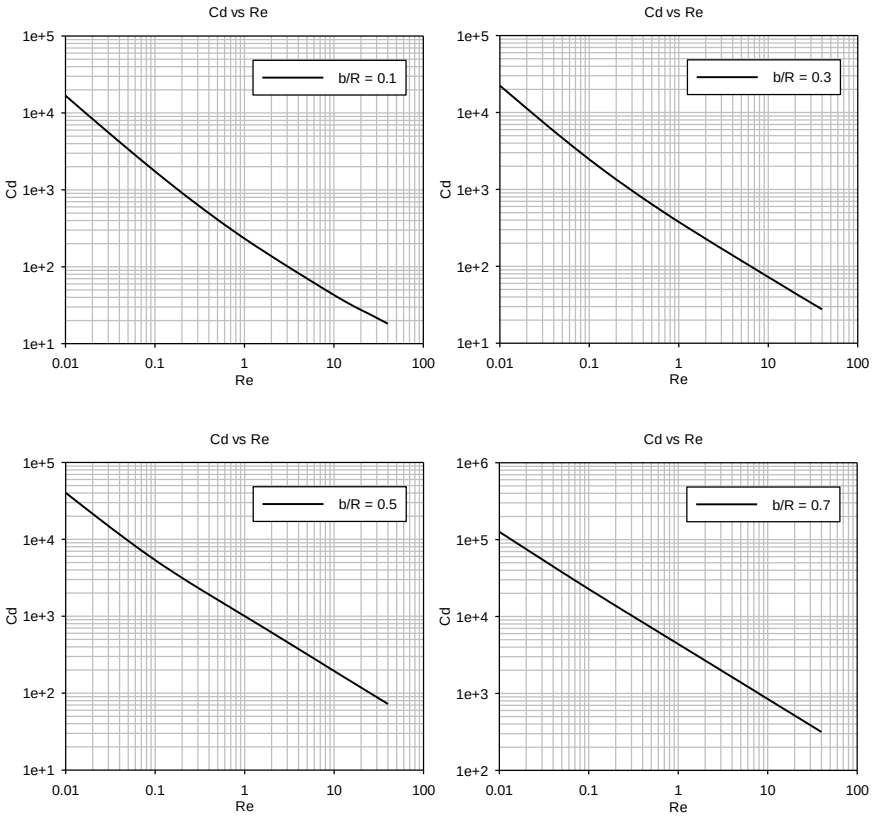

Figure 150: Cd vs Re for Case 4, n = 0.6, Cassini Oval $(c/d)^2 = 0.1$ (individual cases)

7.2.1.1.2 $(c/d)^2 = 0.7$

Table 40: Numerical results for Case 4, n = 0.6, Cassini Oval $(c/d)^2 = 0.7$

	Cd			
Re	**b/R = 0.1**	**b/R = 0.3**	**b/R = 0.5**	**b/R = 0.7**
0.0100	10994.9722	16959.6060	38574.7428	171546.0044
0.1000	1298.4213	2356.7273	6888.0306	32988.0311
1.0000	201.6689	437.7131	1327.4547	6368.3905
10.0000	37.8318	84.5488	256.3722	1229.7540
20.0000	23.7810	51.6337	156.3263	749.6593
40.0000	15.3279	31.6219	95.3664	457.0744

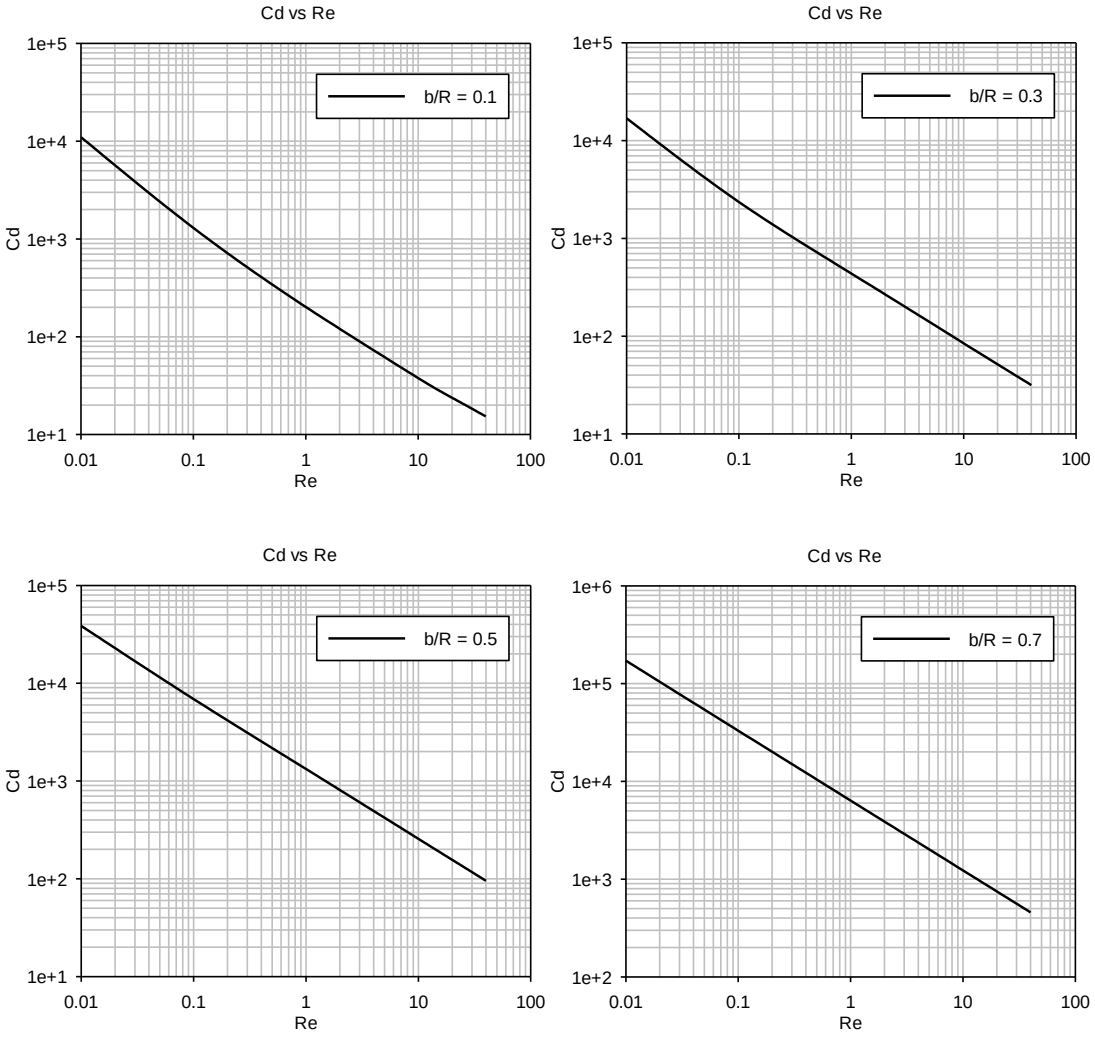

Figure 151: Cd vs Re for Case 4, n = 0.6, Cassini Oval $(c/d)^2 = 0.7$ (individual cases)

7.2.1.1.3 $(c/d)^2 = 0.95$

Table 41: Numerical results for Case 4, n = 0.6, Cassini Oval $(c/d)^2 = 0.95$

	Cd			
Re	**b/R = 0.1**	**b/R = 0.3**	**b/R = 0.5**	**b/R = 0.7**
0.0100	12396.6789	19716.1854	44508.5903	182565.2919
0.1000	1576.3790	3018.5363	8279.4772	35194.5174
1.0000	258.8234	575.7034	1597.6808	6794.8446
10.0000	49.4239	111.2306	308.5570	1312.0446
20.0000	30.7807	67.8944	188.1376	799.7985
40.0000	19.5731	41.5363	114.7678	487.6768

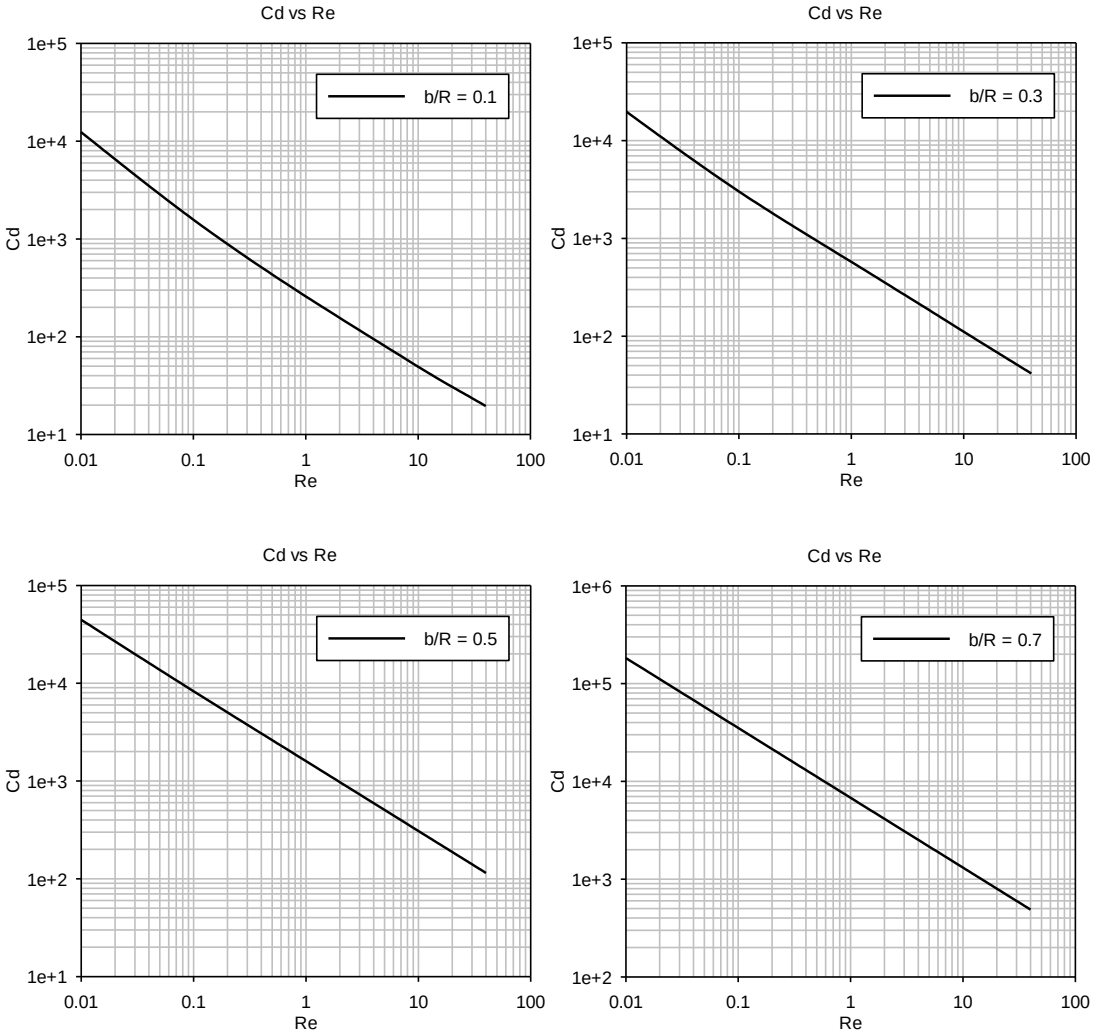

Figure 152: Cd vs Re for Case 4, n = 0.6, Cassini Oval $(c/d)^2 = 0.95$ (individual cases)

7.2.1.2 n = 0.8

7.2.1.2.1 $(c/d)^2 = 0.3$

Table 42: Numerical results for Case 4, n = 0.8, Cassini Oval $(c/d)^2 = 0.3$

	Cd			
Re	**b/R = 0.1**	**b/R = 0.3**	**b/R = 0.5**	**b/R = 0.7**
0.0100	11259.6872	17406.6531	39072.3593	156227.7327
0.1000	1201.1947	1998.5488	5207.8142	22732.9195
1.0000	160.8542	284.8635	763.4184	3336.4931
10.0000	26.2682	42.2976	112.2195	489.9600
20.0000	16.3446	24.2738	63.1775	275.1800
40.0000	10.5655	14.3620	35.7774	154.7322

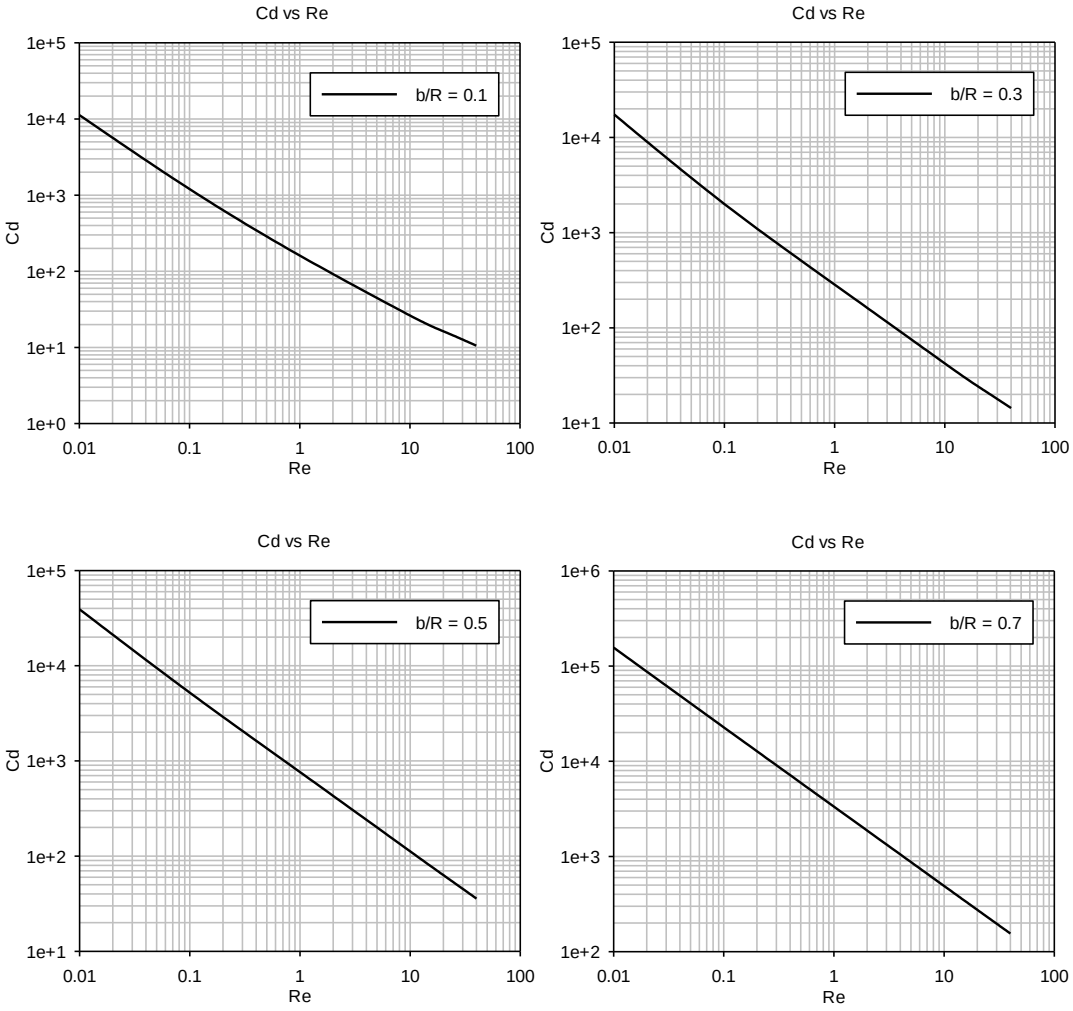

Figure 153: Cd vs Re for Case 4, n = 0.8, Cassini Oval $(c/d)^2 = 0.3$ (individual cases)

7.2.1.2.2 $(c/d)^2 = 0.7$

Table 43: Numerical results for Case 4, n = 0.8, Cassini Oval $(c/d)^2 = 0.7$

	Cd			
Re	**b/R = 0.1**	**b/R = 0.3**	**b/R = 0.5**	**b/R = 0.7**
0.0100	7153.7711	13871.2459	39312.8271	187661.9013
0.1000	865.1063	1893.1907	5739.9176	27536.8154
1.0000	121.5986	277.6099	842.5182	4042.0327
10.0000	19.2587	40.9470	123.7967	593.5606
20.0000	11.7473	23.1910	69.5960	333.2993
40.0000	7.4279	13.3150	39.2376	187.2517

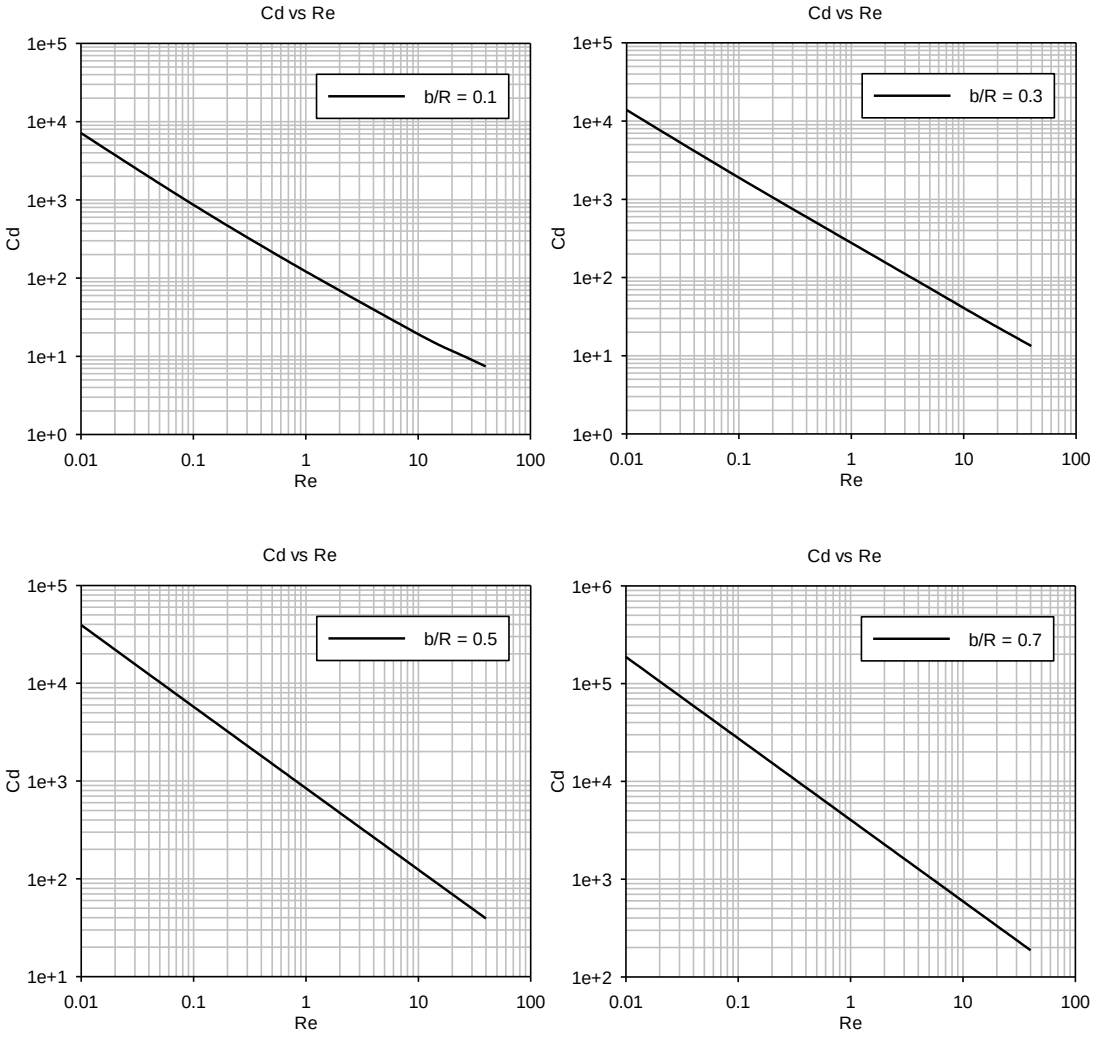

Figure 154: Cd vs Re for Case 4, n = 0.8, Cassini Oval $(c/d)^2 = 0.7$ (individual cases)

7.2.1.2.3 $(c/d)^2 = 0.95$

Table 44: Numerical results for Case 4, n = 0.8, Cassini Oval $(c/d)^2 = 0.95$

	Cd			
Re	**b/R = 0.1**	**b/R = 0.3**	**b/R = 0.5**	**b/R = 0.7**
0.0100	8132.3317	16293.7123	43825.5443	186145.8290
0.1000	1038.4862	2314.8219	6423.7790	27320.1691
1.0000	148.9693	339.7136	942.9389	4010.1855
10.0000	23.1908	50.0739	138.5540	588.9160
20.0000	13.9704	28.3333	77.8974	330.6423
40.0000	8.7274	16.2291	43.9338	104.1458

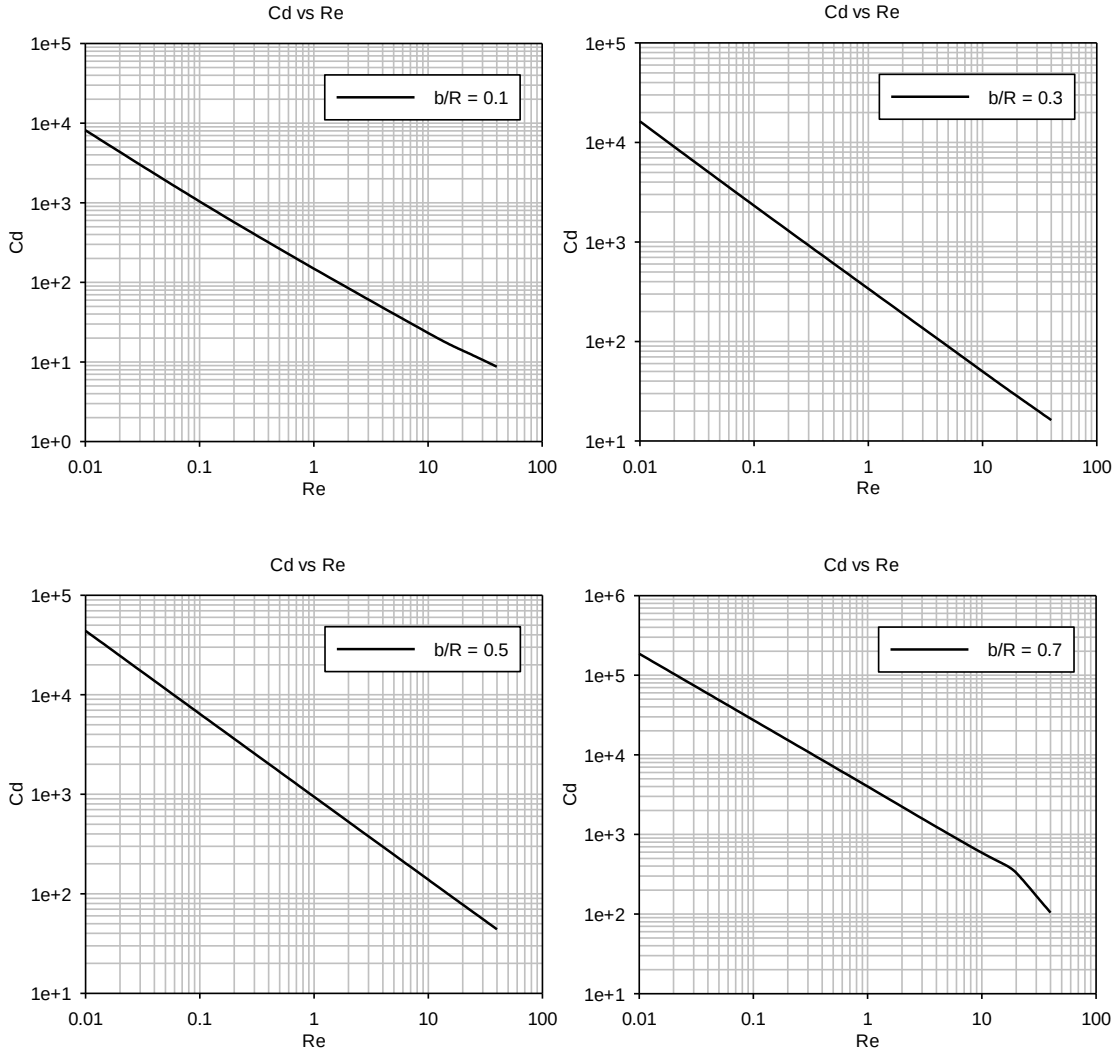

Figure 155: Cd vs Re for Case 4, n = 0.8, Cassini Oval $(c/d)^2 = 0.95$ (individual cases)

7.2.1.3 n = 1.2

7.2.1.3.1 $(c/d)^2 = 0.3$

Table 45: Numerical results for Case 4, n = 1.2, Cassini Oval $(c/d)^2 = 0.3$

	Cd			
Re	**b/R = 0.1**	**b/R = 0.3**	**b/R = 0.5**	**b/R = 0.7**
0.0100	4539.5690	8703.9823	23596.2050	103184.1717
0.1000	275.5284	495.2993	1327.6920	5802.8708
1.0000	18.7409	28.5627	74.9115	326.6196
10.0000	2.7684	3.1095	2.8882	20.4455
20.0000	1.7846	1.9390		
40.0000				

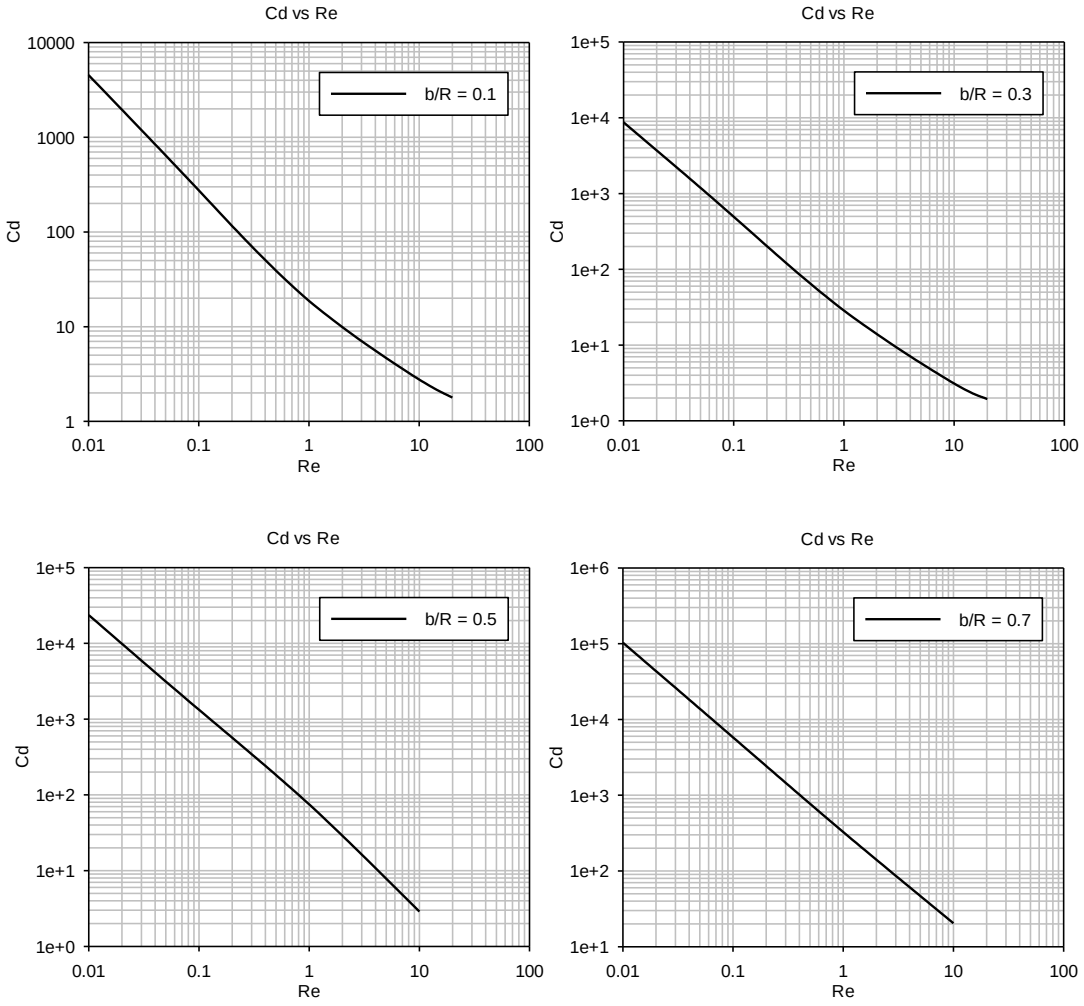

Figure 156: Cd vs Re for Case 4, n = 1.2, Cassini Oval $(c/d)^2 = 0.3$ (individual cases)

7.2.1.3.2 $(c/d)^2 = 0.7$

Table 46: Numerical results for Case 4, n = 1.2, Cassini Oval $(c/d)^2 = 0.7$

	Cd			
Re	**b/R = 0.1**	**b/R = 0.3**	**b/R = 0.5**	**b/R = 0.7**
0.0100	1970.1754	4555.6365	13829.1411	66350.0087
0.1000	112.2366	256.2721	777.7624	3731.3713
1.0000	8.1215	14.8581	43.9999	210.2343
10.0000	1.2050	1.5601	3.3810	13.3886
20.0000	0.7570	0.9451		
40.0000				

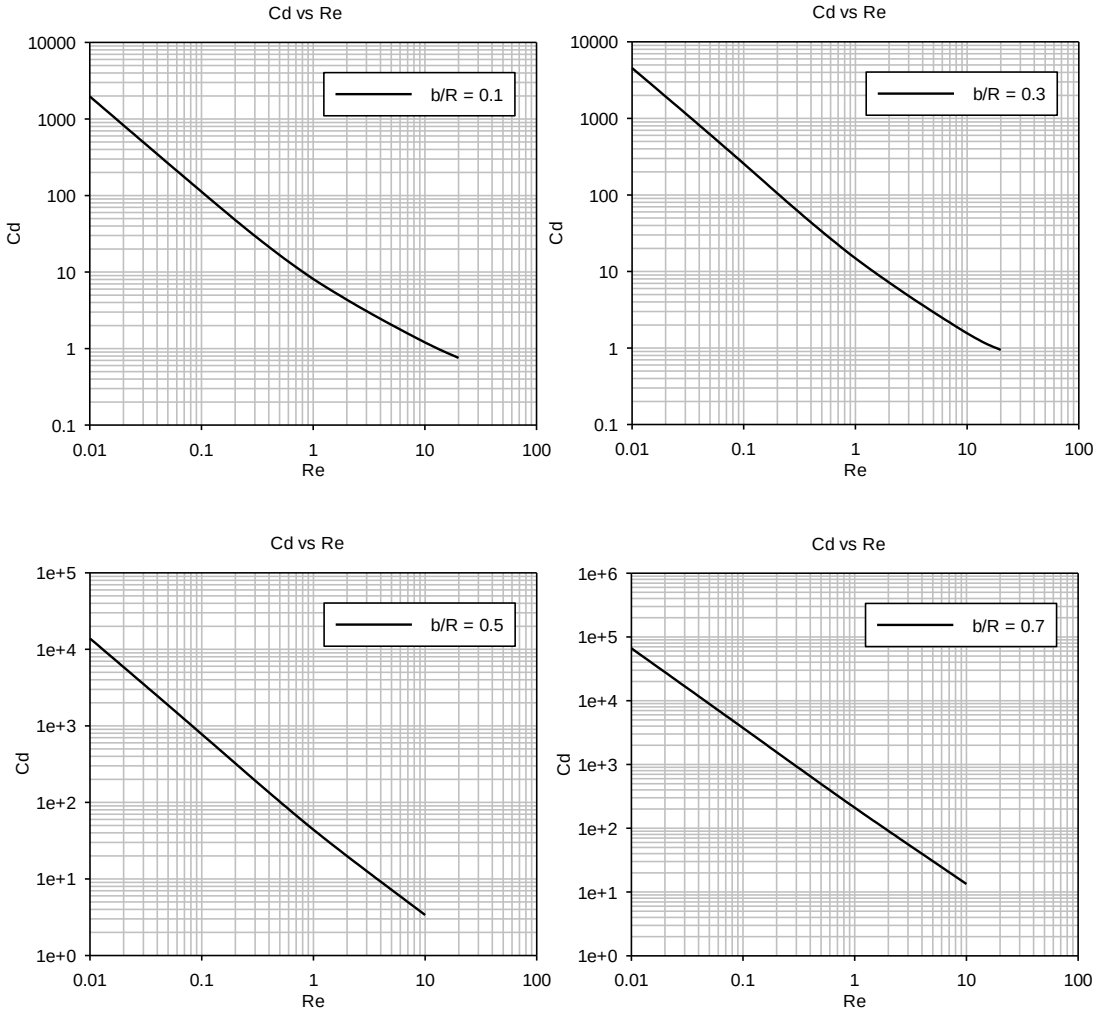

Figure 157: Cd vs Re for Case 4, n = 1.2, Cassini Oval $(c/d)^2 = 0.7$ (individual cases)

7.2.1.3.3 $(c/d)^2 = 0.95$

Table 47: Numerical results for Case 4, n = 1.2, Cassini Oval $(c/d)^2 = 0.95$

	Cd			
Re	**b/R = 0.1**	**b/R = 0.3**	**b/R = 0.5**	**b/R = 0.7**
0.0100	1890.1816	4322.8100	11999.7449	51035.1894
0.1000	106.7895	243.1551	674.8856	2870.1095
1.0000	7.8351	14.2384	38.3222	161.8174
10.0000	1.1847	1.5648	3.2403	11.3485
20.0000	0.7466	0.9845		
40.0000				

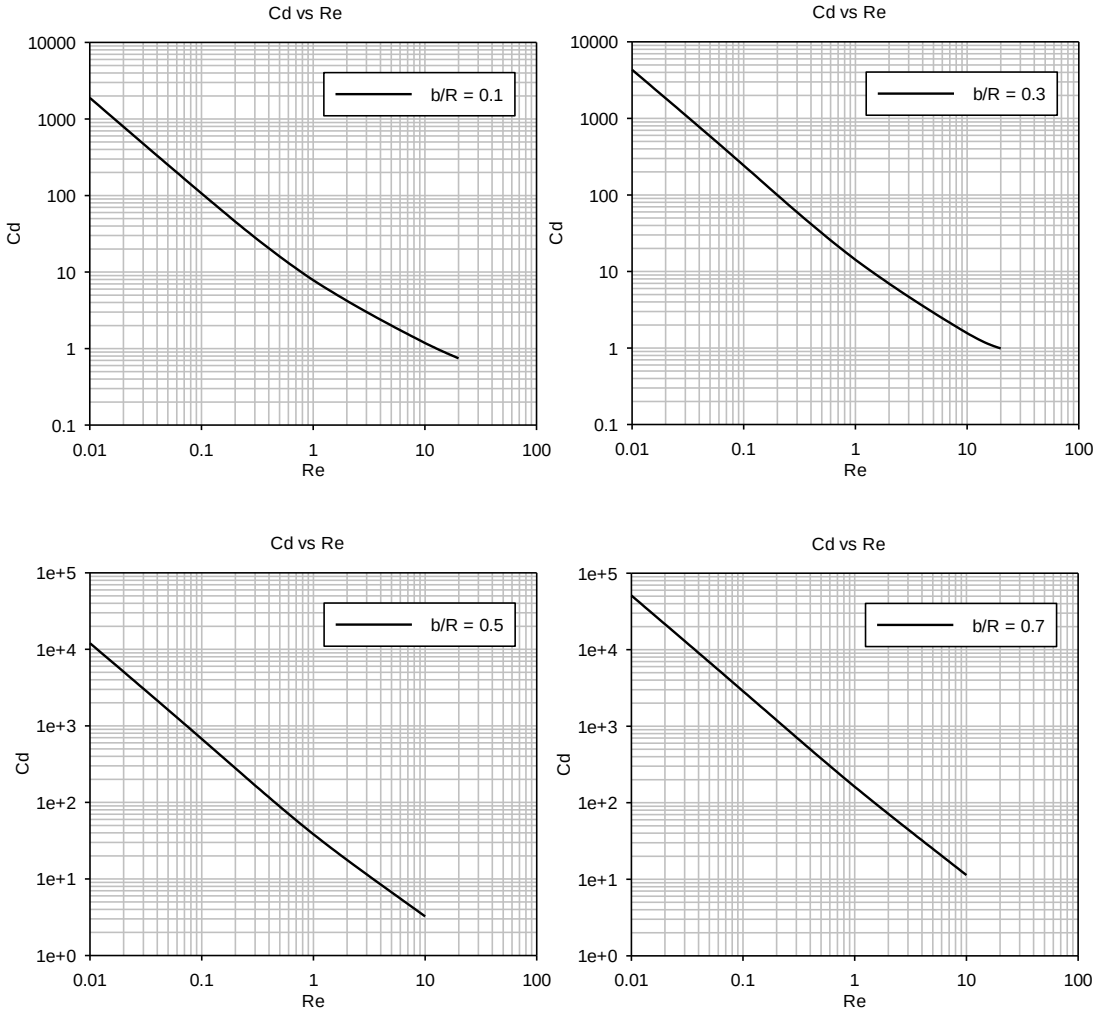

Figure 158: Cd vs Re for Case 4, n = 1.2, Cassini Oval $(c/d)^2 = 0.95$ (individual cases)

7.2.1.4 n = 1.4

7.2.1.4.1 $(c/d)^2 = 0.3$

Table 48: Numerical results for Case 4, n = 1.4, Cassini Oval $(c/d)^2 = 0.3$

	Cd			
Re	**b/R = 0.1**	**b/R = 0.3**	**b/R = 0.5**	**b/R = 0.7**
0.0100	1294.8949	2347.4860	6293.2228	27505.6152
0.1000	30.9895	50.9981	135.7305	592.8191
1.0000	2.2863	2.5283	4.5860	15.3772
10.0000				
20.0000				
40.0000				

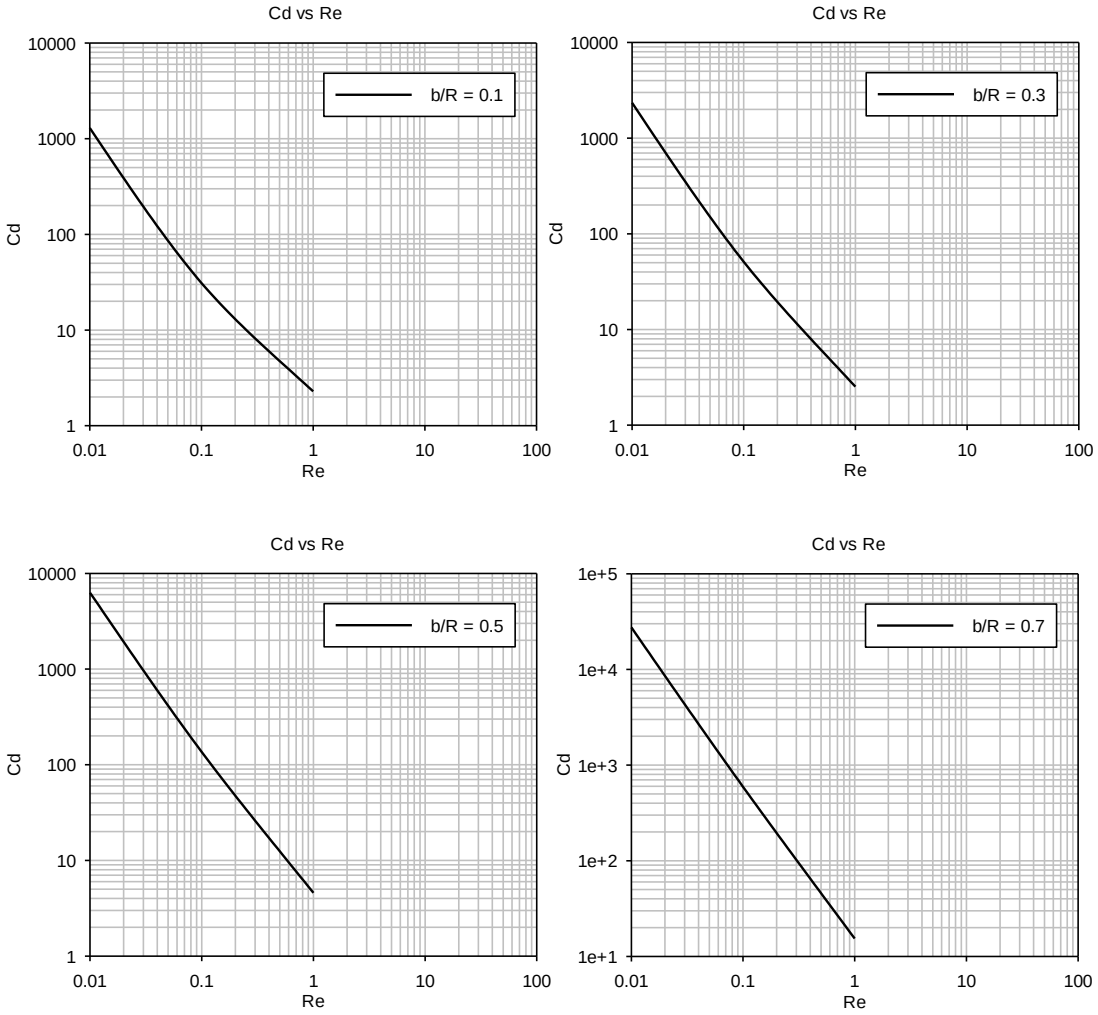

Figure 159: Cd vs Re for Case 4, n = 1.4, Cassini Oval $(c/d)^2 = 0.3$ (individual cases)

7.2.1.4.2 $(c/d)^2 = 0.7$

Table 49: Numerical results for Case 4, n = 1.4, Cassini Oval $(c/d)^2 = 0.7$

	Cd			
Re	**b/R = 0.1**	**b/R = 0.3**	**b/R = 0.5**	**b/R = 0.7**
0.0100	281.6281	644.6465	1956.6258	9387.4414
0.1000	7.8935	14.3481	42.4274	202.6622
1.0000	0.7095	0.8808		
10.0000				
20.0000				
40.0000				

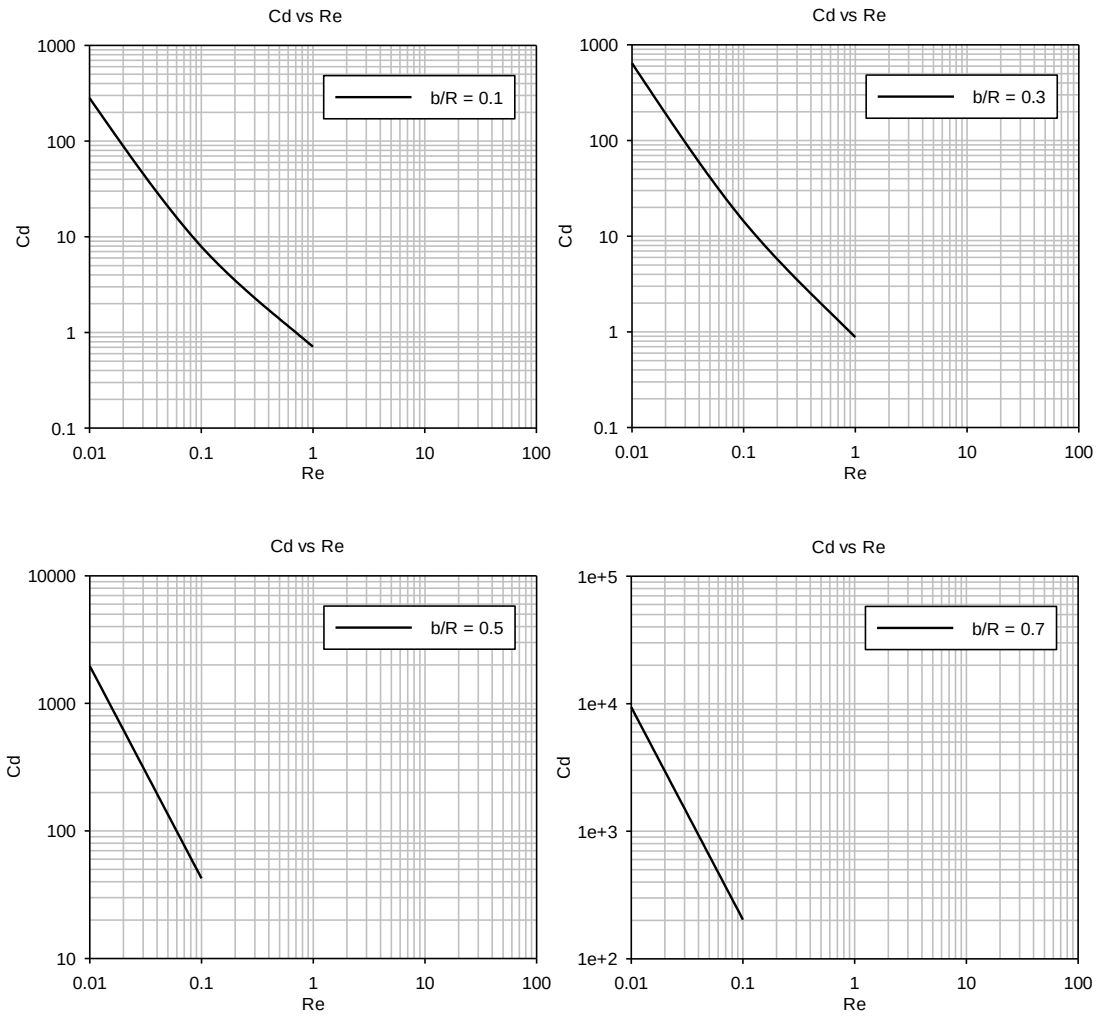

Figure 160: Cd vs Re for Case 4, n = 1.4, Cassini Oval $(c/d)^2 = 0.7$ (individual cases)

7.2.1.4.3 $(c/d)^2 = 0.95$

Table 50: Numerical results for Case 4, n = 1.4, Cassini Oval $(c/d)^2 = 0.95$

	Cd			
Re	**b/R = 0.1**	**b/R = 0.3**	**b/R = 0.5**	**b/R = 0.7**
0.0100	207.7503	474.2009	1316.2942	5598.0528
0.1000	6.2832	10.8690	28.8178	121.1098
1.0000				
10.0000				
20.0000				
40.0000				

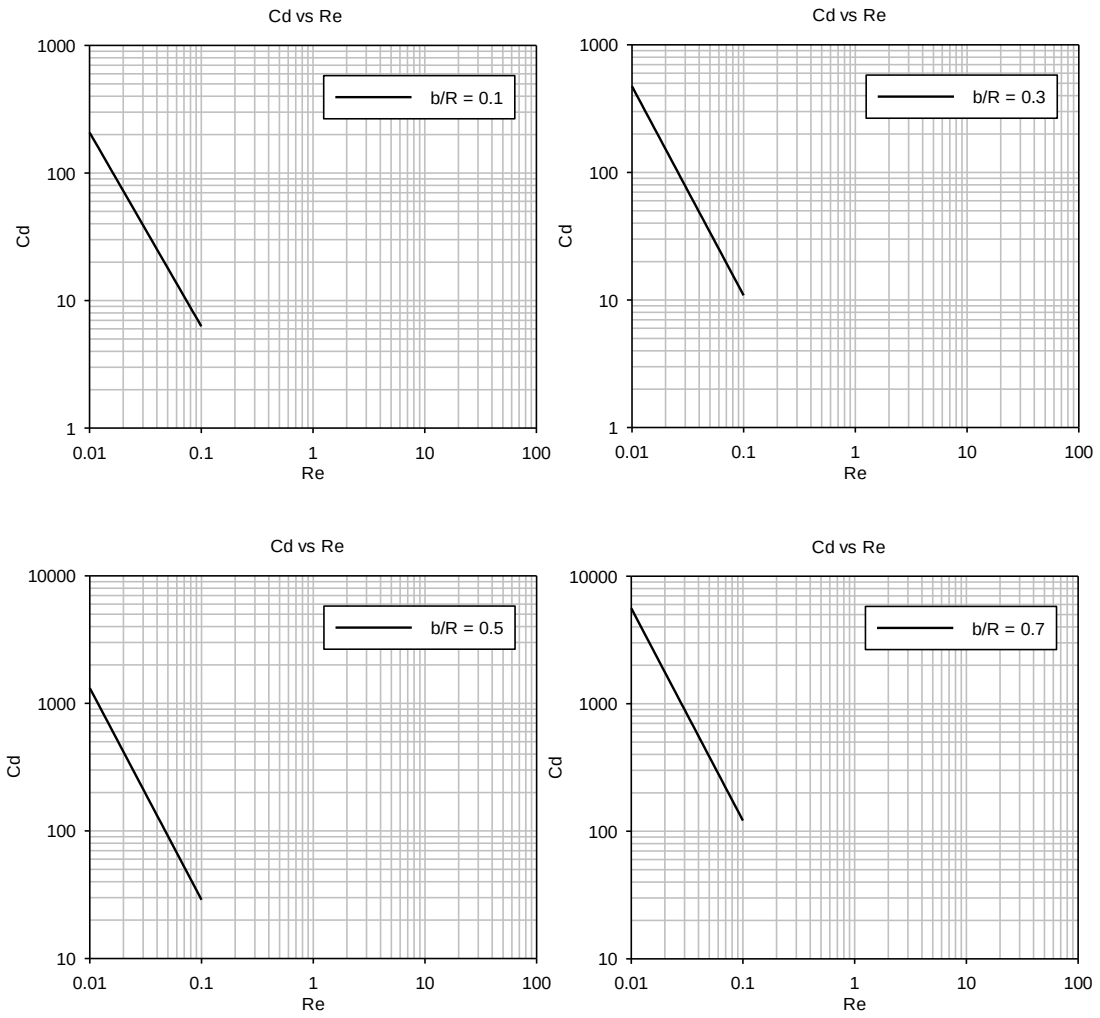

Figure 161: Cd vs Re for Case 4, n = 1.4, Cassini Oval $(c/d)^2 = 0.95$ (individual cases)

7.2.2 Effect of Confinement Ratio

The effect of confinement ratio also follow the same trend as all previous cases. This can be seen in figures 162-173.

7.2.2.1 n = 0.6

7.2.2.1.1 $(c/d)^2 = 0.3$

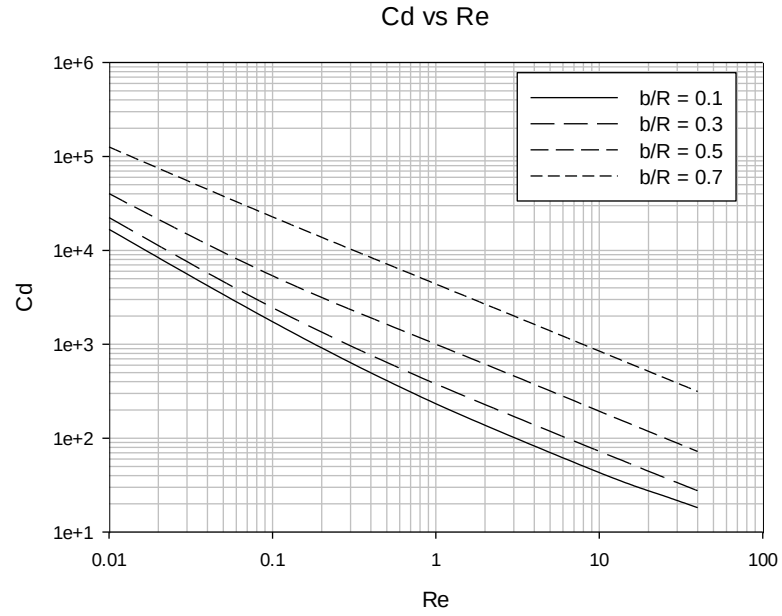

Figure 162: Cd vs Re for different confinement ratios, Case 4, n = 0.6, Cassini Oval $(c/d)^2 = 0.1$

7.2.2.1.2 $(c/d)^2 = 0.7$

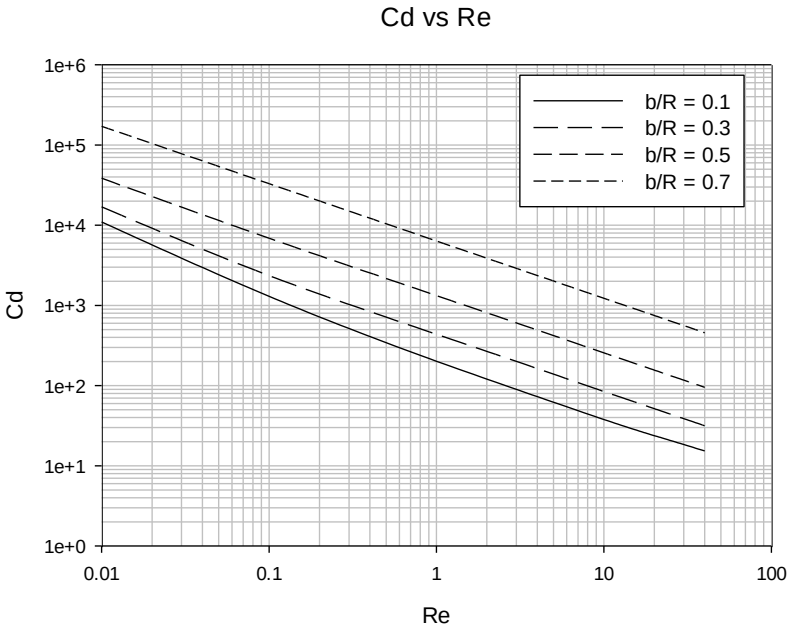

Figure 163: Cd vs Re for different confinement ratios, Case 4, n = 0.6, Cassini Oval $(c/d)^2 = 0.7$

7.2.2.1.3 $(c/d)^2 = 0.95$

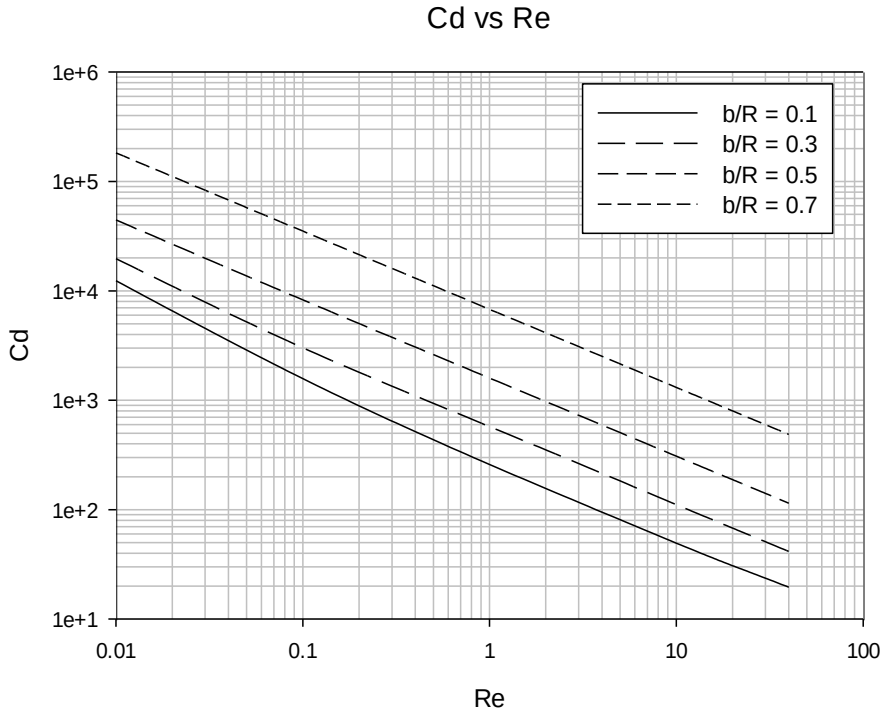

Figure 164: Cd vs Re for different confinement ratios, Case 4, n = 0.6, Cassini Oval $(c/d)^2 = 0.95$

7.2.2.2 n = 0.8

7.2.2.2.1 $(c/d)^2 = 0.3$

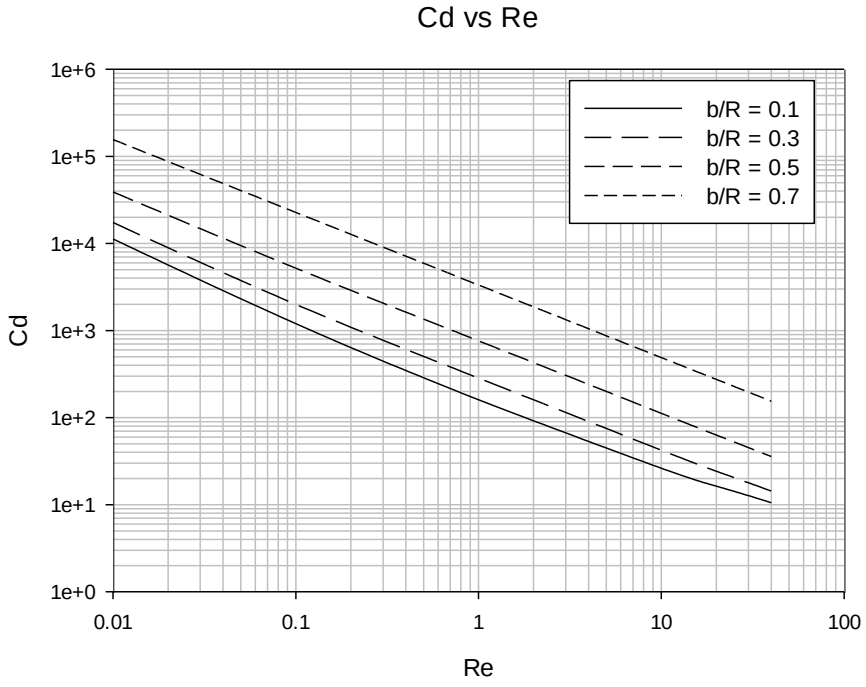

Figure 165: Cd vs Re for different confinement ratios, Case 4, n = 0.8, Cassini Oval $(c/d)^2 = 0.3$

7.2.2.2.2 $(c/d)^2 = 0.7$

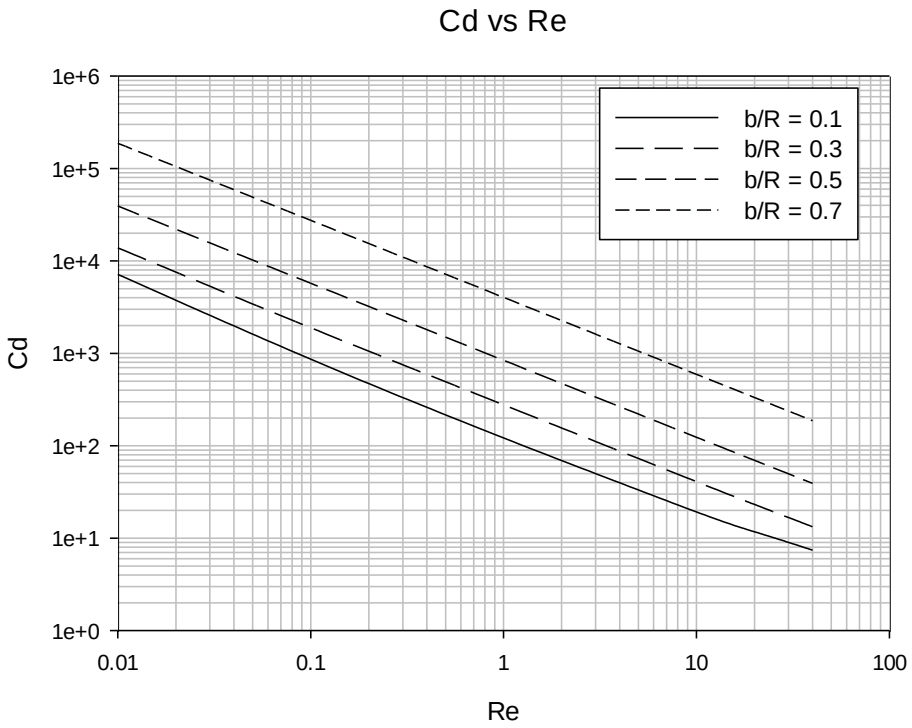

Figure 166: Cd vs Re for different confinement ratios, Case 4, n = 0.8, Cassini Oval $(c/d)^2 = 0.7$

7.2.2.2.3 $(c/d)^2 = 0.95$

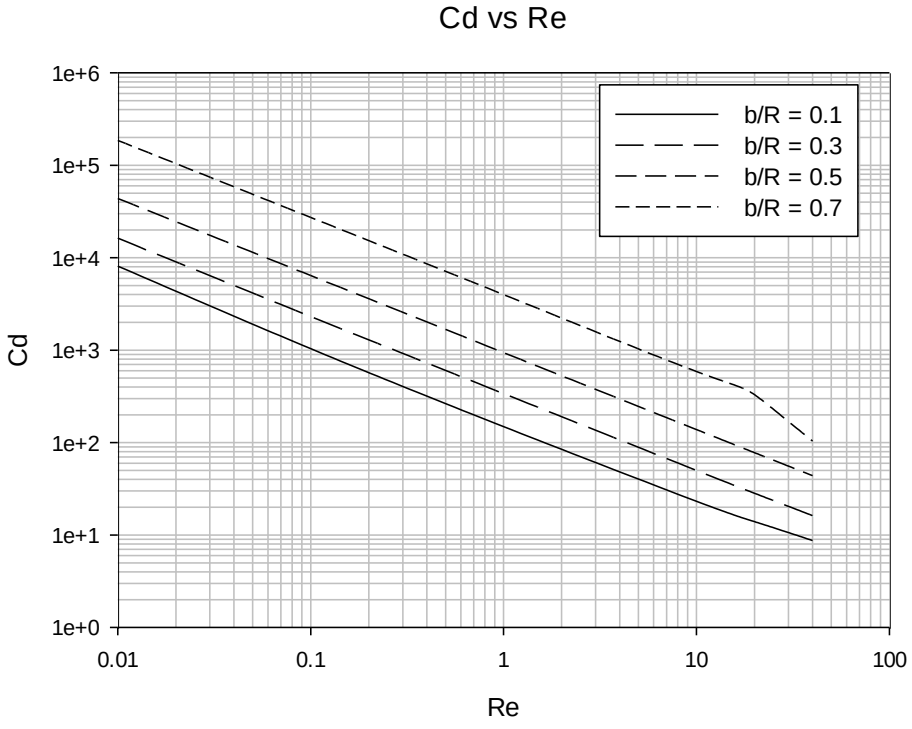

Figure 167: Cd vs Re for different confinement ratios, Case 4, n = 0.8, Cassini Oval $(c/d)^2 = 0.95$

7.2.2.3.n = 1.2

7.2.2.3.1 $(c/d)^2 = 0.3$

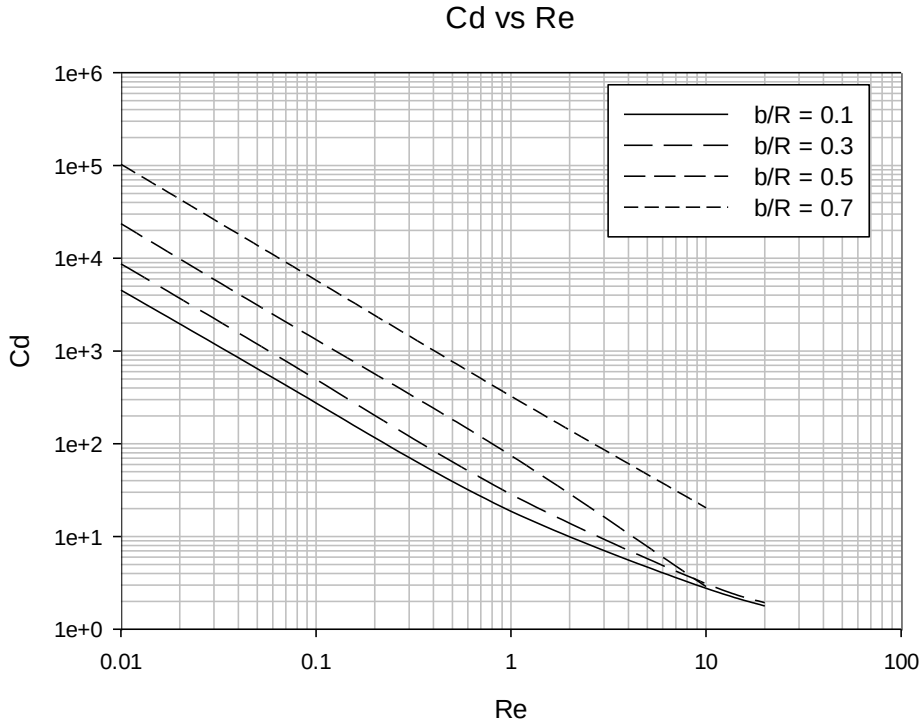

Figure 168: Cd vs Re for different confinement ratios, Case 4, n = 1.2, Cassini Oval $(c/d)^2 = 0.3$

7.2.2.3.2 $(c/d)^2 = 0.7$

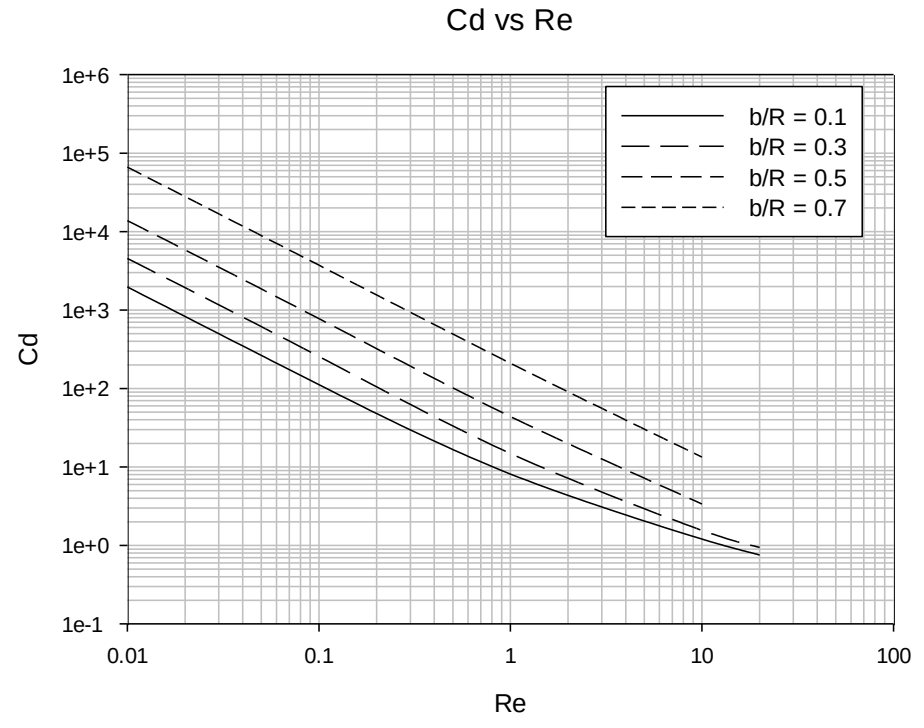

Figure 169: Cd vs Re for different confinement ratios, Case 4, n = 1.2, Cassini Oval $(c/d)^2 = 0.7$

7.2.2.3.3 $(c/d)^2 = 0.95$

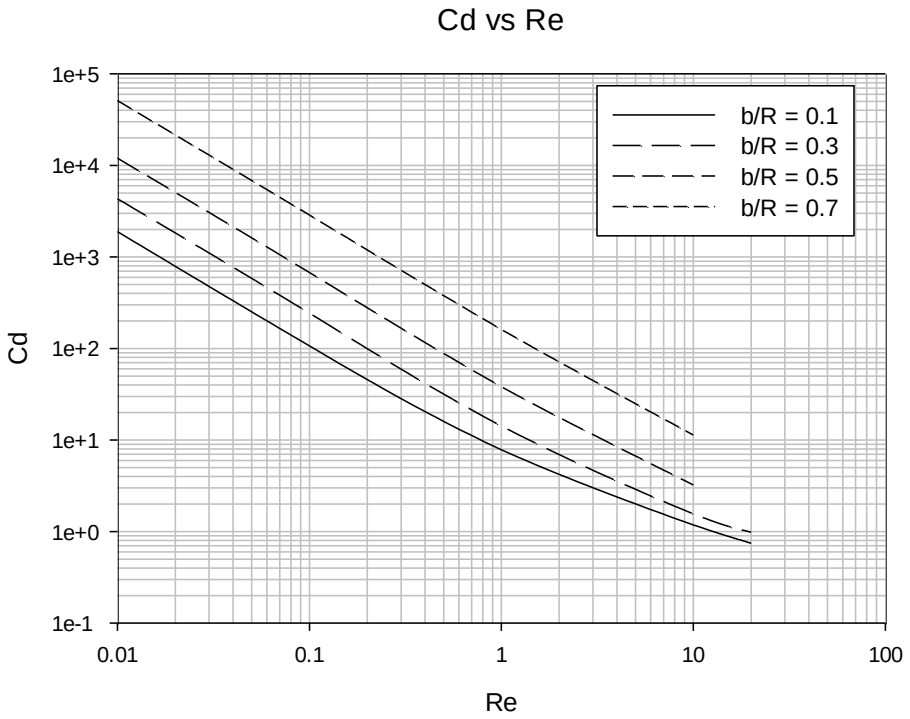

Figure 170: Cd vs Re for different confinement ratios, Case 4, n = 1.2, Cassini Oval $(c/d)^2 = 0.95$

7.2.2.4 n = 1.4

7.2.2.4.1 $(c/d)^2 = 0.3$

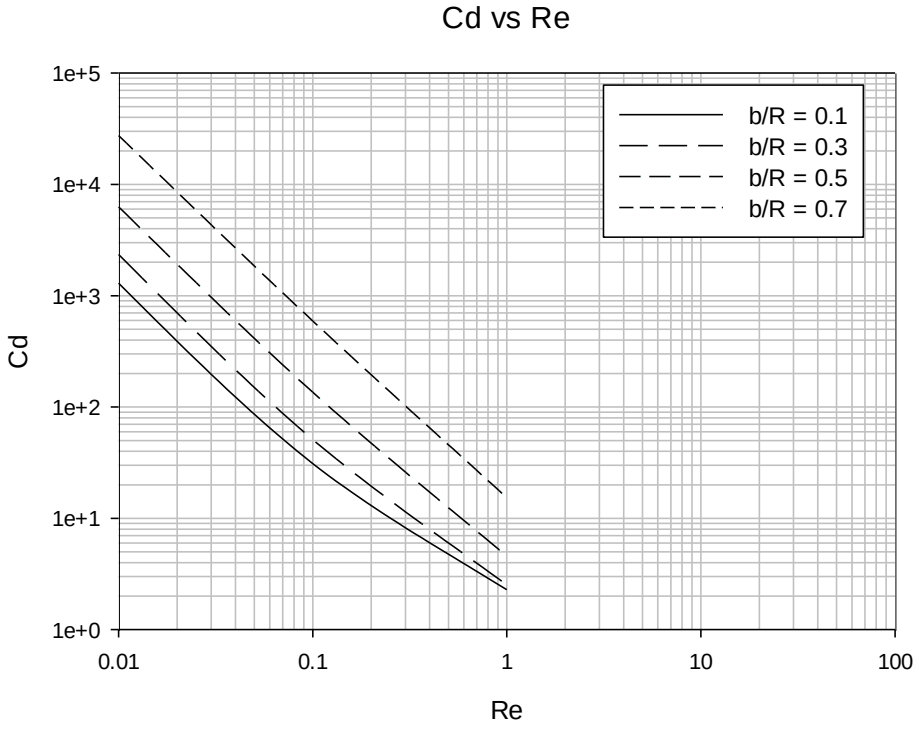

Figure 171: Cd vs Re for different confinement ratios, Case 4, n = 1.4, Cassini Oval $(c/d)^2 = 0.3$

7.2.2.4.2 $(c/d)^2 = 0.7$

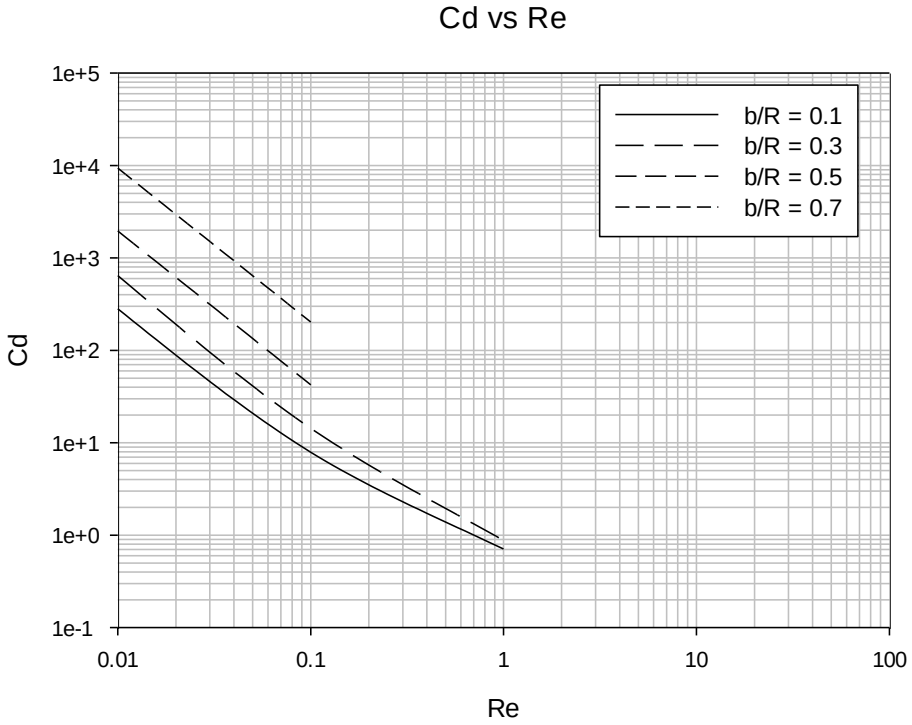

Figure 172: Cd vs Re for different confinement ratios, Case 4, n = 1.4, Cassini Oval $(c/d)^2 = 0.7$

7.2.2.4.3 $(c/d)^2 = 0.95$

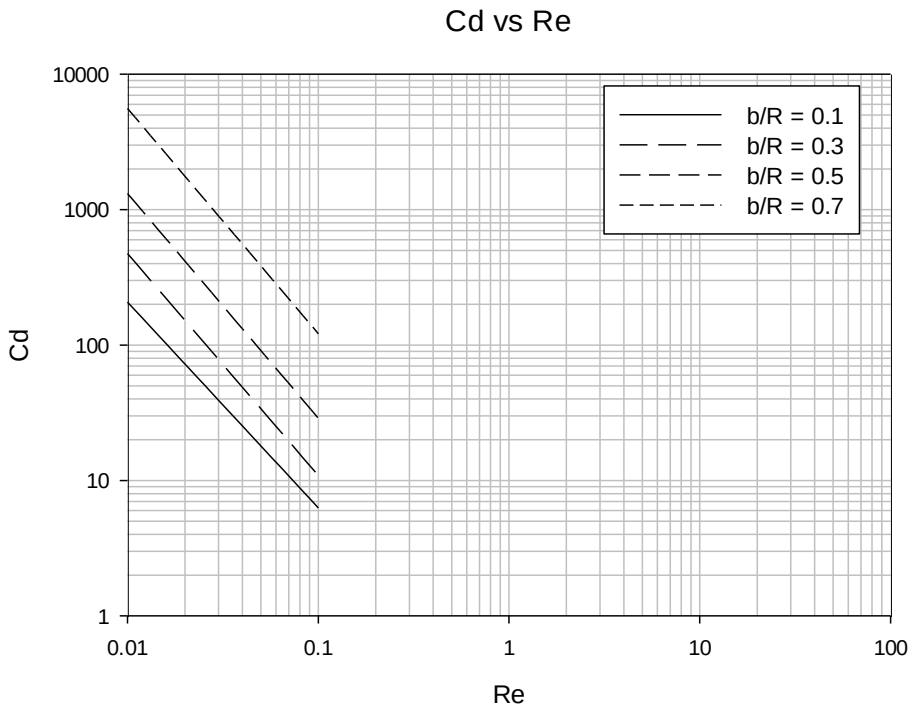

Figure 173: Cd vs Re for different confinement ratios, Case 4, n = 1.4, Cassini Oval $(c/d)^2 = 0.95$

7.2.3 Effect of Particle Shape

7.2.3.1 n = 0.6

7.2.3.1.1 b/R = 0.1

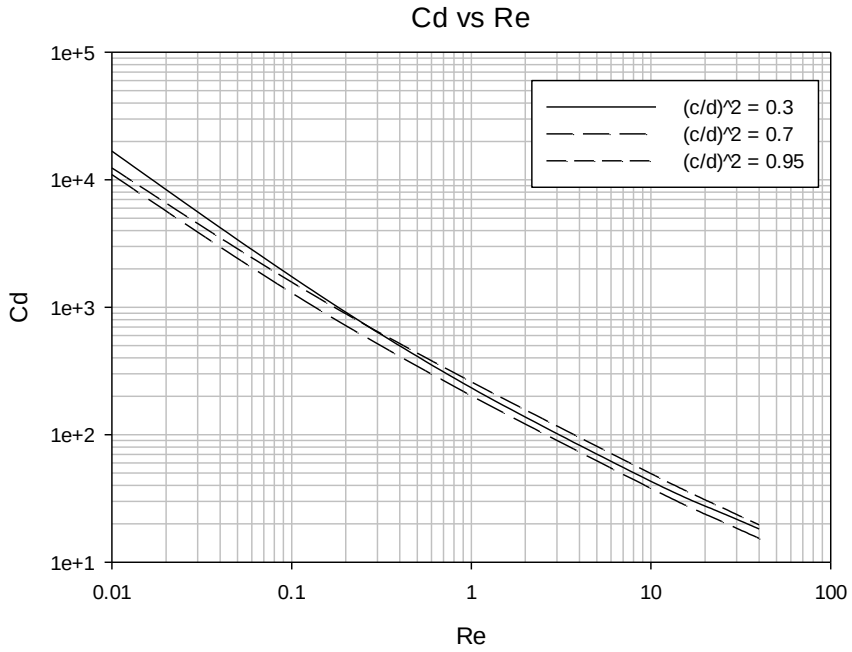

Figure 174: Cd vs Re for different shape factors, Case 4, n = 0.6, Cassini Oval, b/R = 0.1

7.2.3.1.2 b/R = 0.3

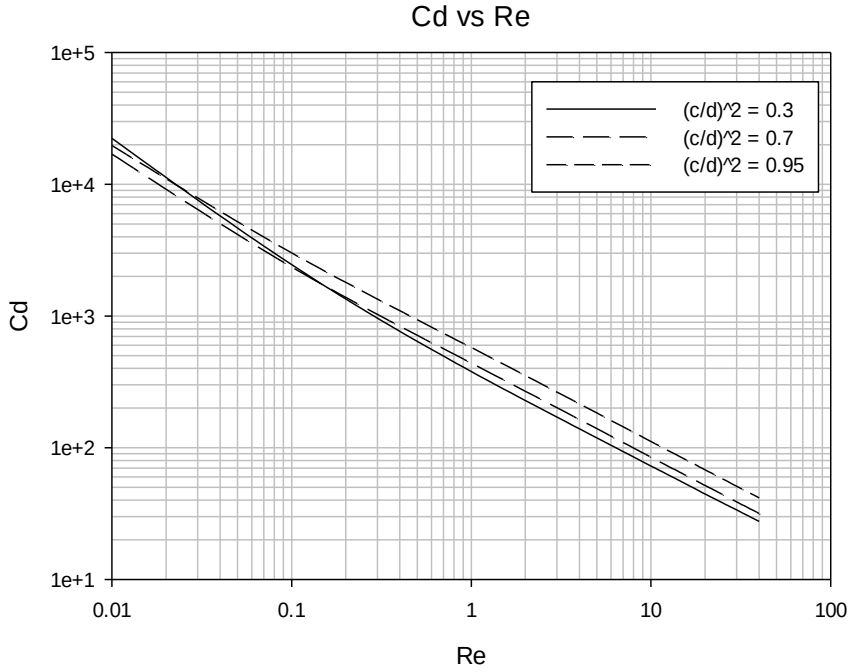

Figure 175: Cd vs Re for different shape factors, Case 4, n = 0.6, Cassini Oval, b/R = 0.3

7.2.3.1.3 b/R = 0.5

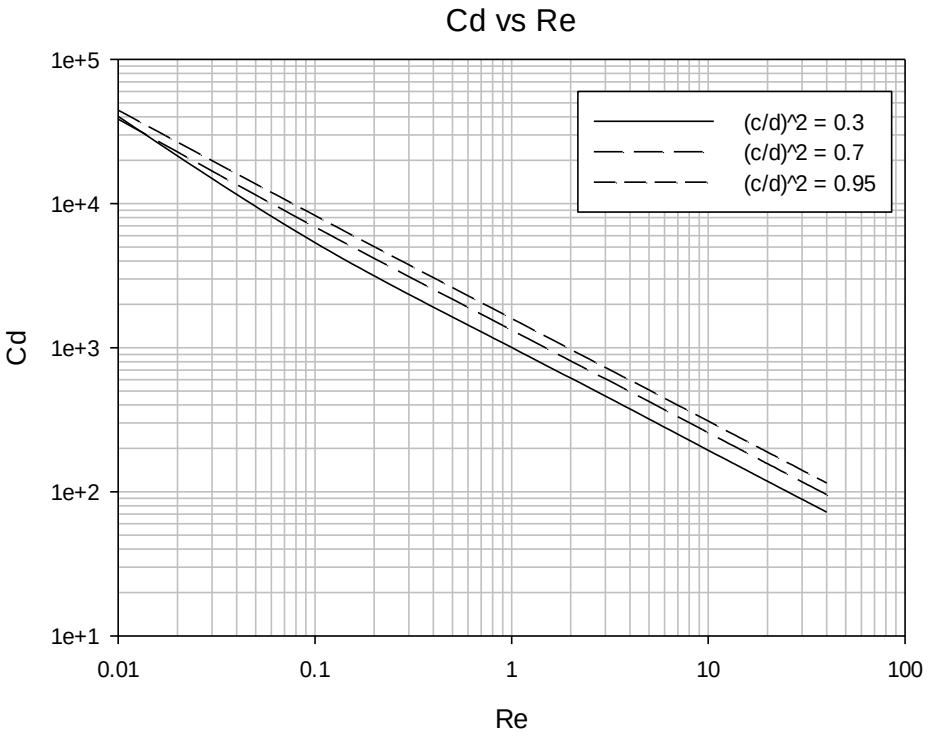

Figure 176: Cd vs Re for different shape factors, Case 4, n = 0.6, Cassini Oval, b/R = 0.5

7.2.3.1.4 b/R = 0.7

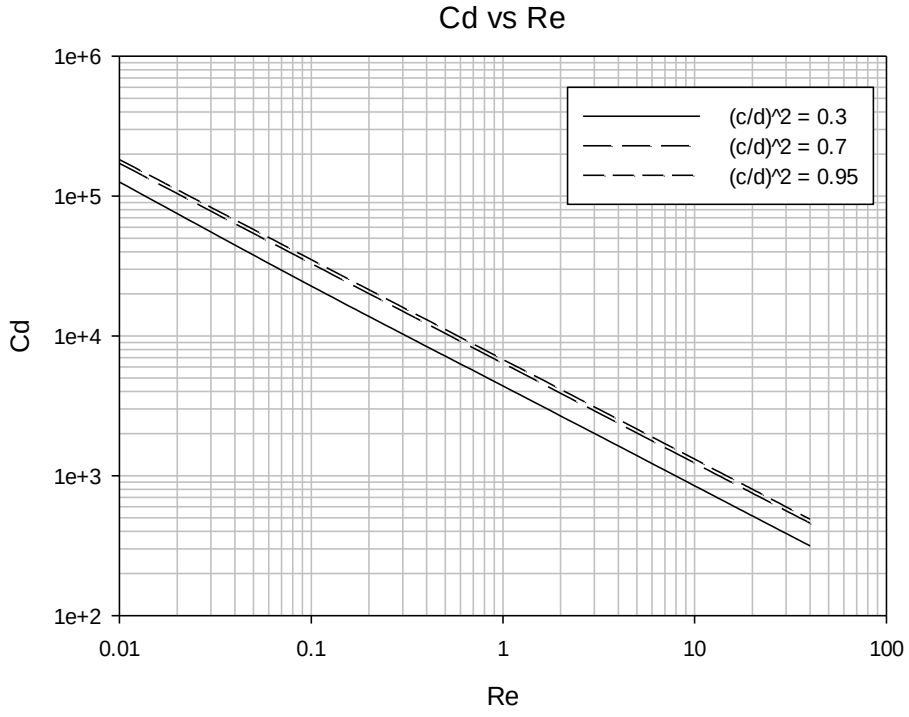

Figure 177: Cd vs Re for different shape factors, Case 4, n = 0.6, Cassini Oval, b/R = 0.7

7.2.3.2 n = 0.8

7.2.3.2.1 b/R = 0.1

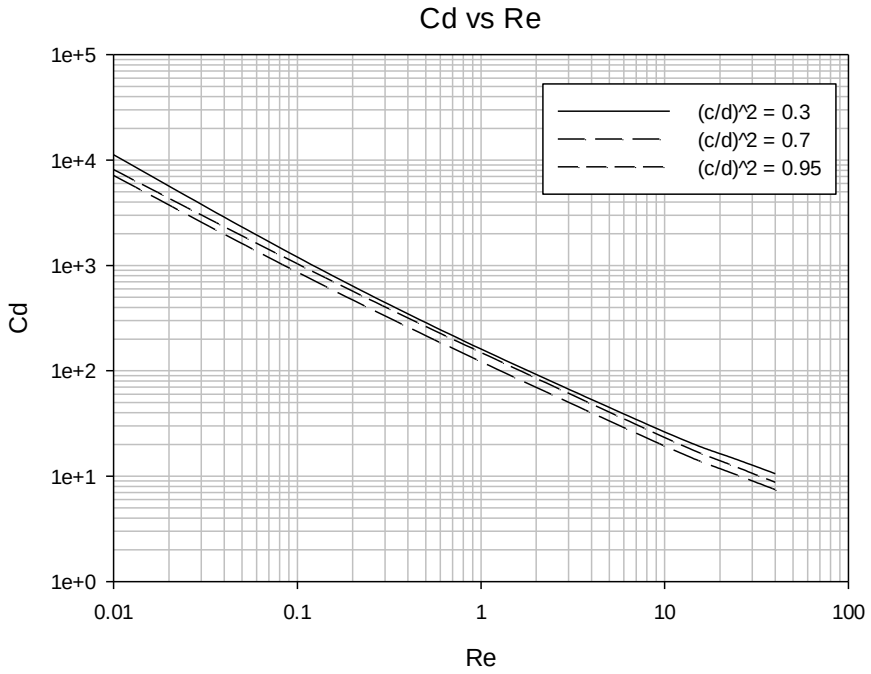

Figure 178: Cd vs Re for different shape factors, Case 4, n = 0.8, Cassini Oval, b/R = 0.1

7.2.3.2.2 b/R = 0.3

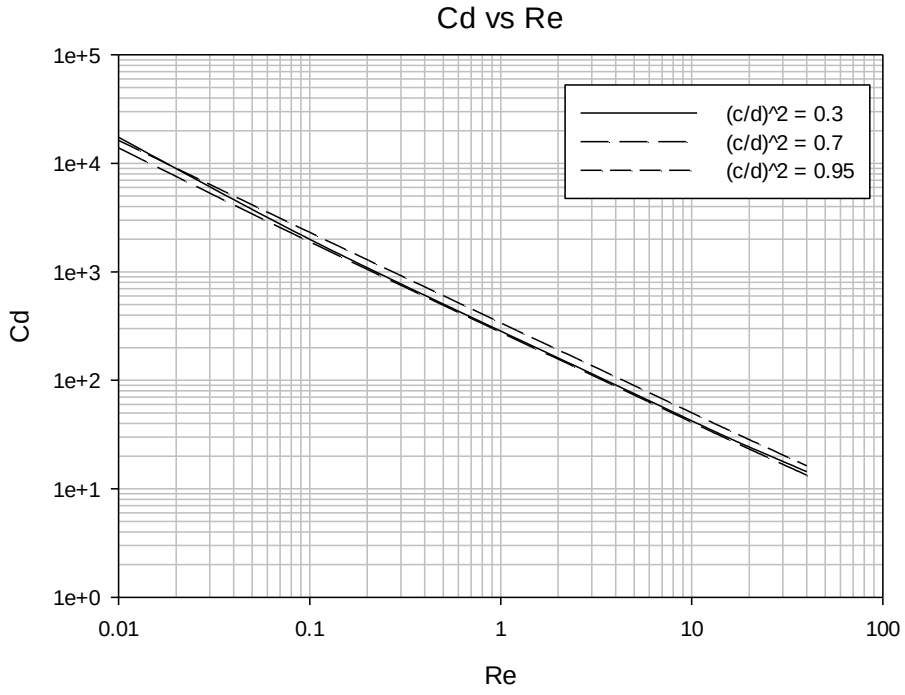

Figure 179: Cd vs Re for different shape factors, Case 4, n = 0.8, Cassini Oval, b/R = 0.3

7.2.3.2.3 b/R = 0.5

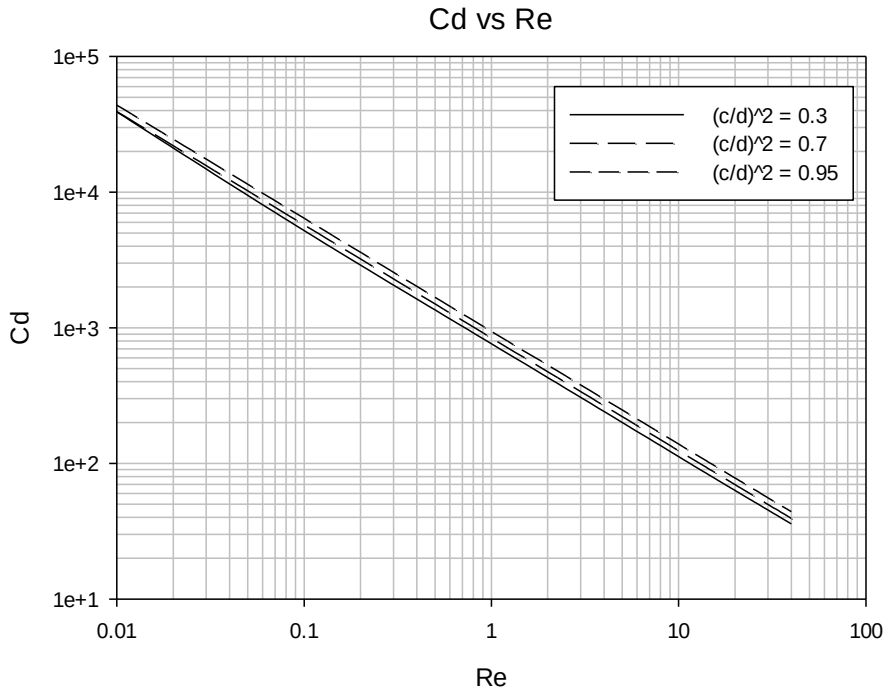

Figure 180: Cd vs Re for different shape factors, Case 4, n = 0.8, Cassini Oval, b/R = 0.5

7.2.3.2.4 b/R = 0.7

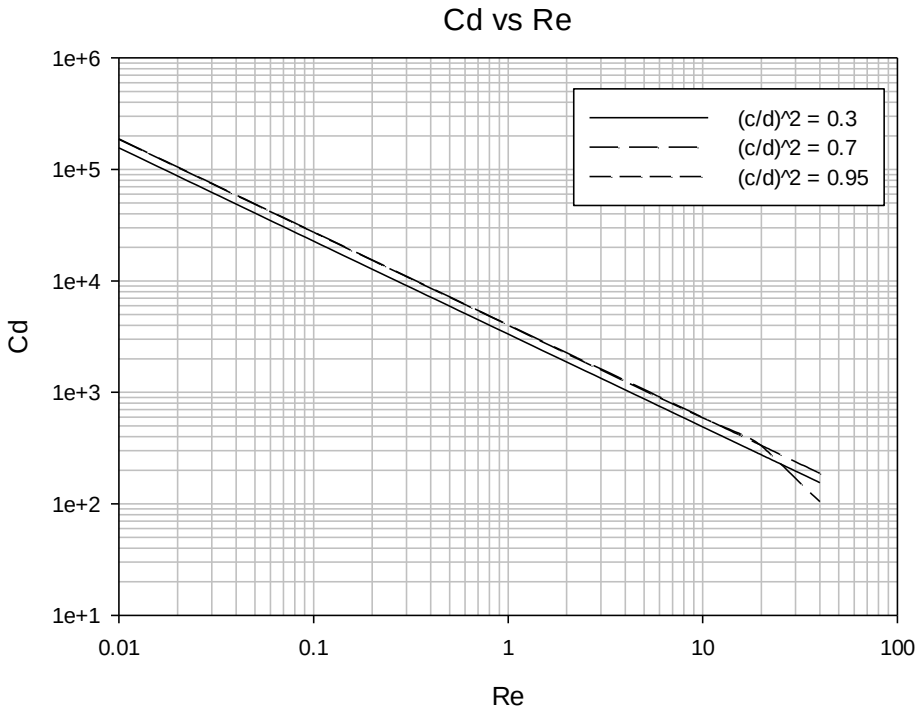

Figure 181: Cd vs Re for different shape factors, Case 4, n = 0.8, Cassini Oval, b/R = 0.7

7.2.3.3 n = 1.2

7.2.3.3.1 b/R = 0.1

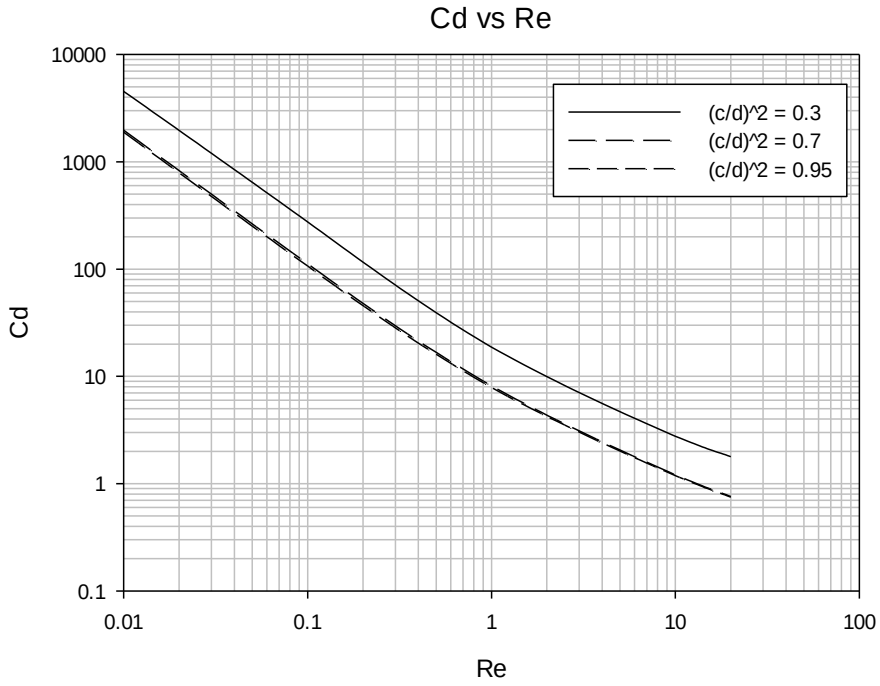

Figure 182: Cd vs Re for different shape factors, Case 4, n = 1.2, Cassini Oval, b/R = 0.1

7.2.3.3.2 b/R = 0.3

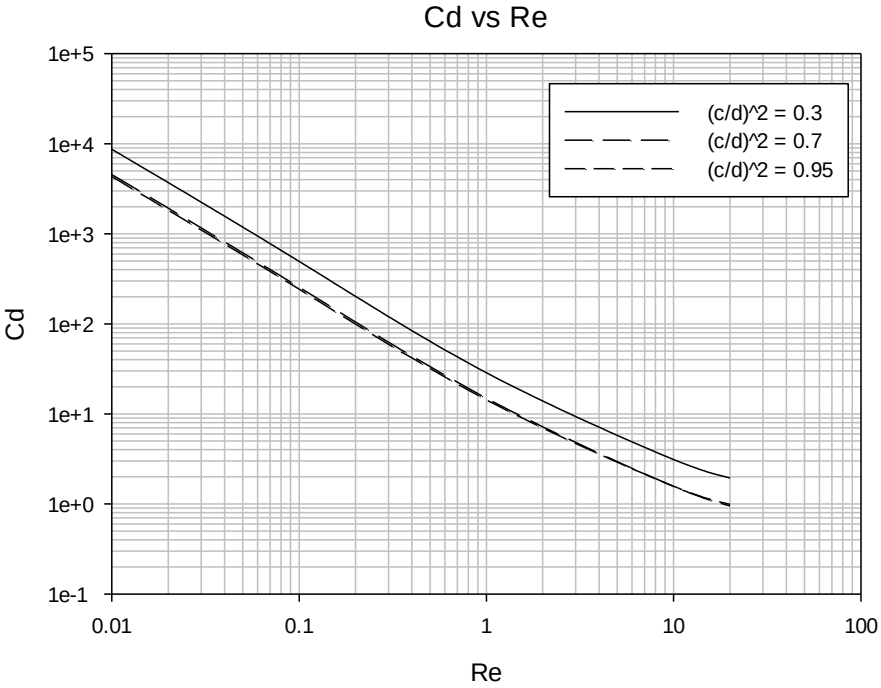

Figure 183: Cd vs Re for different shape factors, Case 4, n = 1.2, Cassini Oval, b/R = 0.3

7.2.3.3.3 b/R = 0.5

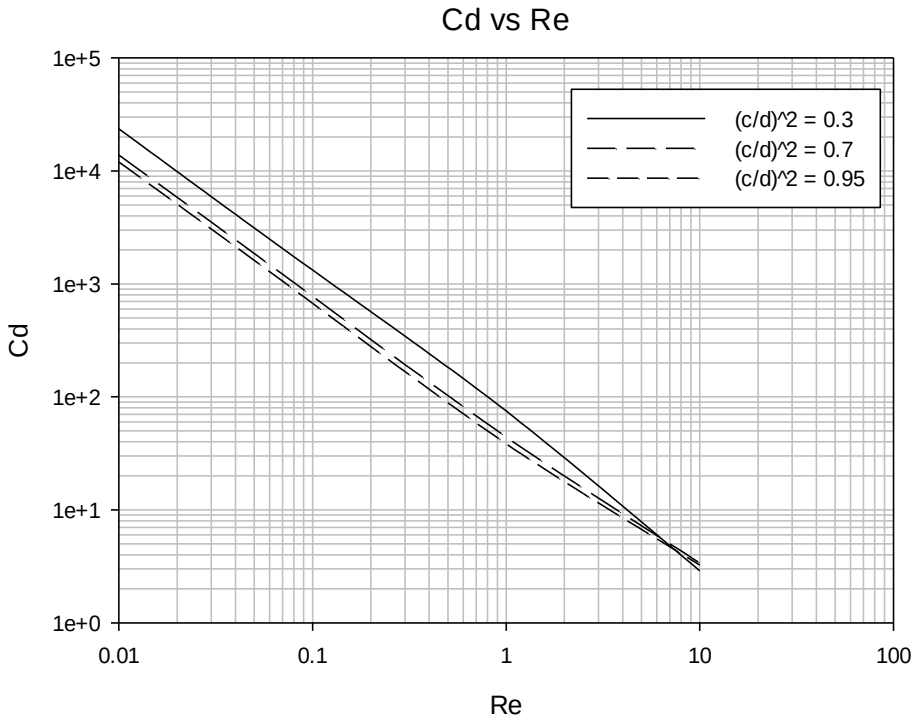

Figure 184: Cd vs Re for different shape factors, Case 4, n = 1.2, Cassini Oval, b/R = 0.5

7.2.3.3.4 b/R = 0.7

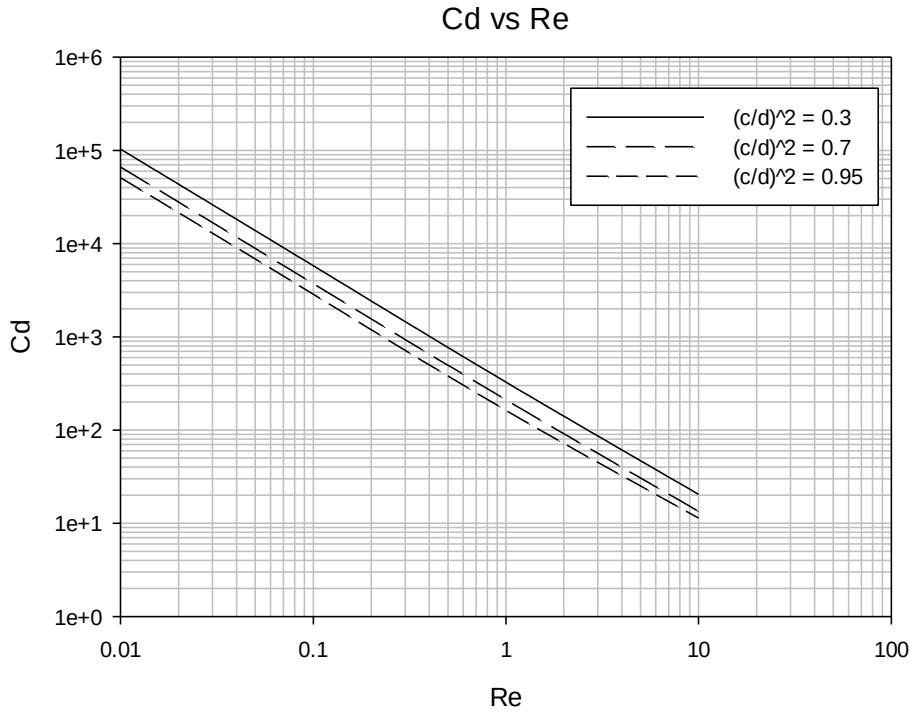

Figure 185: Cd vs Re for different shape factors, Case 4, n = 1.2, Cassini Oval, b/R = 0.7

7.2.3.4 n = 1.4

7.2.3.4.1 b/R = 0.1

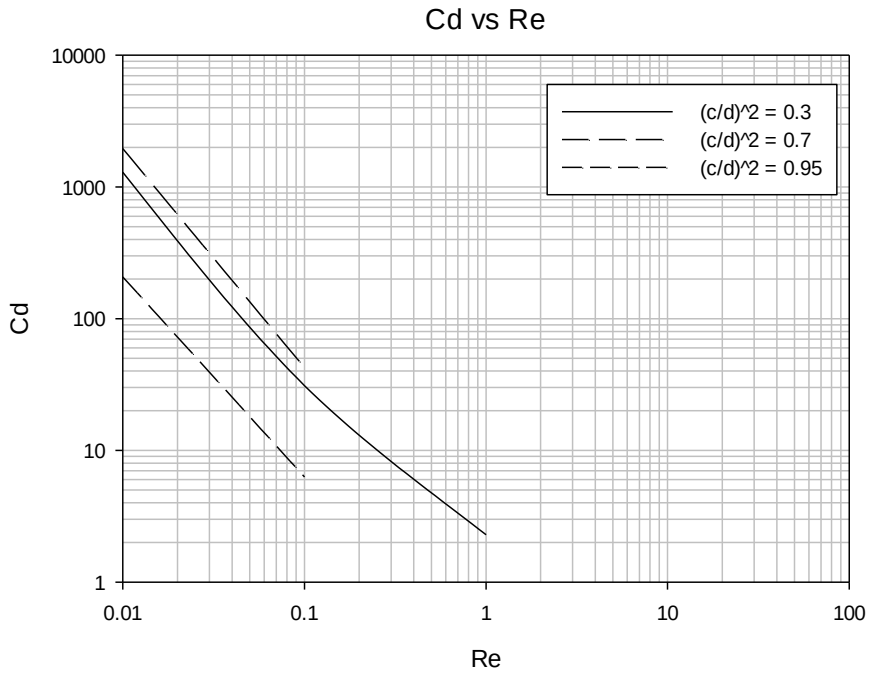

Figure 186: Cd vs Re for different shape factors, Case 4, n = 1.4, Cassini Oval, b/R = 0.1

7.2.3.4.2 b/R = 0.3

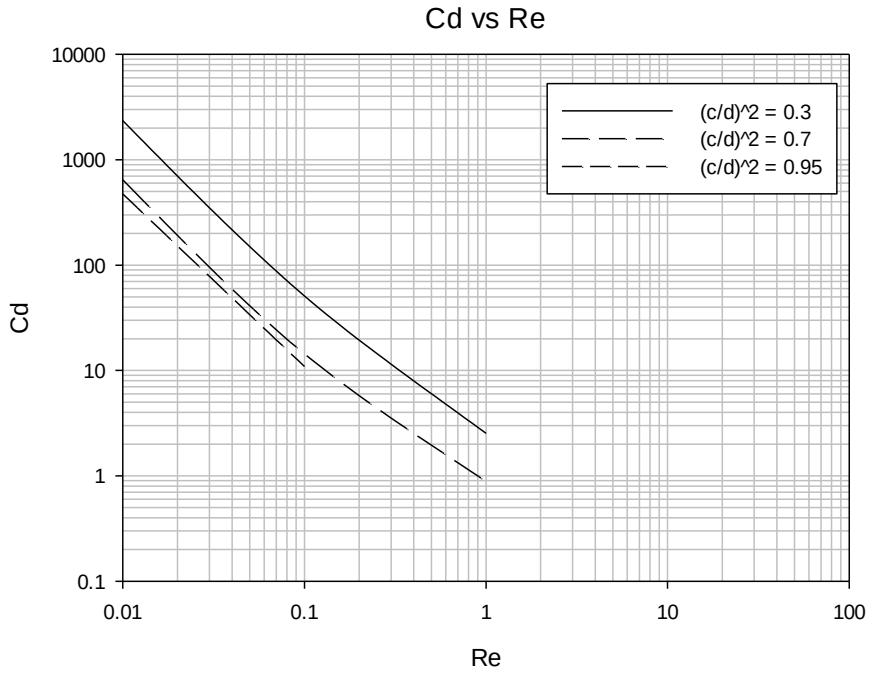

Figure 187: Cd vs Re for different shape factors, Case 4, n = 1.4, Cassini Oval, b/R = 0.3

7.2.3.4.3 b/R = 0.5

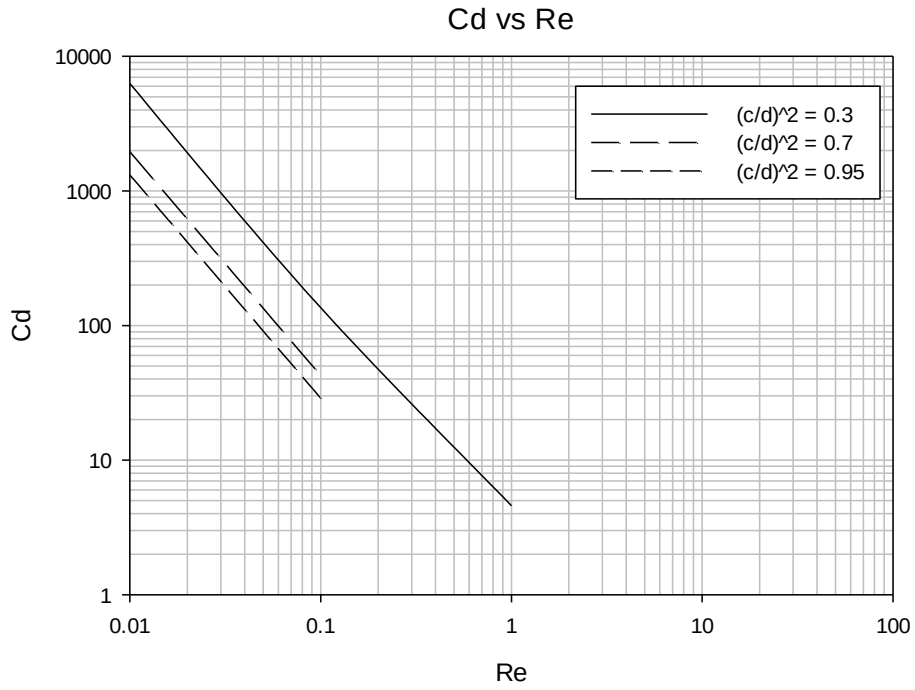

Figure 188: Cd vs Re for different shape factors, Case 4, n = 1.4, Cassini Oval, b/R = 0.5

7.2.3.4.4 b/R = 0.7

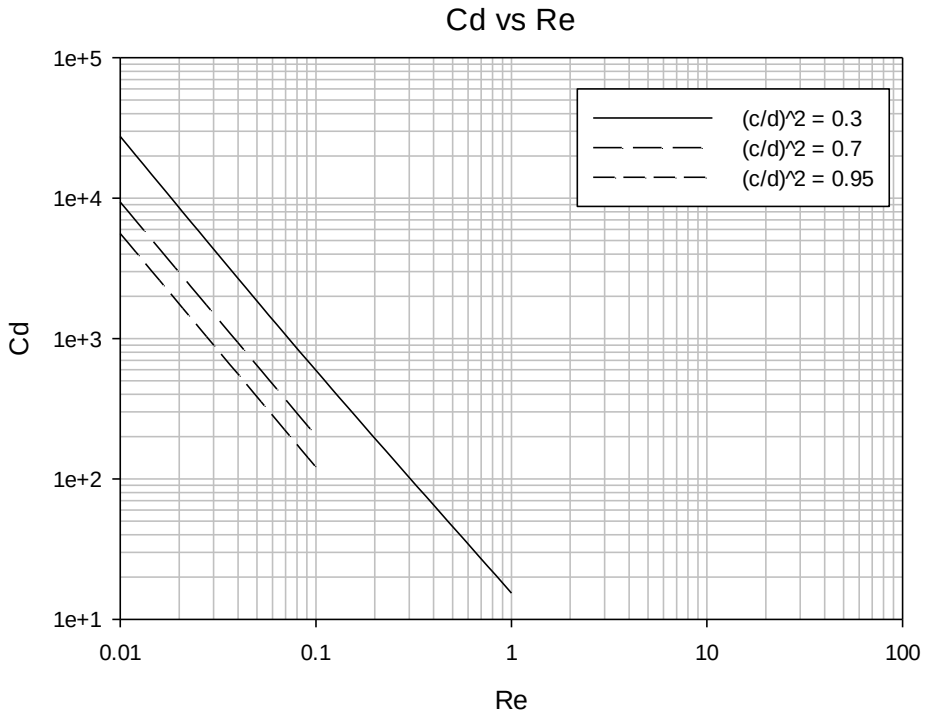

Figure 189: Cd vs Re for different shape factors, Case 4, n = 1.4, Cassini Oval, b/R = 0.7

7.2.4 Effect of Power-Law Index

Similar to spheroids, Cd decreases with increase in power law index value n.

7.2.4.1 $(c/d)^2 = 0.3$

7.2.4.1.1 b/R = 0.1

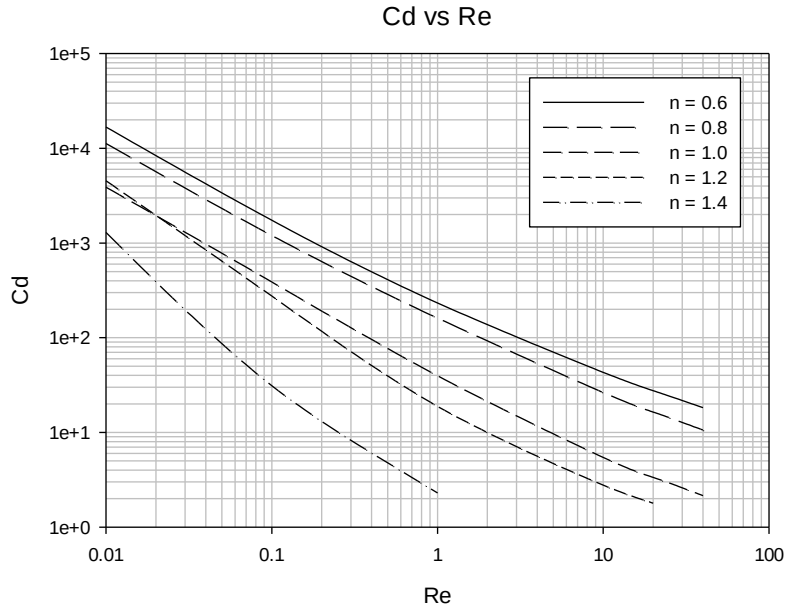

Figure 190: Cd vs Re for different power law values. Case 4, Cassini Oval, $(c/d)^2 = 0.3$, b/R = 0.1

7.2.4.1.2 b/R = 0.3

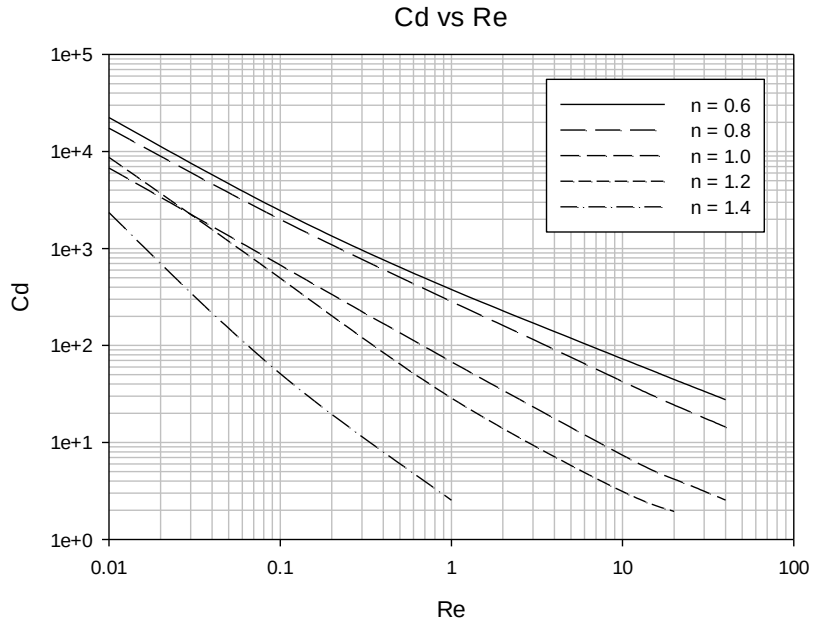

Figure 191: Cd vs Re for different power law values. Case 4, Cassini Oval, (c/d)2 = 0.3, b/R = 0.3

7.2.4.1.3 b/R = 0.5

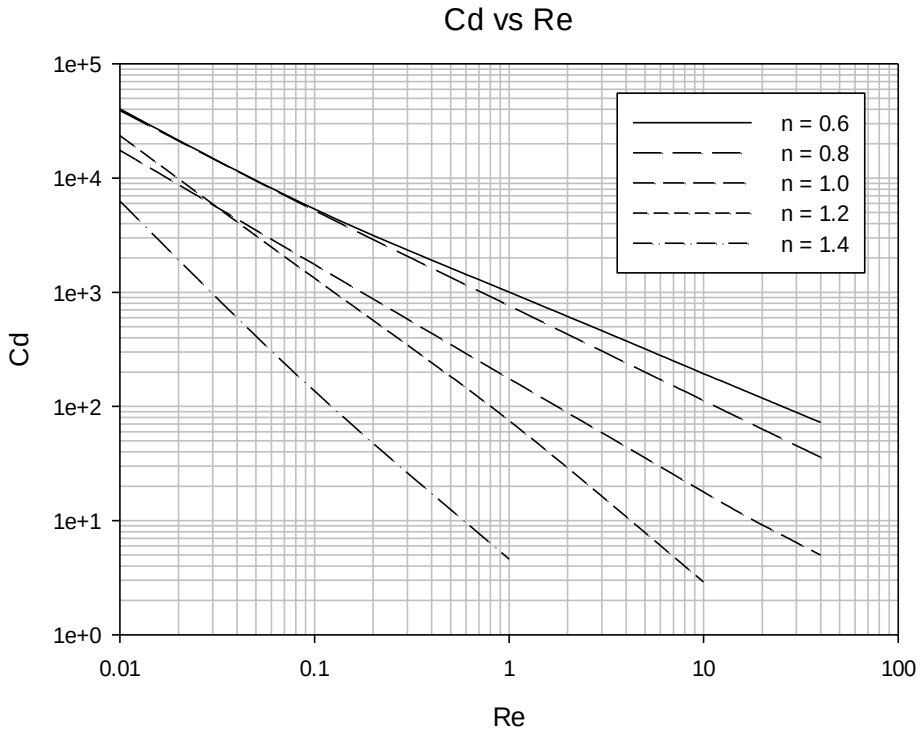

Figure 192: Cd vs Re for different power law values. Case 4, Cassini Oval, (c/d)2 = 0.3, b/R = 0.5

7.2.4.1.4 b/R = 0.7

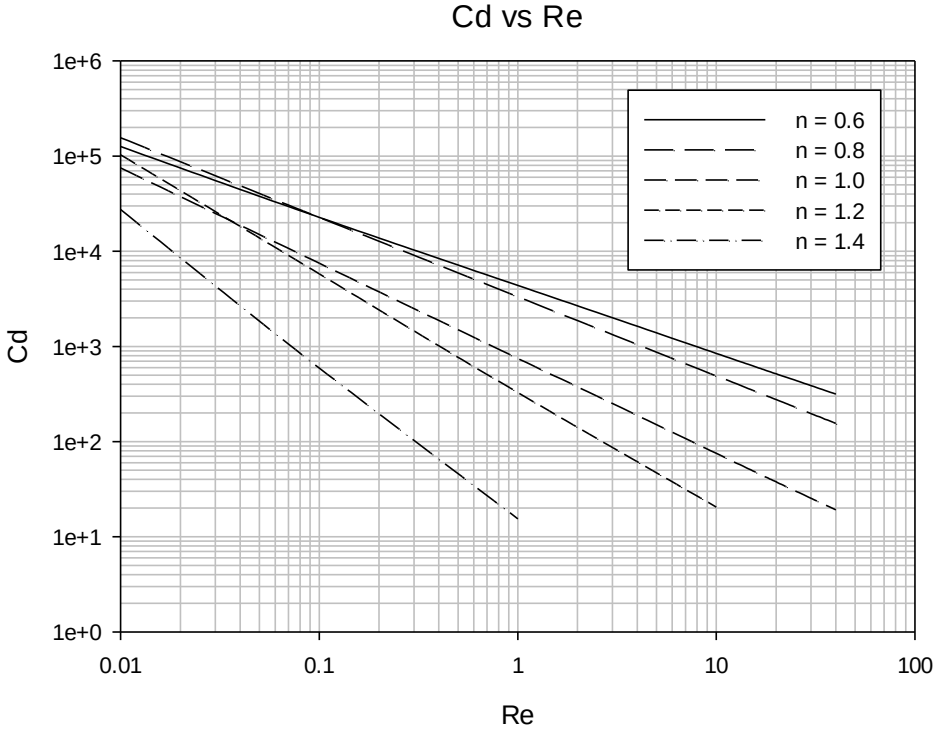

Figure 193: Cd vs Re for different power law values. Case 4, Cassini Oval, (c/d)2 = 0.3, b/R = 0.7

7.2.4.2 $(c/d)^2 = 0.7$

7.2.4.2.1 b/R = 0.1

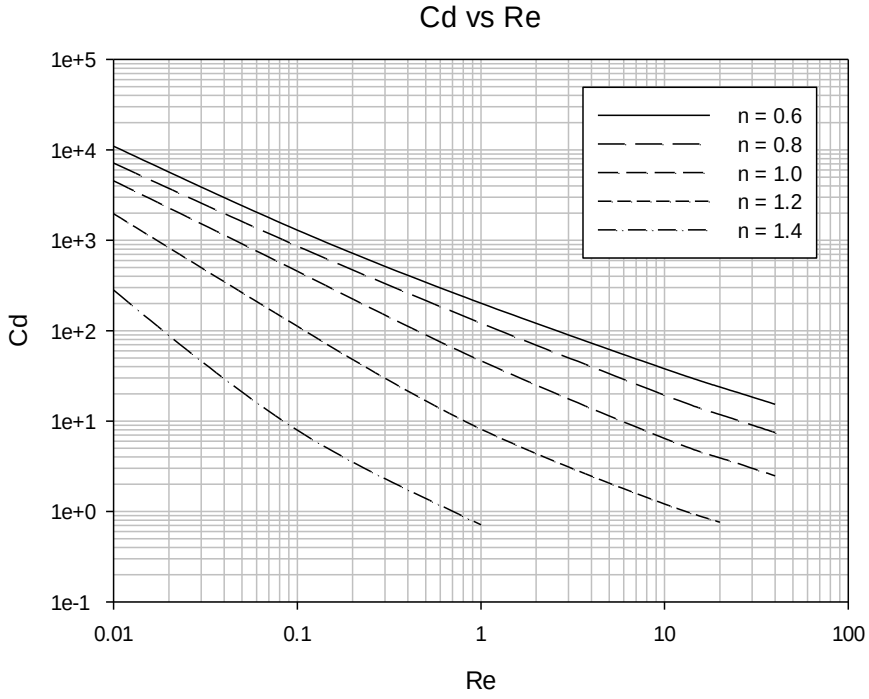

Figure 194: Cd vs Re for different power law values. Case 4, Cassini Oval, (c/d)2 = 0.7, b/R = 0.1

7.2.4.2.2 b/R = 0.3

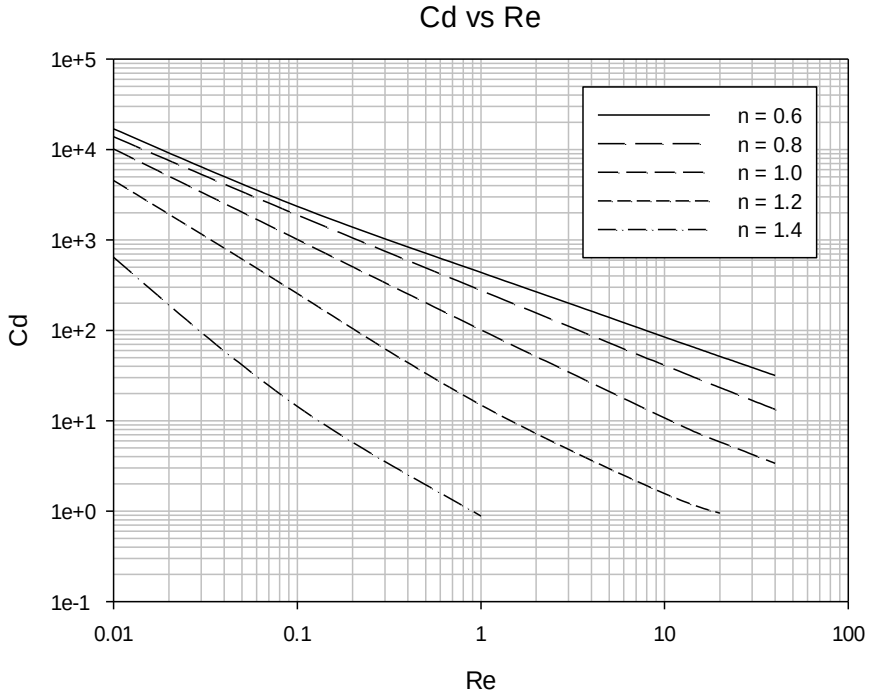

Figure 195: Cd vs Re for different power law values. Case 4, Cassini Oval, (c/d)2 = 0.7, b/R = 0.3

7.2.4.2.3 b/R = 0.5

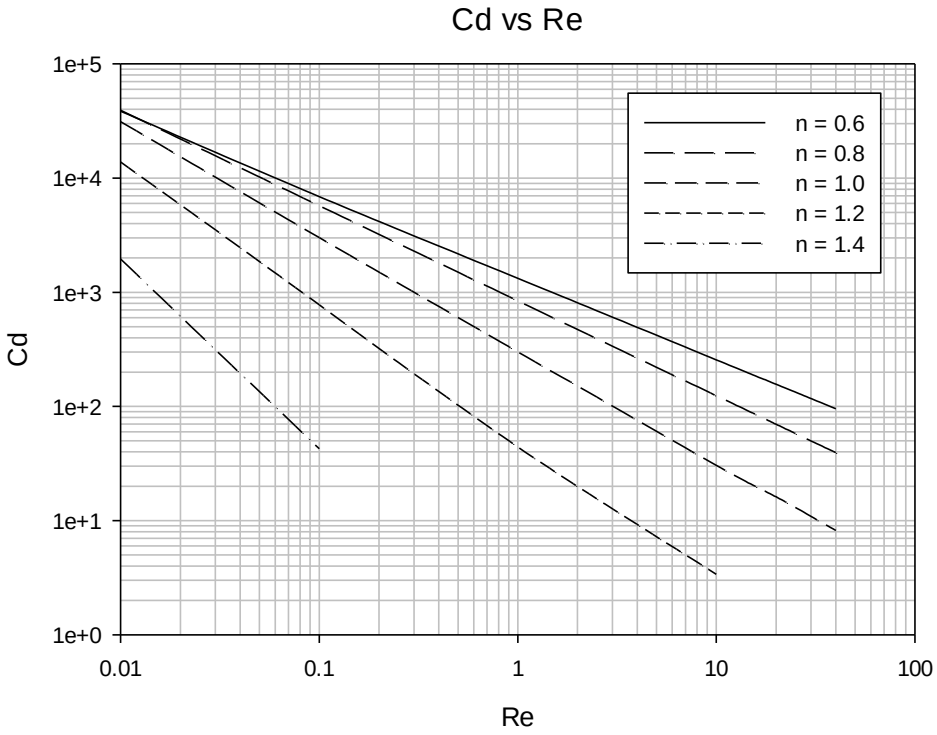

Figure 196: Cd vs Re for different power law values. Case 4, Cassini Oval, (c/d)2 = 0.7, b/R = 0.5

7.2.4.2.4 b/R = 0.7

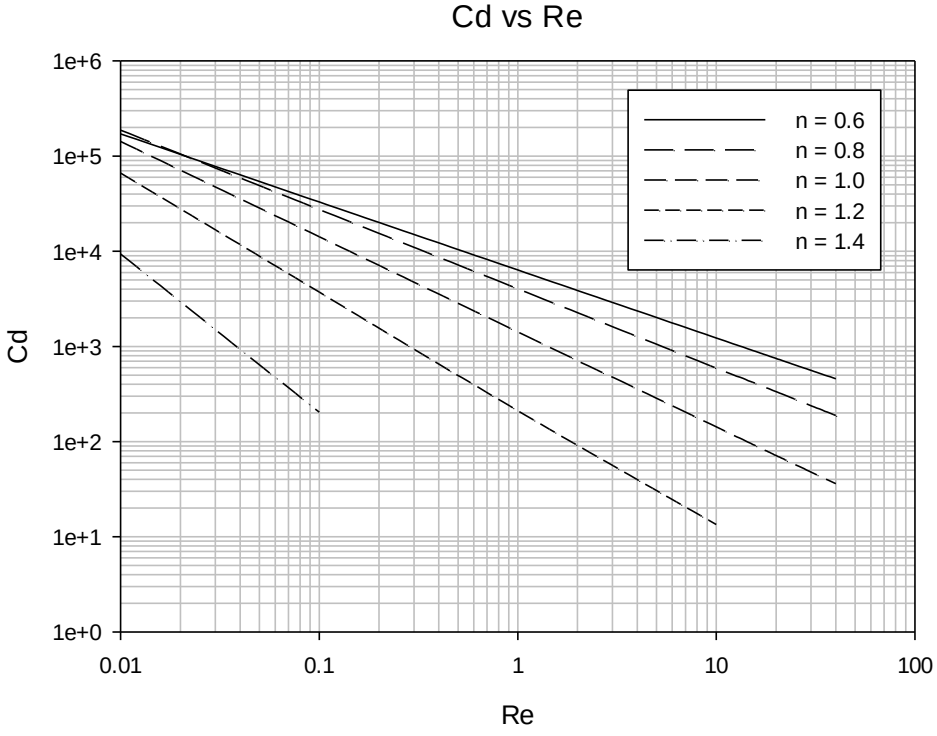

Figure 197: Cd vs Re for different power law values. Case 4, Cassini Oval, (c/d)2 = 0.7, b/R = 0.7

7.2.4.3 $(c/d)^2 = 0.95$

7.2.4.3.1 b/R = 0.1

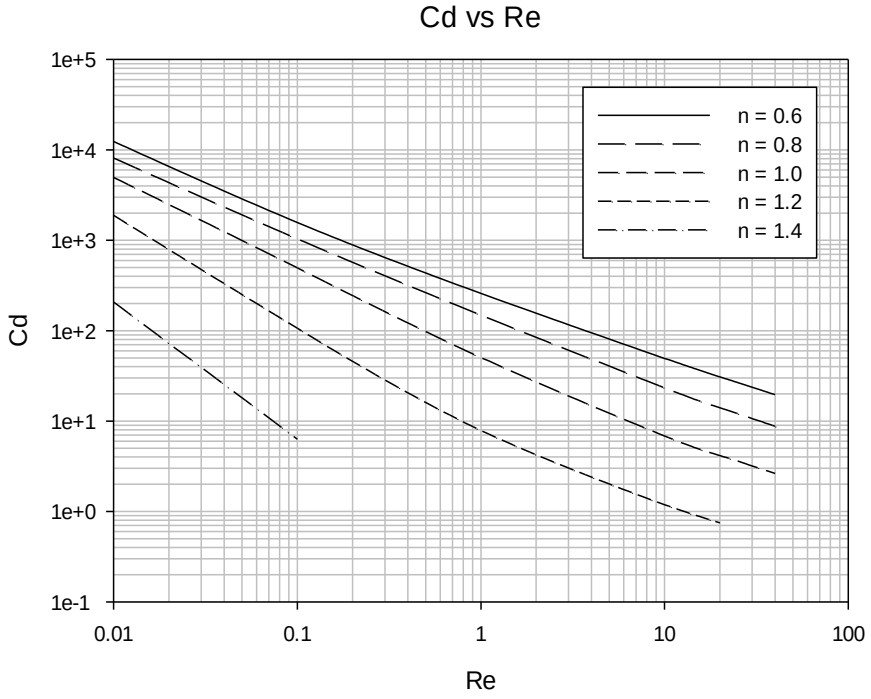

Figure 198: Cd vs Re for different power law values. Case 4, Cassini Oval, (c/d)2 = 0.95, b/R = 0.1

7.2.4.3.2 b/R = 0.3

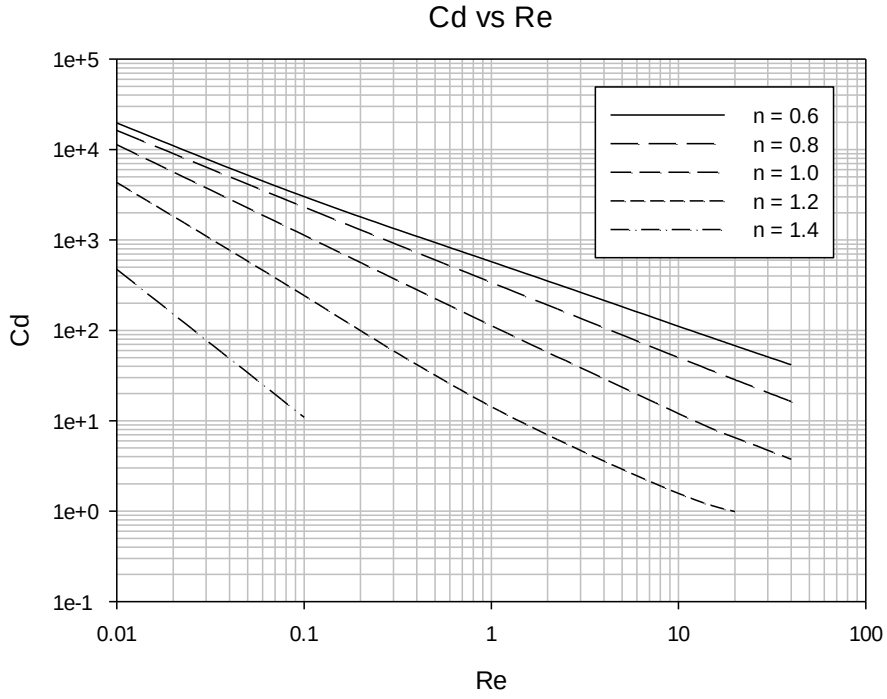

Figure 199: Cd vs Re for different power law values. Case 4, Cassini Oval, (c/d)2 = 0.95, b/R = 0.3

7.2.4.3.3 b/R = 0.5

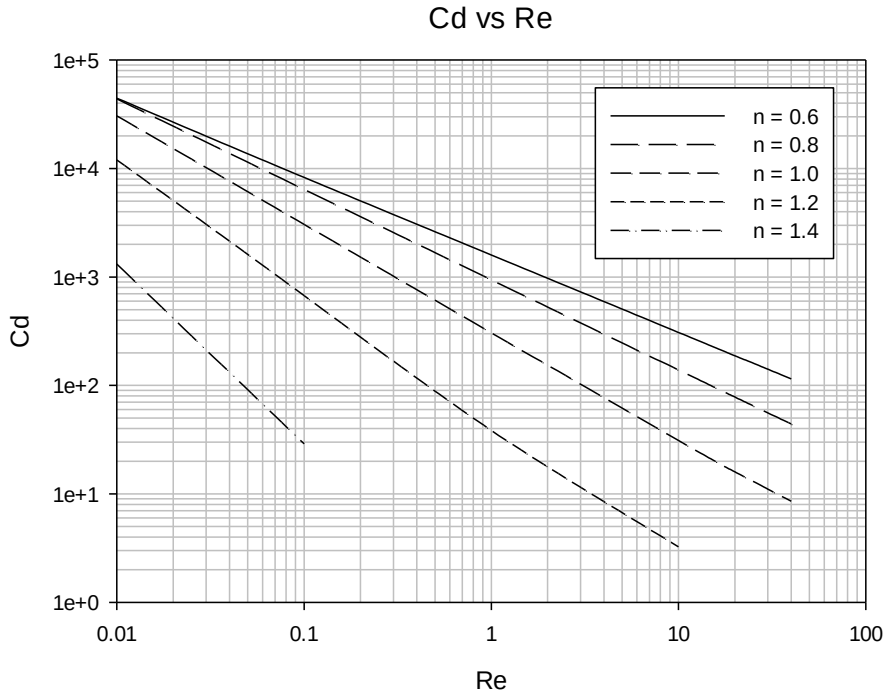

Figure 200: Cd vs Re for different power law values. Case 4, Cassini Oval, (c/d)2 = 0.95, b/R = 0.5

7.2.4.3.4 b/R = 0.7

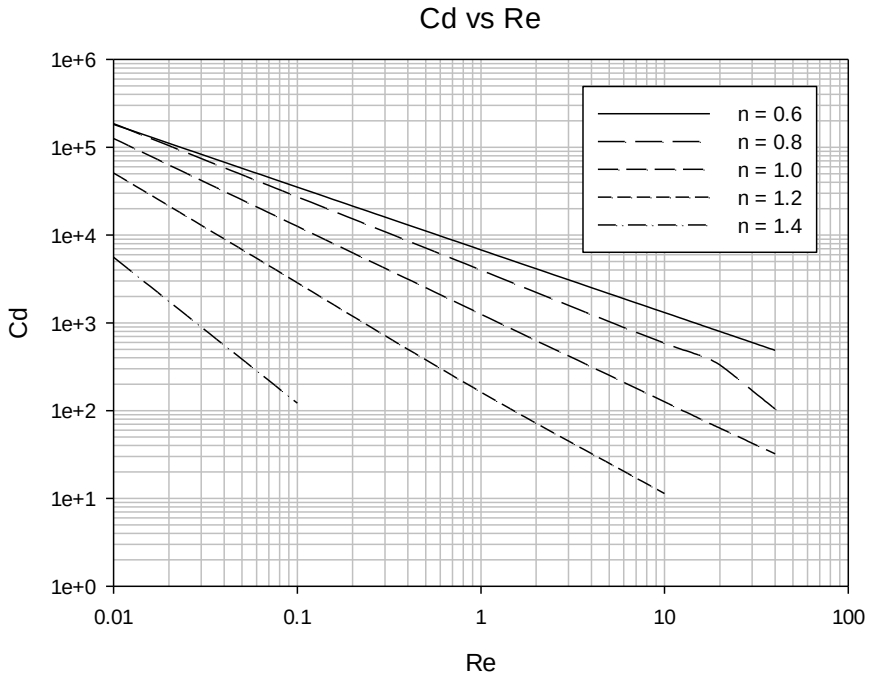

Figure 201: Cd vs Re for different power law values. Case 4, Cassini Oval, (c/d)2 = 0.95, b/R = 0.7

7.3 Velocity Streamlines and Pressure Contours (Selected Cases)

As an example, the velocity streamlines and the pressure contours for the case of Cassini oval with shape factor $(c/d)^2 = 0.3$, with confinement ratio $b/R = 0.5$ for power law index $n = 1.2$ are shown here. The velocity streamlines are shown in figures 202-205, while the pressure contours are shown in figures 206-209. It was observed from the streamlines that for higher power law indexes, the flow separates more easily at lower Reynolds number. Little to no separation is seen for the shear thinning and Newtonian fluids. Similar trend of the flow becoming unsteady at lower Reynolds numbers for higher power law indexes was also observed.

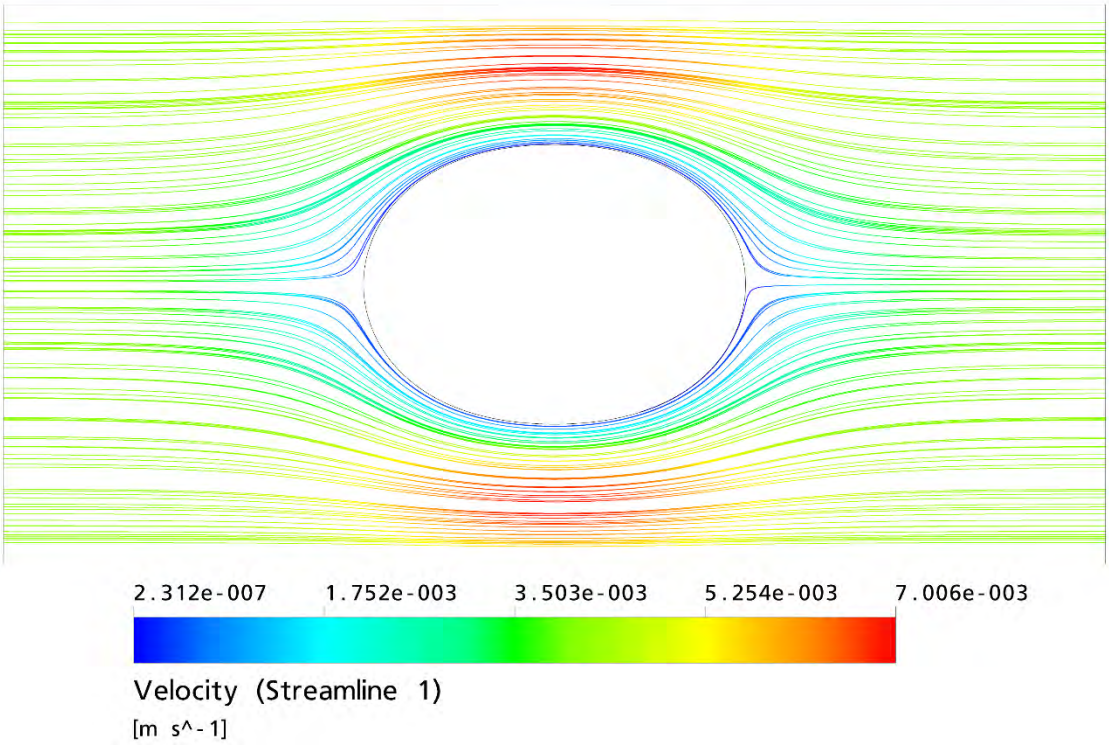

Figure 202: Velocity streamlines, Case 4, Cassini oval (c/d)2 = 0.3, b/R = 0.5, n = 1.4, Re = 0.01

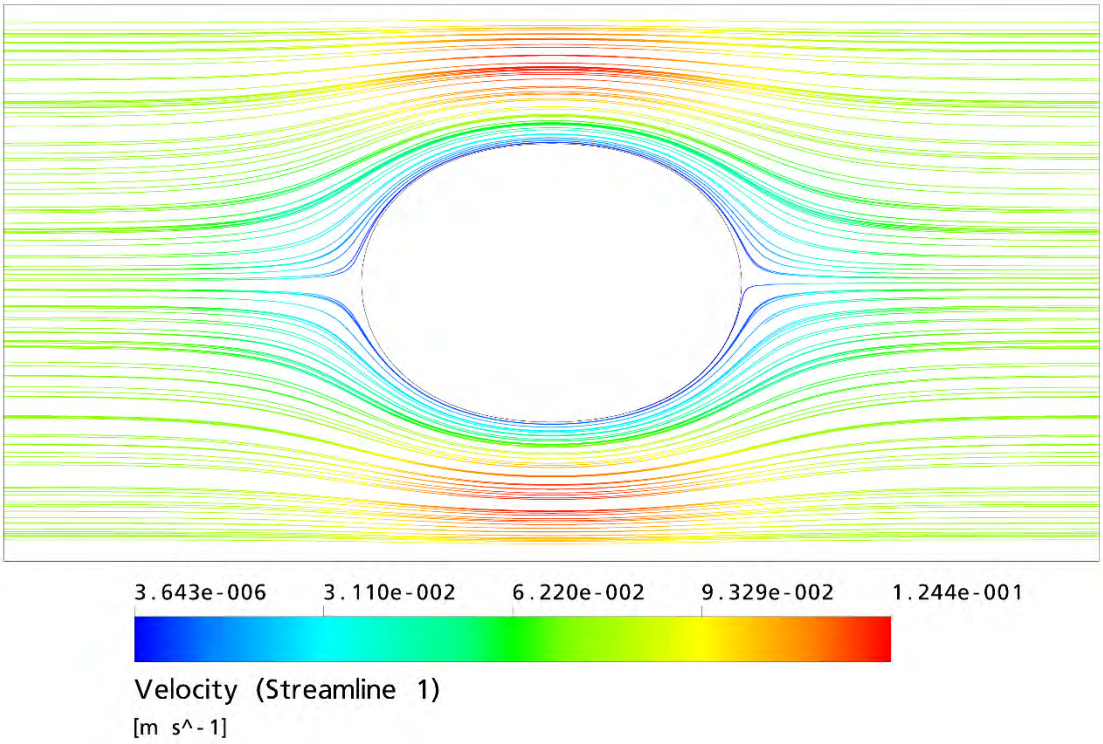

Figure 203: Velocity streamlines, Case 4, Cassini oval (c/d)2 = 0.3, b/R = 0.5, n = 1.4, Re = 0.1

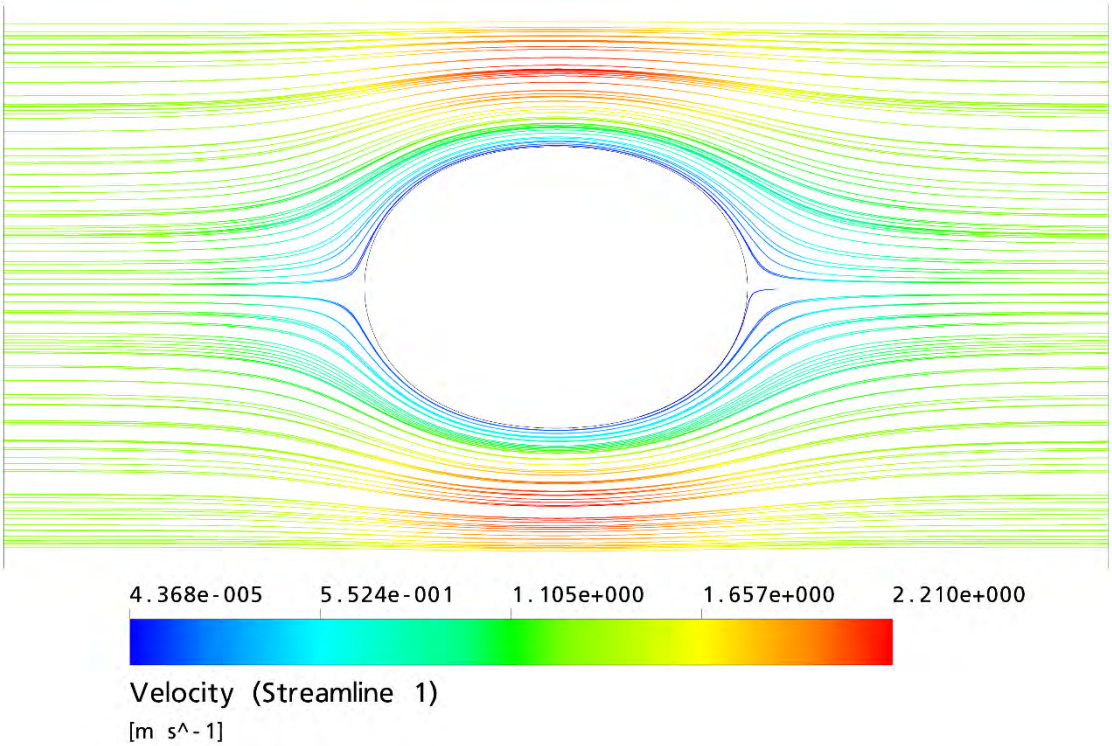

Figure 204: Velocity streamlines, Case 4, Cassini oval (c/d)2 = 0.3, b/R = 0.5, n = 1.4, Re = 1

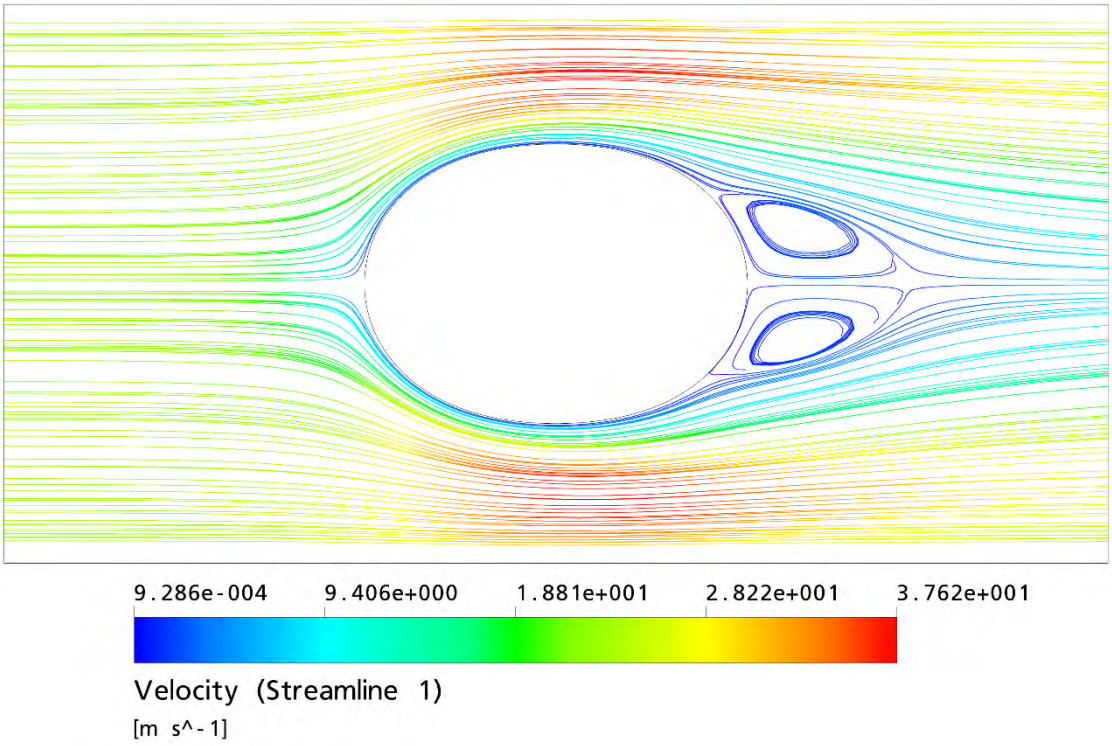

Figure 205: Velocity streamlines, Case 4, Cassini oval (c/d)2 = 0.3, b/R = 0.5, n = 1.4, Re = 10

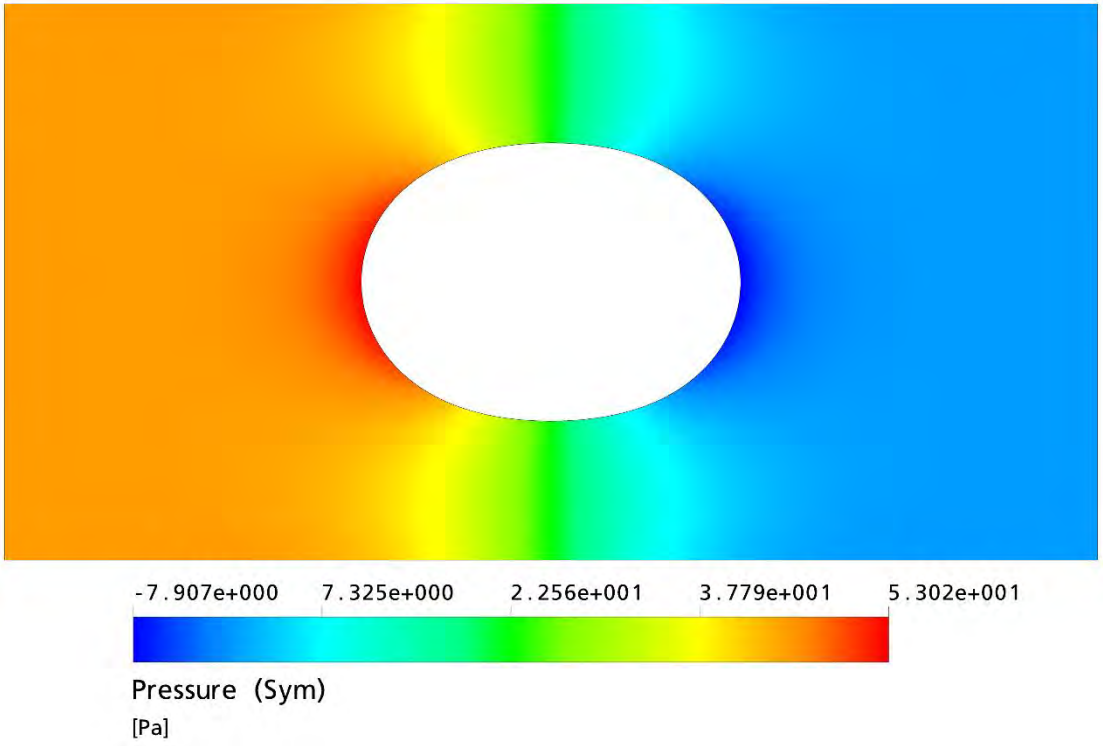

Figure 206: Pressure contours, Case 4, Cassini oval (c/d)2 = 0.3, b/R = 0.5, n = 1.4, Re = 0.01

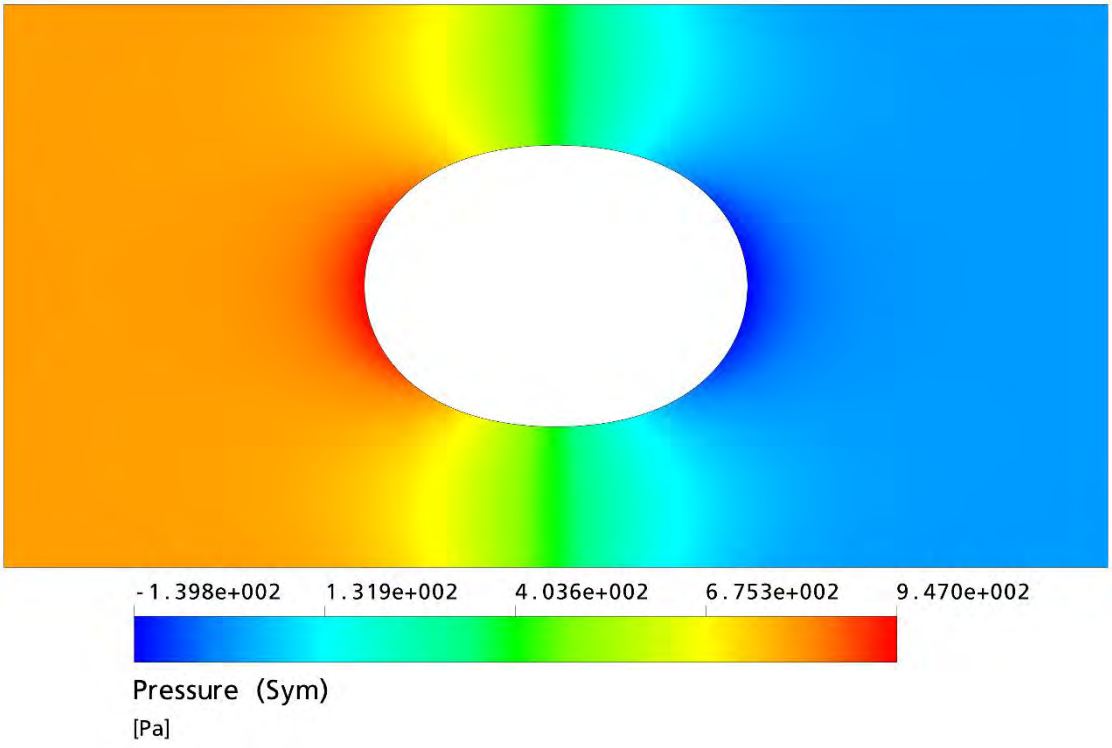

Figure 207: Pressure contours, Case 4, Cassini oval (c/d)2 = 0.3, b/R = 0.5, n = 1.4, Re = 0.1

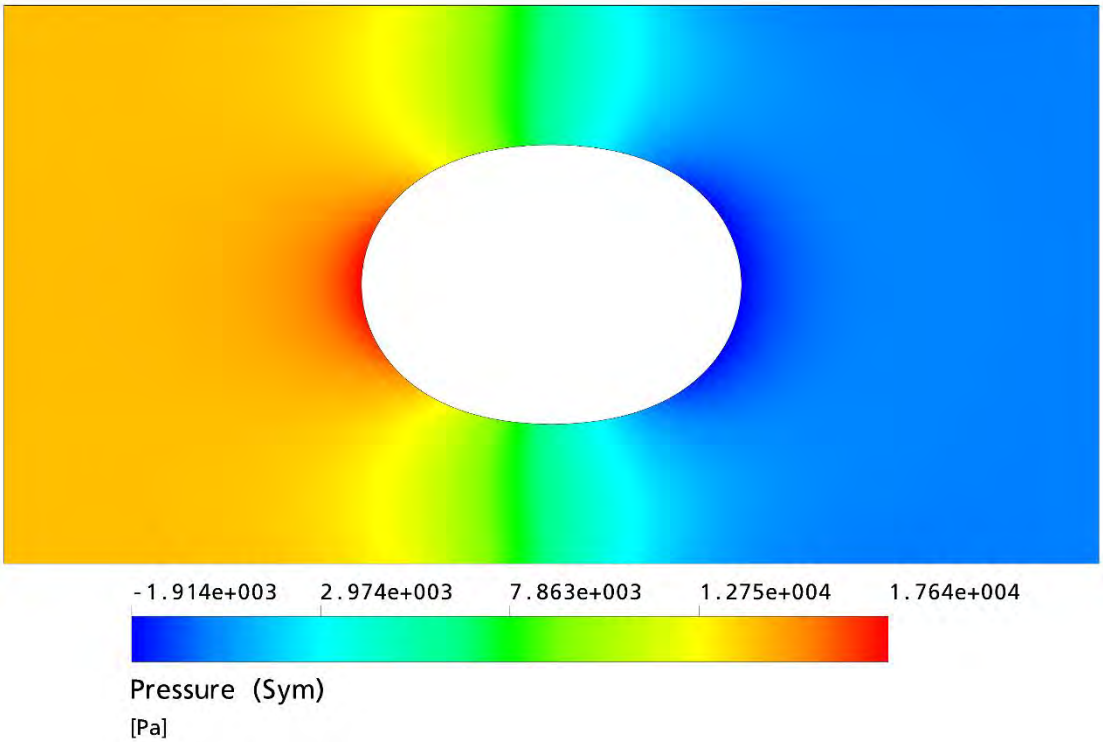

Figure 208: Pressure contours, Case 4, Cassini oval (c/d)2 = 0.3, b/R = 0.5, n = 1.4, Re = 1

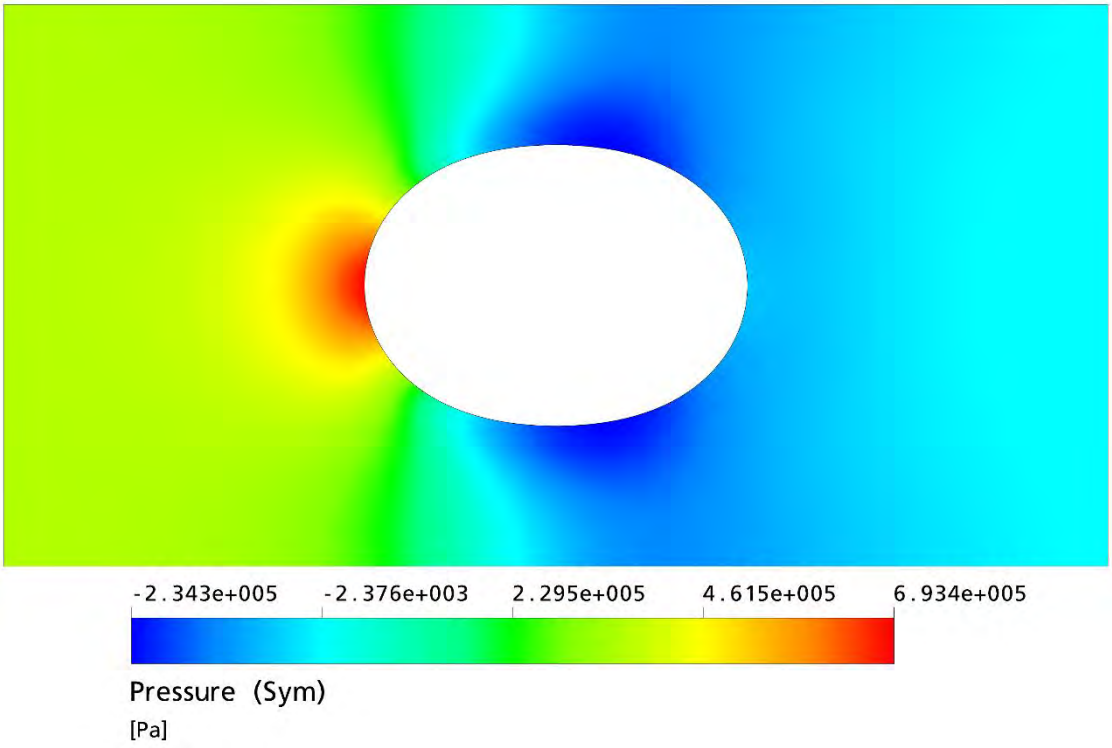

Figure 209: Pressure contours, Case 4, Cassini oval (c/d)2 = 0.3, b/R = 0.5, n = 1.4, Re = 10

Chapter 8. Conclusion

A numerical investigation was carried out in this study for the flow caused by the translational motion of micro-scale axisymmetric prolate spheroid and Cassini oval particles in a stationary viscous fluid along the axis of revolution of a coaxial cylindrical pore bounding the flow. A parametric study was carried out to investigate the effects of wall confinement, Reynolds number, and Newtonian and non-Newtonian characteristics of the fluid on the flow regime and the drag force experienced by the particles.

- For the case of creeping motion of prolate particles in Newtonian fluids, it was seen that as the confinement ratio increased, the normalized drag force on the particles also increased. The force increased rapidly for higher confinement ratio. The results are in agreement with the physics of the problem and were validated against the analytical solution of Yeh and Keh [51].
- For the case of low Reynolds number motion of prolate particles in Newtonian fluids, it was seen that for the same confinement ratio, the coefficient of drag decreased with increase in Reynolds number. It was also seen that for the same Reynolds number, the coefficient of drag increased with increase in the confinement ratio. Analytical results for unbounded flow over a sphere were only available [50]. These results were used as a benchmark to relate and justify the rest of the results.
- For the case of creeping motion of prolate particles in non-Newtonian fluids, it was seen that for the same power law index as the confinement ratio increased, the drag coefficient on the particles also increased. It was also seen that for the same confinement ratio, the coefficient of drag force increased while the coefficient of drag decreased with increase in the power law index. Analytical results for unbounded flow over a sphere for shear thinning were only available [81]. These results were used as a benchmark to relate and justify the rest of the results.
- For the case of low Reynolds number motion of prolate particles in non-Newtonian fluids, it was seen that for the same confinement ratio and the same power law index, the coefficient of drag decreased with increase in Reynolds

number. It was also seen that for the same Reynolds number and the same confinement ratio, the coefficient of drag decreased with increase in power law index. Furthermore, it was seen that for the same Reynolds number and the same power law index, the coefficient of drag increased with increase in the confinement ratio. It was noted that for shear thickening fluids, the flow separation was induced at lower Reynolds number when compared to Newtonian and shear thinning fluids. Following the same idea, the shear thickening flows became unsteady at lower Reynolds number compared to Newtonian and shear thinning fluids. Analytical results for unbounded flow over a sphere for shear thinning were only available [52]. These results were used as a benchmark to relate and justify the rest of the results.

- The present study contributes towards the development of the standard drag curve for non-Newtonian fluids. It also contributes the data on wall effects for shapes other than the sphere. These are useful in studies focusing on the motion and settling of particles inside a tube. As evident from the literature review, existing data on shear thinning and specially shear thickening fluids is insufficient. This study provides such results through numerical simulations, thus, opening more research options for the case of shear thinning and shear thickening fluids by providing a reference point.
- Future research ideas may include simulations at higher Reynolds number. Efforts were made to simulate the non-Newtonian flow for Reynolds number high enough to induce vortex shedding in the wake region since research on non-Newtonian vortex shedding is scarce. Although these simulations were unsuccessful in the present case, it is a valid problem that can be studied in future research. Furthermore, the particles in the present study exhibit translation only. It is of interest to investigate the combined translational and rotational motion of such particles. Unfruitful efforts were made to simulate such flows for non-Newtonian. These can investigated in future studies.

References

[1] A. Sakashita, N. Urakami, P. Ziherl, and M. Imai, "Three-dimensional analysis of lipid vesicle transformations," *Soft Matter,* vol. 8, pp. 8569-8581, 2012.

[2] K. Helal, T. Biben and J.P. Hansen, "Influence of capillary confinement on the equilibrium shape of vesicles," *Journal of Physics: Condensed Matter,* vol. 11, issue 6, pp. L51-L58, 1999.

[3] J. Hong, C. Fu, H. Lin, and W. Tan, "Non-Newtonian effects on low-density lipoprotein transport in the arterial wall," *Journal of Non-Newtonian Fluid Mechanics,* vol. 189-190, issue 1, pp. 1-7, 2012

[4] F.J.H. Gijsen, E. Allanic, F.N. van de Vosse, and J.D. Janssen, "The influence of the non-Newtonian properties of blood on the flow in large arteries: unsteady flow in a 90° curved tube," *Journal of Biomechanics,* vol. 32, issue 6, pp. 705-713, 1999.

[5] D. Wang and J. Bernsdorf, "Non-Newtonian blood flow simulation on cerebral aneurysms," *Computers and Mathematics with Applications,* vol. 58, issue 5, pp. 1024-1029, 2009.

[6] B.M. Johnston, P.R. Johnston, S. Corney, and D. Kilpatrick, "Non-Newtonian blood flow in human right coronary arteries: steady state simulations," *Journal of Biomechanics,* vol. 37, issue 5, pp. 709-720, 2004.

[7] M.G. Rabby, A. Razzak, and M.M. Molla, "Pulsatile non-Newtonian blood flow through a model of arterial stenosis," *Procedia Engineering,* vol. 56, pp. 225-231, 2013.

[8] H.G. Morales, I. Larrabide, A.J. Geers, M.L. Aguilar, and A.F. Frangi, "Newtonian and non-Newtonian blood flow in coiled cerebral aneurysms," *Journal of Biomechanics,* vol. 46, issue 13, pp. 2158-2164, 2013.

[9] F.J.H. Gijsen, F.N. van de Vosse, and J. D. Janssen, "The influence of the non-Newtonian properties of blood on the flow in large arteries: steady flow in a carotid bifurcation model," *Journal of Biomechanics,* vol. 32, issue 6, pp. 601-608, 1999.

[10] J. Venkatesan, D.S. Sankar, K. Hemalatha, and Y. Yatim, "Mathematical analysis of casson fluid model for blood rheology in stenosed narrow arteries," *Journal of Applied Mathematics*, pp. 1-11, 2013.

[11] K. Sharma, and S.V. Bhat, "Non-Newtonian rheology of leukemic blood and plasma: are n and k parameters of power law model diagnostic?," *Physiological chemistry and physics and medical NMR*, vol. 24, issue 4, pp. 307-312, 1992.

[12] J. Bertgier and P. Silberzan, *Microfluidics for Biotechnology*. Norwood, MA: Artech House, 2006.

[13] A. Folch, *Introduction to BioMEMS*. Boca Raton: CRC Press, 2013.

[14] M. Koch, A. Evans, and A. Brunnschweiler, *Microfluidic Technology and Applications*. Hertfordshire, England: Research Studies Press, 2000.

[15] Y. Nahmias and S. Bhatia, *Microdevices in Biology and Medicine*. Norwood, MA: Artech House, 2009.

[16] W. Wei, W. Pengyu, L. Kai, D. Jimiao, W. Kunyi, and G. Jing, "Prediction of the apparent viscosity of non-Newtonian water-in-crude oil emulsions," *Petroleum Exploration and Development*, vol. 40, issue 1, pp. 130-133, 2013.

[17] S.D. Dhole, R.P. Chhabra, and V. Eswaran, "Mass transfer from a spherical bubble rising in power-law fluids at intermediate Reynolds numbers," *International Communications in Heat and Mass Transfer*, vol. 34, issue 8, pp. 971-978, 2007.

[18] G.S. Hansford, M. Litt, "Mass transport from a rotating disk into power-law liquids," *Chemical Engineering Science,* vol. 23, issue 8, pp. 849-864, 1968.

[19] C.-O. Ng, "Mass transport in a layer of power-law fluid forced by periodic surface pressure," *Wave Motion*, vol. 39, issue 3, pp. 241-259, 2004.

[20] A.V. Shenoy, "Momentum/heat transfer analogy for power-law fluids during turbulent boundary layer flow with mild pressure gradients," *International Journal of Heat and Mass Transfer*, vol. 35, issue 1, pp. 53-62, 1992.

[21] J.C. Kurniaa, A.P. Sasmitob, and A.S. Mujumdar, "Laminar heat transfer performance of power law fluids in coiled square tube with various configurations," *International Communications in Heat and Mass Transfer,* vol. 57, pp. 100-108, 2014.

[22] O. Turan, J. Lai, R.J. Poole, and N. Chakraborty, "Laminar natural convection of power-law fluids in a square enclosure submitted from below to a uniform heat flux density," *Journal of Non-Newtonian Fluid Mechanics,* vol. 199, pp. 80-95, 2013.

[23] M.A. Vakili, M.H. Saidi, and A. Sadeghi, "Thermal transport characteristics pertinent to electrokinetic flow of power-law fluids in rectangular microchannels," *International Journal of Thermal Sciences,* vol. 79, pp. 76-89, 2014.

[24] N. Bagdassarov and H. Pinkerton, "Transient phenomena in vesicular lava flows based on laboratory experiments with analogue materials," *Journal of Volcanology and Geothermal Research,* vol. 132, issues 2-3, pp. 115-136, 2004.

[25] L. Huang, C.-O. Ng, and A.T. Chwang, "A Fourier–Chebyshev collocation method for the mass transport in a layer of power-law fluid mud," *Computer Methods in Applied Mechanics and Engineering,* vol. 195, issues 9-12, pp.1136-1153, 2006.

[26] E. Bovet, B. Chiaia, and L. Preziosi, "A new model for snow avalanche dynamics based on non-Newtonian fluids," *Meccanica,* vol. 45, issue 6, pp. 753-765, 2010.

[27] R.M. Iverson, "The physics of debris flows," *Reviews of Geophysics,* vol. 35, issue 3, pp. 245-296, 1997.

[28] G.V. Madhav and R.P. Chhabra, "Drag on non-spherical particles in viscous fluids," *International Journal of Mineral Processing,* vol. 43, issues 1-2, pp. 15-29, 1995.

[29] R.P. Chhabra, "Wall effects on free-settling velocity of non-spherical particles in viscous media in cylindrical tubes," *Powder Technology,* vol. 85, issue 1, pp. 83-90, 1995.

[30] L.E. Becker, G.H. McKinley, and H.A. Stone, "Sedimentation of a sphere near a plane wall: weak non-Newtonian and inertial effects," *Journal of Non-Newtonian Fluid Mechanics,* vol. 63, issues 2-3, pp. 201-233, 1996.

[31] S.N. Shah, Y. El Fadili, and R.P. Chhabra, "New model for single spherical particle settling velocity in power law (visco-inelastic) fluids," *International Journal of Multiphase Flow,* vol. 33, issue 1, pp. 51-66, 2007.

[32] N. Kishan, and S. Jagadha, "MHD effects on non-Newtonian micro polar fluid with uniform suction/blowing and heat generation in the presence of chemical reaction and thermophoresis," *International Journal of Research in Engineering and Technology,* vol. 2, issue 9, pp. 350-358, 2013.

[33] R.M. Wu and D.J. Lee, "Hydrodynamic drag on non-spherical floc and free-settling test," *Water Research,* vol. 35, issue 13, pp. 3226-3234, 2001.

[34] T.O. Chimamkpam, M.G. Rasteiro, F.A.P. Garcia, E. Antunes, P. Ferreira, D. Hunkeler*, et al.*, "Solution viscosity and flocculation characteristics of linear polymeric flocculants in various media," *Chemical Engineering Research and Design,* vol. 89, issue 7, pp. 1037-1044, 2011.

[35] G.G. Stokes, "On the effect of the internal friction of fluids on the motion of pendulums," *Transactions of the Cambridge Philosophical Society,* vol. 9, pp. 8-106, 1851.

[36] C.W. Oseen, *Neuere Methoden und Ergebnisse in der Hydrodynamik, Akademische.* Leipzig: Verlagsgesellschaft m.b.h., 1927 (in German).

[37] I. Proudman and J.R.A. Pearson, "Expansions at small Reynolds numbers for the flow past a sphere and a circular cylinder," *Journal of Fluid Mechanics,* vol. 2, issue 3, pp. 237-262, 1957.

[38] J.R. Ockendon and G.A. Evans, "The drag on a sphere in low Reynolds number flow," *Journal of Aerosol Science,* vol. 3, issue 4, pp. 237-242, 1972.

[39] S. Goldstein, "The steady flow of viscous fluid past a fixed spherical obstacle at small Reynolds number," *Proceedings of the Royal Society of London,* vol. 123A, issue 791, pp. 225-235, 1929.

[40] W. Chester, D.R. Breach, and I. Proudman, “On the flow past a sphere at low Reynolds number,” *Journal of Fluid Mechanics,* vol. 37, issue 4, pp. 751-760, 1969.

[41] S.-J. Liao, “An analytic approximation of the drag coefficient for the viscous flow past a sphere,” *International Journal of Non-Linear Mechanics,* vol. 37, issue 1, pp. 1-18, 2002.

[42] M.D. Van Dyke, “Extension of Goldstein’s series for the Oseen drag of a sphere,” *Journal of Fluid Mechanic,* vol. 44, issue 2, pp. 365-372, 1970.

[43] V.G. Jenson, “Viscous flow around a sphere at low Reynolds number (<40),” *Proceedings of the Royal Society of London,* vol. 249A, pp. 346-366, 1959.

[44] B.P. Le Clair and A.E. Hamielec, “Viscous flow through particle assemblages at intermediate Reynolds numbers: steady state solutions for flow through assemblages of cylinders,” *Industrial & Engineering Chemistry Fundamentals,* vol. 9, issue 4, pp. 608-613, 1970.

[45] B. Fornberg, “Steady viscous flow past a sphere at high Reynolds numbers,” *Journal of Fluid Mechanic,* vol. 190, pp. 471-489, 1988.

[46] A.J. Weisenborn and B.I.M. Ten Bosch, “Analytical approach to the Oseen drag on a sphere at infinite Reynolds number,” *SIAM Journal of Applied Mathematics,* vol. 53, issue 3, pp. 601-620, 1993.

[47] T.A. Johnson and V.C. Patel, “Flow past a sphere up to a Reynolds number of 300,” *Journal of Fluid Mechanics,* vol. 378, issue 1, pp. 19-70, 1999.

[48] K.A. Cliffe, A. Spence, and S.J. Tavener, “O(2)-symmetry breaking bifurcation: with application to the flow past a sphere in a pipe,” *International Journal for Numerical Methods in Fluids,* vol. 32, issue 2, pp. 175-200, 2000.

[49] R. Mittal, “A Fourier-Chebyshev spectral collocation method for simulating flow past spheres and spheroids,” *International Journal for Numerical Methods in Fluids,* vol. 30, issue 7, pp. 921-937, 1999.

[50] R. Clift, J.R. Grace, and M.E. Weber, *Bubbles, Drops and Particles*. NewYork: Academic Press, 1978, p. 56.

[51] H.Y. Yeh and H.J. Keh, “Axisymmetric creeping motion of a prolate particle in a cylindrical pore,” *European Journal of Mechanics - B/Fluids,* vol. 39, pp. 52-58, 2013.

[52] K. Ceylan, S. Herdem, and T. Abbasov, “A theoretical model for estimation of drag force in the flow of non-newtonian fluids around spherical solid particles,” *Powder Technology,* vol. 103, issue 3, pp. 286-291, 1999.

[53] Y. Tomita, “On the fundamental formula of non-Newtonian flow,” *Bulletin of JSME,* vol. 2, issue 7, pp. 469-474, 1959.

[54] G.C. Wallick, J.G. Savins, and D.R. Arterburn, “Tomita solution for the motion of a sphere in a power-law fluid,” *Physics of Fluids,* vol. 5, issue 3, pp. 367-368, 1962.

[55] J.C. Slattery, “Flow of a simple non-Newtonian fluid past a sphere,” *Applied Scientific Research,* vol. 10, issue 1, pp. 286-294, 1961.

[56] R.D. Foster and J.C. Slattery, “Creeping flow past a sphere of a Reiner-Rivlin fluid,” *Applied Scientific Research,* vol. 12, issue 3, pp. 213-222, 1963.

[57] D.C. Leigh, “Non-Newtonian Fluids and the Second Law of Thermodynamics,” *Physics of Fluids,* vol. 5, issue 4, pp.501-502, 1962.

[58] A.I. Leonov, “Extremum principles and exact two-side bounds of potential: Functional and dissipation for slow motions of nonlinear viscoplastic media,” *Journal of Non-Newtonian Fluid Mechanics,* vol. 28, issue 1, pp. 1-28, 1988.

[59] A.J. Ziegenhagen, R.B. Bird, and M.W. Johnson, “Non-Newtonian flow around a sphere,” *Transaction of the Society of Rheology,* vol. 5, pp. 47-49, 1961.

[60] J.C. Slattery, “Approximations to the drag force on a sphere moving slowly through either an Ostwald-de Waele or a Sisko fluid,” *American Institute of Chemical Engineers,* vol. 8, issue 5, pp. 663-667, 1962.

[61] A.J. Ziegenhagen, “The very slow flow of a Powell-Eyring fluid around a sphere,” *Applied Scientific Research,* vol. 14, issue 1, pp. 43-56, 1964.

[62] N. Mitsuishi, A. Yamanaka, and F. Miyahara, “A study on the drag coefficient of the spheres falling in the non-Newtonian fluids,” *Technical Report Kyushu University,* vol. 44, p. 192, 1971.

[63] R.P. Chhabra, C. Tiu, and P.H.T. Uhlherr, “Shear-thinning effects in creeping flow about a sphere” in *Rheology,* vol. 2. G. Astarita, G. Marrucci, L. Nicolais, Ed. New York: Plenum Press, 1980, pp. 9-16.

[64] R.P. Chhabra and P.H.T. Uhlherr, “Creeping motion of spheres through shear-thinning elastic fluids described by the Carreau viscosity equation,” *Rheologica Acta,* vol. 19, issue 2, pp. 187-195, 1980.

[65] M.L. Wasserman and J.C. Slattery, “Upper and lower bounds on the drag coefficient of a sphere in a power-model fluid,” *American Institute of Chemical Engineers,* vol. 10, issue 3, pp. 383-388, 1964.

[66] Y.I. Cho and J.P. Hartnett, “Drag coefficients of a slowly moving sphere in non-Newtonian fluids,” *Journal of Non-Newtonian Fluid Mechanics,* vol. 12, issue 2, pp. 243-247, 1983.

[67] S.W. Hopke and J.C. Slattery, “Upper and lower bounds on the drag coefficient of a sphere in an Ellis model fluid,” *American Institute of Chemical Engineers,* vol. 16, issue 2, pp. 224-229, 1970.

[68] R.P. Chhabra, I. Machač, and P.H.T. Uhlherr, “Some further observations on the creeping motion of spheres through Ellis model fluids,” *Rheologica Acta,* vol. 23, issue 4, pp. 457-460, 1984.

[69] A. Acharya, R.A. Mashelkar, and J. Ulbrecht, “Flow of inelastic and viscoelastic fluids past a sphere,” *Rheologica Acta,* vol. 15, issue 9, pp. 454-470, 1976.

[70] M.A. Lockyear, J.M. Davies, and T.E.R. Jones, “The importance of rheology in the determination of the carrying capacity of oil-drilling fluids,” in *Rheology*, vol. 2. G. Astarita, G. Marrucci, L. Nicolais, Ed. New York: Plenum Press, 1980, p. 127.

[71] Y. Kawase and J.J. Ulbrecht, “Drag and mass transfer in non-newtonian flows through multi-particle systems at low Reynolds numbers,” *Chemical Engineering Science,* vol. 36, issue 7, pp. 1193-1202, 1981.

[72] Y. Kawase and J. Ulbrecht, “The influence of walls on the motion of a sphere in non-Newtonian fluids,” *Rheologica Acta*, vol. 22, p. 27, 1983.

[73] S.L. Rathna, “Slow motion of a non-Newtonian liquid past a sphere,” *The Quarterly Journal of Mechanics and Applied Mathematics,* vol. 15, issue 4, pp. 427-434, 1962.

[74] N. Yoshioka and R. Nakamura, “On the creeping flow of generalized Newtonian fluid around a sphere,” *Kagaku Kogaku,* vol. 4, p. 130, 1966.

[75] A. Koizumi, Ph.D. dissertation, “Non-simple flows of a visco-plastic fluid,” University of Delaware, Newark, Delaware, 1974.

[76] Y. Kawase and M. Moo-Young, “Approximate solutions for power-law fluid flow past a particle at low Reynolds numbers,” *Journal of Non-Newtonian Fluid Mechanics,* vol. 21, issue 2, pp. 167-177, 1986.

[77] Y.I. Shmakov and L.M. Shmakova, “Viscosity of a dilute suspension of rigid spherical particles in a non-Newtonian fluid,” *Journal of Applied Mechanics and Technical Physics,* vol. 18, issue 5, pp. 655-659, 1977.

[78] K. Adachi, N. Yoshioka, and K. Yamamoto, “On non-Newtonian flow past a sphere,” *Chemical Engineering Science,* vol. 28, issue 11, pp. 2033-2043, 1973.

[79] K. Adachi, N. Yoshika, and K. Sakai, “An investigation of non-Newtonian flow past a sphere,” *Journal of Non-Newtonian Fluid Mechanics,* vol. 3, issue 2, pp. 107-125, 1977.

[80] M.J. Crochet, A.R. Davies, and K. Walters, “Finite element calculation of generalized Newtonian fluid,” in *Numerical Simulation of Non-Newtonian Flow*. Amsterdam: Elsevier, 1984.

[81] G. Dazhi and R.I. Tanner, “The drag on a sphere in a power-law fluid,” *Journal of Non-Newtonian Fluid Mechanics,* vol. 17, issue 1, pp. 1i12, 1985.

[82] A. Tripathi, R.P. Chhabra, and T. Sundararajan, “Power law fluid flow over spheroidal particles,” *Industrial & Engineering Chemistry Research,* vol. 33, issue 2, pp. 402-410, 1994.

[83] A. Tripathi and R.P. Chhabra, “Drag on spheroidal particles in dilatant fluids,” *American Institute of Chemical Engineers,* vol. 41, issue 3, pp. 728-731, 1995.

[84] D.I. Graham and T.E.R. Jones, “Settling and transport of spherical particles in power-law fluids at finite Reynolds number,” *Journal of Non-Newtonian Fluid Mechanics,* vol. 54, pp. 465-488, 1994.

[85] M.J. Whitney and G.J. Rodin, “Force–velocity relationships for rigid bodies translating through unbounded shear-thinning power-law fluids,” *International Journal of Non-Linear Mechanics,* vol. 36, issue 6, pp. 947-953, 2001.

[86] N. Kishore, R.P. Chhabra, and V. Eswaran, “Drag on a single fluid sphere translating in power-law liquids at moderate Reynolds numbers,” *Chemical Engineering Science,* vol. 62, pp. 2422-2434, 2007.

[87] R.I. Tanner, “Observations on the use of Oldroyd-type equations of state for viscoelastic liquids,” *Chemical Engineering Science,* vol. 19, pp. 349-355, 1964.

[88] P. Rajitha, R.P. Chhabra, N.E. Sabiri, and J. Comiti, “Drag on non-spherical particles in power law non-Newtonian media,” *International Journal of Mineral Processing,* vol. 78, issue 2, pp. 110-121, 2006

[89] R.G. Pereira, “Additional effects on internal flow of non-Newtonian fluids in the presence of a particle,” *Journal of Non-Newtonian Fluid Mechanics,* vol. 95, issues 2-3, pp. 85-100, 2000.

[90] A. K. Sahu, R. P. Chhabra, and V. Eswaran, ”Two-dimensional laminar flow of a power-law fluid across a confined square cylinder,” *Journal of Non-Newtonian Fluid Mechanics,* vol. 165, issues 13-14, pp. 752-763, 2010.

[91] W. Ostwald, “Uber die Geschwindigkeitsfunktion der Viskositat disperser Systeme. I,” *Colloid and Polymer Science,* vol. 36, pp. 99-117, 1925 (in German).

[92] A. de Waele, “Viscometry and plastometry,” *Journal of the Oil and Colour Chemists' Association,* vol. 6, issue 38, pp. 33-69, 1923.

[93] P.J. Carreau, “Rheological Equations from Molecular Network Theories,” *Transaction of the Society of Rheology,* vol. 16, issue 1, p. 99-127, 1972.

[94] K. Yasuda, “Investigation of the analogies between viscometric and linear viscoelastic properties of polystyrene fluids,” Ph.D. thesis, Massachusetts Institute of Technology. Dept. of Chemical Engineering, 1979.

[95] N. Casson, “Rheology of disperse systems,” in *Flow Equation for Pigment Oil Suspensions of the Printing Ink Type. Rheology of Disperse Systems,* C.C. Mill, Ed. London, UK: Pergamon Press, pp. 84-102, 1959.

[96] M.M. Cross, “Rheology of non-Newtonian fluids: A new flow equation for pseudoplastic systems,” *Journal of Colloid Science,* vol. 20, issue 5, pp. 417-437, 1965.

[97] R.L. Replogle, H.J. Meiselman, and E.W. Merrill, "Clinical Implications of Blood Rheology Studies," *American Heart Association,* vol. 36, pp. 148-160, 1967.

[98] R. Darby, "Fluid properties in perspective," in *Chemical Engineering Fluid Mechanics,* 2nd ed., New York: Marcel Dekker, pp. 66-67, 2001.

[99] T.G. Myers, "Application of non-Newtonian models to thin film flow," *Physical Review E,* vol. 72, p. 066302, 2005.

[100] M.A. Hussain, S. Kar, and R.R. Puniyani, "Relationship between power law coefficients and major blood constituents affecting the whole blood viscosity," *Journal of. Bioscience,* vol. 24, issue 3, pp. 329-337, 1999.

[101] R.P. Chhabra and J.F. Richardson, "Non-Newtonian flow in the process industries: Fundamentals and engineering applications," *Canadian Society for Chemical Engineering,* vol. 79, issue 3, pp. 471-472, 1999.

[102] A.B. Metzner and J.C. Reed, "Flow of non-Newtonian fluids—correlation of the laminar, transition, and turbulent-flow regions," American Institute of Chemical Engineers, vol. 1, issue 4, pp. 434-440, 1955.

[103] L.M. Milne-Thomson, *Theoretical Aerodynamics*. 1st ed., New York: Dover Publications, 1973.

[104] L.F. Richardson and S. Chapman, *Weather prediction by numerical process.* New York: Dover Publications, 1965.

[105] J.C.R. Hunt, "Lewis Fry Richardson and his contributions to mathematics, meteorology, and models of conflict," *Annual Review of Fluid Mechanics,* vol. 30, pp. xiii-xxxvi, 1998.

[106] N.L. Johnson, "The legacy and future of CFD at Los Alamos," in *Proceedings of the 1996 Canadian CFD Conference Invited talk*, Ottawa, Canada, 1996.

[107] F.H. Harlow, "Fluid dynamics in group t-3 Los Alamos National Laboratory," *Journal of Computational Physics,* vol. 195, pp. 414-433, 2004.

[108] F.H. Harlow, "A machine calculation method for hydrodynamic problems," Los Alamos Scientific Laboratory report LAMS-1956, 1955.

[109] R.A Gentry, R.E. Martin, and B.J. Daly, "An Eulerian differencing method for unsteady compressible flow problems," *Journal of Computational Physics,* vol. 1, issue 1, Pages 87-118, 1966.

[110] J.E. Fromm and F.H. Harlow, "Numerical solution of the problem of vortex street development," *Physics of Fluids,* vol. 6, issue 7, pp. 975-982, 1963.

[111] F. H. Harlow and J. E. Welch, "Numerical calculation of time-dependent viscous incompressible flow of fluid with a free surface," *Physics of Fluids,* vol. 8, issue 12, pp. 2182-2189, 1965.

[112] J.L. Hess and A.M.O. Smith, "Calculation of potential flow about arbitrary bodies," *Progress in Aerospace Sciences,* vol. 8, pp. 1-138, 1967.

[113] P.E. Rubbert and G.R. Saaris, “Review and evaluation of a three-dimensional lifting potential flow analysis method for arbitrary configurations,” presented at the AIAA 10th Aerospace Sciences Meeting, San Diego California, 1972, Paper 72-188.

[114] R. Carmichael and L.L. Erickson, “PAN AIR - a higher order panel method for predicting subsonic or supersonic linear potential flows about arbitrary configurations,” presented at the AIAA 14th Fluid and Plasma Dynamics Conference, Palo Alto California, 1981, Paper 81-1255.

[115] H.H. Youngren, E.E. Bouchard, R.M. Coopersmith, and L.R. Miranda, “Comparison of panel method formulations and its influence on the development of QUADPAN, an advanced low order method,” presented at the AIAA Applied Aerodynamics Conference, Danvers, Massachusetts, 1983, Paper 83-1827.

[116] J.L. Hess and D.M. Friedman, “Analysis of complex inlet configurations using a higher-order panel method,” presented at the AIAA Applied Aerodynamics Conference, Danvers, Massachusetts, 1983, Paper 83-1828.

[117] D.R. Bristow, “Development of panel methods for subsonic analysis and design,” NASA, Saint Louis, MO, Rep. NASA-CR-3234, 1980.

[118] D.L. Ashby, M.R. Dudley, S.K. Iguchi, L. Browne, and J. Katz, “Potential flow theory and operation guide for the panel code PMARC”, NASA, Moffett Field, CA, Rep. NASA-TM-102851, 1991.

[119] F.A. Woodward, F.A. Dvorak and E.W. Geller, “A computer program for three-dimensional lifting bodies in subsonic inviscid flow,” USAAMRDL, Ft. Eustis, Virginia, Rep. TR 74-18, 1974.

[120] J. Katz and B. Maskew, “Unsteady low-speed aerodynamic model for complete aircraft configurations,” presented at the AIAA Atmospheric Flight Mechanics Conference, Williamsburg Virginia, 1986, Paper 86-2180.

[121] B. Maskew, “Prediction of subsonic aerodynamic characteristics: a case for low-order panel methods,” presented at the AIAA 19th Aerospace Sciences Meeting, St. Louis, Missouri, 1981, Paper 81-0252.

[122] B. Maskew, “Program VSAERO theory document: A computer program for calculating nonlinear aerodynamic characteristics of arbitrary configurations,” NASA, Redmond, WA, Rep. NASA CR-4023, 1987.

[123] D. Pinella and P. Garrison, “Digital wind tunnel CMARC; Three-dimensional low-order panel codes,” Aerologic, 2009.

[124] R. Eppler and D.M. Somers, “A computer program for the design and analysis of low-speed airfoils,” NASA, Hampton, VA, Rep. NASA-TM-80210, 1980.

[125] M. Drela, “XFOIL: An analysis and design system for low Reynolds number airfoils,” *Springer-Verlag Lecture Notes in Engineering,* vol. 54, pp. 1-12, 1989.

[126] E. Murman and J. Cole, “Calculation of plane steady transonic flow,” presented at the AIAA 8th Aerospace Sciences Meeting, New York, 1970, Paper 70-188.

[127] F. Bauer, P. Garabedian, and D. Korn, “A theory of supercritical wing sections, with computer programs and examples,” Springer-Verlag Lecture Notes in Economics and Mathematical Systems, vol. 66, 1972.

[128] H.R. Mead and R.E. Melnik, “GRUMFOIL: A computer code for the viscous transonic flow over airfoils,” NASA, Bethpage, NY, Rep. NASA-CR-3806, 1985.

[129] A. Jameson and D. Caughey, “A finite volume method for transonic potential flow calculations,” presented at the Third AIAA Computational Fluid Dynamics Conference, Alburquerque, New Mexico, 1977, Paper 77-635.

[130] S.S. Samant, J.E. Bussoletti, F.T. Johnson, R.H. Burkhart, B.L. Everson, R.G. Melvin, *et al*., “TRANAIR: A computer code for transonic analyses of arbitrary configurations,” presented at the AIAA 25th Aerospace Sciences Meeting, Reno, Nevada, 1987, Paper 87-0034.

[131] A. Jameson, W. Schmidt, and E. Turkel, “Numerical solution of the Euler equations by finite volume methods using Runge-Kutta time-stepping schemes,” presented at the AIAA 14th Fluid and Plasma Dynamics Conference, Palo Alto, California, 1981, Paper 81-1259.

[132] P. Raj and J.E. Brennan, “Improvements to an Euler aerodynamic method for transonic flow simulation,” presented at the 25th Aerospace Sciences Meeting, Reno, Nevada, 1987, Paper 87-0040.

[133] D.M. Tidd, D.J. Strash, B. Epstein, A. Luntz, A. Nachshon, and T. Rubin, “Application of an efficient 3-D multigrid Euler method (MGAERO) to complete aircraft configurations,” presented at the AIAA 9th Applied Aerodynamics Conference, Baltimore, Maryland, 1991, Paper 91-3236.

[134] A. Jameson, T.J. Baker, and N.P. Weatherill, “Calculation of inviscid tramonic flow over a complete aircraft,” presented at the AIAA 24th Aerospace Sciences Meeting, Reno Nevada, 1986, Paper 86-0103.

[135] ANSYS, Inc., *ANSYS CFX Introduction,* pp. 1-2, Canonsburg, PA: 2012.

Appendix

Appendix A: Flowchart guide to ANSYS CFX processes

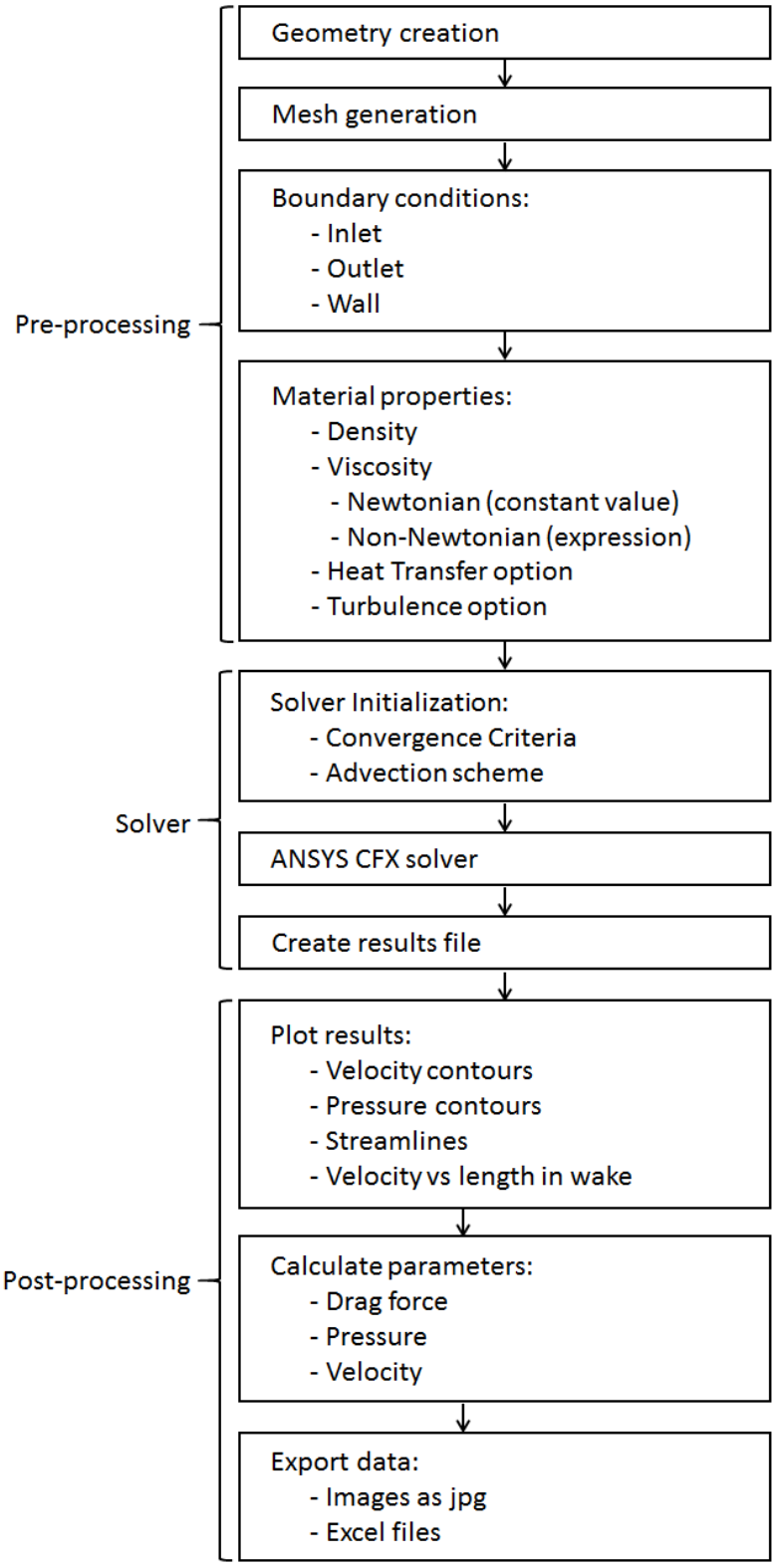

Vita

Muhammad Jasim Muhammad Rafiq was born on February 25, 1991, in Sharjah, United Arab Emirates. He joined the American University of Sharjah in 2008, from which he graduated cum laude in 2012 with a degree in Bachelor of Science in Mechanical Engineering. Soon after, he began the Master's program in Mechanical Engineering at the American University of Sharjah with a full-time scholarship as a graduate teaching assistant at the Mechanical Engineering department.